# TRANSIENT STUDY OF TURBULENT FLOW AND PARTICLE TRANSPORT DURING CONTINUOUS CASTING OF STEEL SLABS

BY

**QUAN YUAN**

B.E., Beijing University of Aeronautics & Astronautics, 1996
M.E., Beijing University of Aeronautics & Astronautics, 1999

**DISSERTATION**

Submitted in partial fulfillment of the requirements
for the degree of Doctor of Philosophy
in Department of Mechanical Engineering
in the College of Engineering of the University of Illinois at Urbana-Champaign, 2004

Urbana, Illinois

# ABSTRACT

This thesis investigates turbulent flow and impurity-particle transport during continuous casting of steel slabs, which are important to product quality. Velocities in the nozzle and mold regions were computed using Large Eddy Simulation (LES). The accuracy of these complex flow simulations was examined by comparing with measurements such as Particle Image Velocimetry (PIV) and hotwire anemometry. The computed time-averaged and *rms* velocities along the jet, across the top surface and in the lower region agreed reasonably with the measurements. The evolution of transient flow structures was investigated along with the corresponding time scales. Oscillating flow in the mold region caused asymmetrical particle transport. The top surface interface profile and fluctuations were estimated from the computed static-pressure distribution and agreed favorably with measurements. Interactions between flow in the two halves of the mold were found to cause large velocity fluctuations on the top surface. The differences between flow in a steel caster and in its corresponding water model were also quantified.

Using the computed three-dimensional time-dependent flow velocities, the motion and capture of impurity particles during continuous casting were simulated using a Lagrangian approach. A criterion was developed to model particle pushing and capture by the solidifying shell and was incorporated into the particle transport model. The criterion was validated by reproducing experimental results in different systems. The particle transport model was applied to a full-scale water model and reproduced the measured particle removal fractions of 27±5% for 0-10s and 26±2% for 10-100s. The model was then applied to simulate the motion and capture of slag particles in a thin-slab steel caster. The magnitudes of the steady and unsteady forces acting on the particles,

including the drag, lift, pressure gradient and stress gradient, added mass and Basset history, lubrication, Van der Waals interfacial and concentration gradient forces, were quantified. The simulations found that only about 8% of the small particles ($\leq$ 40μm) were safely removed by the top surface slag layer. This removal fraction was independent of both particle size and density. However, a higher removal fraction of about 12-70% was found for the larger (100μm-400μm) particles. The computational results were processed to predict the ultimate distribution of impurity particles in the solid thin-slab. The results of this work confirm the important role of flow transients in the transport and capture of particles during continuous casting, and can serve as a benchmark for future simplified models.

*To my family*

# ACKNOWLEDGEMENTS

# TABLE OF CONTENTS

page

# LIST OF TABLES

page

# LIST OF FIGURES

page

# NOMENCLATURE

| | |
|---|---|
| $a_0$ | liquid atomic radius (m) |
| $A_c$ | Particle accelerating parameter |
| $A_p$ | Particle surface area ($m^2$) |
| $C$ | weight concentration (wt pct) |
| $C_A$ | Correction factor on added mass force |
| $C_H$ | Correction factor on Basset history force |
| $d_p$ | particle diameter (m) |
| $D$ | diffusion coefficient ($m^2/s$) |
| $f$ | Frequency (Hz) |
| $\mathbf{F}_{\mathrm{A}}$ | Added mass force (N) |
| $\mathbf{F}_{\mathrm{B}}$ | Buoyancy force (N) |
| $\mathbf{F}_{\mathrm{D}}$ | Drag force (N) |
| $\mathbf{F}_f$ | Friction force (N) |
| $\mathbf{F}_{\mathrm{G}}$ | Gravitational force (N) |
| $\mathbf{F}_{\mathrm{Grad}}$ | Surface energy gradient force (N) |
| $\mathbf{F}_{\mathrm{I}}$ | Van der Waals interfacial force (N) |
| $\mathbf{F}_{\mathrm{H}}$ | Basset history force (N) |
| $\mathbf{F}_{\mathrm{L}}$ | Lift force (N) |
| $\mathbf{F}_{\mathrm{N}}$ | Reaction force (N) |
| $\mathbf{F}_{\mathrm{Press}}$ | Pressure gradient force (N) |
| $\mathbf{F}_{\mathrm{stress}}$ | Stress gradient force (N) |
| $\mathbf{g}$ | Gravitational acceleration vector ($m^2/s$) |

| | |
|---|---|
| $G$ | Velocity gradient of a shear flow (1/s) |
| $h_0$ | Distance between particle and dendrite tip (m) |
| $h_0^{cr}$ | Critical value of $h_0$ (m) |
| $k$ | Distribution coefficient ($=C_s/C_l$) |
| $m$ | empirical constant in equation (B.2) ($J/m^2$) |
| M | mass (kg) |
| $n$ | empirical coefficient in equation (B.2) (1/wt pct) |
| $p$ | Pressure (Pa) |
| $R_p$ | Particle radius (m) |
| Re | Reynolds number |
| $r_d$ | Dendrite tip radius (m) |
| $t$ | Time (s) |
| $t_p$ | Particle integral time after injection (s) |
| $\Delta t$ | Integral time step size for flow simulation (s) |
| $\Delta t_p$ | Integral time step size for particle simulation (s) |
| $T_L$ | Liquidus temperature (K) |
| $T_s$ | Solidus temperature (K) |
| $v_i$ | Velocity component in i direction (i = x, y, z) (m/s) |
| $v_{sol}$ | Solidification interface advancing speed (m/s) |
| $\mathbf{V}$ | **V**elocity vector (m/s) |
| $V_{casting}$ | Casting speed (m/s) |
| x | Mold width direction (m) |
| y | Mold thickness direction (m) |

| | |
|---|---|
| z | Casting direction (m) |
| $\alpha$ | Constant for surface energy gradient force, defined in Equation (7.34) |
| $\beta$ | Constant for surface energy gradient force, defined in Equation (7.34) (m) |
| $\gamma$ | Surface energy (please see $\sigma$) (J/m$^2$) |
| $\rho$ | Fluid density (kg/m$^3$) |
| $\rho_p$ | Particle density (kg/m$^3$) |
| $\tau_v$ | Particle velocity response time (s) |
| $\sigma_{ij}$ | Surface energy between i and j (J/m$^2$) |
| $\Delta\sigma_0$ | Surface energy difference defined in Equation (7.28) (J/m$^2$) |
| $x$ | Distance between dendrite tip center to particle center (m) |
| $d_c$ | Concentration boundary layer thickness (m) |
| $\chi$ | Solidification direction (m) |
| $\eta$ | Direction across the solidification |
| w | Vorticity vector ($=\nabla\times\mathbf{V}$) (rad/s) |
| $\mu$ | Fluid dynamic viscosity (Pa-s) |
| $n_0$ | Fluid laminar dynamic viscosity (m$^2$/s) |
| $n_t$ | Fluid turbulent eddy viscosity (m$^2$/s) |
| $n_{eff}$ | Turbulent effective viscosity (m$^2$/s) |

Subscripts:

| | |
|---|---|
| $c$ | Concentration |
| $C$ | Carbon |

| | |
|---|---|
| *i* | Coordinate directions (i = x, y, z or $\chi,\eta$ ) |
| *l* | Liquid |
| *p* | Particle |
| *s* | Solid |
| *S* | Sulfur |
| *sol* | Solidification |
| *cr* | Critical value |

# CHAPTER 1. INTRODUCTION

Continuous casting is the predominant way by which steel is produced worldwide. Turbulent flow in the mold region during continuous casting of steel slabs is associated with costly failures (e.g. shell-thinning breakout) and the formation of many defects (e.g. slivers) by affecting important phenomena such as top surface level fluctuations and the transport of impurity particles and superheat. [1-4] The continuous casting process is schematically shown in Figure 1.1. Molten steel is fed by a tundish to flow through a submerged entry nozzle (SEN) and enters a slab-caster mold. The flow rate is controlled using either a stopper rod or a slide gate by adjusting the opening area. The bifurcated or trifurcated nozzle ports direct the superheated liquid steel into the mold region at a jet angle with various levels of turbulence and swirl. In the mold cavity, molten steel freezes against the water-cooled mold to solidify into a shell, which is continuously pulled downward at the casting speed. Inside the tapering domain enclosed by the shell, molten steel recirculates to form a liquid pool, as illustrated in Figure 1.1.

Impurity particle trapped in solid steel slabs can cause costly defects. During the continuous casting process, non-metallic particles such as deoxidation products (e.g. alumina), reoxidation products (from air exposure) and exogenous inclusions (e.g. loose dirt) may enter the molten steel. [1] Impurity inclusions may also be generated from unexpected chemical reactions. [1] As shown in Figure 1.1, impurity particles are carried by the jet to enter the mold cavity. Additional inclusions may be introduced into the liquid pool by excessive fluid velocities across the top surface, which shears off fingers of liquid slag to emulsify into the steel. [2] If the flow pattern in the mold region encourages these impurity particles to float to the top surface, they would most likely be safely absorbed by the liquid slag layer. Otherwise, these particles will eventually be trapped by the solidifying shell and cause defects in final products. If detected, defects caused by inclusions lower the yield. Otherwise, inclusions degrade steel quality by lowering the minimum strength, fatigue life, and surface appearance.

Turbulent flow in steel casters is closely associated with the formation of many defects. Flow in the caster mold region is turbulent with Reynolds numbers in the order of $10^5$, based on the hydrodynamic diameter of the nozzle port, and involves complex time-evolving structures even under nominally “steady-state” casting conditions. Although many experimental studies have proved that transient flow conditions (involving changes in flow patterns) are associated with many quality problems, [4] they have not been investigated. The turbulent jets traversing the mold width impinge on the narrow face to build up an unsteady heat flux, which might cause shell-thinning breakouts if the instantaneous flux is too high. [5] Molten steel in the mold is covered by a liquid slag layer (see Figure 1.1) on the top to prevent it from being re-oxidized. The liquid slag creeps into the interfacial gap between the mold and the shell as a lubricant to prevent surface defects. Excessive fluctuations of the steel-slag interface profile (which is also called top surface standing wave) interrupt steady supply of the liquid slag into the interfacial gap and cause heat transfer variations, resulting in longitudinal cracks, [6] transverse depressions [7] and other defects. [8] The velocities of the molten steel across the top surface also fluctuate with time. Excessive local surface velocity can shear off liquid slag and form harmful mold slag inclusions, [2] causing skin delaminations, slivers and other defects in rolled sheet product.[4]

Turbulent flow in the mold cavity also plays an important role in transporting impurity particles. If the flow generates excessive level fluctuations or insufficient liquid temperatures on the top surface, particles are likely to be captured by the solidifying meniscus before they can enter the liquid slag layer. Studies suggest that particles trapped near the meniscus generate surface delamination, and may initiate surface cracks. [9] Particles which are entrained into the lower recirculation zone by the turbulent flow can gradually spiral and may be trapped by the solidifying shell, leading to defects such as internal cracks, slivers and blisters in the final rolled products. Plant observations have found that these defects occur intermittently, [10] indicating the importance of flow transients. Therefore, understanding the unsteady turbulent flow and particle behavior in the continuous steel caster mold region is an important step towards decreasing particle defects.

Due to the high operating temperature during the continuous casting process, many previous studies of the turbulent liquid-particle flow in this complex system were carried out using mathematical models, typically through a Reynolds averaged approach. However, this steady-state approach has limited capability of predicting unsteady flows. This thesis is a part of a larger project. It aims at generating fundamental understandings on the flow transients and the motion and capture of impurity particles in continuous caster molds. In the first part of the thesis, the turbulent flow velocities in the nozzle and mold regions are investigated using Large Eddy Simulation (LES). The LES was first applied to predict velocities in water models to acquire validations by comparing results with experiments such as Particle Image Velocimetry (PIV). Computational issues such as the domain extent and inlet boundary conditions were investigated. After the accuracy being examined, the LES was then used to compute the turbulent flow velocities in a thin-slab steel caster using a velocity boundary condition accounting for the solidification effect. The predicted flow fields were compared with the available experimental data, including velocities along the jet and across the top surface, the profile of the top surface interface profile and a spectral analysis. Unsteady flow structures in both the nozzle and the mold regions were visualized and the corresponding time-scales were quantified. Flow asymmetries in the mold along with the cause and subsequent effects were studied based on the computed results. This thesis also quantified the differences between flow in the water model and its corresponding steel caster.

Using the computed three-dimensional time-dependent flow fields in Part I, the second part of the thesis studied particle behavior in continuous steel caster molds through a Lagrangian approach. A simple criterion was developed to model particle pushing and capture at the solidifying shell front. The Lagrangian particle transport model was validated by experiments in a full-scale water model. The computational model was applied to simulate the motion and capture of spherical slag particles in a thin-slab caster. Different hydrodynamic forces acting on particles were compared to determine their significance. Particle distributions in the mold region were associated with transient flow structures. The removal and capture fractions were quantified for particles with different sizes. The distribution of entrapped particles in steel slabs was predicted under conditions of short-term sudden "burst" and continuous injection.

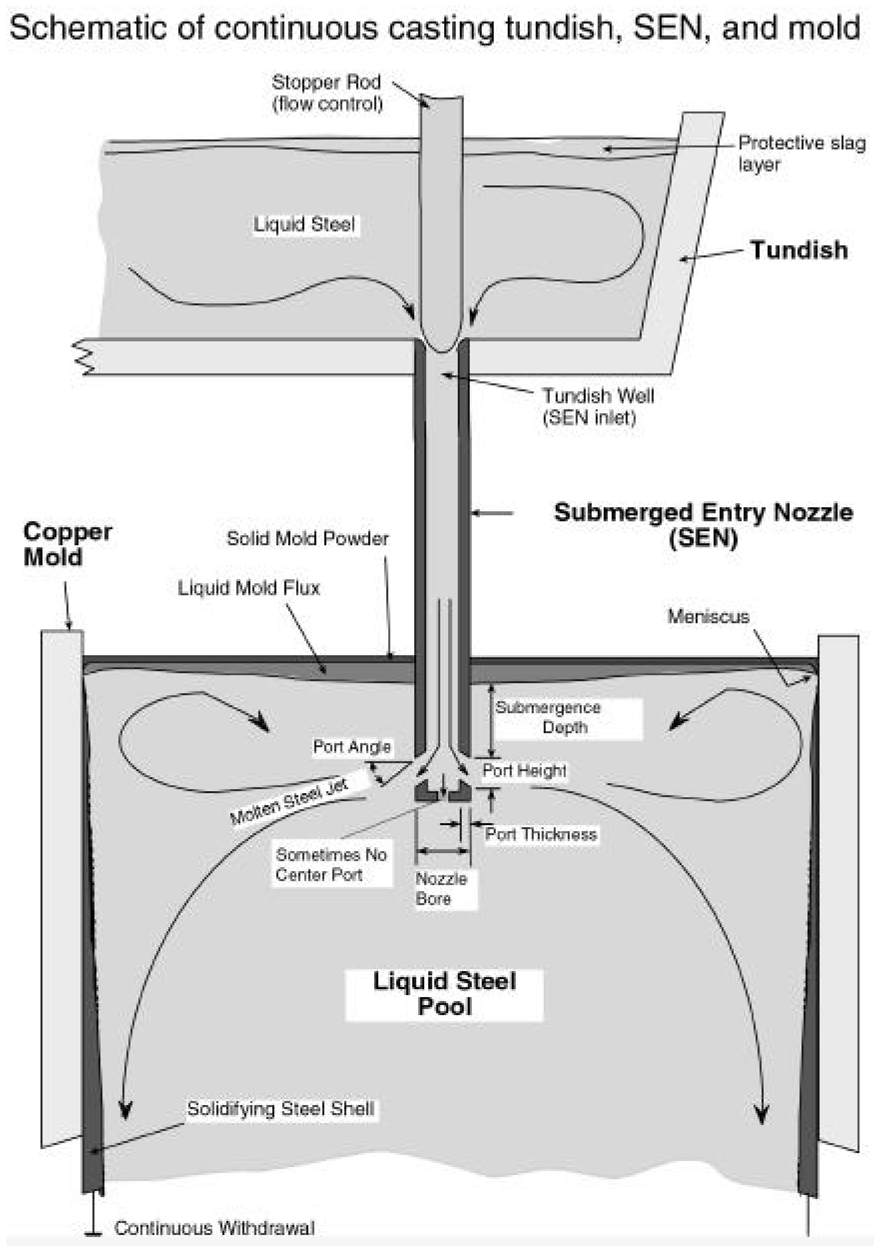


**Figure 1.1. Schematics of the continuous steel casting process.**

# PART I. TURBULENT FLOW DURING CONTINUOUS CASTING

# CHAPTER 2. LITERATURE REVIEW - FLOW

Various tools have been used to study the turbulent flow in continuous steel-caster molds, which include direct measurements, water modeling and mathematical modeling. Due to the high temperature (~1800K) of molten steel, direct measurements in steel casters are difficult. [11] Assar et al. [12] used electromagnetic sensors to measure the velocities of molten steel near the meniscus in a steel caster. In [12, 13] nail-board experiments were performed to study the profile of the liquid slag layer on the top surface. These studies provided valuable information on the flow in actual steel casters. However, they only generated limited insights into the physics. In addition, the accuracy of these measurement techniques was found to be sometimes unreliable. [11] Therefore, water modeling and numerical simulations have been the two main methods for investigating flows during the continuous casting process. This chapter gives a selective review of the previous studies.

## 2.1 Water Modeling

Owing to the nearly equal kinematic viscosities of molten steel and water (~20% of difference), physical water models have been extensively employed to model the flow in steel casters. [12, 14-18] The dimensions and operating conditions of a water model are usually chosen to have geometry and Froude number (or sometimes Reynolds number) similarities [19] with the actual steel caster. The walls of the tundish, nozzle and mold are usually made of transparent plastic plates. The mold sidewalls are sometimes curved to represent the internal tapering flow domain enclosed by the solidifying shell. During the operation, water flows downward from the tundish, passes through the nozzle, enters the mold cavity and exits from outlet ports on the bottom plate.

One advantage of water modeling is that water models are easier to operate and allows accurate measurements. Thomas and Huang [20] used hotwire anemometer to measure velocities in a full-scale water model for the purpose of validating predictions from numerical simulations. Honeyands and Herberton [21] used ultrasonic flow sensors to study the transient flow phenomena in a thin-slab water model. The ultrasonic sensors were mounted on the top of the water surface to measure the fluctuation of the top surface profile. Gupta and Lahiri found similar results: [16] the profile was found to oscillate with time periods of 5s and 50s for a closed bottom mold and an open bottom mold respectively. The amplitude of the surface wave was found to increase with increasing casting speeds.

The transparent walls of a water model enable measurements based on flow visualization such as dye-injection [16, 22-24] and laser velocimetry. [25] Gupta and Lahiri [16] performed dye-injection measurements in water models with two different configurations to investigate the extent of flow asymmetries. Asymmetrical flow patterns were always observed to oscillate in long molds with aspect ratio of 1:6.25 or more (with/height). The oscillating periods were found to vary from 2s to 75s. The mold bottom wall appeared to suppress flow asymmetries in the lower region. Gupta et al. further conducted a parametric study on this by including the effects of the mold dimensions, the casting speed and the nozzle position and angle. [16, 22]

Water models also allow accurate measurements using the non-intrusive optical laser velocimetry techniques. [25] Two typical methods are Laser-Doppler Velocimetry

(LDV) [25, 26] and Particle Image Velocimetry (PIV). [25, 27] LDV is a technique to measure instantaneous flow velocities at a single point or multiple points by detecting the Doppler frequency shift of the laser light. [25] It allows high sampling frequencies with typical values of $10^3$KHz, compared to 10-50Hz for PIV. Lawson and Davidson used LDV to measure the oscillatory flow in a 0.33-scale thin-slab water model. [28] Both jets were found to have most oscillatory energy at frequencies below 5Hz with high-energy low frequency modes occurring below 0.2Hz. [28] This proved the importance of low-frequency oscillations in the mold region. The results also suggest that the sampling speed for PIV is adequate.

The principle of PIV is to measure a planar instantaneous velocity field by correlating it with the displacement of laser illuminated particle images in a known short time interval. [25] The first attempt of applying PIV to measure turbulent velocities in continuous casting water models was made by Xu et al. [29] Velocities in two planes parallel to the wide face were measured with and without argon gas injection and compared with computational predictions using the k-ε turbulence model embedded in FIDAP. [29] Recently Sivaramakrishnan [30] and Assar [12] measured the velocities in a 0.4-scale water model at former LTV Steel Technology Center (Cleveland, OH) using PIV. The mold was divided into the upper, middle and lower regions. Measurements in each region was performed for 40-200s and repeated 3-10 times. The measured flow velocities were reported together with the related time scales. Sivaramakrishnan [30] also attempted to simulate the turbulent flow through an LES with simplified domain geometry and approximated inlet velocities. Considering the simplifications made for the LES, the agreement between the results is encouraging.

It should be noted that despite of its favorable advantages, the water model are still different from the represented steel caster mainly in two aspects. First, the stationary sidewalls of a water model do not represent the solidification phenomena occurring at the shell front. Second, the water model has a horizontal bottom plate with outlet ports, while in a continuous steel caster molten steel flows into a tapering section resulting from the solidification. The two major differences give rise to different flow phenomena, as will be shown in CHAPTER 5. In this thesis, water models were mainly used to validate the LES for complex flow configurations by comparing results with measurements.

## 2.2 Computational Modeling

Computational modeling of turbulent flows can be categorized into the Reynolds-Averaged Navier-Stokes (RANS) approach, Large Eddy Simulation (LES) and Direct Numerical Simulation (DNS). [31] Because of their low computational cost, the Reynolds-averaged approach, typically with the two-equation (k-ε) turbulence model, has been extensively adopted to simulate flow in continuous caster nozzles [32-35] and molds. [17, 36-40] Huang and Thomas [39] employed an Unsteady RANS (URANS) model to investigate the transient flow evolution in a caster mold induced by sudden changes of nozzle inlet conditions and rapid fluctuations of the steel-slag layer interface. However, in the test cases of this thesis, the velocities obtained from this approach remained stationary so long as a steady-state boundary condition was employed. This is likely due to the high numerical dissipation involved in the scheme.

LES and DNS provide two ways for modeling the unsteady velocity field of a turbulent flow. Because of the prohibitive computational cost of DNS at high Reynolds numbers, LES is a more feasible approach for modeling the flow during continuous casting. In LES, only the large-scale (energy-containing) eddies are resolved. The dissipative small eddies are "filtered". This filtering creates a residual stress tensor [31] similar to the Reynolds stress tensor for RANS, which is represented by a sub-grid scale (SGS) model.

Studies of LES have been mainly conducted on fundamental turbulent flows with simple configurations such as channel flows, where homogeneous directions exist. SGS models have been developed and investigated for these simple flow configurations. [41-44] As the more powerful computational facilities become available, LES have been applied to more complex and realistic flows such as turbulent impinging jets [45, 46] and flow around a bluff body. [47-50] A detailed review of LES and its applications can be found in [47]. Computational issues such as the computational grid, boundary condition, SGS model and numerical scheme were discussed.

The application of LES to continuous casting is recent, [30, 51] probably due to the challenges including: the prescription of appropriate unsteady inlet velocities and resolution of the complex domain geometry, moving solidification boundary and long-term transients. Sivaramakrishnan [30] simulated single-phase turbulent flow in a 0.4-scale water model with a grid consisting of 1.5 million cells. A few simplifications were made in the computation to reduce the computational complexity. The domain only included half of the mold region by assuming symmetric flow in the two halves. The sidewalls were modeled as vertical boundaries with neglecting their actual curvatures. The unsteady inlet velocities from the nozzle port were approximated by collecting data from a large eddy simulation of a fully-developed turbulent pipe flow. The computed velocities were compared with PIV measurements with favorable agreement. [30] The major difference occurred at the top surface and along the oblique impinging jet. Takatani et al. [51] investigated the transient flow structures in a water model and a fused metal hot model using LES with relatively coarse grids. Flow velocities and the level profile on the top surface were also measured using propeller velocimeters and rulers respectively. The LES predictions were found to agree with the measurements. The preliminary studies above suggest that LES is capable of predicting the flow transients in the continuous steel-caster mold region. In this thesis, this transient flow-modeling tool is employed to provide more systematic validations and explore the physics of the flow.

# CHAPTER 3. LARGE EDDY SIMULATION OF TURBULENT FLOWS

This chapter describes the Large Eddy Simulation (LES) model used throughout the thesis. The computational domain may vary between cases depending on the purpose of the simulation. The simulation for the 0.4-scale water model had the most complete domain, which started from the tundish exit and included the entire nozzle, the slide gate and the complete mold region. For the other simulations, to reduce the computational cost, separate simulations were performed to simulate flow in the nozzle and acquire unsteady inlet velocities for the mold simulations.

## 3.1 Governing Equations

In the context of LES, only the large-scale flow structures are resolved. The dissipative effect of eddies smaller than the filter size is represented by a sub-grid scale (SGS) model. The governing equations for the filtered variables accounting for the conservation of mass and momentum are expressed as follows: [31]

$$\frac{\partial \mathrm{v}_i}{\partial x_i} = 0 \qquad (3.1)$$

$$\frac{D\mathrm{v}_i}{Dt} = -\frac{1}{r}\frac{\partial p}{\partial x_i} + \frac{\partial}{\partial x_j} n_{eff} \left( \frac{\partial \mathrm{v}_i}{\partial x_j} + \frac{\partial \mathrm{v}_j}{\partial x_i} \right) \qquad (3.2)$$

$$?_{eff} = ?_0 + ?_t \qquad (3.3)$$

where the symbols p and $\mathrm{v}_i$ in Equations (3.1) and (3.2) represent the pressure and filtered velocities. The subscripts i and j represent the three Cartesian directions and repeated subscripts imply summation. The residual stresses, which arise from the unresolved small eddies, are modeled by a turbulent eddy-viscosity ($?_t$).

An important issue here is the selection of an appropriate SGS model for this complex inhomogeneous turbulent flow. In the past, a class of SGS turbulent kinetic energy (SGS k) models has been developed for flow with simple configurations. [42-44, 52, 53] The SGS k model employed in this thesis requires solving the following transport equation, which includes advection, production, dissipation and viscous diffusion. [44, 53]

$$\frac{\partial \mathrm{k_{sgs}}}{\partial t} + \mathrm{v_i}\frac{\partial \mathrm{k_{sgs}}}{\partial \mathrm{x_i}} = ?_t \left|\tilde{\mathbf{S}}\right|^2 - \mathrm{C}_e \frac{\mathrm{k_{sgs}^{3/2}}}{\Delta} + \frac{\partial}{\partial \mathrm{x_i}}\left(\left(n_0 + C_{kk}K_G^{1/2}\Delta\right)\frac{\partial \mathrm{k_{sgs}}}{\partial \mathrm{x_i}}\right) \tag{3.4}$$

where:

$$\Delta = \left(\Delta_x \Delta_y \Delta_z\right)^{1/3} \tag{3.5}$$

$$n_t = C_v \Delta k_{sgs}^{1/2} \tag{3.6}$$

where $|\tilde{\mathbf{S}}|$ is the magnitude of the strain-rate tensor, defined as:

$$\left|\tilde{S}\right| = \sqrt{2\tilde{\mathrm{S}}_{\mathrm{ij}}\tilde{\mathrm{S}}_{\mathrm{ij}}} \tag{3.7}$$

where

$$\tilde{\mathrm{S}}_{\mathrm{ij}} = \frac{1}{2}\left(\frac{\partial \mathrm{v_i}}{\partial \mathrm{x_j}} + \frac{\partial \mathrm{v_j}}{\partial \mathrm{x_i}}\right) \tag{3.8}$$

The parameters $C_e$, $C_{kk}$ and $C_v$ can be treated as constants [44] or evaluated dynamically during the simulation by assuming similarity between the sub-grid stress tensor and the large scale Leonard stress tensor. [53] This thesis adopted a static SGS k model with constant values 1.0, 0.1 and 0.05 for $C_e$, $C_{kk}$ and $C_v$ respectively. [44]

## 3.2 Boundary Conditions

### 3.2.1 Inlet

Flow in the mold is fed by a bifurcated or trifurcated nozzle, which has an important influence on the flow pattern. The unsteady flow velocities exiting the nozzle ports were obtained from large eddy simulations in the nozzles with realistic shapes. Constant inflow velocity profiles were imposed at the tundish bottom for the nozzle simulations, as the inlet is far from the nozzle ports and the downstream effects should be small. To reduce the computational cost, except for the simulation of the 0.4-scale water model, the nozzle simulations were conducted separately. The transient flow velocities at the nozzle port outer plane were collected every 0.01-0.02s, stored and recycled periodically as the inlet velocities for simulations in the mold regions. More details are available in later chapters.

### 3.2.1 Outlet

The outlet boundaries for the water model and steel caster systems are different. Water models have outlet ports on the plastic bottom wall, while in steel casters the shell containing the molten steel gradually tapers into a solid section due to solidification. For computational efficiency, the steel caster simulations only computed flow inside the shell from the top surface to a depth below the region of interest. This created an artificial outlet plane on the bottom. A condition with constant pressure and zero normal gradients for the other variables was employed at the outlet port or plane for both systems, where the flow becomes nearly uniform.

### 3.2.1 Symmetry Center Plane and Top Surface

A symmetry condition was imposed at the center plane between narrow faces in the half mold simulations. Errors arising from this assumption are discussed in CHAPTER 4. The same condition was imposed on the top surface. Specifically, along these two boundaries the normal velocity was constrained to zero, and the gradients of the other two velocity components were set to zero. Computations and measurements of this work suggest that the top surface is relatively flat, so no model of free surface deformation is necessary.

### 3.2.1 Narrow Face and Wide Face Boundaries

The boundary conditions at the narrow face and wide face are very different for water models and steel casters. In water models, the plastic sidewalls representing the mushy zone front [54] are stationary. Thus all the three velocity components were set to zero in water model simulations. However, the side boundaries for steel caster computations represents the front of the downward moving mushy zone [54], where solidification occurs to take away mass from the molten steel. The solidification also causes the domain to taper with depth. To account for the effect from the solidification and the downward motion of the shell, a velocity boundary condition given by Equations (3.9) and (3.10) was used:

$$\mathrm{v}_{\mathrm{horiz}} = V_n \cos q - V_t \sin q = \left( \frac{r_s}{r_l} - 1 \right) \sin q \cos q V_{casting} \tag{3.9}$$

$$\mathrm{v}_{\mathrm{vert}} = V_n \sin q + V_t \cos q = \left( \frac{r_s}{r_l} \sin^2 q + \cos^2 q \right) V_{casting} \tag{3.10}$$

Derivation of Equations (3.9) and (3.10) can be found in. In both systems, no wall functions were used to represent near wall turbulence because of a relatively fine mesh near the wall.

## 3.3 Solution Procedure

The time-dependent three-dimensional filtered Navier-Stokes equation (3.2) was discretized using the Harlow-Welch fractional step procedure. [55] Second order central differencing was used for the convection terms and the Crank-Nicolson scheme [56] was used for the diffusion terms. The Adams-Bashforth scheme [57] was used to discretize in time with second order accuracy. The pressure Poisson equation was solved using an algebraic multi-grid (AMG) solver. [58] The computational domains were discretized using unstructured Cartesian grids consisting of ~$10^6$ collocated finite-volumes. Smaller grid spacings were set at the nozzle outlet port and near the narrow face walls. The numerical scheme can be concisely expressed as follows. The discretized Navier-Stokes equations have the following form:

$$\frac{\mathrm{v}_i^{n+1}-\mathrm{v}_i^{n}}{\Delta t}=\frac{3}{2}H_i^{n-1}-\frac{1}{2}H_i^{n}+\frac{1}{2}\frac{\partial}{\partial x_j}\left[\left(n_0+n_t\right)\left(\frac{\partial \mathrm{v}_i^{n}}{\partial x_j}+\frac{\partial \mathrm{v}_i^{n+1}}{\partial x_j}\right)\right]-\frac{1}{r}\frac{\partial p^{n+1}}{\partial x_i} \qquad (3.11)$$

where:

$$H_i^{n}=-\frac{\partial}{\partial x_j}\left(\mathrm{v}_i^{n}\mathrm{v}_j^{n}\right) \qquad (3.12)$$

To solved the equations efficiently, an intermediate velocity field $\hat{\mathrm{v}}_\mathrm{i}$ is solved from the following equation:

$$\frac{\hat{\mathrm{v}}_i^{n+1}-\mathrm{v}_i^{n}}{\Delta t}=\frac{3}{2}H_i^{n-1}-\frac{1}{2}H_i^{n}+\frac{1}{2}\frac{\partial}{\partial x_j}\left[\left(n_0+n_t\right)\left(\frac{\partial \mathrm{v}_i^{n}}{\partial x_j}+\frac{\partial \hat{\mathrm{v}}_\mathrm{i}}{\partial x_j}\right)\right] \qquad (3.13)$$

This velocity does not satisfy the mass-conservation equation. The correct velocity field $v_i^{n+1}$ should satisfy the mass-conservation equation:

$$\frac{\partial v_j^{n+1}}{\partial x_j} = 0 \tag{3.14}$$

subtracting (3.13) from (3.11) yields the following equation:

$$\frac{v_i^{n+1} - \hat{v}_i^n}{\Delta t} = \frac{1}{2}\frac{\partial}{\partial x_j}\left[(n_0 + n_t)\frac{\partial\left(v_i^{n+1} - \hat{v}_i\right)}{\partial x_j}\right] - \frac{1}{r}\frac{\partial p^{n+1}}{\partial x_i} \tag{3.15}$$

Expressing the right hand side of equation (3.15) in terms of the gradient of a single scalar variable $\Phi$ gives:

$$\frac{v_i^{n+1} - \hat{v}_i^n}{\Delta t} = -\frac{\partial \Phi}{\partial x_i} \tag{3.16}$$

A Poisson equation for $\Phi$ can be obtained by applying the divergence operator to Equation (3.16) and using Equation (3.14) to have the form:

$$\nabla^2 \Phi^{n+1} = \frac{1}{\Delta t}\frac{\partial \hat{v}_i}{\partial x_i} \tag{3.17}$$

and

$$p^{n+1} = r\left[\Phi^{n+1} - \frac{\Delta t}{2}(n_0 + n_t)\nabla^2 \Phi\right] \tag{3.18}$$

Equations (3.13) and (3.17) were solved along with (3.16) to obtain the velocity field at time step $n$+1. To do this, a Gauss-Siedel iterative solver was first used for the momentum equations. The AMG solver was then used to solve Equation (3.17). Finally Equation (3.16) was used to correct the velocity field.

The time steps ($\Delta t$) were chosen based on the CFL condition (CFL= $\Delta t \max\left(\frac{\bar{v}_x}{\Delta x} + \frac{\bar{v}_y}{\Delta y} + \frac{\bar{v}_z}{\Delta z}\right)$<1) [59] to ensure that the simulation is stable. Time mean and variation values were calculated after the flow reached a statistically stationary state. [60] Variations were characterized by their root mean square values (*rms*), such as $\left(\overline{v'v'}\right)^{1/2}$, which is computed by $\left(\frac{1}{(t_2 - t_1)}\sum_{t_i = t_1}^{t_2}\left(v(t_i) - \overline{v}\right)^2 \Delta t\right)^{1/2}$, where $(t_2 - t_1)$ is the time interval for the average and *Dt* is the time step size.

# CHAPTER 4. MODEL VALIDATIONS IN WATER MODELS

The application of LES to flows with complex configurations such as the continuous casting process is still in the preliminary stage. [48] The accuracy of LES for these systems has not yet been quantified. Therefore, it is necessary to validate the LES model in the continuous steel caster system by comparing results with accurate measurements such as PIV and hotwire anemometry. In this chapter, turbulent flows in a 0.4-scale water and a full scale water model (denoted as *Case 1*) were computed using LES. The results are presented in such a way as to unveil the transient flow structures as well as to make comparisons with prior experimental data. [20, 30] Additional validations by experiments are presented for a thin-slab caster in CHAPTER 5.

## 4.1 The Water Models

Figure 4.1 schematically depicts the dimensions of two water models investigated in this chapter. The 0.4-scale water model was constructed from transparent plastic plates at former LTV Steel Technology Center (Cleveland, OH). [12, 30] The flow rate in it is controlled by a slide gate, which moves in the mold thickness (y) direction. The bifurcated submerged entry nozzle (SEN) shown in the figure has two downward-angled square nozzle ports, with the top and bottom edge angles of $40^o$ and $15^o$ respectively. The Reynolds number at the nozzle port based on the hydrodynamic diameter is ~12,000. The mold thickness tapers from the top (95mm) to the bottom (65mm), so the mold cavity only represents the liquid portion in the steel caster. Water flows into the mold cavity, recirculates and finally exits from three 35mm outlet holes spaced 180mm apart along the plastic bottom wall. A photograph of flow in this water model is given in Figure 4.20 visualized using dye-injection. PIV data are available in the complete mold domain from literature. [12, 30]

The full-scale water model, denoted as *Case 1* throughout the thesis, illustrated in Figure 4.1(b) represents a standard-thickness slab caster at former Armco Steel Inc. (Middletown, OH). [20] Dye-injection measurements suggest that the jets entering the mold from the bifurcated oval nozzle ports have downward angles of approximately 25 degrees. [20] Water exits the model from four outlet pipes on the wide face near the bottom, as shown in the figure. Velocities along four vertical lines were measured using hotwire anemometry in a previous study. [20] Table 4.1 gives details on the dimensions and the operating conditions of the two water models. Further details are available elsewhere. [12, 20, 30]

## 4.2 Computational Details

The computational domain for the 0.4-scale water model is depicted in Figure 4.1(c), including the complete upper tundish nozzle (UTN), the slide gate, the submerged entry nozzle (SEN) and the entire mold region. The domain was discretized with an unstructured Cartesian grid consisting of ~1.5 million finite-volumes. Smaller grid spacing (~0.8mm) was set at the nozzle outlet port and near the narrow face walls. A constant downward inlet velocity with magnitude of 1.15m/s was prescribed at the tundish bottom port. No symmetry plane was imposed as the computational domain includes the complete nozzle and mold region. The time step size ($\Delta t$) was set to 0.0003s to keep the simulation stable. The computational time was 24 hours for 1s of integration time on a Pentium IV 3.2GHz PC (Linux 8.0). The mean and *rms* velocities were calculated for 51s (170,000 time steps) and 20s (70,000 time steps) respectively.

Figure 4.1 (d) shows the domain for the full-scale water model (*Case 1*), which only includes half of the mold cavity. A symmetry plane was imposed mid-way between narrow faces. The nozzle port was modeled as an opening on the symmetry plane. Inlet velocities were obtained from a prior turbulent pipe flow simulation using LES. The pipe was 38% open at the entry where a constant velocity profile was imposed. Transient velocities were collected 7.5 pipe diameters away from the entry for 1.6s and then rotated 25° downward to feed the mold simulation. The outlet port, which is far from the flow region of our interest, was approximated as a square opening with the same area as the physical port. This computational domain was discretized with a structured Cartesian grid consisting of 1.6 million cells. The time step of the simulation was 0.0008s.

## 4.3 PIV Measurements in The 0.4-Scale Water Model [12, 30]

This thesis employs the PIV data obtained from previous measurements [30] [12] in the 0.4-scale water model. To make the later comparisons easier, this section quotes some measurement details reported in [30]. Aluminum powder with particle diameters approximately 30μm was seeded into the fluid before the measurements. A Nd:YAG laser was used to illuminate the flow field. The CCD camera used in the measurements has a resolution of 768×480 pixels. To generate enough particle images in each interrogation area for an accurate average, an image resolution of 32×32 pixels per interrogation was used for post-processing. This produced a measured field of 32×19 vectors. In addition, to avoid problems arising from crossover of particles near area edges moving between adjacent areas, the interrogation areas were made to overlap each other by 25%.

Because of the interest in the relatively large-scale flow structures in the water model, a large measurement area was selected at the expense of the relatively low overall resolution (compared to the computation in this thesis). Owing to the limited number of camera pixels, the illuminated flow domain was divided into three regions as shown in Figure 4.2: the upper region (0-0.25m) containing the jet and the upper two rolls, the middle region (0.25-0.65m) and the lower region (0.65-0.77m) containing the two lower rolls. Because the SEN blocks the laser, flow in each half of the upper region was measured separately. During measurements, the time interval between two consecutive laser pulses was set at 1ms. The number of snapshots (pairs of pulses) collected and the time interval between them varied 0.2s-1s in the respective regions, depending on the time scales of the flow. The collected data totaled 900 snapshots of one half of the mold spaced 0.2s apart for the top portion, 2000 snapshots of both halves spaced 1s apart and 400 snapshots of one half spaced 0.2s apart for the middle region and 200 snapshots of both halves spaced 0.2s apart for the bottom region.

## 4.4 Flow in the SEN of the 0.4-Scale Water Model

Flow in the nozzle is important because a detrimental flow pattern may lead to problems such as nozzle clogging, which both limits productivity and causes defects. [61] In addition, the SEN ports direct the fluid into the mold cavity, which controls the jet angle, the flow pattern, and the corresponding steel quality issues. However, flow in the UTN and SEN could not be reliably measured using PIV due to the curvature and partial opacity of the nozzle wall. Thus, this section presents the computed velocities in the nozzle region. Comparisons between the computational results with measurements are only made at the port outlets.

Figure 4.3 gives an overall view of the computed velocities in the UTN and SEN at the centerline slice (x=0). The plot on the left shows a representative instantaneous velocity field. The time-dependent velocities in the nozzle were averaged over 51s and are shown in the right two close-up plots. In both the instantaneous and time-averaged plots, the narrowed flow passage at the slide gate induces large downward velocities (~3m/s). These velocities exceed the mean velocity at the nozzle ports by 7 times and diminish gradually with distance down the nozzle. A recirculation flow is seen in the cavity of the slide gate. A large, elongated recirculation zone is also observed in the SEN beneath the slide gate and extends almost to the nozzle ports. This recirculation zone involves complex flow structures, and actually exhibits multiple transient recirculation regions. These recirculation flows encourage the accumulation of impurity particles in the molten steel by increasing their residence time, and may cause problems such as clogging. The plot on the right bottom reveals a clock-wise swirl in the y-z plane near the SEN bottom. This swirl is clearly induced by the partial opening of the slide-gate. It is transported downstream with the flow to exit the nozzle ports as shown in Figure 4.4, which depicts the time-averaged velocity vectors leaving the nozzle ports. In Figure 4.4(a), the cross-stream velocities in the outer plane of the nozzle port (x=0.027m) are plotted for the view looking into the port. The single swirl also persists here. Figure 4.4 (b) shows the velocity vectors at the centerline slice y=0, and indicates that most of the fluid exits the nozzle from the lower half of its ports. Reverse flow is observed in the upper portion of the port. This result is consistent with previous work [34, 62] and is expected because the port to bore area ratio (2.47) greatly exceeds 1. Comparing the velocity vectors in Figures 4.4(a) and (b), the cross-stream velocity components are seen to be comparable in magnitude to the stream-wise components.

Figure 4.5 shows the time-averaged flow speed $\left(\overline{v_x}^2 + \overline{v_z}^2\right)^{1/2}$ along the nozzle port vertical centerline. The PIV data shown here were collected in the mold cavity close to the nozzle ports.[63] They are the average of 50 PIV snapshots spaced 0.2s apart. [63] The computed speed is seen to have a similar distribution to that obtained from PIV. In both LES and PIV, the "peak" speed occurs 3mm above the lower edge of the nozzle port. The computed speeds are consistently larger than the measured values in the lower portion of the port, however. In previous work, misalignment of the laser plane was suspected to explain this discrepancy. [34] Another suspected reason is that the relatively large off-plane velocity component ($\overline{v}_y$, 0.2-0.3m/s) in the lower portion of the port makes the tracer particles in the water model move 0.2-0.3mm during the 1ms time interval between two consecutive laser pulses. The typical thickness of the laser sheet is 1mm. Particles moving in and out of the illuminated plane could confuse the measurement.

Figure 4.6 presents a sequence of the computed instantaneous snapshots of the flow at the nozzle outlet port to reveal a transient evolution. In Figure 4.6(a), a strong clockwise swirl is seen to occupy almost the whole port area. After 4 seconds, the size of this swirl reduces to 2/3 of the port area, with cross-stream velocities in the other 1/3 portion dropping close to zero (Figure 4.6 (b)). It then breaks into many distinct small vortices 1s later as shown in Figure 4.6 (c), and further evolves into a nearly symmetric double swirl another 4s later (Figure 4.6(d)). The flow at the nozzle port was seen to fluctuate between these four representative patterns in the simulation. This same behavior was observed in visual observations of the water model. However, the strong cross-stream flow disappears if the slide-gate is replaced by a stopper rod. [24]

## 4.5 Flow in the Mold Cavity of the 0.4-Scale Water Model

The jet exiting the SEN feeds into the mold cavity, where it controls the flow pattern to affect the steel quality. If insufficient superheat is transported with the jet to the top surface, then the meniscus may freeze to form subsurface hooks, which many entrap inclusions, and cause slivers. The contour of the top surface beneath the flowing liquid steel affects flux infiltration into the gap between the shell and the mold, which controls lubrication and surface cracks. Excessive flow fluctuations can cause fluctuations in the top surface level, disrupting meniscus solidification and causing surface defects. Excessive velocity across the top surface can shear off liquid mold flux into the steel can consequently introduce additional impurity particles in the process. [64] The mold region is the last step where impurity particles could be removed without being entrapped in the solid steel slabs. Knowledge of the turbulent flow in the mold region is critical for understanding the above phenomena. This section presents the details of the turbulent flow in the mold cavity of the 0.4-scale water model obtained from the LES along with comparisons with the PIV data.

### 4.5.1 Time-Averaged Flow Structures

After the flow in the simulation reached a statistically stationary state, [60] the means of all variables were computed by averaging the instantaneous flow fields obtained at every time step. Figure 4.7 presents the simulated flow field at the center plane y=0 in the mold cavity averaged over 51s. For clarity, velocity vectors are only shown at about every third grid point in each direction. The usual double-roll flow pattern [17, 36] is reproduced in each half of the mold. The two jets emerging from the nozzle ports spread and bend slightly upwards as they traverse the mold region. The two lower rolls are slightly asymmetric, even in this time-averaged plot. This indicates that flow transients exist with periods longer than the 51s of averaging time.

Figure 4.7 gives a closer view of the upper roll. The PIV plot shown on the left is a 60s average of 300 instantaneous measurements. [30] The right half shows some of the computed velocity vectors plotted with a resolution comparable to that of the PIV. A jet angle of approximately $29^{o}$ is implied by the LES results, which is consistent with the flow visualization. [30] A larger jet angle of $34^{o} – 38^{o}$ is seen in the PIV vectors. This may be due to the manually adjusted laser sheet being off the center plane (y=0). It might be due to insufficient averaging time. In both LES and PIV, the jet diffuses as it moves forward and becomes nearly flat 0.2m away from the center. The eyes of the upper rolls are seen to be nearly 0.2m away from the SEN center and 0.1m below the top surface. The main difference between the computed and measured velocities in the upper region is that the computed velocities are consistently higher than the measured values in the low-velocity regions. Perhaps this is because the PIV system is tuned to accurately measure velocities over a specific range (e.g. by adjusting the pulse interval), which might decrease accuracy in regions where the velocities are either much higher or much lower.

The time-averaged flow in the lower region is given in Figures 4.9(a) and (b). Both plots are for the center plane y=0. The LES data clearly show that the lower roll in the left half is smaller and about 0.1m higher than the right one. This confirms that a flow asymmetry exists in the lower roll region that persists longer than 51s (the averaging time). In this region, ten sets of PIV measurements were conducted. [30] Each set of measurements consists of 200 snapshots taken over 200s. Figure 4.9(b) presents the velocity field averaged from all of the measurements. [30] For all ten averages, the lower roll in the right half is larger and slightly lower than the left one. This proves that the asymmetry of the flow is persistent over long times, exceeding several minutes. It was also observed that for all the ten sets of PIV data, the downward velocities close to the right narrow face are always greater than those down the left side. It is not known whether this is due to the flow asymmetry or errors in the experiments (e.g. laser light diminishing as it traverses the flow field). This long-term flow asymmetry in the lower roll has been observed in previous work and may explain why inclusion defects may alternately concentrate on different sides of the steel slabs. [65]

### 4.5.2 Velocities along Jets

Figure 4.10 compares the computed time-averaged speed $\left(\overline{v}_x^2+\overline{v}_y^2\right)^{1/2}$ with PIV measured values [30] along the jet centerline. The solid line denotes the speed obtained from the LES and averaged for 51s. It shows that the jet exits the nozzle port at a speed ~0.7m/s and slows down as it advects forward. It is seen that the 51s average almost suppresses the differences between the left and right jets. Except in the region close to the nozzle port, a reasonable agreement between the computation and PIV is observed.

### 4.5.3 Velocities on The Top Surface

In a steel caster, the flow conditions at the interface between the molten steel and the liquid flux on the top surface are crucial for steel quality. Therefore accurately predicting velocities across the steel-flux interface is important for a computational model. Figure 4.11 shows the time-averaged x velocity component ($\bar{v}_x$) towards the SEN along the top surface centerline. Due to a lack of measurements at the current casting speed, two sets of averaged data from other PIV measurements (provided by Assar)[66] are used to compare with the LES predictions. Each one of these is the average of a group of measurements conducted on the same water model at a constant casting speed slightly higher (0.791m/min) or lower (0.554m/min) than that in this work. It can be seen that this velocity component increases away from the SEN, reaches a maximum midway between the SEN and the narrow face and then decreases as it approaches the narrow face. The maximum of ~0.15m/s is about 1/3 of the mean velocity in the nozzle bore and 1/5 of the maximum velocity of the jet exiting the nozzle. The comparison suggests that the computation agrees reasonably well with the PIV measurements.

The computed *rms* value of this velocity component is plotted in Figure 4.12. No PIV data are available for the *rms* on the top surface. The figure suggests that the *rms* of the x velocity component ($\left(\overline{v_x'v_x'}\right)^{1/2}$) decreases slightly from the SEN to the narrow face. The results also suggest that the *rms* can be as high as 80% of the mean velocity, indicating very large velocity fluctuations.

Figure 4.13 compares the time-variation of the horizontal velocity towards the SEN near the top surface for the simulation and the measurement. [30] The data were taken at a point 20mm below the top surface, midway between the SEN center and the narrow face. The mean of the PIV signal is lower than the expected value from the measurements shown in Figure 4.11, indicating variations between the PIV measurements taken at different times. The velocity fluctuations are seen to be large with magnitude comparable to the local mean velocities. Both the computation and measurement reveal a large fluctuating component of the velocity with approximately the same high frequency (e.g. the velocity drops from ~0.21m/s towards the SEN to a velocity in the opposite direction within 0.7s). This velocity variation is important, because the liquid level fluctuations accompanying it are a major cause of defects in the process. Figure 4.14 shows the spectra of signals in Figure 4.13. The computed signal reproduced most of the features seen in the measurements. The signal also reveals a lower frequency fluctuation with a period of about 45s. A spectral analysis of the surface pressure signal near the narrow face on the top surface reveals predominant oscillations with periods of ~7s and 11-25s, that are superimposed with a wide range of higher frequency, lower-amplitude oscillations. Knowing that model surface pressure is proportional to level [24], this result compares with water model measurements of surface level fluctuations by Lahri [67] that appear to have a period of ~0.4s and by Honeyands and Herbertson [21] of ~12s.

### 4.5.4 Velocities in The Lower Roll Region

Figure 4.15 shows the downward velocity profile across the width of the mold centerline in the lower roll zone (0.4m below the top surface). As stated earlier, ten sets of 200s 200-snapshot PIV measurements were conducted in both halves of the mold. The average of all sets is shown as open symbols. The error bars denote the range of the averages of all ten sets of measurements. The solid symbols correspond to a data set with large upward velocities near the center (x=0). In all data sets, the largest downward velocity occurs near the narrow face (x=0.363). The computation is seen to over-predict the upward velocity measured right below the SEN. This may partially be due to the shorter averaging time (51 seconds) in LES compared to PIV, as the PIV results indicate significant variations even among the ten sets of 200s time averages. This inference is further supported by the *rms* of the same velocity component along the same line shown in Figure 4.16. The open symbols and error bars again represent the *rms* velocities averaged for the ten sets of measurements and the range. The results indicate large fluctuations of the vertical velocity in this region (e.g. near the center, the *rms* value is of the same magnitude as the time-averaged velocity). Both the time-averages and *rms* are seen to change significantly across these 200s measurements, indicating that some of the flow structures evolve with periods much longer than 200s. Accurate statistics in the lower roll therefore require a long-term sampling. This agrees with measurements of the flow-pattern oscillation with periods of ~40s (2-75s range) conducted in a much deeper water model. [22]

Figure 4.17 presents the downward velocity along two lines across the mold thickness, in the center-plane midway between the narrow faces (x=0) in the lower roll. These results show a nearly flat profile of this velocity in the interior region along the thickness direction. It suggests that a slight misalignment of the laser sheet off the center plane should not introduce significant errors in the lower roll region.

### 4.5.5 Instantaneous Flow Structures

The instantaneous flow pattern can be very different from the time-averaged one. The time-dependent flow structures in the mold cavity are presented in this sub-section. Figure 4.18(a) gives an instantaneous velocity vector plot of the flow field in the center plane (y=0) measured with PIV. [30] It is a composite of the top, middle and bottom regions shown in Figure 4.2 for each half. Each of the six frames was measured at a different instant in time. Figure 4.18(b) shows a corresponding typical instantaneous velocity field obtained from LES. The flow consists of a range of scales, as seen by the spatial variations of the velocity within the flow field. The jets in both halves consist of alternate bands of vectors with angles substantially lower and higher than the jet angle at the nozzle port. The velocities near the top surface and the upper roll structure are observed to be significantly different between individual time instants and between the two halves. The jet in both halves is observed to entrain the fluid from a region below the SEN but at different heights. Therefore the shape and size of the two lower rolls appear significantly different for both PIV and LES.

Figure 4.19 gives a closer view of flow structures in the upper region obtained by LES and PIV. [30] The upper plot shows a computed instantaneous velocity field at the center plane y=0. The lower velocity vector plot is a composite of two instantaneous PIV snapshots, [30] divided by a solid line, obtained from measurements of the same flow field. A "stair-step" type of jet is observed in the left vector plot for both the simulation and measurement. This flow pattern is believed to result from the swirl in the jet (Figure 4.6): the swirling jet moves up and down and in and out of the center plane as it approaches the narrow face, causing a stair-step appearance in the center plane. The flow displayed in the right snapshot shows a shallower jet. The jet bends upward after traveling ~0.25m in the x direction and splits into two vortices. In the actual steel casting process, this upward-bending jet may cause excessive surface level fluctuation, resulting in surface defects, while the deeper jet shown in the left plot may carry more inclusions into the lower roll region, leading to inclusion defects. These are the two representative instantaneous flow patterns in the upper region. Flow in this region is seen to randomly switch between the two patterns in both LES and PIV. [30] Analysis of many frames reveals that the staircase pattern oscillates with a time-scale of ~0.5-1.5s. This is consistent with a spectral analysis of the velocity signal at this location, which shows strong frequency peaks at 0.6 and 0.9Hz, and many other smaller peaks at different frequencies. The LES results also suggest that the instantaneous flow in the two halves of the mold can be very asymmetric. The asymmetry does not appear to last long in the upper mold because a 51s average is seen to eliminate this asymmetry (see Figure 4.7,

Figure 4.10 and Figure 4.11). The instantaneous asymmetric flow in the upper roll is also evidenced by the dye-injection photograph in Figure 4.20. This picture suggests a flow pattern similar to that shown in Figure 4.19.

Two sequences of flow structures, obtained from LES and PIV [30] respectively, are compared in Figure 4.21, showing the evolution of the flow in the lower region. In the first plot (a), a vortex can be seen in the left half approximately 0.35m below the top surface and 0.15m from the center. This vortex is seen in the next two plots to be transported downstream by the flow. In both LES and PIV, the vortex is transported about 0.15m down in the 15s interval. The computed instantaneous flow also shows that the sizes of the two lower rolls change in time, causing oscillations between the two halves. Asymmetric flow in the two halves is seen in both the computation and measurements. The long-term experimental data implies that the period of the flow asymmetry in the lower region is longer than 200s. The asymmetrical flow structures shown here are likely one reason for the intermittent defects observed in steel slabs. [68]

## 4.6 Simplified Computations in the Mold Cavity of the 0.4-Scale Water Model

Although less expensive than DNS, LES still requires considerable computational resources for applications to industrial problems such as continuous casting of steel slabs. The domain of the LES shown in Figure 4.1 includes the complete upper tundish nozzle, the slide-gate, the submerged entry nozzle and the entire mold cavity. The computational cost of LES may be lowered by reducing the domain extent, for instance, by simplifying the upstream domain that determines the inlet conditions, and / or by simulating flow in only half of the mold cavity with assuming symmetric flow in the two halves of the mold.

This section presents results of two half-mold simulations with simplified inlet conditions for the 0.4-scale water model. The curved tapering cavity was simplified to be a straight domain, with constant thickness equal to the actual value 0.3m below the top surface. The time-dependent inlet velocities from the nozzle port were obtained from two simplified separate simulations. The results are compared with the complete domain simulation and PIV measurements presented earlier.

For the first simplified simulation (denoted simplified LES1), the unsteady velocities exiting the nozzle ports were obtained from a two-step simulation. In the first step, turbulent flow in a 32mm diameter pipe with a 39% opening inlet (Fig. 3.21) was computed using LES. Instantaneous velocities were collected every 0.01s for 10s at a plane 0.312m downstream of the inlet. They were then fed into a 32mm x 32mm rectangular duct (Figure 4.22) representing the flow passage in the nozzle bottom containing the bifurcated nozzle ports. Instantaneous velocities were then collected every 0.01s for 10s at planes 27mm from the center of the duct. These velocities were turned by 30$^{o}$ (to match the measured jet angle) and employed as the unsteady inlet conditions for the first mold simulation. The velocities were recycled periodically for the duration of the mold simulation.

The second simplified simulation (simplified LES2) denotes a work by Sivaramakrishnan on this same water model. [30] The inlet velocities were computed from a simulation of fully developed turbulent flow in a 32mm square-duct. The unsteady velocities were again collected every 0.01s for 10s, inclined 30$^{o}$, and fed into the mold as the inlet conditions. Figure 4.23 shows the time-averaged cross-stream inlet velocities for these two simulations. A strong dual-swirl pattern is seen in the outlet plane of the nozzle port in the first simulation (left). The cross-stream velocities for the second simulation (right) [30] are very small. Both of the simplified upstream simulations produce different inlet conditions from that in the complete nozzle-mold simulation (Figure 4.4).

The turbulent flow in the half-mold cavity was next computed using the inlet velocities obtained above. [30] The mean velocity fields at the center plane (y=0) are shown in Figure 4.24. Both the two plots reveal a double-roll flow pattern similar to the complete nozzle-mold simulation and PIV measurements. Comparisons of the time-averaged velocities in both the upper and lower regions (not shown here) also suggest that these two simplified simulations roughly agree with results of the full-mold simulations and PIV. However, a straight jet is observed in the second simulation, which differs from those of the first simplified simulation, the complete nozzle-mold simulation and the PIV. Lack of cross-stream velocities in the jet is believed to be the reason for the straight jet. Neither of these simplified half-mold simulations captured the instantaneous stair-step shaped jet observed earlier. Both simulations missed the phenomena caused by the interaction between flow in the two halves, which is reported to be important to flow transients. [21] Figure 4.25 illustrates this with sample velocity signals at a point 20mm below the top surface, mid-way from the SEN and the narrow face, compared with PIV. It is observed that both the simplified simulations only capture part of the behavior of the measured signal. The sudden jump of the instantaneous x velocity component, which is reproduced by the full-mold simulation (Figure 4.13), is missing from both half-mold simulations. This suggests that the sharp velocity fluctuation is caused by the interaction of the flow in the two halves. The selection of the computational domain must be decided based on a full consideration of the available computational resources, the interested flow phenomena (e.g. flow asymmetry) and the desired accuracy.

## 4.7 Flow in the Full-Scale Standard-Thickness-Slab Water Model

The full-scale water model of *Case 1* has a much large domain with a volume approximately twenty times of that of the 0.4-scale water model. To reduce the computational cost, the computational domain for *Case 1* only included half of the mold region. The computed three-dimensional time-dependent flow field was further used for a Lagrangian particle simulation presented in CHAPTER **8**. The transient inflow velocities for *Case 1*, obtained from the prior pipe simulation, are averaged temporally and shown in Figure 4.26. Higher velocities are revealed in the lower portion. This is consistent with previous measurements and predictions on similar nozzles. [35, 62] The outward and downward velocity components along the port centerline are depicted in Figure 4.26 (b), with maximum values at approximately one third distance from the port bottom.

A typical instantaneous velocity field in the liquid pool is shown in Figure 4.27. A double flow pattern is observed here which matches experimental observations. [17, 69] No stair-step shaped jet was observed during the simulation, as expected for this stopper rod controlled system. A closer view of the turbulent structures in the upper roll is presented in Figure 4.28 for two time instants. The figure shows that the upper roll consists of a relatively simple vortex at the first instant, which evolves to a pattern involving more complex multiple vortices at the second instant. The upper roll alternates irregularly between the two extremes in the simulation. It is also found that, only close to the top surface is the velocity direction consistently horizontal. This is important in understanding the accuracy of the indirect measurement of the flow velocity in steel casters using electromagnetic sensors, [66] which requires a consistent flow direction passing the sensors.

Figure 4.29 compares the results of the simulation with measurements. The time-averaged speed, $(v_x^2+ v_y^2)^{1/2}$, of the fluid was measured using hot-wire anemometers in a previous work. [17] The measurement was made along four vertical lines in the center plane at specified distances from the SEN. The computation agrees reasonably well with the measurements. The biggest discrepancy occurs along the line 460mm from the SEN, where the predicted maximum speed location is approximately 100mm deeper than the measurement in Set 1. This might be due to uncertainties in the measurements. It should be noted that significant differences exist between the measured time averages taken at different times, likely due to insufficient time for calculating statistics.

## 4.8 Summary

The three-dimensional turbulent flows in two water models were studied using LES. The computed velocity fields were compared with PIV and hotwire anemometer measurements. The following observations are made from this work:

(1) Considering the uncertainties with the measurements, the LES predictions generally agree with the experimental data with reasonable accuracy.

(2) The partial opening of the slide-gate induces a long, complex recirculation zone in the SEN. It further causes strong swirling cross-stream velocities in the jets exiting from the nozzle ports. Complex flow structures consisting of single and multiple vortices are seen to evolve in time at the outlet plane of the nozzle port.

(3) A downward jet with an approximate inclination of 30 degrees is seen in the 0.4-scale water model in both LES and PIV. The computed velocities agree reasonably well with measurements in the mold region. The jet usually wobbles with a period of 0.5-1.5s.

(4) The instantaneous jets in the upper mold cavity alternate between two typical flow patterns in the 0.4-scale water model: a stair-step shaped jet induced by the cross-stream swirl in the jet, and a jet that bends upward midway between the SEN and the narrow face. The stair-step flow pattern, which is missing in the stopper rod controlled full-scale water model, is likely due to the cross-stream swirl in the jet induced by the slide gate. The flow in the upper region is seen to oscillate between a large single vortex and multiple vortices of various smaller sizes. Large, downward-moving vortices are seen in the lower region.

(5) Significant asymmetry is seen in the instantaneous flow in the two halves of the mold cavity in the 0.4-scale water model. A 51s average reduces this difference in the upper region. However, asymmetric flow structures are seen to persist longer than 200s in the lower rolls.

(6) The instantaneous top surface velocity is found to fluctuate with sudden jumps from –0.01m/s to 0.24m/s occurring in as little as ~0.7s in the 0.4-scale water model. These velocity jumps are seen in both the full nozzle-mold simulations and the PIV measurements. Level fluctuations near the narrow face occur over a wide range of frequencies, with the strongest having periods of ~7 and 11-25s.

(7) The velocity fields obtained from half-mold simulations with approximate inlet velocities generally agree with the results of the full domain simulations and PIV measurements. However, they do not capture the interaction between flows in the two halves, such as the instantaneous sudden jumps of top surface velocity.

**Table 4.1 Dimension and Operating Conditions of the 0.4-Scale Water Model and the Full-Scale Water Model**

| Dimensions/Conditions | 0.4-Scale Water Model | Full-Scale Water Model |
|---|---|---|
| Slide-gate orientation | $90^o$ | - |
| Slide-gate opening (area) | 39% | - |
| SEN bore diameter | 32mm | - |
| SEN submergence depth | 75mm | 150mm |
| Port height $\times$ width | 32mm $\times$ 31mm | 51$\times$56 (see Figure 4.1) |
| Port thickness | 11mm | - |
| Port angle, lower edge | $15^o$ down | - |
| Port angle, upper edge | $40^o$ down | - |
| Bottom well recess depth | 4.8mm | - |
| Water model height | 950mm | 2152mm |
| Water model width | 735mm | 1830mm |
| (corresponding full scale caster width) | 1829mm (72 inch) | 1830mm |
| Water model thickness | 95mm(top) to 65mm(bottom) | 238mm |
| (corresponding full scale caster thickness) | 229mm (9 inch) | 238mm |
| Outlet at the bottom of the water model | 3 round 35mm diameter holes | 4 round 200mm diameter holes |
| Inlet volumetric flow rate through each port | $3.53\times10^{-4}$ $m^3/s$ | 3.44$\times$10-4 $m^3/s$ |
| Mean velocity inside nozzle bore | 0.439 m/s | 1.69 m/s |
| Casting speed (top thickness) | 10.2mm/s (0.611m/min) | 15.2mm/s (0.912m/min) |
| Water density | 1000 $kg/m^3$ | 1000 $kg/m^3$ |
| Water kinematic viscosity | 1.0$\times$10-6 $m^2/s$ | 1.0$\times$10-6 $m^2/s$ |
| Gas injection | 0% | 0% |

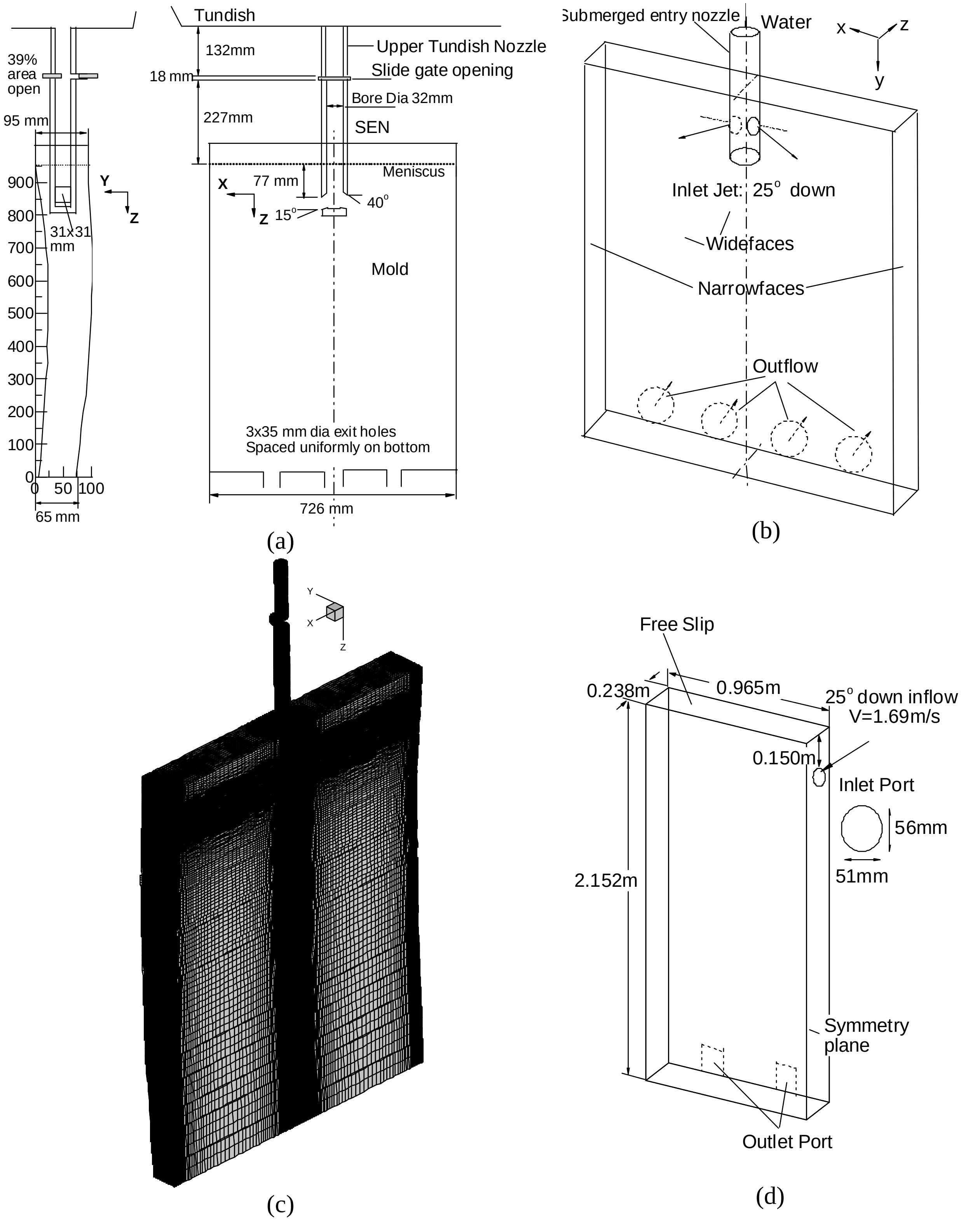


**Figure 4.1. Schematics of (a) the 0.4-scale water model and (b) the full-scale water model and (c-d) the corresponding computational domains.**

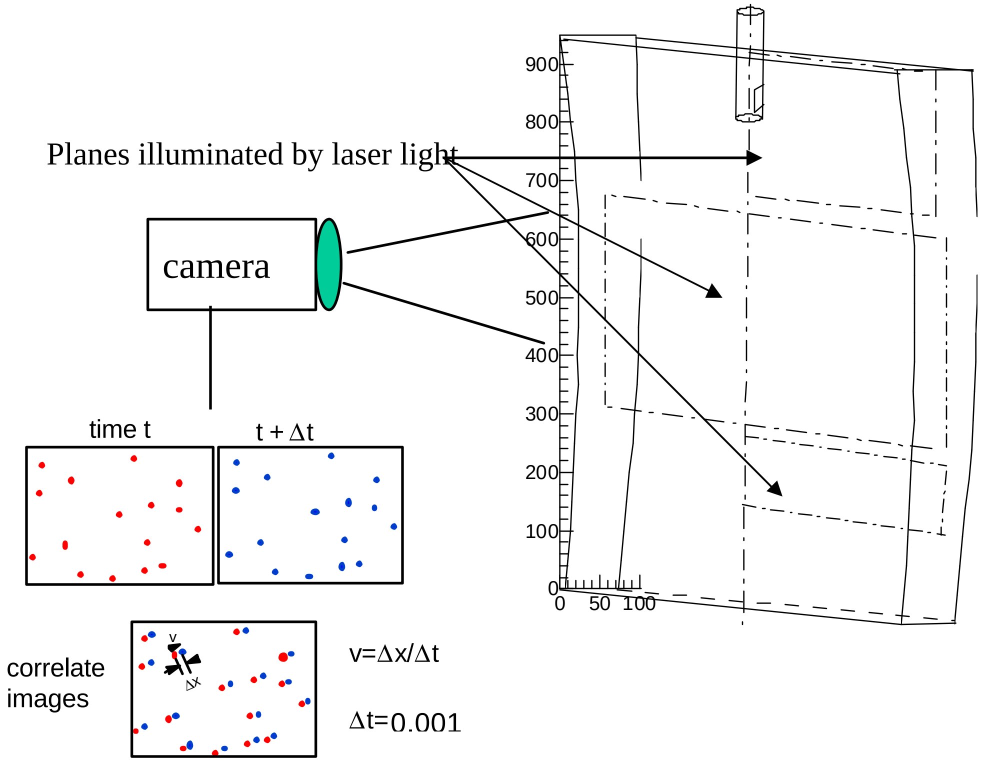


**Figure 4.2. Schematics showing the PIV measurement regions. [30]**

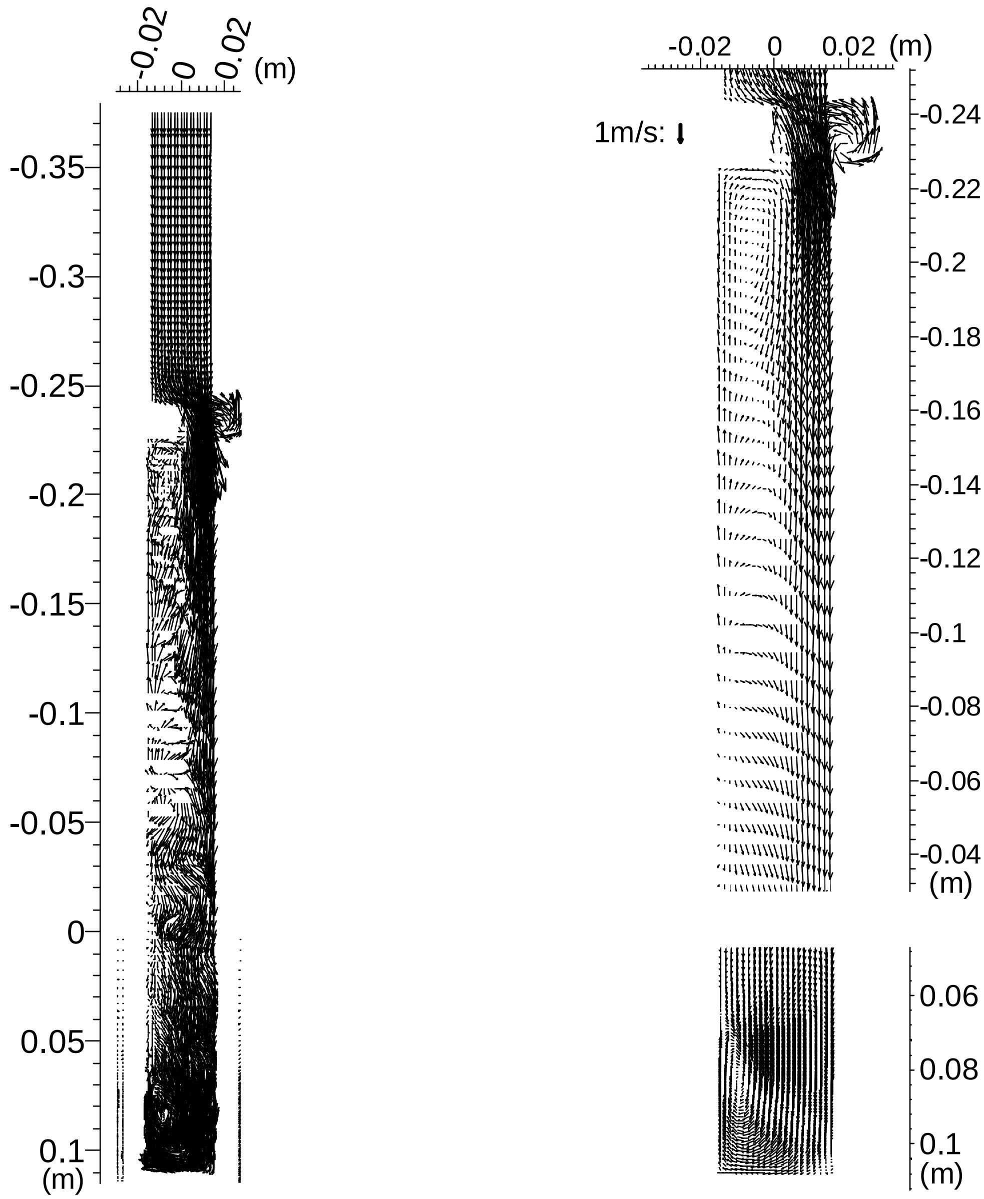


**Figure 4.3. Computed time-averaged velocity field at the center plane x=0 of the SEN in the 0.4-scale water model.**

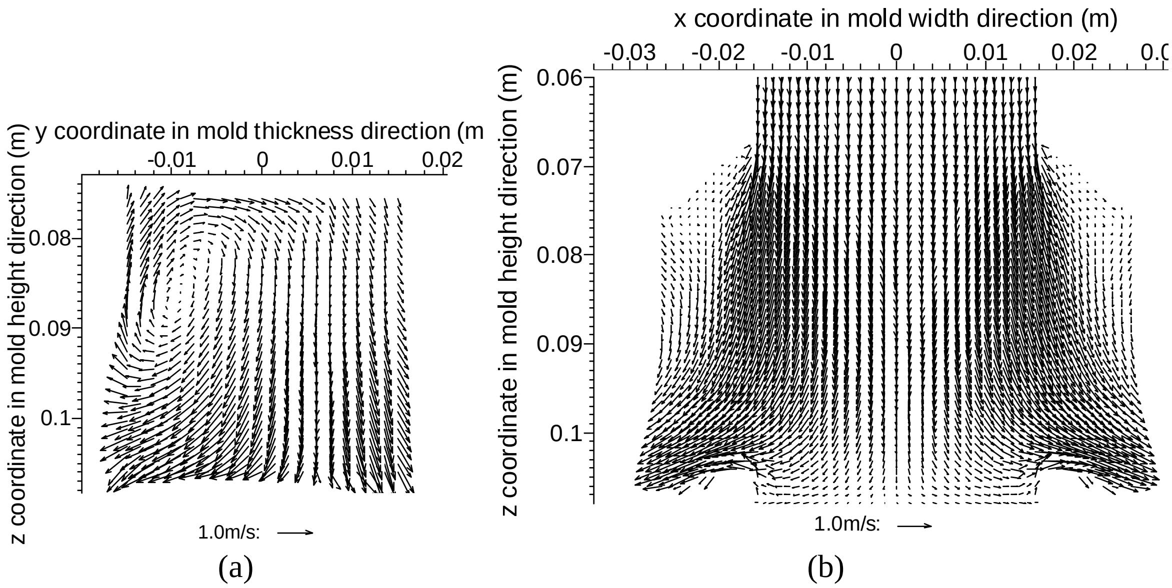


**Figure 4.4. Computed time-averaged velocity field exiting nozzle ports: (a) view into the port and (b) slice y = 0.**

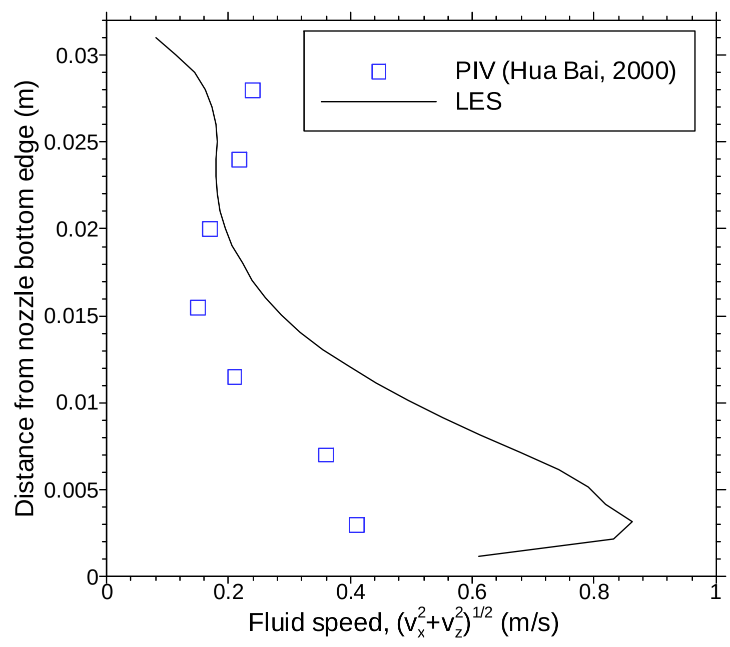


**Figure 4.5. Time-averaged fluid speed $\left(\overline{v_x}^2 + \overline{v_z}^2\right)^{1/2}$ along the vertical centerline of the SEN nozzle ports, obtained from LES and PIV. [63]**

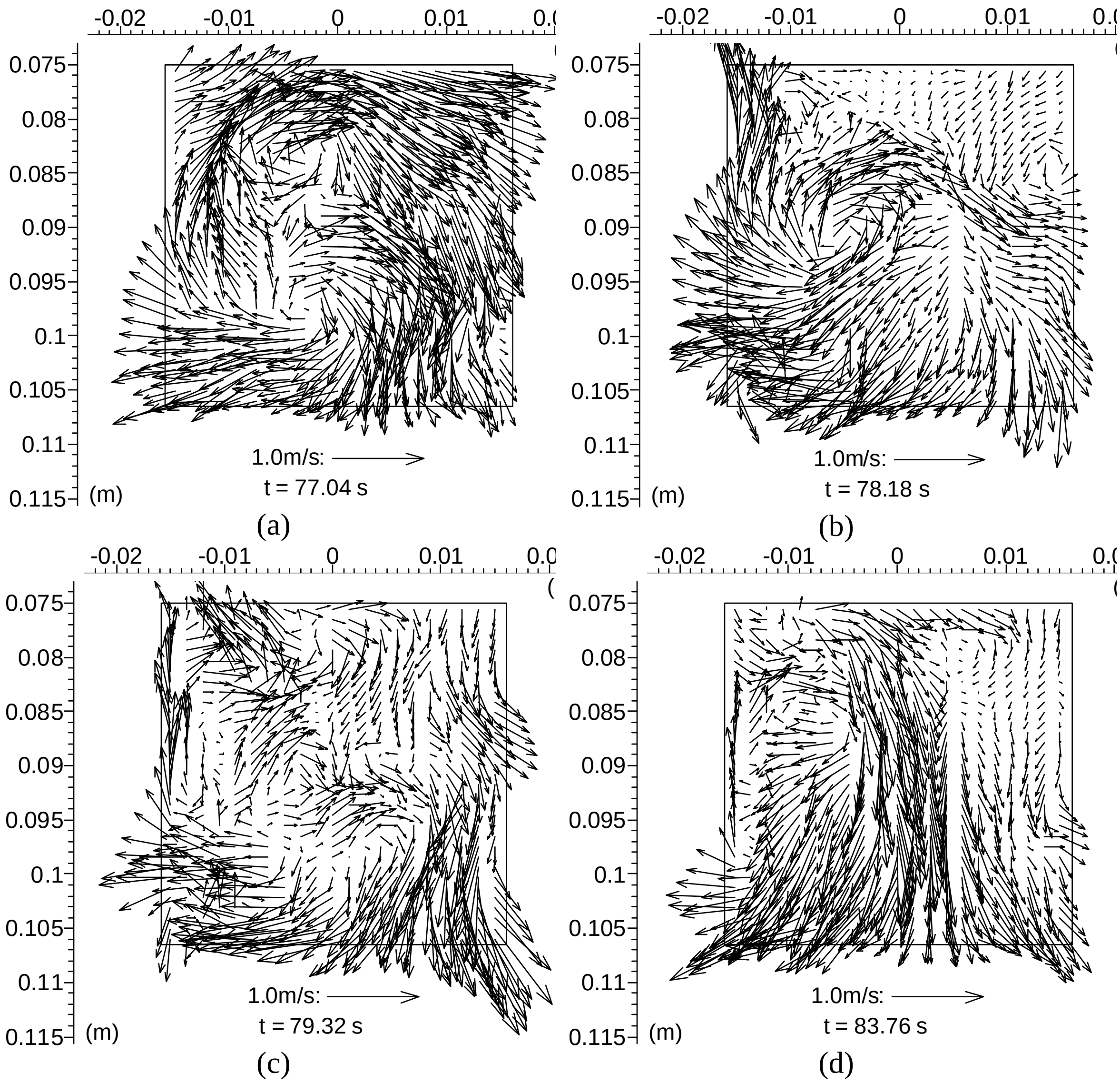


**Figure 4.6. Representative instantaneous cross-stream flow patterns exiting the nozzle port obtained from LES, view into the port.**

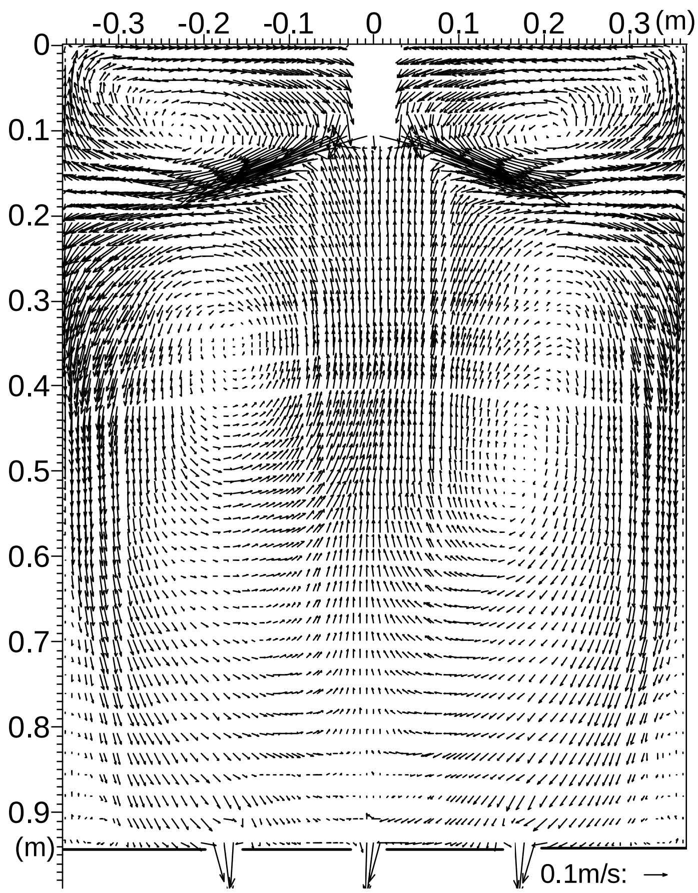


**Figure 4.7. Time-averaged velocity vector plot in the mold region obtained from LES.**

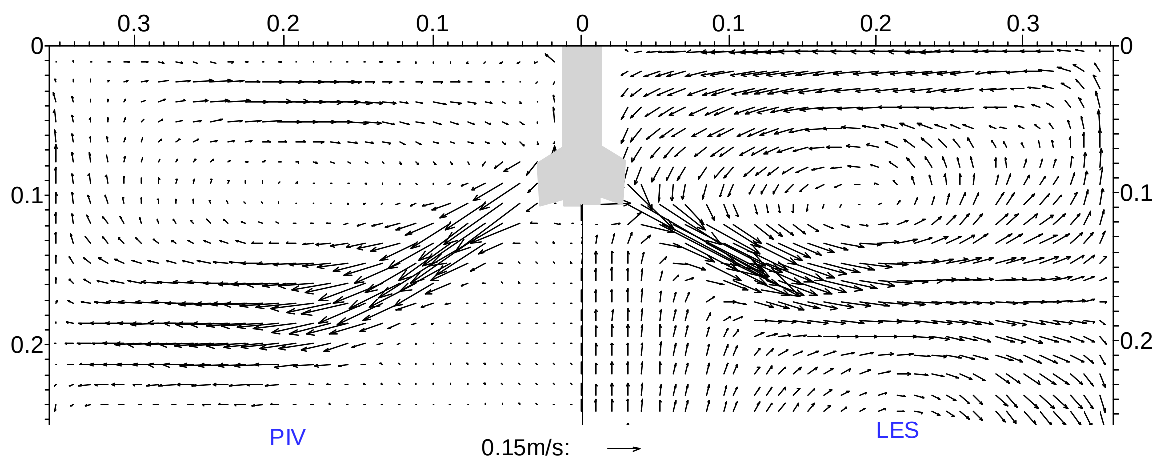


**Figure 4.8. Time-averaged velocity vectors in the upper roll sliced at y=0, obtained from LES and PIV. [30]**

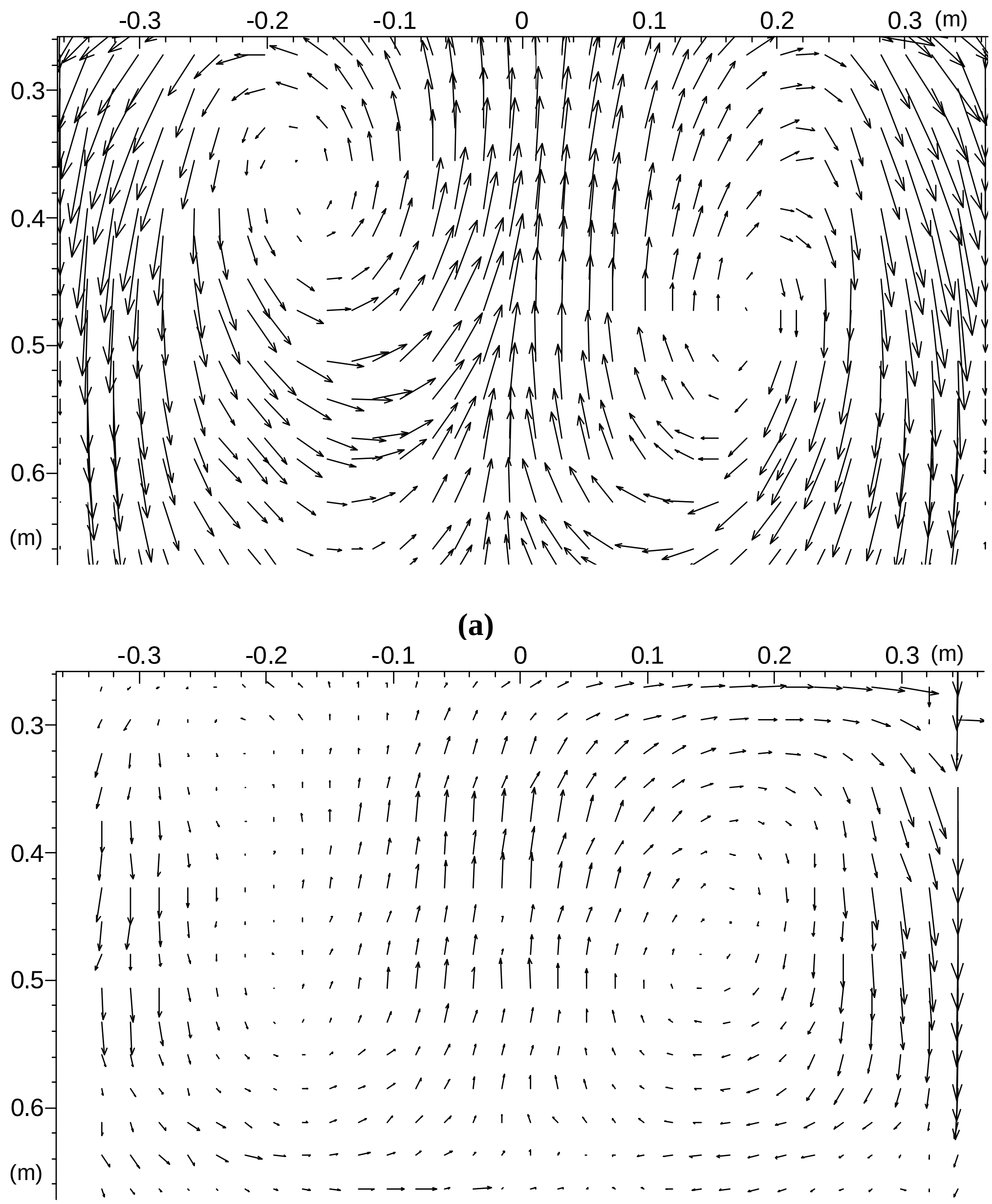


**(b)**

**Figure 4.9. Time-averaged velocity vectors in the lower roll region, obtained from (a) LES and (b) PIV measurements. [30]**

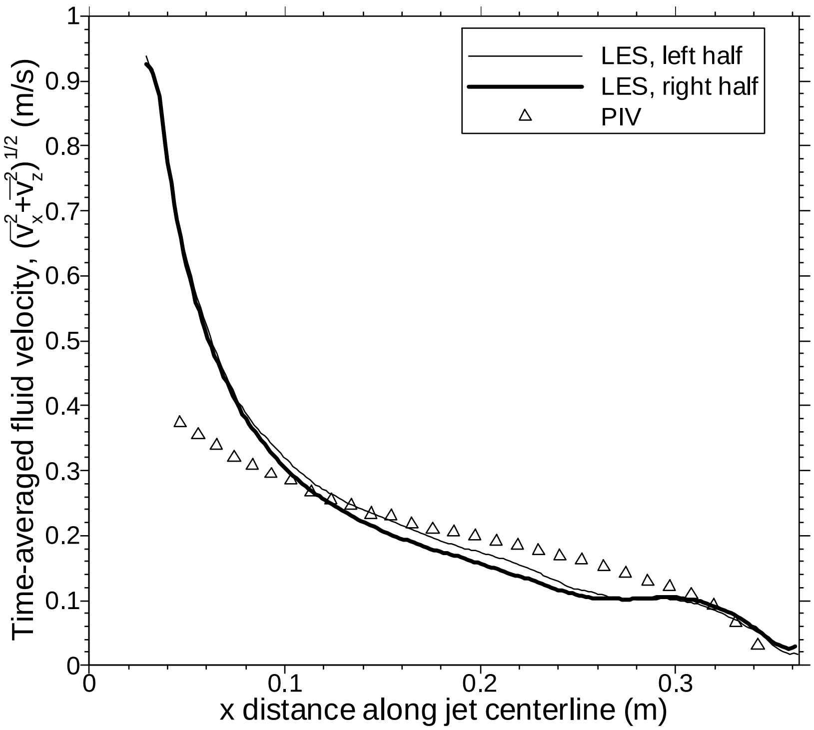


**Figure 4.10. Time-averaged fluid speed $\left(\overline{v}_x^2+\overline{v}_y^2\right)^{1/2}$ along jet centerline, obtained from LES (SGS-k model) and PIV measurements. [30]**

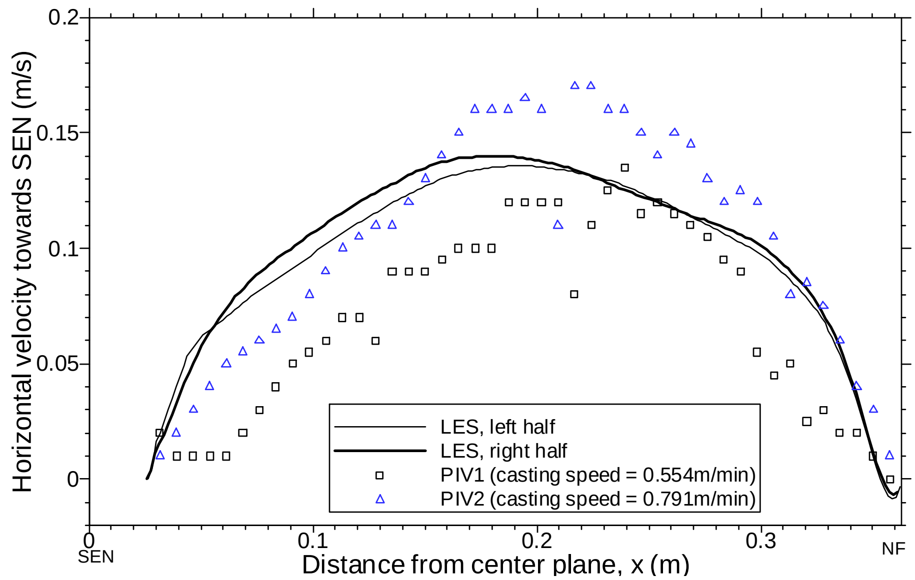


**Figure 4.11. Time-averaged horizontal velocity towards SEN along the top surface centerline, obtained from LES and PIV. [70]**

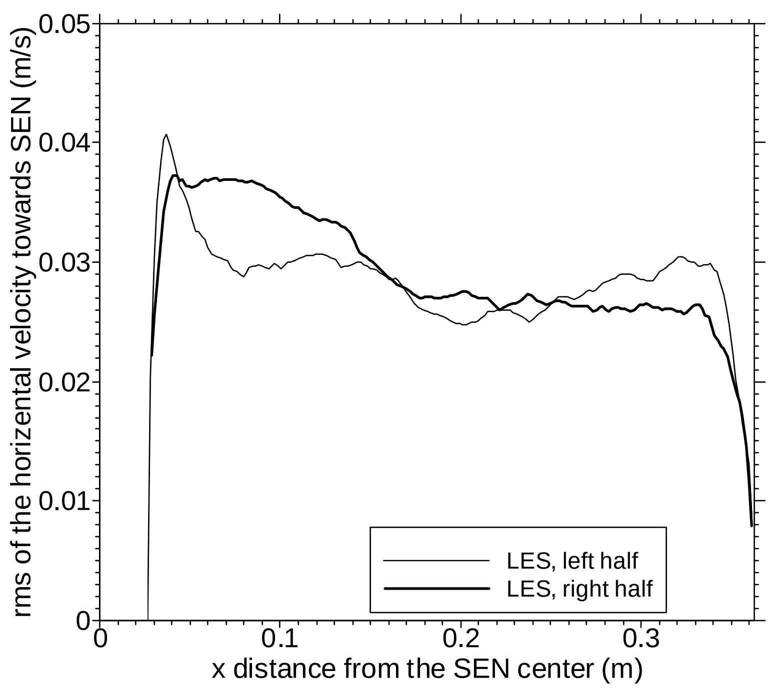


**Figure 4.12. *rms* of u velocity component along the top surface centerline.**

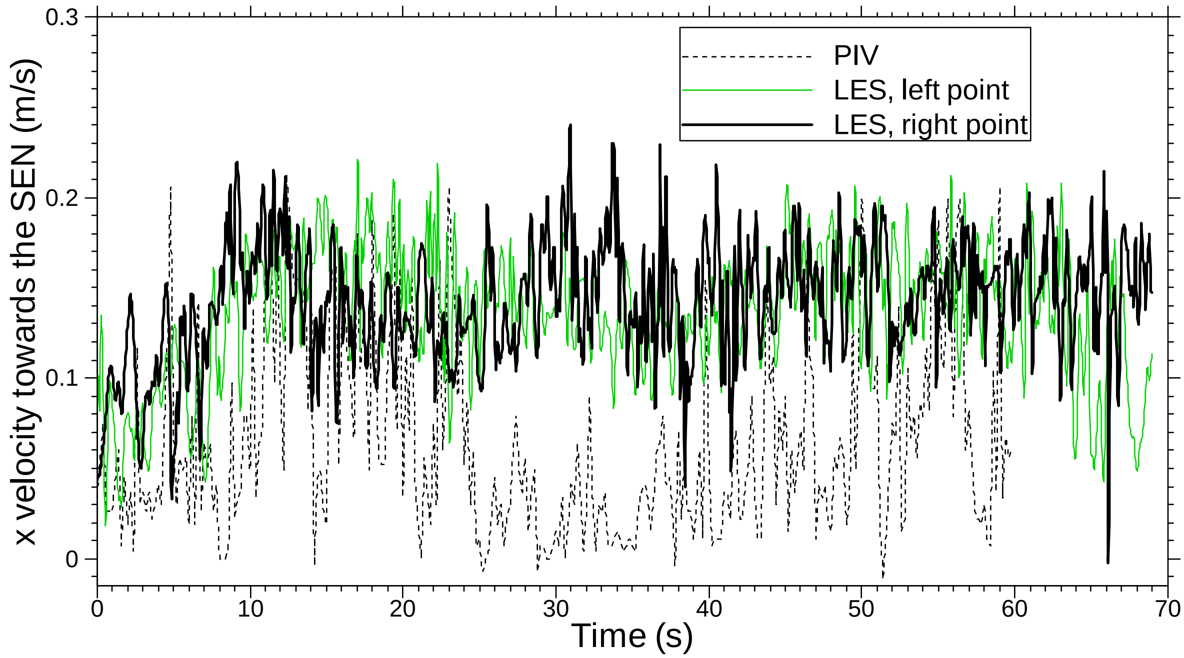


**Figure 4.13. Fluctuations of the horizontal velocity towards SEN (20mm below the meniscus, midway between the SEN and narrow face), obtained from LES and PIV. [30]**

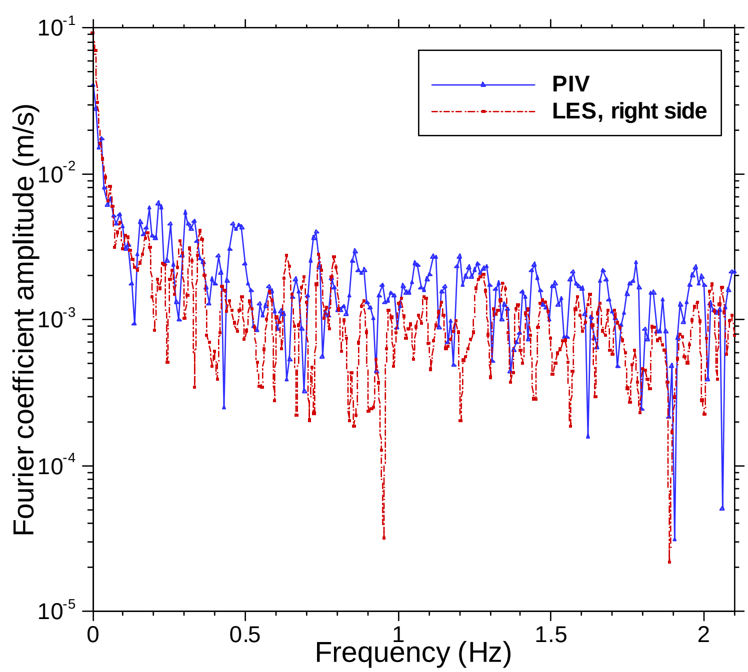


**Figure 4.14. Spectra of the signals shown in Figure 4.13.**

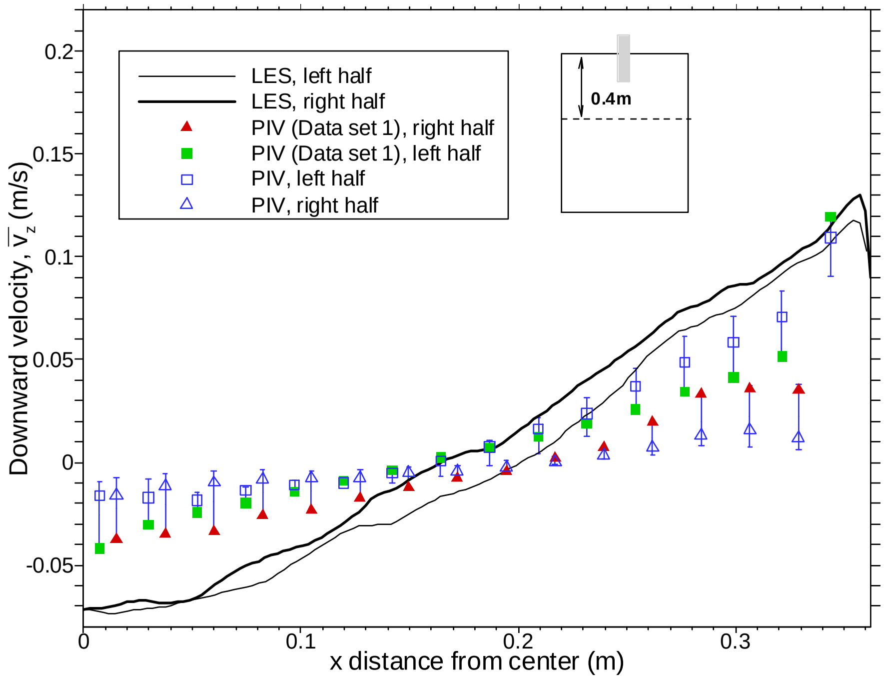


**Figure 4.15. Time-averaged downwards velocity component across the width (along the horizontal line 0.4m below the top surface, mid-way between wide faces), obtained from LES and PIV. [30]**

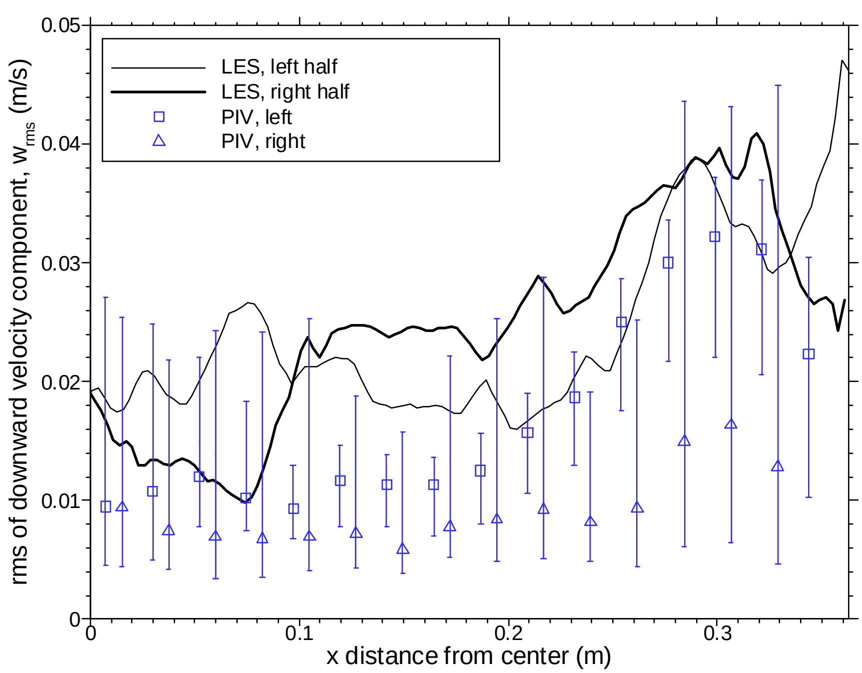


**Figure 4.16. *rms* of the downward velocity component along the line in Fig. 4.15.**

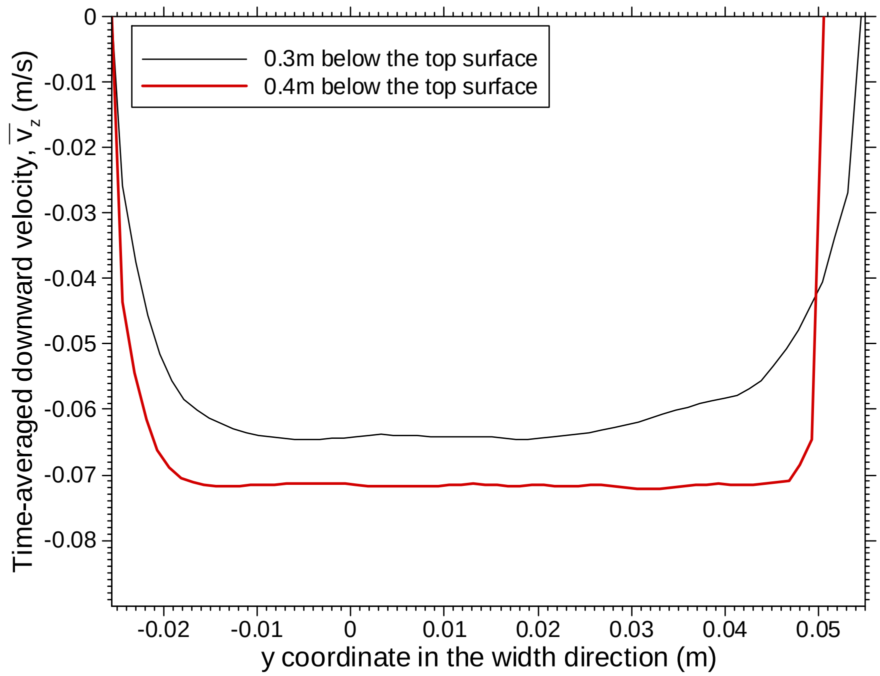


**Figure 4.17. Spatial variation of the downward velocity across the thickness direction (beneath SEN) in the 0.4-scale water model.**

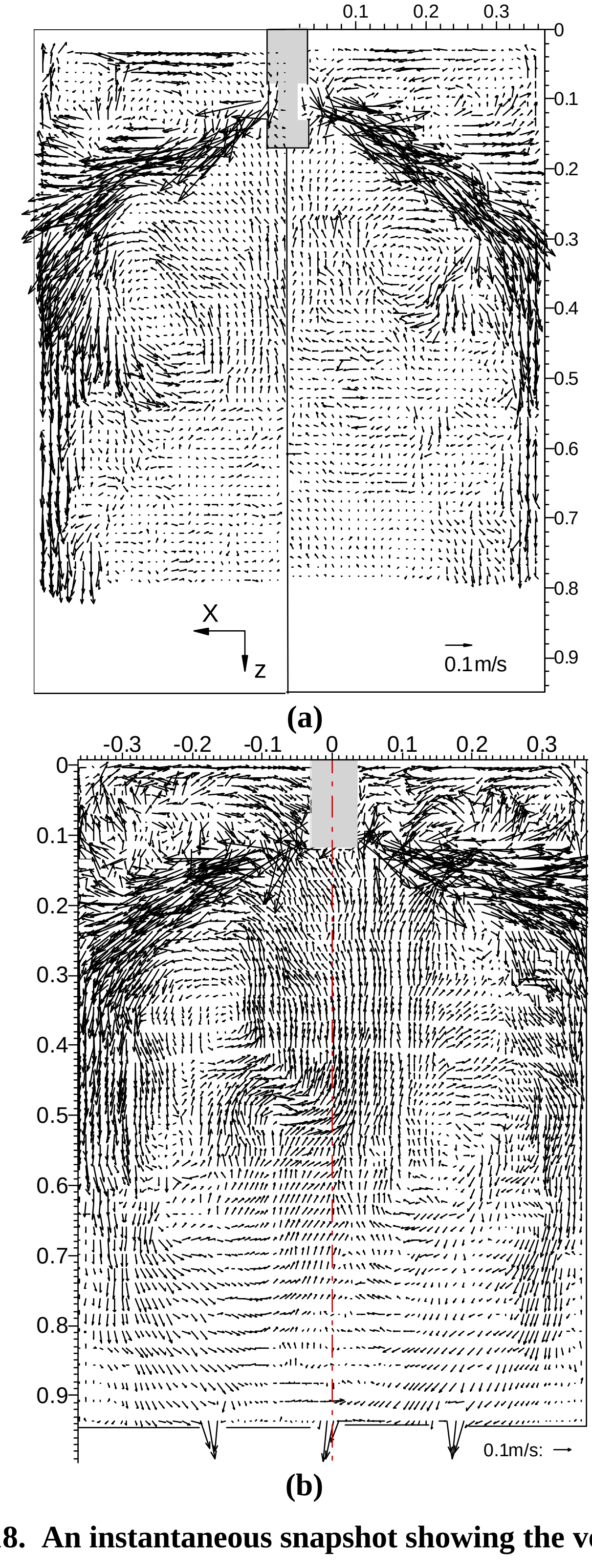


**(b)**

**Figure 4.18. An instantaneous snapshot showing the velocity field in the 0.4-scale water model, obtained from (a) PIV measurements [30] and (b) LES.**

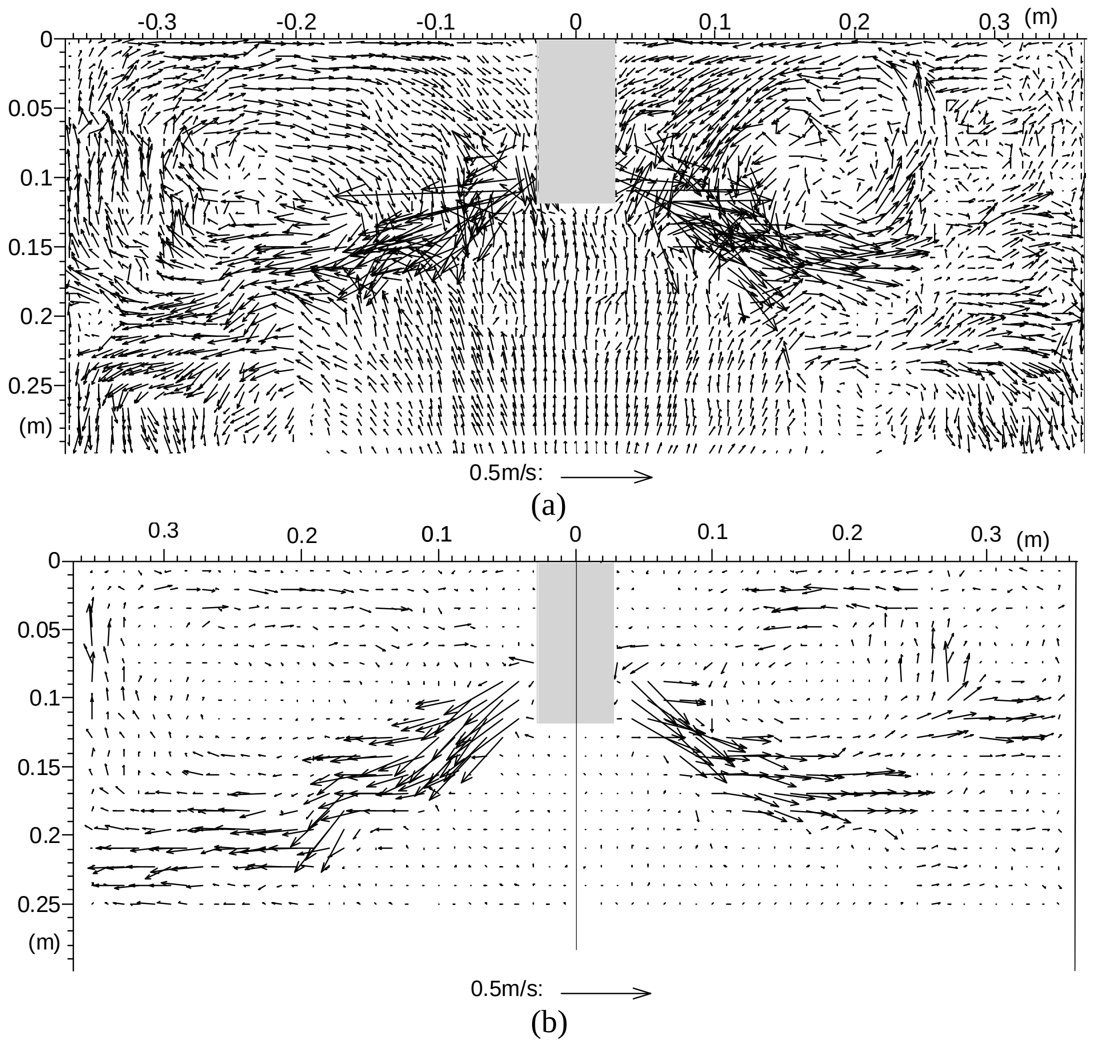


**Figure 4.19. Instantaneous velocity vector plots in the upper region obtained from (a) LES and (b) PIV measurements. [30]**

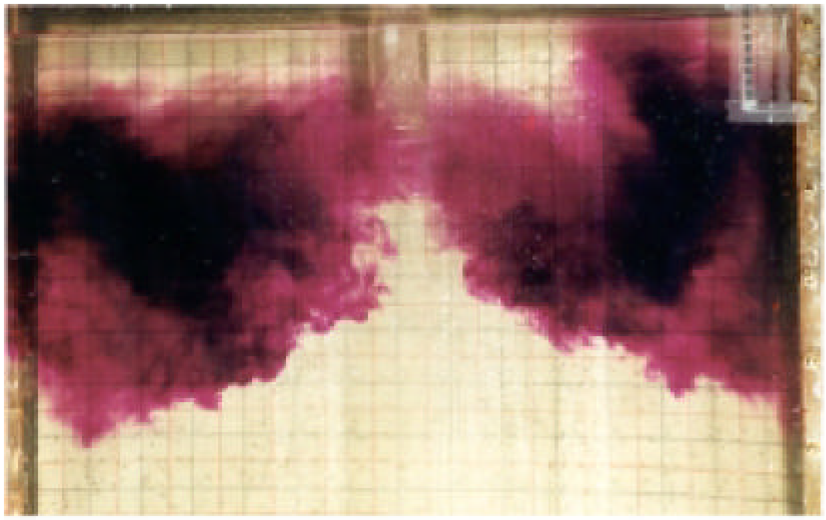

**Figure 4.20. Snapshot of dye injection in the water model, showing asymmetry between the two upper rolls. [30]**

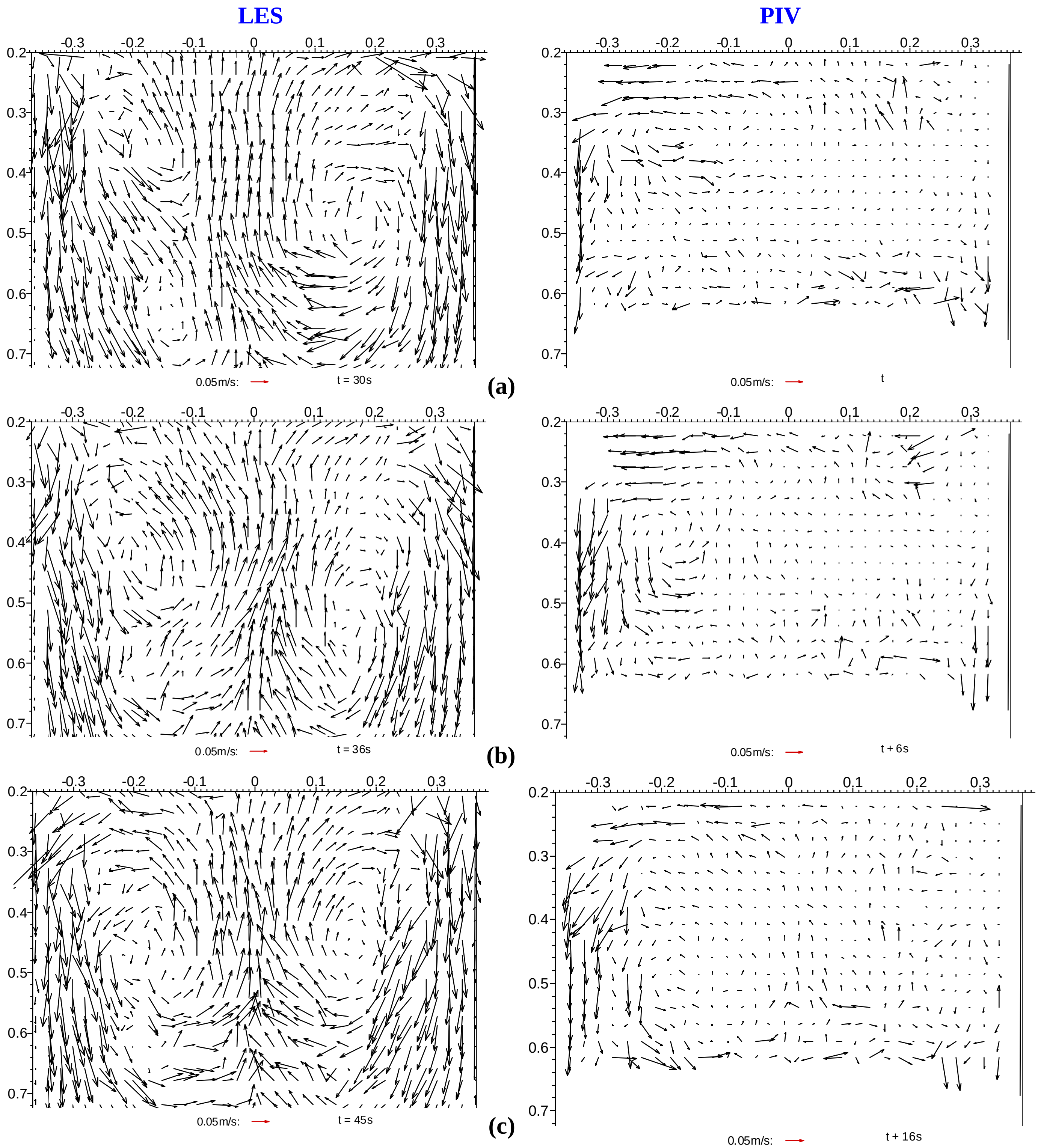


**Figure 4.21. A sequence of instantaneous velocity vector plots in the lower roll region obtained from LES and PIV measurements, [30] showing evolution of flow structures.**

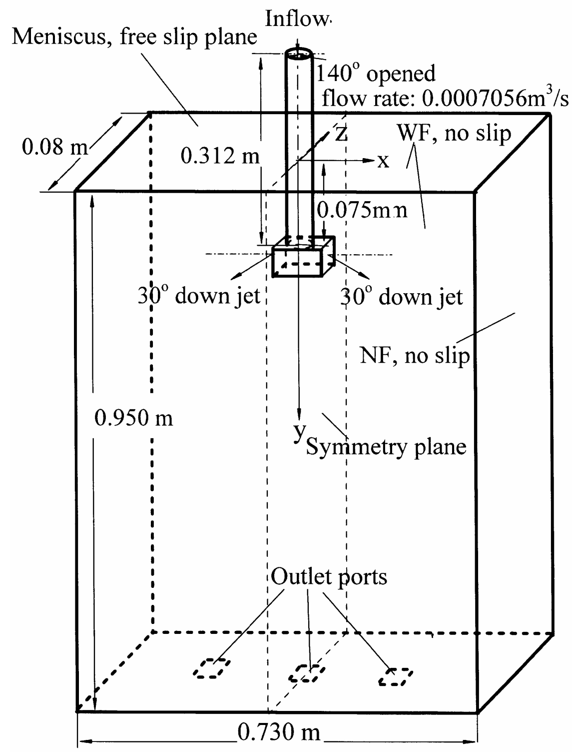


**Figure 4.22. Schematics showing the simplified simulations of the 0.4-scaled water model.**

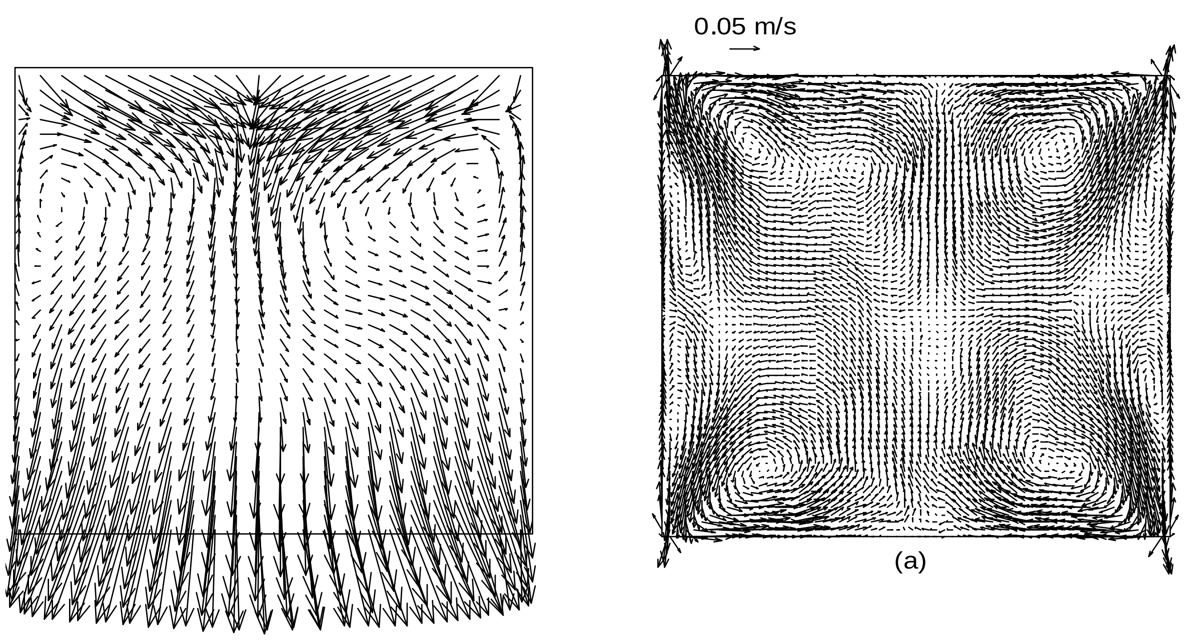


(Scale: 0.5m/s) (Scale: 0.05m/s)

**Figure 4.23. Cross-stream flow patterns exiting the nozzle port in the simplified simulations.**

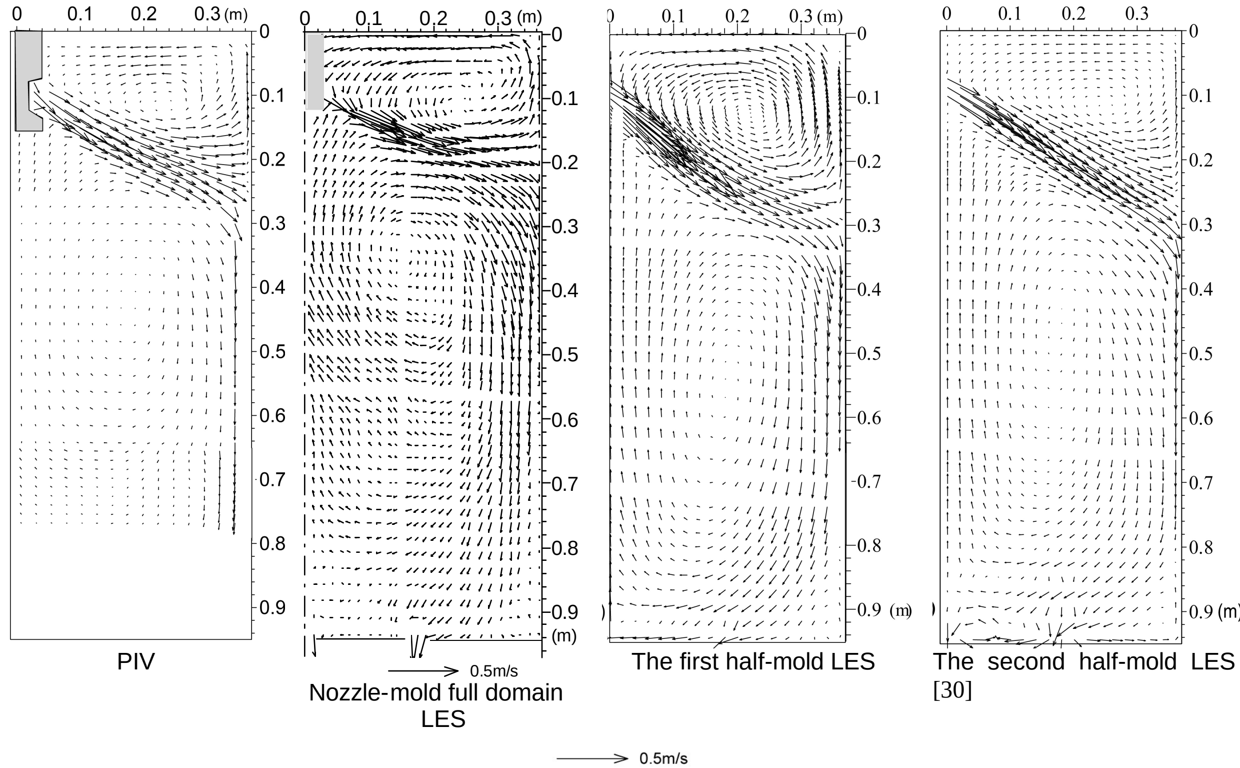


**Figure 4.24. Time-averaged velocity vector plots obtained from the simplified simulations, compared with full nozzle-mold simulation and PIV measurement. [30]**

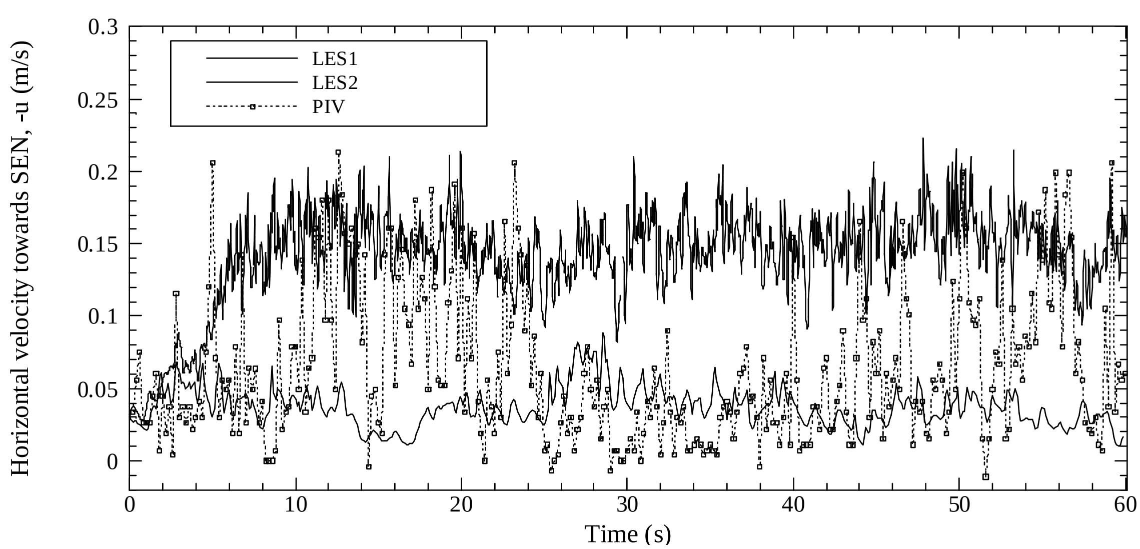


**Figure 4.25. Time history of horizontal velocity towards SEN at points 20mm below the top surface, mid-way between the SEN and narrow faces.**

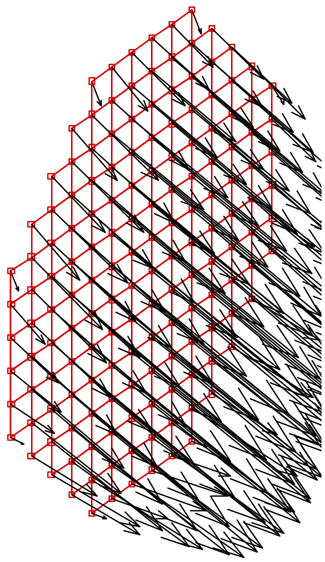

**(a)**

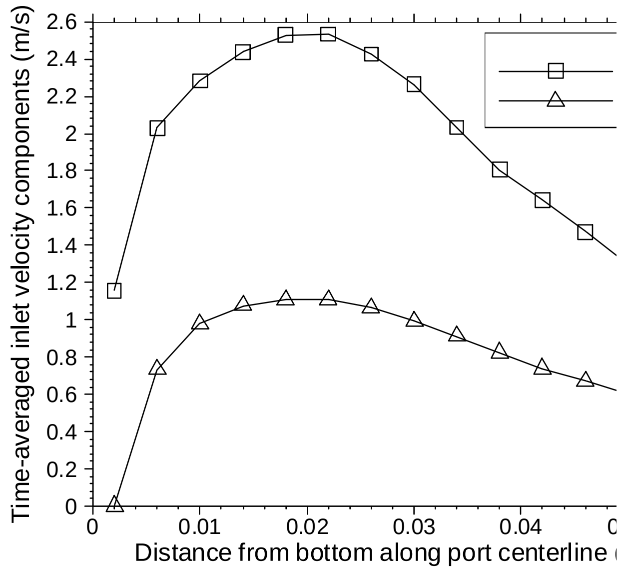


**(b)**

**Figure 4.26. Inlet velocities of the standard slab caster water model:**

**(a) time-averaged velocity vectors at the inlet port and (b) transverse (x) and downward (z) velocity components along nozzle port centerline.**

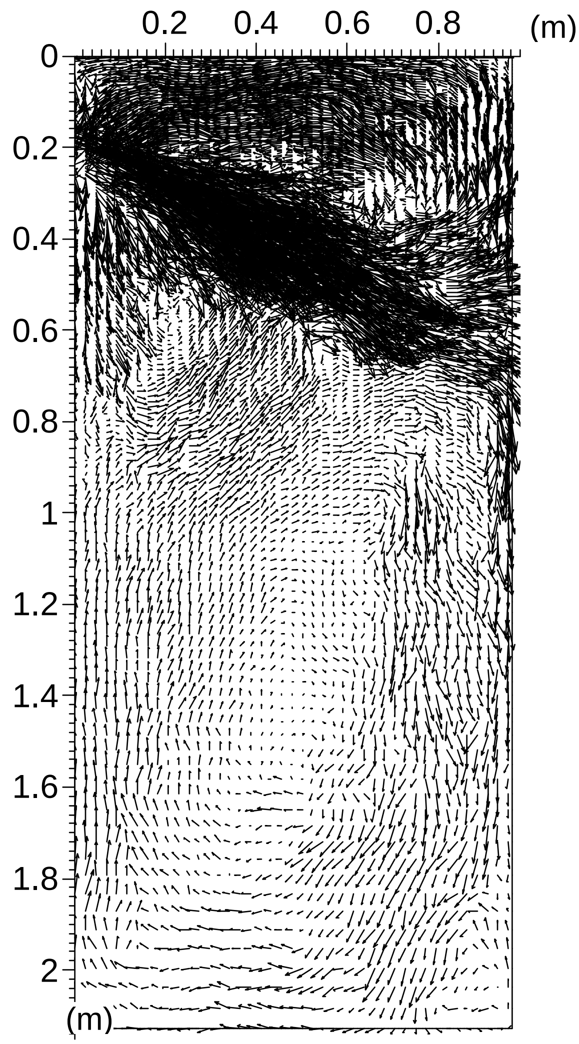


(Scale : ⟶ 0.25 m/s)

**Figure 4.27. Typical instantaneous velocity vector plot at the center plane between wide faces of the full-scale water model, obtained from LES.**

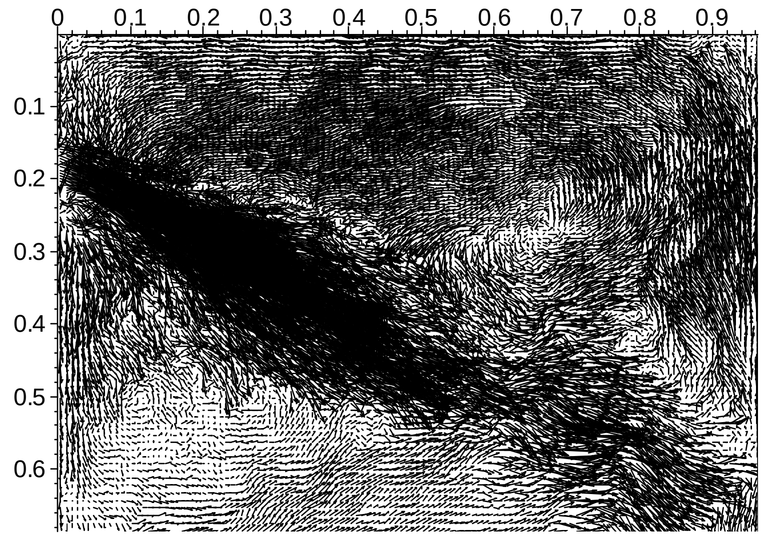


(Scale : → 0.25m/s)

**(a)**

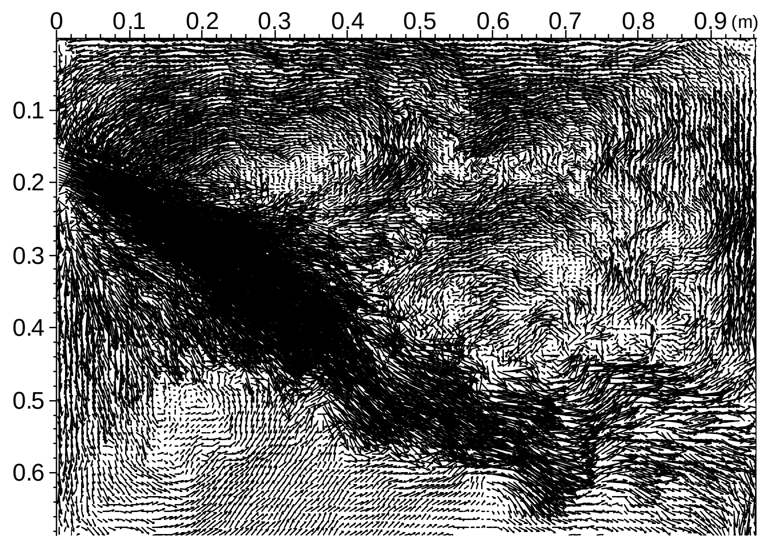


**(b)**

**Figure 4.28. Predicted chaotic flow patterns in the upper recirculation zone of the full-scale water model: (a) simple vortices and (b) complex multiple vortices.**

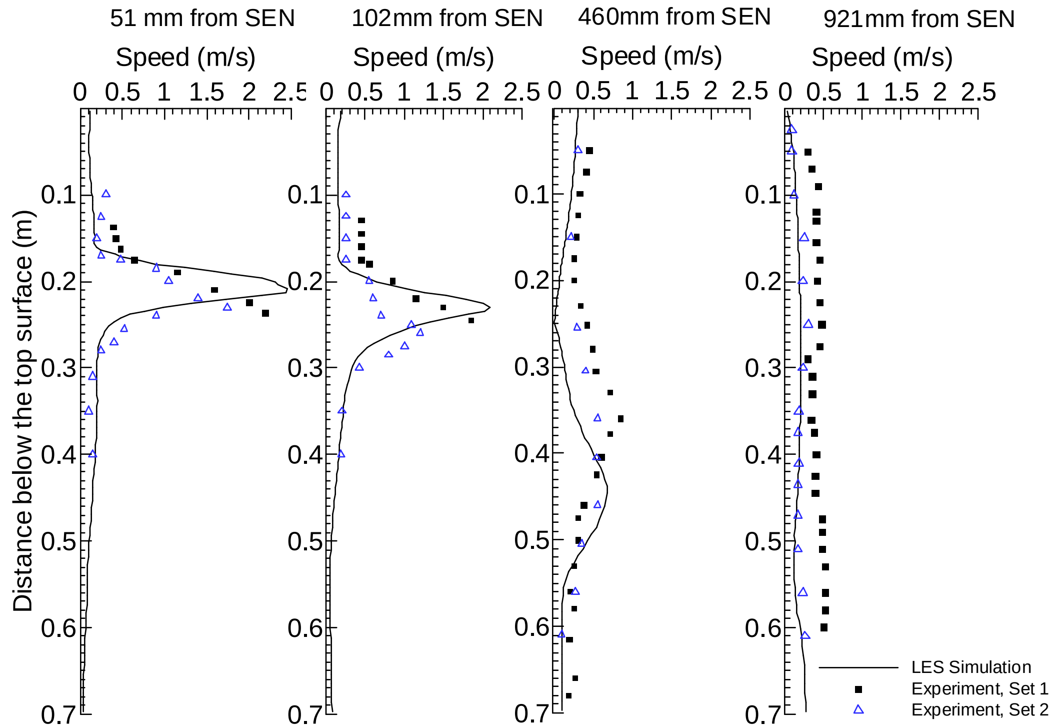


**Figure 4.29. Comparison between the prediction and measurement [17] of the time-averaged speed $(v_x^2+v_z^2)^{1/2}$ along four vertical lines at different distances from SEN(*Case 1*).**

# CHAPTER 5. TURBULENT FLOW IN A THIN-SLAB STEEL CASTER

The accuracy of the LES predicted results was examined by comparing with measurements in water models in the last chapter. It should be re-addressed that the water model differs from the steel caster mainly in its stationary plastic sidewalls and closed-bottom. In addition, the kinematic viscosity of liquid steel is approximately 20% smaller than that of water. Therefore, the two systems may have different flow patterns under the same operating conditions. In this chapter, the LES is applied to predict the turbulent flow in a thin-slab steel caster along with a full-scale water model corresponding to the caster, denoted as *Case 2-S* and *Case 2-W* respectively. The unsteady flow in the actual steel caster is investigated. Quantitative comparisons are made between the two systems. The computed velocities were used for particle transport simulations in CHAPTER 9.

## 5.1 The Thin-Slab Steel Caster and Its Full-Scale Water Model

Domains of a thin-slab stainless-steel caster (*Case 2-S*) and a full-scale water model (*Case 2-W*) corresponding to it are presented in Figure 5.1. The dimensions and operating conditions for both systems are shown in Table 5.1. Table 5.2 gives the compositions of the stainless steel. [71] The Both systems used the same trifurcated inlet nozzle. A prior nozzle simulation with realistic geometry was performed with an unstructured Cartesian grid consisting 0.6 million finite-volumes. Time-dependent velocities exiting the trifurcated nozzle ports were stored every 0.025s for a duration of

9.45s (10-day computation on PentiumIV 1.7GHz CPU) and used as the inflow velocities for the mold simulations.

Figure 5.1(a) illustrates that the domain for the steel caster has a curved side boundary, which represents the mushy zone front at the liquidus temperature. The boundary shape was obtained from the prediction of an in-house code, CON1D, [72] which is shown to agree with the measured shape of a breakout shell shown in Figure 5.2. [71] It should be noted that the symmetry plane assumption is needed for neither of the simulations.

Unstructured Cartesian grids consisting of 1.4 million and 0.7 million cells were employed for *Case 2-S* and *Case-W* respectively. The former grid features cells centered 0.9mm from the wall in the upper mold including the impingement region. This half-cell size gradually increases to a maximum of 12mm in the lower-gradient interior of the domain. The time step size of 0.001s was used in both simulations. The simulation took 29.5 CPU seconds per time step on a Pentium IV 1.7GHz PC for the 1.4 million cells grid or 24 days for 70,000 time steps (70 seconds of real time) with the AMG solver.

## 5.2 Flow in the SEN

A realistic nozzle simulation was conducted to generate accurate unsteady inlet velocities for the computations in the thin slab caster. The computed results are presented in Figures. 5.3 - 5.6. Two typical instantaneous flow patterns are plotted in Figure 5.3 showing flow exiting the nozzle ports at different times. Supplementary to the vector length the arrow darkness also represents the velocity magnitude. In Figure 5.3(a), a symmetrical flow pattern is observed between the side ports, while it is apparently asymmetrical in Figure 5.3 (b). In the simulation, the downward angles of the two side jets varied in time from ~$30^o$ to $45^o$. The two side jets switched between the two extremes. The jet angle is important because it greatly affects the transport of harmful inclusions carried by the jet entering the liquid pool. Jets at a deeper angle tend to transport more inclusions into the lower roll, encouraging the formation of internal defects such as slivers and blisters (discussed in more detail in Part II). The jet angle is also important as it influences the velocity and the profile of the top surface liquid level. Jets at smaller downward angles are likely to increase the velocity and the liquid level fluctuations along the top surface, by carrying more fluid and momentum into the upper roll. This can cause quality problems as discussed in the previous sections. Accurate prediction of this angle is essential for optimizing the nozzle design. The center jet velocity was seen in the simulation to fluctuate considerably but the flow pattern in the mold stays nearly the same.

Figure 5.4 shows the fluctuation of the downward velocity component ($v_z$) sampled at two points, which are symmetrically located on the side-port outlet planes with a distance 40mm below the upper edge. Both signals reveal a mean value of ~0.6m/s but with significant fluctuations. The highest frequency of the signals is around 10Hz. The velocity component is mostly positive, indicating that the flow was mostly downward with occasional upward excursions. Short-term velocity differences are observed between the two sides. However, averaging over a short time is seen to result in approximately the same flow field (see Figures 5.5 and 5.6).

The computed instantaneous velocities in the nozzle were averaged over 9.45s (37800 time instants) and plotted in Figure 5.5. The velocities of the side jets are quantitatively shown in Figure 5.6 along the nozzle port centerline. The time-averages of the two side jets are symmetrical even for a short time (9.45s) of average. Most of the fluid exits the ports from the port center region (20mm-80mm below the upper edge), with some small back flow near the upper and lower edges, where the fluid re-enters the nozzle.

## 5.3 Flow in the Full-Scale Water Model

The time-dependent velocities obtained from the trifurcated nozzle simulation were used as the inflow into the thin-slab water model computation. Before showing the computational results, Figure 5.7 first presents snap-shots from the dye-injection experiment on the water model at four instants, showing the evolution of the transient flow in the mold region. Figure 5.7(a) is at 0.5s after the dye exits the nozzle ports, showing instantaneous jet angles of ~42$^o$ (left) and ~35$^o$ (right). The dye flows with the jet and impinges the narrow face 0.7s later as shown in Figure 5.7(b). It then splits into two parts with the flow to move into the lower and upper recirculation zones, as can be seen in plots (c) and (d). The shape of the jets, the lower and upper recirculation zones can be reconstructed from this sequence of four plots. Vortex shedding of the center jet can also be observed, although it is obscured by the external frame of the water model.

Figures 5.8 and 5.9 show a typical instantaneous velocity field and the mean field at the center plane respectively. The mean was obtained over a time of 48.5s. The double roll flow pattern can be seen in both plots. The shapes of the jets and the upper and lower recirculation zones agree with the dye-injection observation. In contrast to the smooth time-averaged plot, the instantaneous vector plot shows local turbulent structures similar to what was seen in CHAPTER 4. The oscillation of the center jet observed in the dye-injection was also seen in the simulation.

Figure 5.10 compares the computed speed $(v_x^2 + v_z^2)^{1/2}$ with the estimated values from the dye injections along the jet centerline. The solid line denotes the predicted value of the speed averaged over 48.5s. The error bar shows the upper and lower bounds of the transient speed during the 48.5s simulation, indicating a large fluctuation. The dots are the estimated transient flow speeds obtained by measuring the development of the dye front on the video images. The predicted values reasonably agree with the measurements.

## 5.4 Numerical Validation

CHAPTER 4 and section 5.3 provided model validation with experimental measurements, comparing the predicted and measured velocities at different positions in the mold region. Further quantitative experimental validation is provided in sections 5.7 and 5.8 for the top surface velocity and interface profile respectively. Computational models also require numerical validation to ensure that the effects of grid resolution, time-step size, turbulence model, and discretization errors associated with the order of the numerical scheme are small. Further related issues are the inlet conditions and the symmetry assumption (including half or full mold), which have been discussed in section 4.6. An example is provided here in Figure 5.11, which compares the computed time-averaged speed $\left(\overline{v}_x^2+\overline{v}_z^2\right)^{1/2}$ along a vertical line in the center plane y=0, midway between the SEN center and the narrow face. This figure compares results from three different computational grids: a coarser grid, the current grid and a finer grid consisting of 0.4-million, 0.7-million and 1.4-million cells respectively. The fine grid included only one half of the domain, so its node spacings are roughly four and eight times finer than the other two grids respectively. The differences between the right and left sides of the domain are more significant than the differences between grids. This indicates that the mesh resolution is adequate. This figure also shows that the effect of adding an SGS k model [44] is very small. This indicates that either the unresolved small turbulent eddies are not very important, or that false diffusion from numerical discretization errors dominates over the sub-grid scale effects.

## 5.5 Flow in the Thin-Slab Caster

The steel caster differs from the water model mainly in the solidifying shell boundary and the outlet. In addition, the kinematic viscosity of the molten steel is ~20% smaller than that of water. These differences might lead to a different flow field in an actual steel caster, even under the same operating conditions as in the water model. To investigate the flow in the real steel caster, a transient simulation of the thin slab caster was performed using the same unsteady inlet velocities as the water model (*Case 2-W*). The computed instantaneous and time-averaged velocity fields are presented in Figures 5.12 and 5.13 and are qualitatively similar to those of the water model. Both the time averages of the two systems were taken over ~50s. It should be noted that in both systems, the time-averaged center jet is slightly slanted to the left, indicating a long-term asymmetry. Asymmetries such as these may likely be the cause for the asymmetrical defects observed in steel products.

Figure 5.14 quantifies the development of the center jet. Both the time-averaged stream-wise velocity ($v_z$) and the *rms* values of all three velocity components ($v_x$, $v_y$ and $v_z$) along the jet centerline are shown in the figure. The results reveal that the jet velocity decreases dramatically starting from the nozzle port. The center jet can only penetrate to around 800mm below the center nozzle port. This result is helpful for understanding the particle transport in the mold. The figure also shows that the *rms* of the downward velocity is dominant along the center jet, suggesting a strong anisotropy of this turbulent flow.

In Figure 5.15, the time-averaged downward velocity and *rms* values are presented along a line 8.5 center-port diameters below the SEN bottom in the center plane y=0. The time-averaged downward velocity at the jet center is seen to decrease to ~45% of the inlet value. The high velocities near the narrow faces are caused by the two oblique side jets. Because of the influence of side jets as well as being confined by the shell, the jet width is smaller than the self-similar free jet [73]. The *rms* distribution again supports the anisotropy of flow in the liquid pool.

## 5.6 Comparison between The Thin-Slab Steel Caster and The Water Model

Flow in the thin-slab caster and the water model have been investigated separately. Comparisons between the two systems are provided here. All the time-mean values presented in the two systems were averaged over approximately 50s. Figure 5.16 presents the mean of horizontal velocity towards the SEN along the centerline on the top surface. The velocity estimated from the dye-injection is also plotted as solid squares in Figure 5.16. All the data show a maximum velocity in the middle between the SEN and the narrow face, with a value ~0.15m/s to ~0.26m/s. A significant asymmetry between the left and right sides is found in the water model (*Case 2-W*), compared to the steel caster (*Case 2-S*). This indicates the existence of a low frequency (lower than 0.02Hz) oscillation between the two sides on the top surface in the water model, which is absent in the simulation of *Case 2-S*. The downward velocity of the shell in the steel caster simulation may have stabilized the flow so that it has less oscillation. A similar oscillation on the top surface with a frequency lower than 0.02Hz was also found in the 0.4-scale water model presented in CHAPTER 4. The reason for the oscillation is still not clear. It should be also noted that the velocity on the left side of the water model is very close to that of the steel caster. The *rms* values of the velocities in Figure 5.16 are presented in Figure 5.17. All the data suggest that the *rms* values reach the maximum at 15mm-30mm away from the SEN and then monotonically decrease towards the narrow face. The predicted *rms* values are again significant compared to the local mean values.

Figures 5.18 and 5.19 compare the time-mean and the *rms* of the downward velocity in both systems. The data were extracted along a horizontal line 1000mm below the top surface and 164mm from the narrow face. Figure 5.18 shows a bigger spatial variation of the downward velocity for the water model. It shows that the steel caster has slower downward flow near the walls (where the shell is found) and less upward (or reverse) flow in the central region. This is likely due to the combined effects of tapering, which restricts the flow domain, the mass loss from solidification, which tends to even the velocity distribution, and the downward withdrawal of the shell, which pulls the flow downwards at the casting speed. An asymmetry between the two sides can be seen for both the water model and the steel caster, again indicating that low frequency oscillations exist with a period longer than the averaging time of ~50s.

## 5.7 Velocity Fluctuation on Top Surface

The top surface velocity greatly influences the entrainment of liquid slag. The velocity fluctuates with time due to the turbulent flow. Instantaneous high values of this velocity can shear off fingers of liquid slag into the liquid steel [64] to cause serious defects. This velocity fluctuation is investigated in Figure 5.20, where the signal represents the computed x velocity component at the top surface center point (midway between the SEN and the narrow face) for the thin-slab steel caster (*Case 2-S*). The direction from the narrow face towards the SEN is defined as the positive direction in Figure 5.20. The amplitude of the fluctuation is seen to be comparable to the mean value (Figure 5.16). The velocity occasionally has a sudden "jump" with considerable amplitude (e.g. the flow velocity drops from ~0.4m/s towards the SEN to the opposite direction in 0.2s). Due to a lack of long-term measurements in this caster or the corresponding water model (*Case 2-W*), this behavior is compared with the PIV measurements [30] in the 0.4-scale water model shown in Figure 4.13 and Figure 4.25. As discussed in section 4.6, the characteristic of large sudden "jumps" was seen in both the PIV measurements and the full-mold simulation; they were missing in both the half-mold simulations. This result supports the conclusion that interactions between the two halves of the caster cause large velocity fluctuations on the top surface. Half-mold simulations suppress the large velocity fluctuations through the imposed artificial symmetry plane.

## 5.8 Steel-Slag Interface Profile across Top Surface

The steel-slag interface profile across the top surface is important because it affects the ability of the liquid slag flux to fill the interfacial gap between the mold and shell, which is important for heat transfer and thereby to surface quality of the final product. Figure 5.21 shows typical transient top surface levels obtained from the simulated static pressure across the top surface for the thin-slab caster and the water model. The top surface interface displacement, $\Delta z$, was estimated from a simple potential energy balance:

$$\Delta z(x, y) = \frac{p(x,y) - p_{mean}}{\left(r_l - r_{top}\right)g} \tag{5.1}$$

Figure 5.21(a) shows the water model prediction compared with the top free-surface profiles measured from video images at three instants. The predicted surface shape is in reasonable agreement with the measurements. It is also consistent with previous water model results. [74] Figure 5.21(b) presents the predicted molten steel profile at the top surface. The profile is always higher near the narrow face, by 2mm in the water model and 4-6 mm in the steel caster. This is because the upward momentum of the liquid near the narrow face lifts the liquid level there. The level change is greater in the steel system because interface movement only requires the displacement of some molten slag. The prediction of the steel caster top liquid profile compares reasonably with industry measurements (Figure 5.21(b)). Each of the nine measurements was obtained by dipping a thin steel sheet into the operating steel caster mold and recording the slag-steel interface shape after removing it. Each point represents the mean deviation of the measurements at that location from the average surface level along the centerline. This average level was determined to be -1.3mm using Equation (5.1). The error bars indicate the range of the measurements at each location. Significant uncertainty in the measurement exists regarding possible rotation of the sheets. The slag layer needs to be thick enough to cover the steel, in order to provide a steady supply of molten flux into the interfacial gap to lubricate the steel, maintain uniform temperature profiles, and to avoid surface defects in the solid steel product. Thus, the height of this "standing wave" is important to steel quality.

## 5.9 Flow Asymmetries

In most Reynolds-averaged simulations, symmetry is assumed between the flow in the two halves of the mold region. This assumption has been shown valid for long-term averages. However, transient flow in the two halves is different, for instance, on the top surface (Figures 5.16 and 5.17) and in the lower roll (Figures 5.18 and 5.19). Figure 5.22 further reveals a significant flow asymmetry in the lower roll. The signals present the variation of the downward velocity at two pairs of monitoring points, each symmetrically located in the thin-slab steel caster. The data were sampled every 0.001s from the simulation results. Shown as solid triangles, the first pair of points is located within the side jets, midway between the SEN and narrow face, 0.3m below the top surface. The other pair is located at 1.2m below the top surface and near (3.5mm to) the narrow faces to illustrate the flow in the lower recirculation zone. The plot on the top shows the velocity history at first pair of points, which shows similar variations to those in Figure 5.4. No long-term asymmetries are observed between signals at the two monitored points in the jets. However, the plot below clearly shows a significant asymmetry which lasted for a relatively long time (e.g. from 37s to 40s). These observations suggest that (1) low frequency long-term asymmetries exist in the lower recirculation; (2) the asymmetries are due to the turbulent nature of the flow in the mold region and not from asymmetries imposed by the inlet jet. A more severe asymmetry between flow in the left half and right half was observed to start from 250s, as shown in Figure 5.23. The first plot shows larger downward flow velocities in the left half, which persisted for more than 50s in the simulation before the flow became balanced for some time. Then a similar unbalanced flow pattern occurred again after another 70s. The strong asymmetrical flow deep in the lower recirculation region was also observed by Gupta and Lahari [16] in water model studies. It will be shown in CHAPTER 9 that the unbalanced pattern is the cause for asymmetrical particle transport deep in mold region. This finding is important to the understanding of impurity-particle behaviors, as particles transported to the lower recirculation zone are likely to become permanently trapped in the steel.

## 5.10 Spectral Analysis

The power spectrum [75] of the turbulent velocity component $v_x$ was calculated at two points in the steel caster, which are symmetrically located in the pool with a distance of 156mm from SEN outlet, 100mm below the top surface. The spectral analysis was made from 137s of simulation data sampled every 0.001s using the equation below [75]:

$$P(f_k)=\begin{cases}\dfrac{1}{N^2}\left|C_k\right|^2, \quad k=0,\dfrac{N}{2}\\ \dfrac{1}{N^2}\left(\left|C_k\right|^2+\left|C_{N-k}\right|^2\right), \quad k=1,\ldots,\dfrac{N}{2}-1\end{cases} \tag{5.2}$$

where:

$$C_k=\sum_{n=0}^{N-1}\mathrm{v}_{\mathrm{x}}\left(t_n\right)e^{\mathbf{i}2p\, f_k t_n} \tag{5.3}$$

$$f_k=\frac{k}{t_{N-1}-t_0}, \quad k=-\frac{N}{2},\ldots,\frac{N}{2}-1 \tag{5.4}$$

The result in Figure 5.24 shows an irregular distribution of the power spectrum, which has high maxima at low frequencies, (less than 1 Hz) and tends to decrease exponentially at higher frequencies, as indicated with the log scale plot. Slight differences exist between the two points, likely due to insufficient sampling time. A similar behavior of the power spectrum was seen in LDV measurements on a scaled water model by Lawson and Davidson. [26]

## 5.11 Summary

Three-dimensional unsteady turbulent flow in a thin-slab caster and a corresponding full-scale water model was computed using LES. The computed velocity fields are compared with measurements and seen to have reasonable agreement. The computed results yield the following observations:

(1) Flow asymmetries are found in full-mold simulations, which include the short-term asymmetry (e.g. at the nozzle port and along the jet) and the long-term intermittent asymmetry (e.g. on the top surface and in the lower roll). The long-term asymmetry in the lower roll is due to the turbulent nature instead of asymmetries in the inflow.

(2) The interaction between the two halves of the liquid pool causes important transient flow behavior (e.g. sudden jumps of top surface velocity). Imposing an asymmetry assumption suppresses sharp sudden jumps in surface velocities and low frequency flow transients in the lower recirculation zones.

(3) Water models are generally representative of steel casters, especially in the upper region far above the water model outlet. However, steel casters are likely to have somewhat more evenly distributed downward flow in the lower roll zone, where the influence of shell thickness becomes significant.

(4) The top surface level can be reasonably predicted from the top surface pressure distribution. The top surface level profile rises more near the narrow face in the steel caster than in the water model, which has no slag layer to displace.

(5) Our analysis shows anisotropy of turbulent flow in the liquid pool. Spectral analysis suggests that most energy is contained in low frequency region (0-5Hz).

(6) The flow transients and asymmetries have important effects on many other phenomena in the liquid pool that are critical to steel quality.

**Table 5.1. Properties and conditions of particle simulations.**

| Parameter/Property | Case 2-W | Case 2-S |
|---|---|---|
| Mold Width (mm) | 984 | 984 |
| Mold Thickness (mm) | 132 | 132 |
| Water Model Length (mm) | 2600 | - |
| Mold Length (mm) | - | 1200 |
| Domain Width (mm) | 984 | 984 (top)<br>934.04 (domain bottom) |
| Domain Thickness (mm) | 132 | 132 (top)<br>79.48 (domain bottom) |
| Domain Length (mm) | 1200 | 2400 |
| Nozzle Port Height $\times$ Thickness (mm $\times$ mm) | $75 \times 32$ (inner bore) | $75 \times 32$ (inner bore) |
| Bottom nozzle Port Diameter (mm) | 32 | 32 |
| SEN Submergence Depth (mm) | 127 | 127 |
| Casting Speed (mm/s) | 25.4 | 25.4 |
| Fluid Kinematic Viscosity ($m^2/s$) | $1.0 \times 10^{-6}$ | $7.98 \times 10^{-7}$ |

**Table 5.2. Composition of the stainless steel in *Case2-S*.**

| | | | |
|---|---|---|---|
| 0.047 % C | 0.39 % Si | 0.10 % Cu | 0.020 % Co |
| 0.48 %Mn | 16.71 % Cr | 0.008 % Sn | 0.026 % V |
| 0.026 % P | 0.20 % Ni | 0.0 % Ti | 0.010 % Nb |
| 0.001 % S | 1.00 % Mo | 0.003 % Al | 0.056 % N |

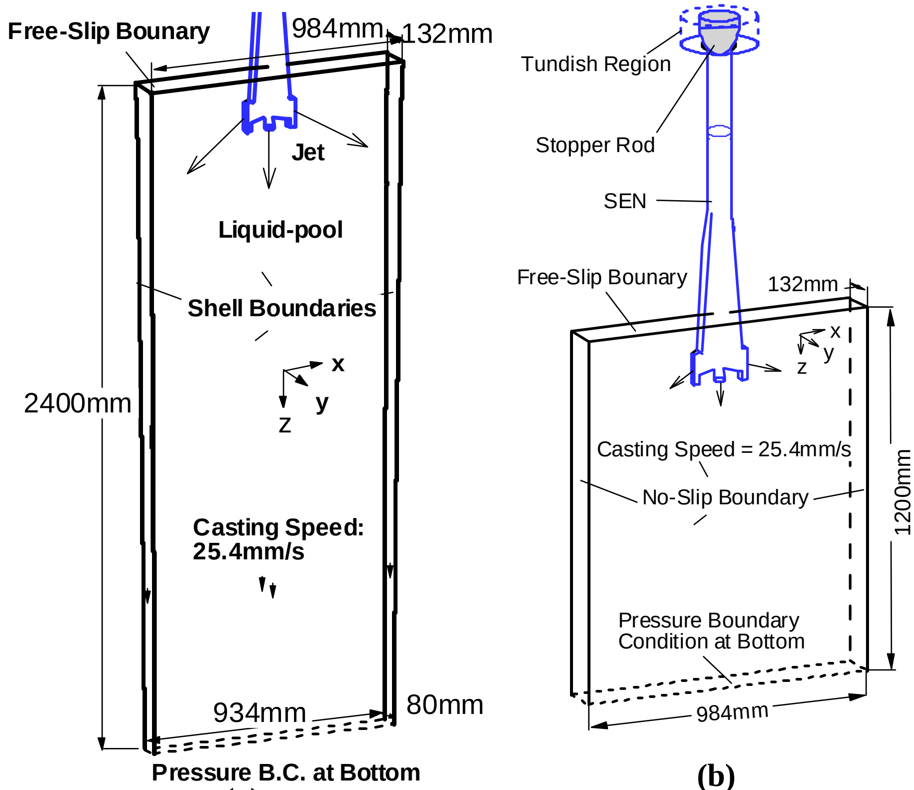


**Figure 5.1. Schematics of the computational domains for (a) the thin-slab steel caster and (b) the corresponding water model.**

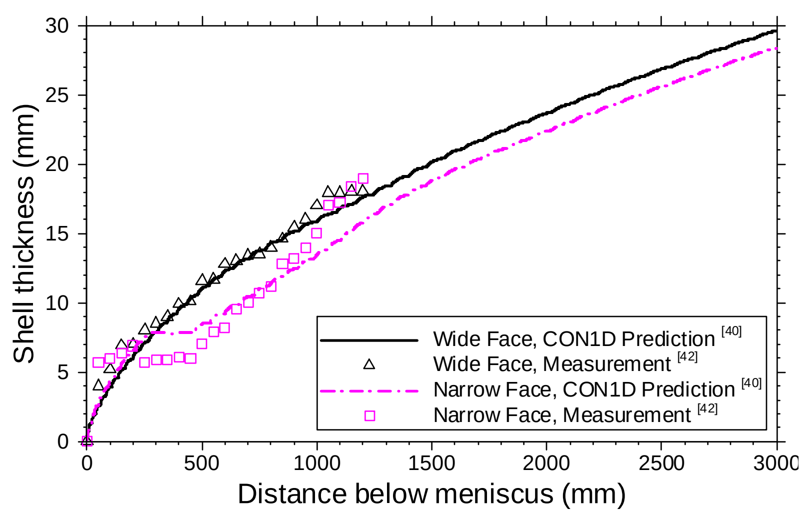


**Figure 5.2. Predicted steel shell thickness of *Case2-S* using CON1D, [72, 76] compared with measurements. [71]**

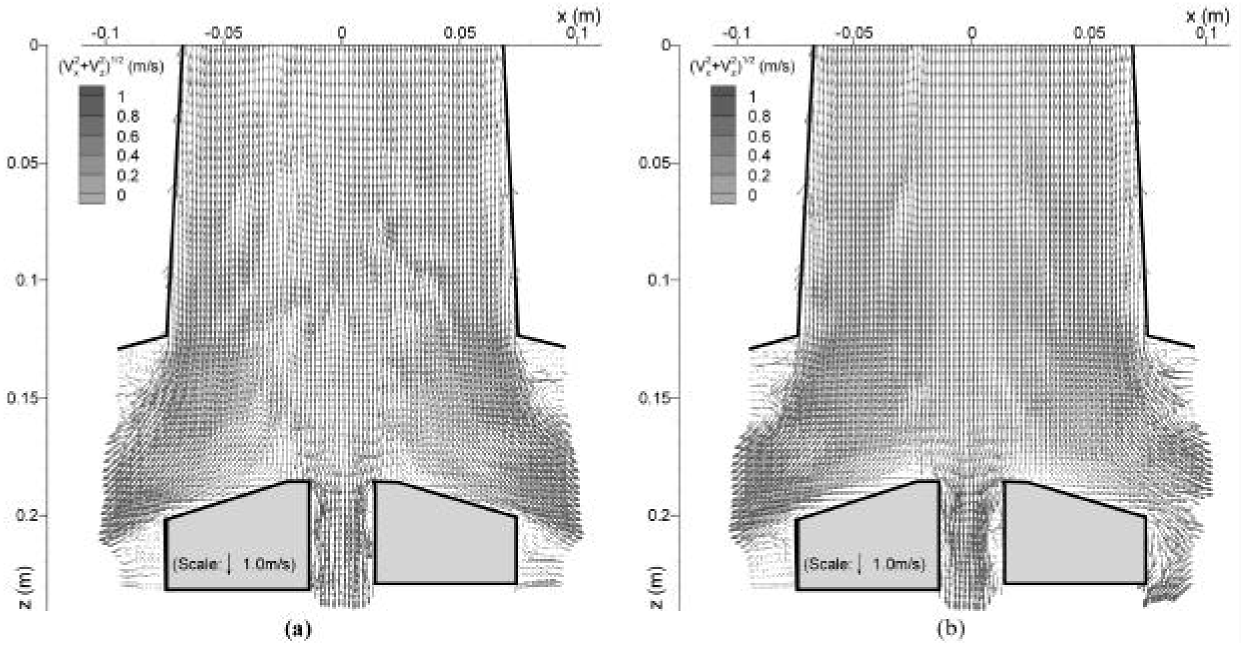

**Figure 5.3. Typical instantaneous velocities near nozzle ports at the center plane between wide faces, obtained from an LES of the nozzle (*Case2-W & 2-S*).**

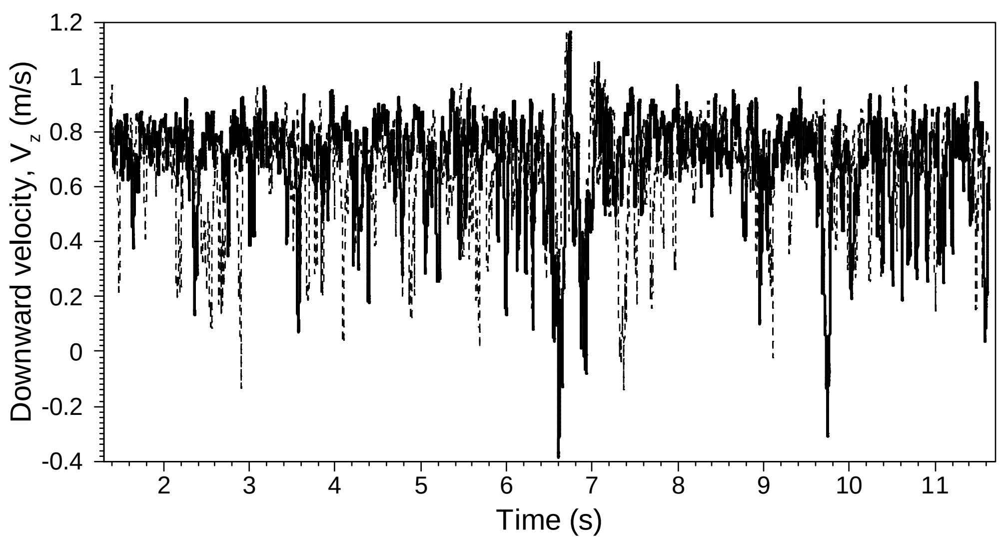


**Figure 5.4. Time variation of downward velocity ($v_z$) at two symmetrical points on the side nozzle ports.**

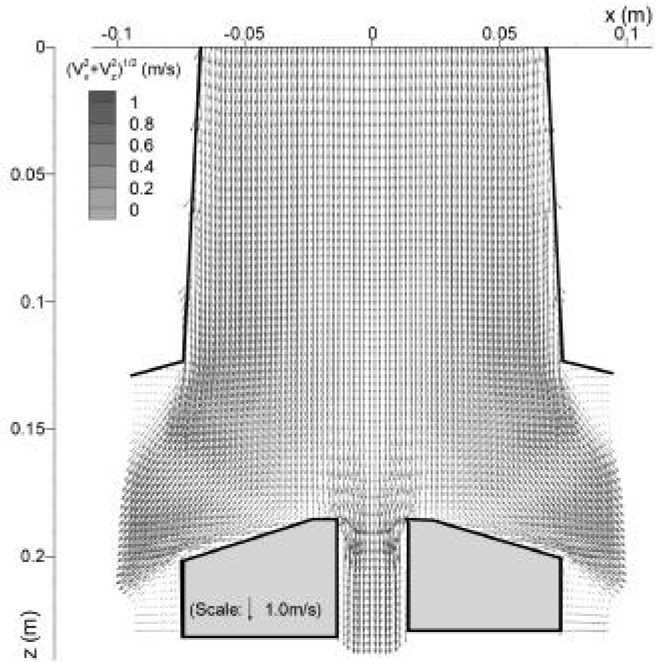


**Figure 5.5. Time-averaged velocity fields near nozzle ports at the center plane between narrow faces, obtained from the simulation (*Case 2-W* & *2-S*).**

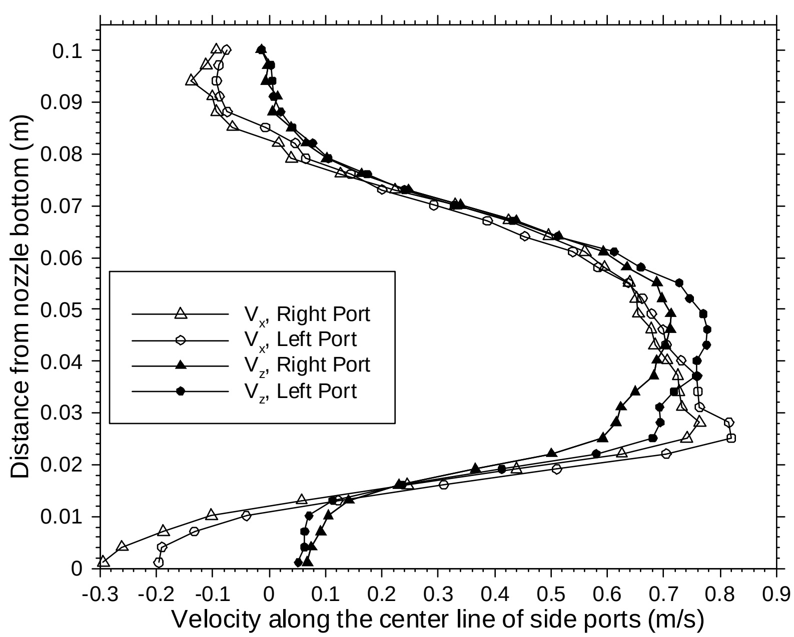


**Figure 5.6. Time-averaged velocities along the nozzle port centerline on both sides.**

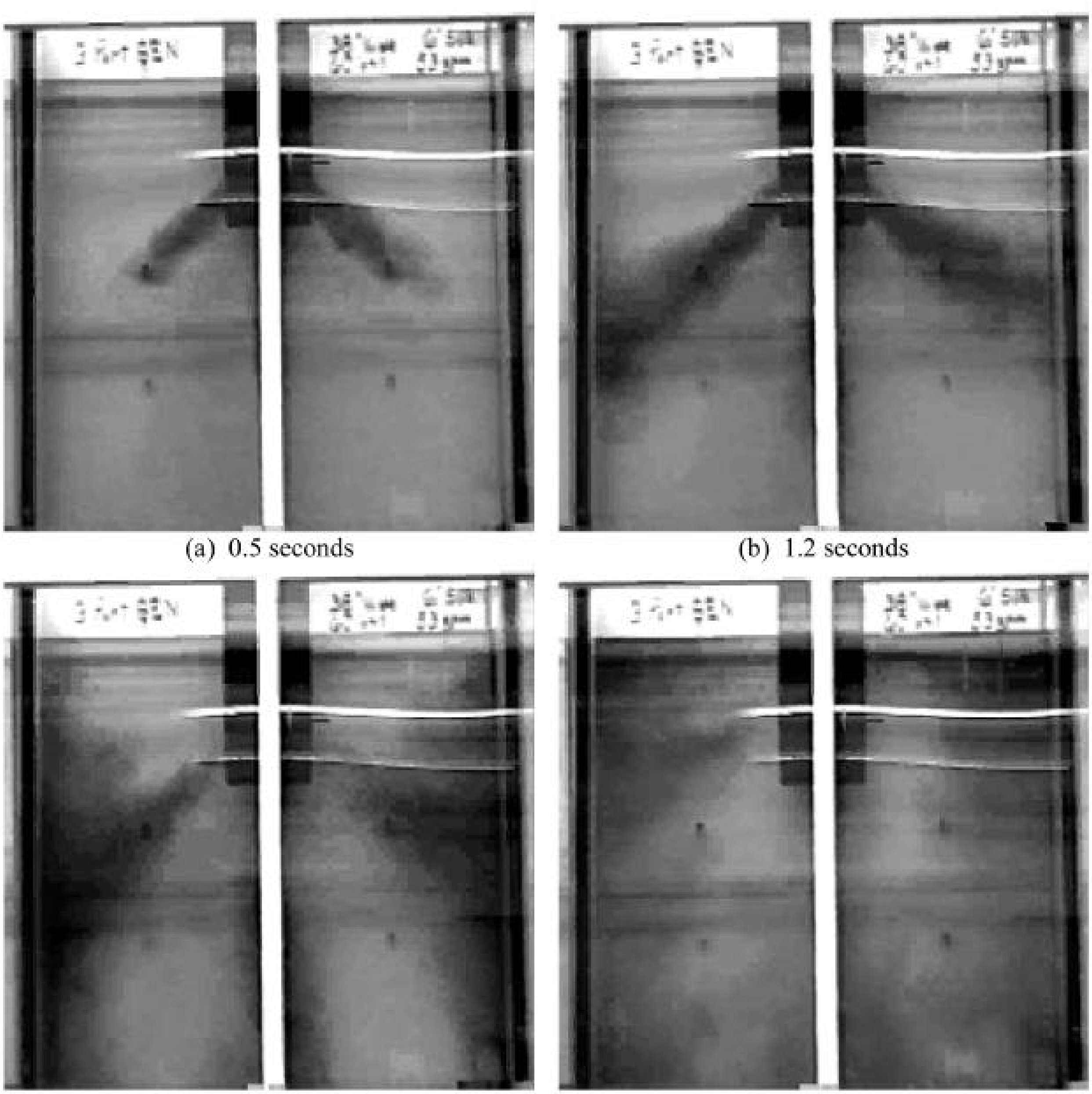

(a) 0.5 seconds (b) 1.2 seconds

(c) 2.8 seconds (d) 5.1 seconds

**Figure 5.7. Dye injection experiment of *Case 2-W* at four instants.**

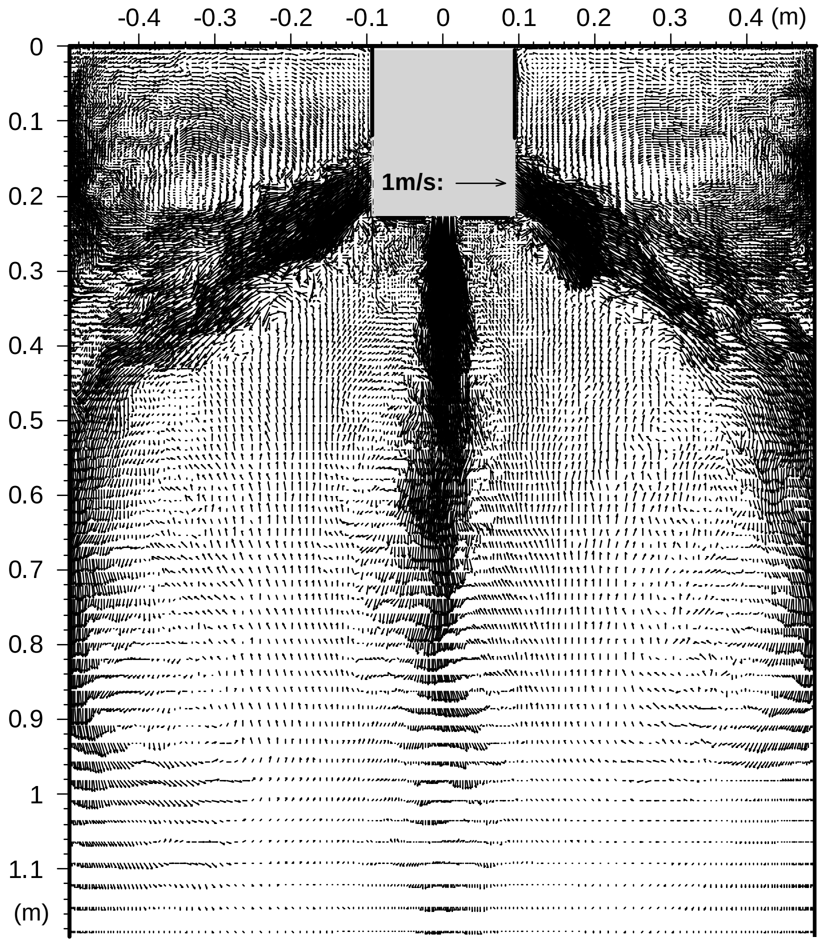


**Figure 5.8. Typical instantaneous velocity vector plot at the center plane between wide faces (*Case 2-W*), obtained from simulation.**

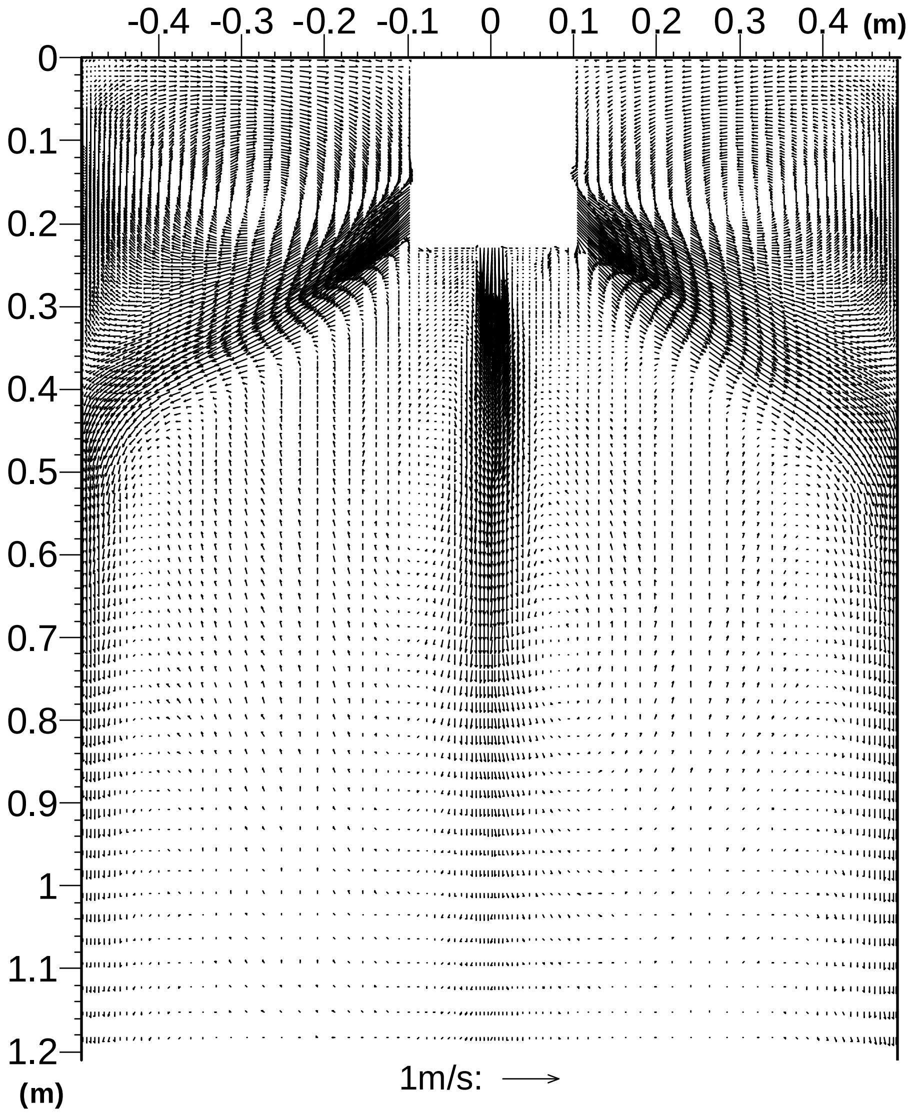


**Figure 5.9. Time-averaged velocity vector plot at the center plane between wide faces (*Case 2-W*), obtained from simulation.**

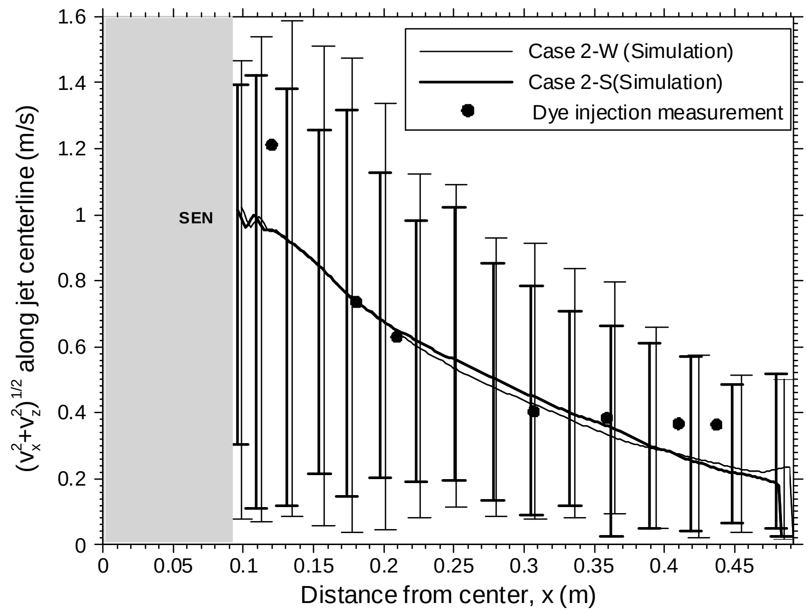


**Figure 5.10. Comparison of time-averaged speed $(v_x^2+v_z^2)^{1/2}$ along side jet centerline between the computation and dye injection estimate (*Case 2-W*).**

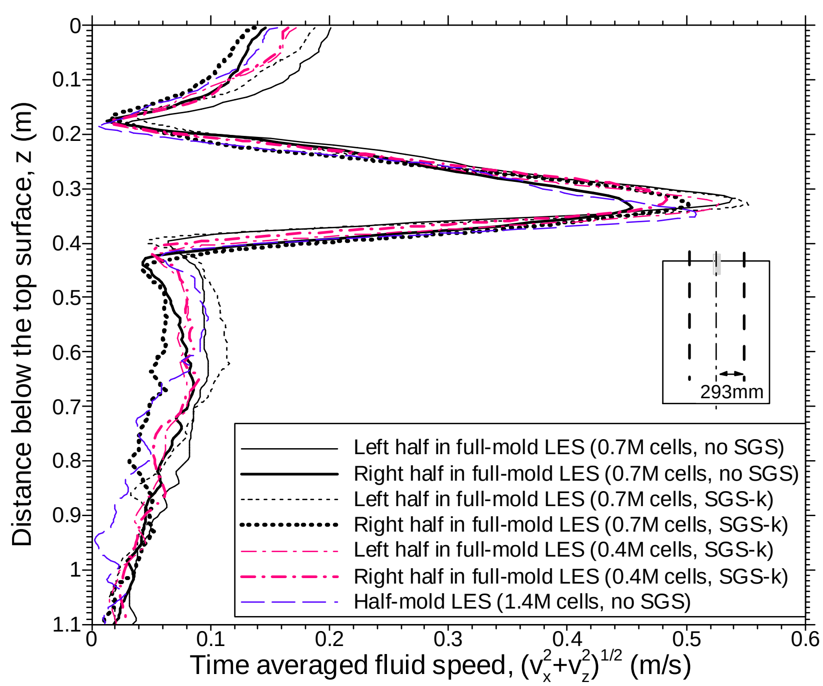


**Figure 5.11. Comparison of computed fluid speeds $(v_x^2+v_z^2)^{1/2}$ along the vertical line in the center plane, obtained from three different grid resolutions (*Case 2-W*).**

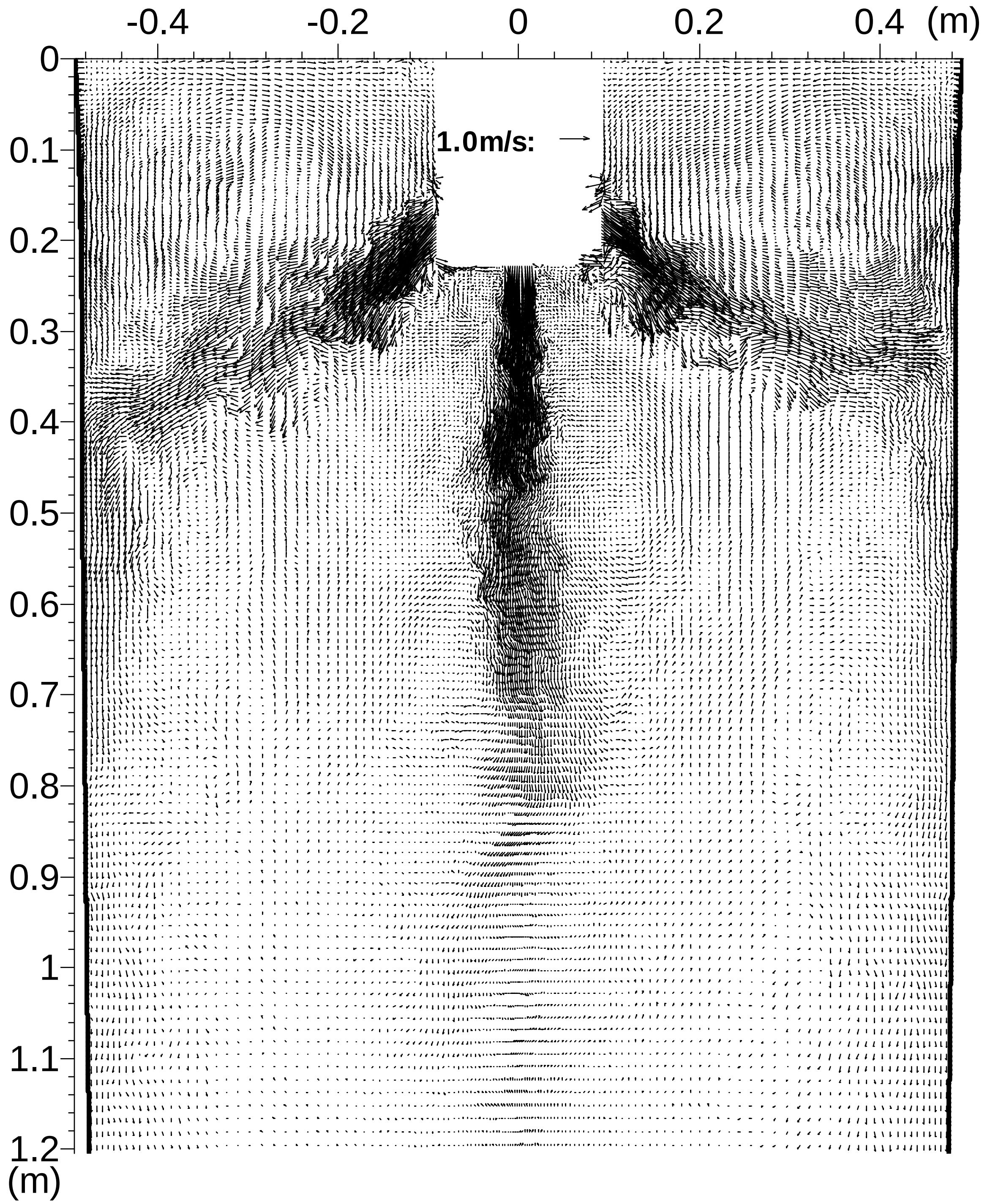


**Figure 5.12. Typical instantaneous velocity vector plot at the center plane between wide faces (*Case 2-S*), obtained from simulation.**

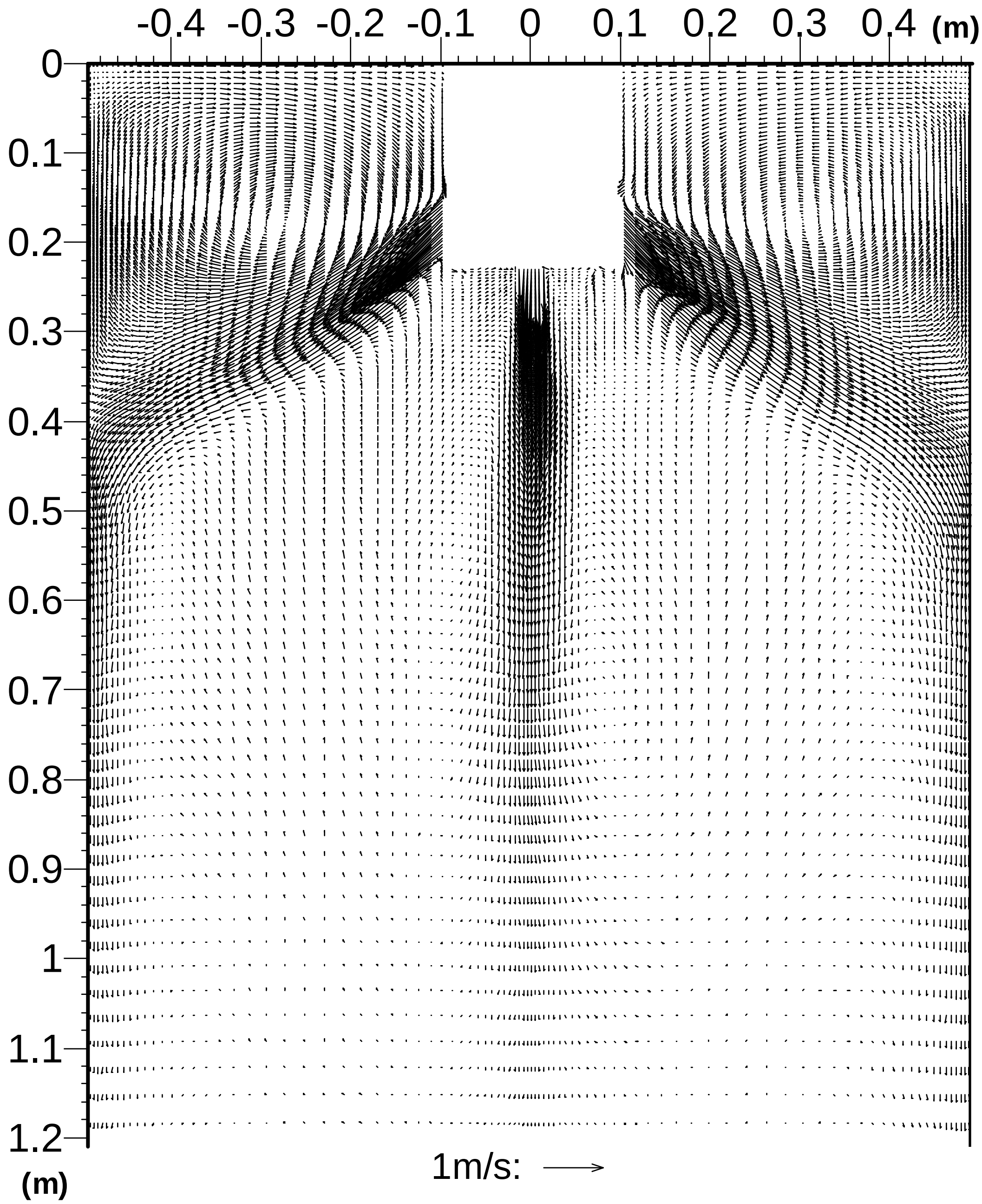


**Figure 5.13. Time-averaged velocity vectors at the center plane between wide faces (*Case 2-S*), obtained from simulation.**

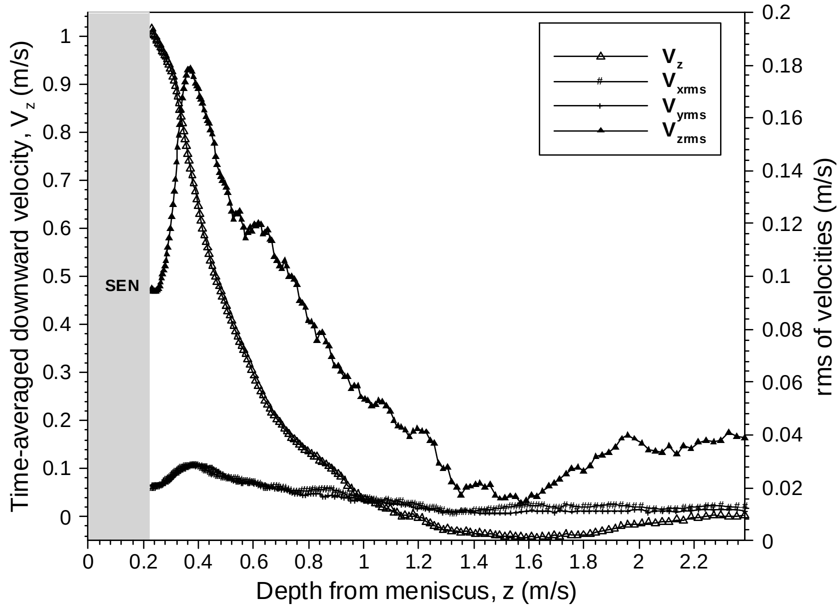


**Figure 5.14. Time averaged and *rms* values of velocities along the center jet centerline (*Case2-S*).**

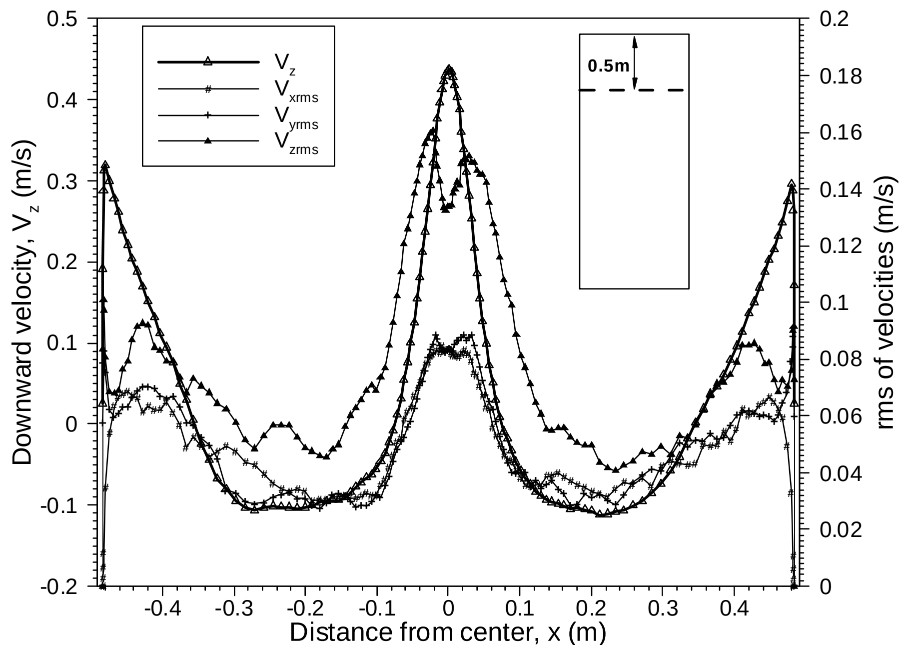


**Figure 5.15. Time averaged and *rms* values of velocities along a horizontal line 0.5m below meniscus half way between wide faces (*Case2-S*).**

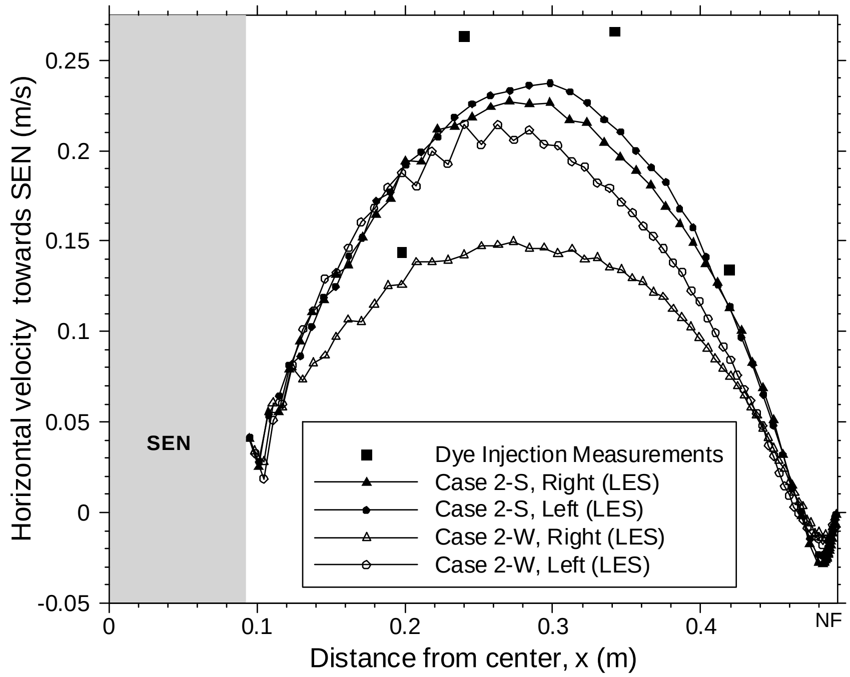


**Figure 5.16. Comparison of time-averaged horizontal velocity towards SEN along top surface centerline between *Case 2-W* and *Case 2-S*.**

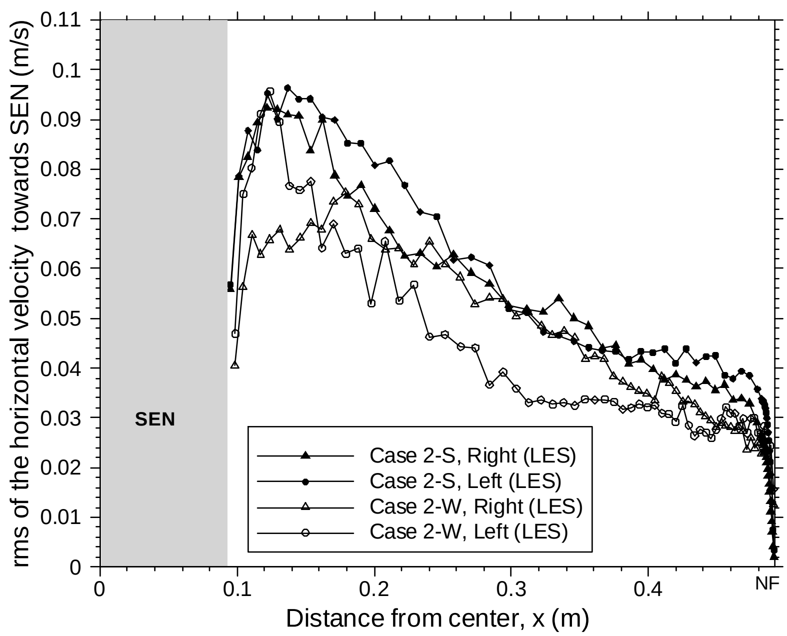


**Figure 5.17. Comparison of the rms values of the velocity in Figure 5.16.**

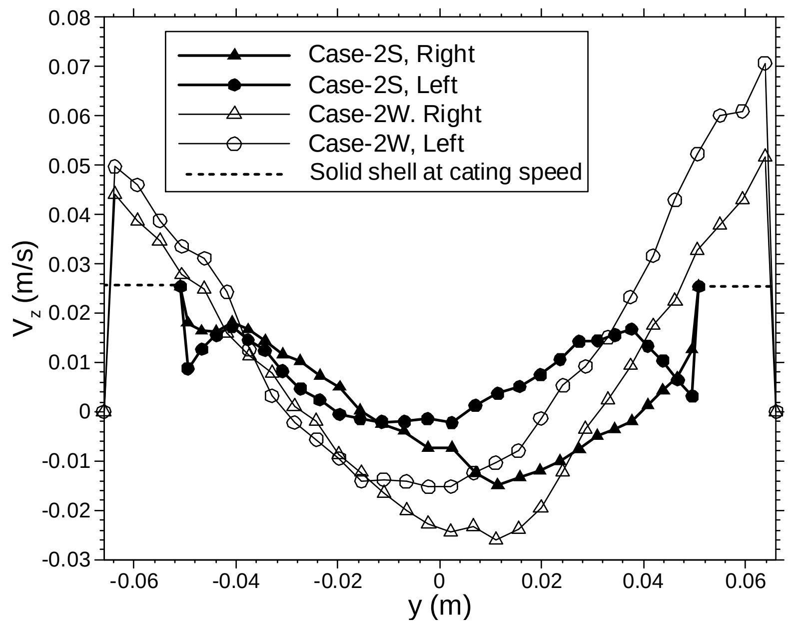


**Figure 5.18. Comparison of the time-averaged downward velocity between *Case 2-W* and *Case 2-S* in the lower recirculation zones.**

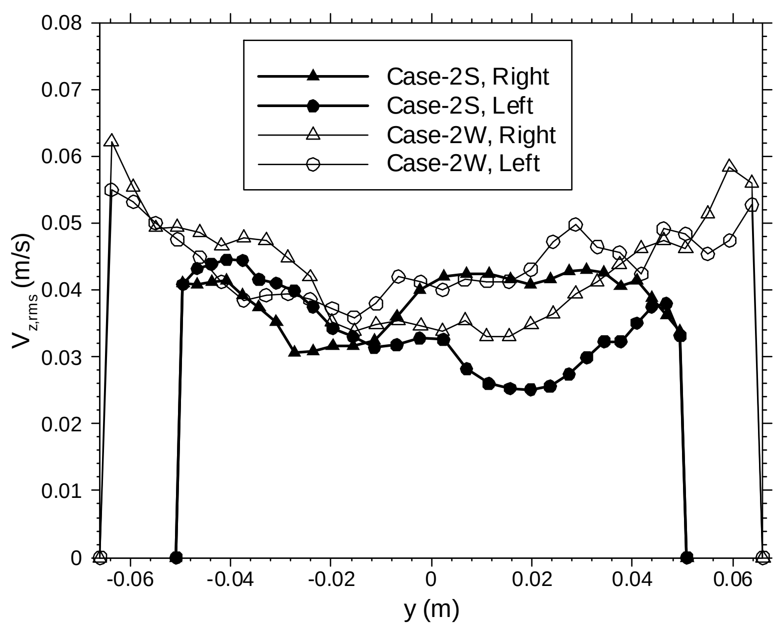


**Figure 5.19. Comparison of the *rms* values of the velocity in Figure 5.18.**

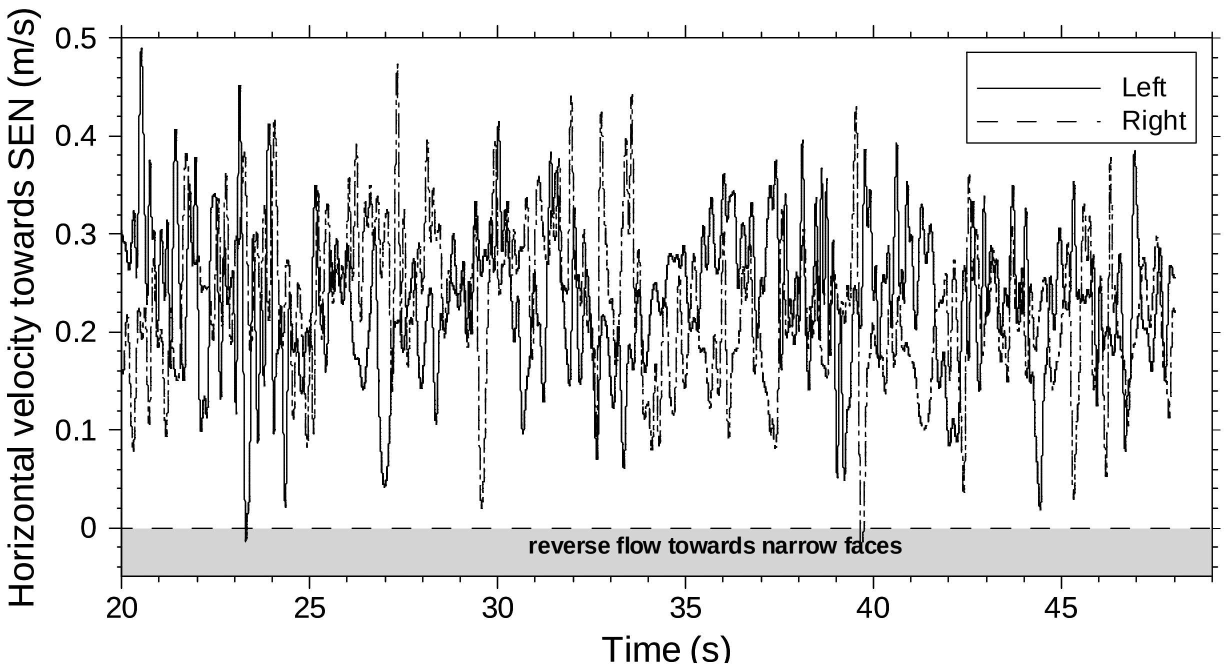


**Figure 5.20. Time variations of the horizontal velocity towards SEN at the center point of the top surface (*Case 2-S*).**

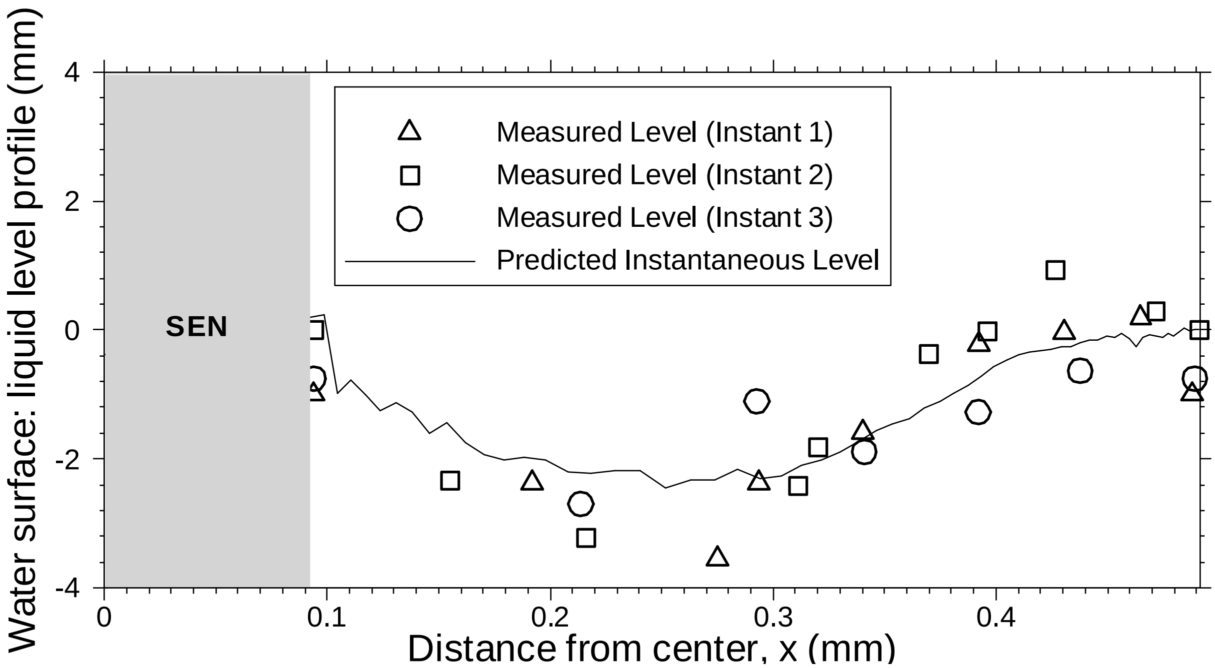


**(a)**

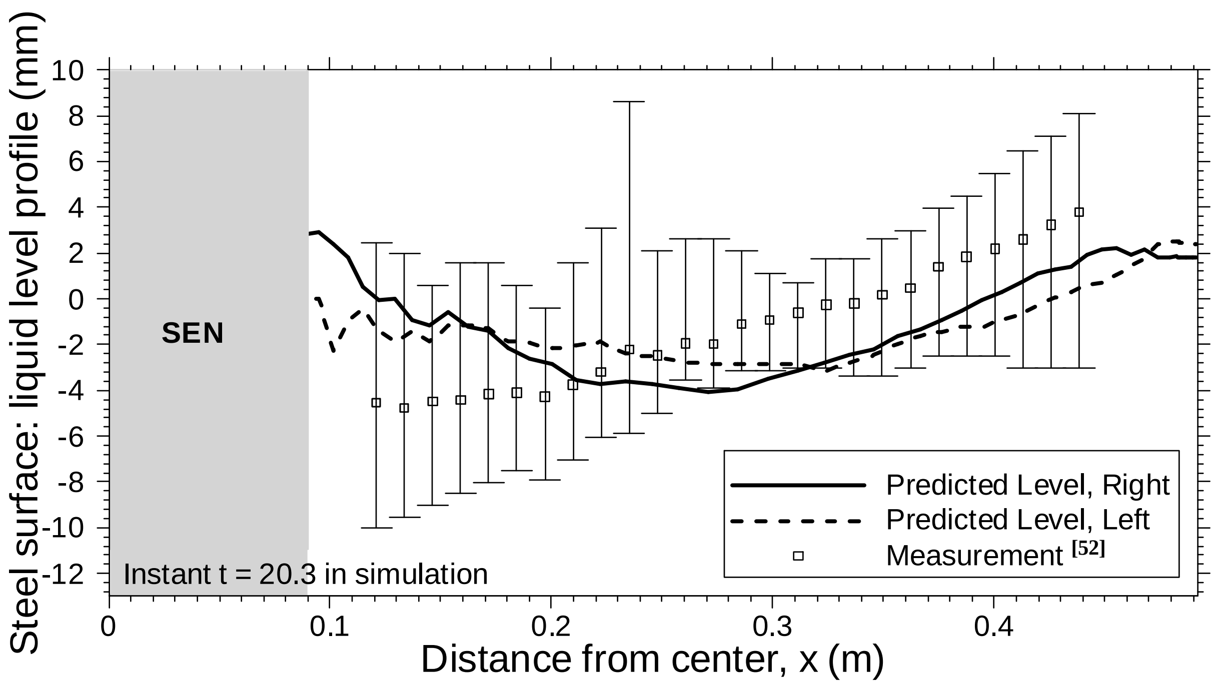


**(b)**

**Figure 5.21. Comparison of predicted and measured top surface liquid levels in (a) *Case 2-W* and (b) *Case 2-S*.**

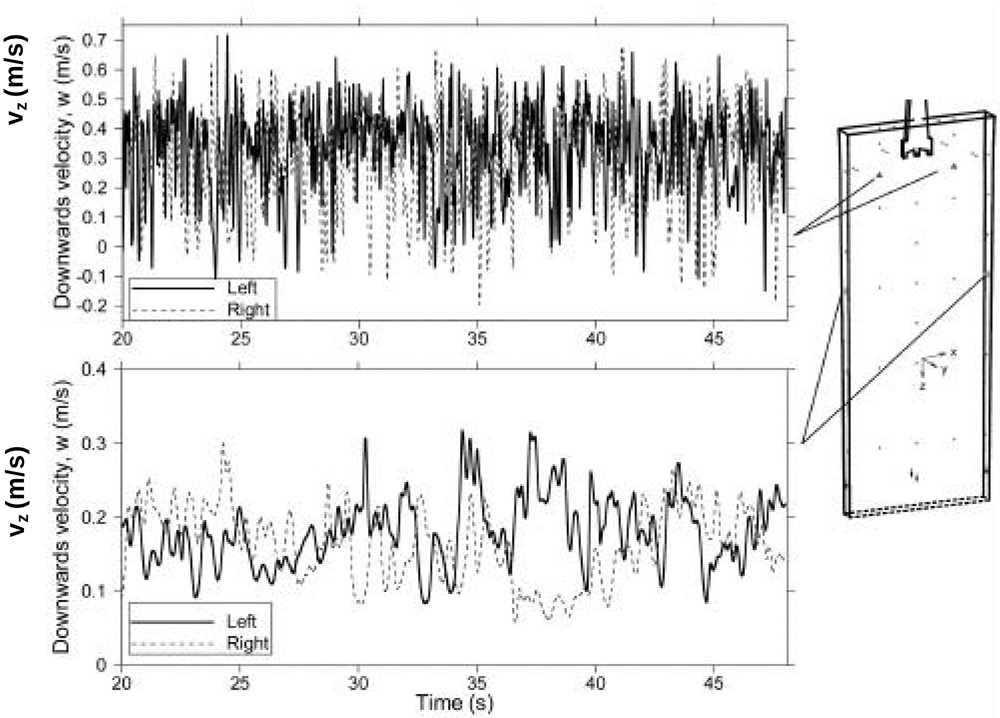


**Figure 5.22. Time variations of the downward velocity at two pairs of symmetrical points, showing low frequency asymmetries in the lower region *(Case 2-S)*.**

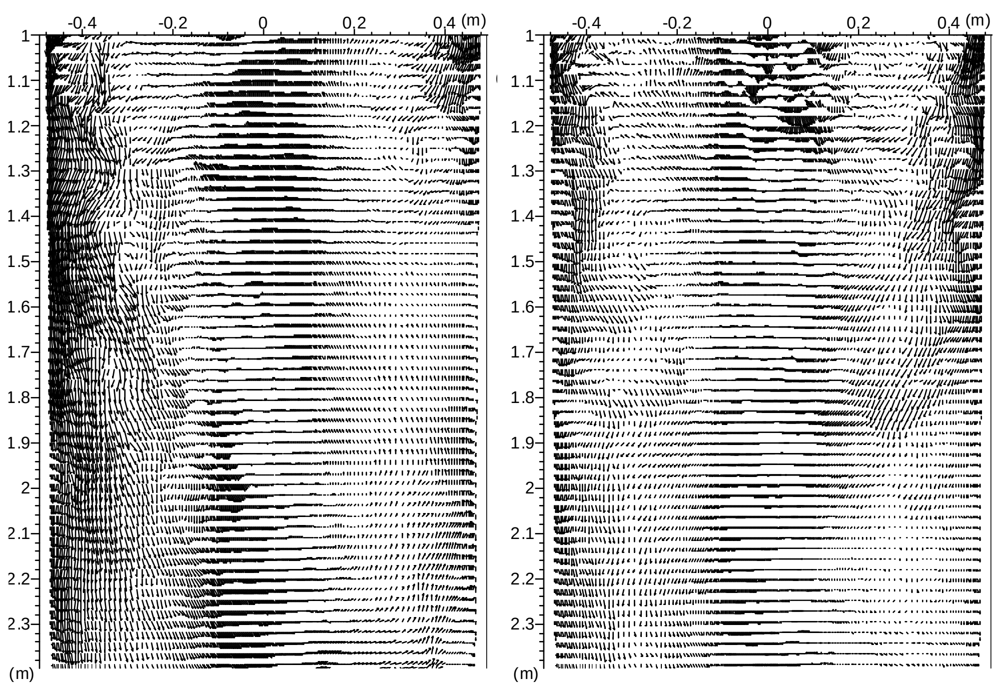


**Figure 5.23. Two instantaneous flow patterns in the lower region of the thin-slab steel caster (*Case 2-S*).**

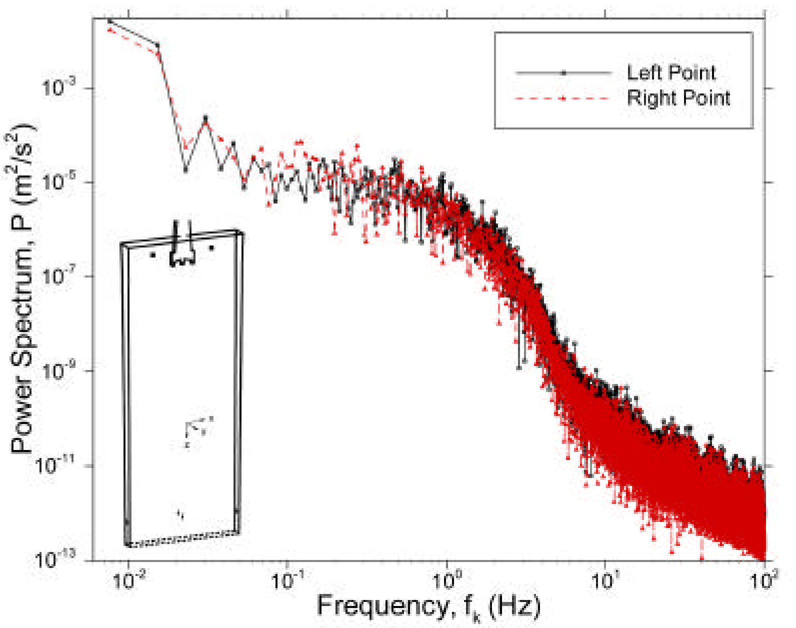


**Figure 5.24. Power spectrum of $v_x$ at two points in the upper mold, obtained from simulation data (*Case 2-S*).**

# PART II. TRANSPORT AND ENTRAPMENT OF IMPURITY PARTICLES DURING CONTINUOUS CASTING

# CHAPTER 6. LITERATURE REVIEW

As introduced in Chapter 1, inclusion defects are difficult to detect and expensive to be removed from steel slabs. They also degrade the steel quality and lower plant yields. Therefore, it is necessary to investigate the motion and capture of impurity particles in the continuous steel caster mold region, which are closely associated with the formation of inclusion defects. Zhang and Thomas [1] reviewed the techniques on the evaluation and control of impurity particles in steel. The review shows that the current knowledge on the particle behavior in steel caster molds is mostly empirical and qualitative. The purpose of this part of the thesis is to generate some fundamental insights into this liquid-particle flow, as a first step to quantitatively predict particle removal rates for different casting conditions.

During the continuous casting process, particles with different chemical compositions and morphologies may be found in the liquid steel. Figure 6.1 [1] gives a few examples of such particles. To reduce the modeling complexity for this first systematic study, this thesis is mainly focused on slag spheres as shown in Figure 6.1 (d). These inclusions can arise from carryover through the nozzle or from entrainment of the slag layer in the mold. They are of great practical importance because they are responsible for many of the sliver defects in the final products. [1]

Due to the difficulties of performing quantitative experiments and measurements in superheated liquid steel (~1800K) during the continuous casting process, computational modeling might be the most feasible way to investigate particle behavior during the continuous casting process. Particles in the mold region encounter two major phenomena that play important roles in the formation of defects: the transport of particles by the turbulent flow and the capture of particles by the solidifying shell. Literature on these two topics are reviewed in the following sub-sections

## 6.1 Computational Modeling of Liquid-Particle Flows

According to the manner in which the particle phase is treated, computational modeling of liquid-particle flows can be classified into the Eulerian and Lagrangian approaches. [77] The former solves transport equations for continuum particle concentrations in an Eulerian framework, while the latter tracks the motion of each individual particle. A comprehensive review on the two approaches is available elsewhere. [77]

Both the Eulerian and Lagrangian approaches have been extensively adopted to simulate fluid-particle flows with different configurations. [78-83] However, only a few such computations can be found for the continuous steel casting process. Grimm et al. [84] simulated the particle motion and separation in the mold region by solving an extra transport equation for the continuum particle volume concentration, based on a constant Schmidt number of one. [18, 84] The fluid velocity field was computed using the $k$-$\varepsilon$ turbulence model. The particle convective velocity was modeled by adding the time-averaged local flow velocity and the particle terminal velocity, which was the only parameter to distinguish different particles. The effect of turbulence on particles was neglected. A crude particle-capture model was used, which assumes particles to be captured by the solidifying shell once they touch each other. No quantitative validation was given for this modeling work.

Due to the low volume fraction (of the order of $10^{-4}$) of particles under normal casting conditions, particle motions during continuous casting of steel can also be computed via one-way coupling Lagrangian simulations, as shown in [69, 85-88]. In these studies, trajectories of several hundred particles were computed to obtain statistics on the particle removal and capture fractions. The time-averaged flow velocities obtained from RANS simulations were used to calculate the hydrodynamic forces acting on the particles. To account for unresolved turbulence dispersion, the velocity of each particle incorporated a component estimated through a model, typically the random-walk model. [18, 86] Particles were assumed to be trapped once they touch the domain boundaries. These preliminary studies produced valuable insights. However, they were not able to generate information on transient particle behaviors. Also, they were not validated. The particle transport computation can be improved with a better-resolved flow field such as that obtained from the LES. In addition, the particle-capture model used in these studies can also be improved with increasingly available experimental data. [89]

Lagrangian modeling of liquid-particle flows can be categorized as: one-way coupling, if the flow affects the particle motion, two-way coupling if the particles also modify the flow, and four-way coupling if the particles further interact with each other. A comprehensive review on this topic can be found elsewhere. [90] The two-way and four-way coupling effects are important when the particle concentration is high. Rani [91] observed that one-way coupling is appropriate if the particle volume fraction is less than 0.1% for heavy particles in turbulent gas flows in a pipe. Considering that the particle density of slag is close to that of the liquid steel (3:7) and the particle volume fraction is small in continuous caster molds, one-way coupling is sufficient for this study.

In the Lagrangian approach, particles may be represented as point-masses or volume-masses with the actual shape included in the computational grid. [77] The latter requires the resolution of the flow boundary layer across the particle surface and therefore is computationally prohibitive when the number of particles is large. The point-mass representation is less computationally demanding and suitable for modeling large number of particles. It requires models for the hydrodynamic forces acting on the Lagrangian particles. Due to the large number of particles involved during continuous casting, the point-mass particle representation was adopted in this thesis. Equations for the hydrodynamic forces are given in section 7.1 of CHAPTER 7.

## 6.2 Insoluble Particles in Front of a Directional-Solidification Interface

Experimental studies have found that insoluble particles in front of a directional-solidification interface may be captured by engulfment (where the particle stops the interface growth and becomes captured inside) or entrapment (where the particle gets captured by surrounding dendrite arms) or continuously pushed forward by the interface, depending upon the morphology and the advancing speed of the interface. Particle engulfment, entrapment and pushing, as schematically illustrated in Fig. 6.2, [92] have drawn much attention from researchers for decades. [89, 92-102] However, the theory for these phenomena is still being disputed. [103, 104] This sub-section selectively reviews theoretical and experimental studies on this topic, along with the debates.

Probably the simplest configuration of this problem is a spherical particle in front of an advancing smooth solidification interface. The Pushing/Engulfment Transition (PET) condition for this system has been extensively investigated in previous studies.

[89, 93-95, 98, 101, 102, 105] Uhlmann and Chalmers [93] were pioneers who systematically and theoretically explained the particle PET. They attributed the particle pushing to the short-range non-retarded Van der Waals interfacial force. [93] The mechanism for the particle PET can be explained as follows. During the solidification process, the solid-liquid interface approaches a stationary insoluble particle suspended in the liquid. As the distance between the particle and the interface becomes sufficiently small, the Van der Waals interfacial force acting on the particle becomes non-negligible. If it is to attract the particle to the interface, spontaneous engulfment should always occur. However, if it is a repulsive force, the particle will be driven to escape from the interface. The particle motion creates a space behind it. A pressure-driven flow is then formed in the gap between the particle and the interface. This flow supplies liquid to maintain the solidification behind the particle. The low pressure in the gap leads to a force attracting the particle to the interface, which is proportional to the particle speed. This force is also known as the lubrication force. [106] It is believed that the gap between the particle tip and the interface needs to be larger than a critical value to allow the liquid flow through, which has been denoted as "critical thickness" or "critical distance" in previous literature. [93, 98, 102] Liquid may lose macroscopic properties such as viscosity and the macroscopic continuity equation may not hold when the gap is narrower than the critical distance. At critical state from pushing to engulfment, the particle moves with the same velocity as the interface and the thickness of the gap between them equals the critical value. A non-zero net attractive force will lead to particle engulfment. Therefore, equating the two forces at the critical distance yields a critical value for the interface advancing speed (or solidification speed in later discussions). Particle pushing occurs if the actual solidification speed is slower than the critical speed, and vice versa. It is apparent that the critical thickness plays a key role in this theory. Unfortunately, no rigorous studies are available regarding the selection of this critical value. To match experimental results, [102, 107] different researchers selected different values, ranging from seven times [98] to a few thousand times [96] of the atomic diameter of the liquid. Additional difficulties arise from the unavailability of the surface energy data for many materials, especially that between the solid and the particle. These have limited the validation and application of the PET theory.

The presence of an interfacial active solute can change the surface energy field in the liquid, cause a surface energy gradient force on the particle and thereby influence the particle PET. Wang et al. [108] measured the pushing and engulfment of air bubbles in solidifying pure water and in a water-C8H17SO3Na solution. It was observed that the C8H17SO3Na solute greatly reduced the critical solidification speed for PET. [108] Wang et al. [108] and Kaptay [100, 101] attribute the reduction of the critical speed to an attractive force caused by the surface energy gradient, which is induced by the solute concentration gradient in front of the solidification interface. Kaptay [100] included this surface energy gradient force in his analysis and reproduced the experimental results.

Due to the difficulties of measurements in high-temperature metal melts, measurements of particle PET in liquid metals are limited. [89, 97, 109] Shibata et al. [89] performed in-situ measurements of the pushing and engulfment of slag spheres and alumina clusters in solidifying steel. Details of this study will be shown in section 7.4.1.

During the continuous steel casting process, the solidification interface has a dendritic shape and particles can be entrapped by dendrite arms as illustrated in Figure

6.2. [92] Wilde and Perepezko [92] found in experiments that entrapment could occur even when the dendrite growth speed was significantly lower than the critical speed for the particle PET. It is not surprising after a simple force analysis illustrated in Figure 6.3. The center of the first particle is aligned with the dendrite tip in the solidification direction. A net attractive or repulsive force will lead to particle capture by "engulfment" or pushing respectively. However, the particle in this position is unstable. Any small perturbation will move it from this location, as illustrated by the second particle. Particle pushing results in a relative velocity for the particle to move into the space between the dendrites. Once a particle is between the primary dendrite arms (as illustrated by particle 3), it has little chance to escape and will eventually be captured. This mechanism is called "entrapment".

All the literature reviewed above studied particles in stationary solidifying liquids. A cross-flow in front of the solidification interface can greatly change the particle pushing and capture (including engulfment and entrapment). Studies on this more complicated topic are rare. Han and Hunt [99, 110] studied particle pushing caused by the cross-flow in a horizontal duct flow of water through experiments. Particles initially settled on the horizontal solidification interface on the bottom. They were found trapped in ice at a solidification speed as low as 4.2μm/s if no cross-flow was introduced. The cross-flow speed was then gradually increased. After it surpassed a value, particles were observed to start moving and consequently avoided being trapped by the ice. The critical cross-flow speed for particle pushing was found to increase with the particle size. It also appeared to slightly increase with the solidification speed. Han et al. [110] also proposed a simple model to predict particle pushing based on a force balance analysis. However, a wrong formulation was used [110] for calculating the drag parallel to the interface. In addition, the estimated friction coefficients and the assumed distance between particle tip and the interface [110] are empirical.

In summary, the literature reviewed in this section shows that particles close to a solidification interface encounter important forces including the Van der Waal's interfacial force, the lubrication drag force and the surface energy gradient force. The cross-flow in front of a solidification interface was observed to influence the particle pushing and entrapment significantly. Base on the experimental data and theoretical analyses in these studies, a simple criterion based on force balance is proposed in section 7.2 to predict the particle pushing and capture by the solidifying shell in continuous steel caster molds.

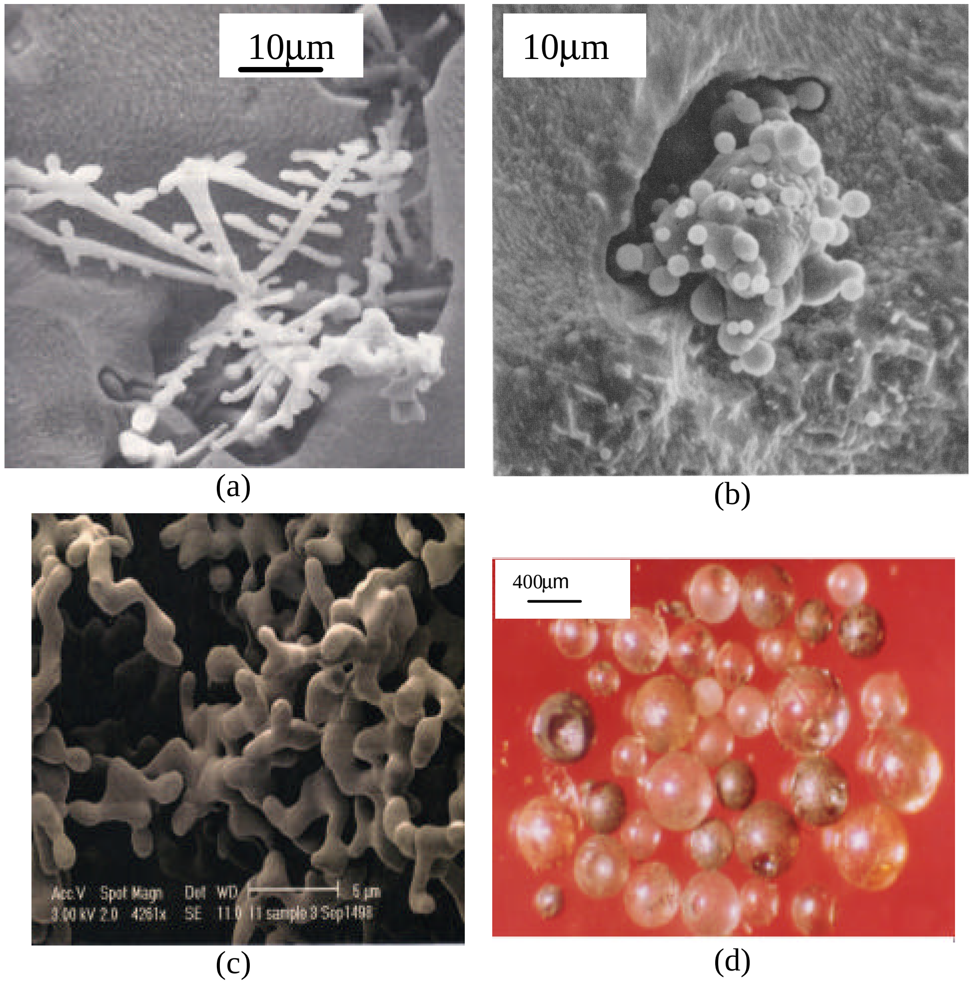


**Figure 6.1. Inclusion morphologies in continuous casting of steel: (a) dendritic alumina, (b) alumina cluster, (c) coral structure alumina and (d) slag inclusions. [1]**

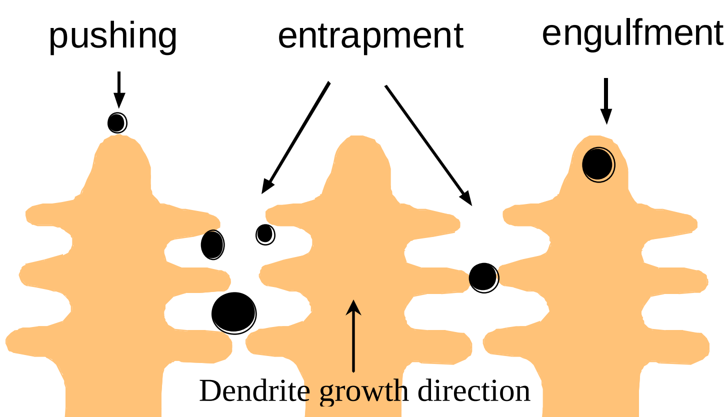


**Figure 6.2. Illustration of particle pushing, entrapment and engulfment.**

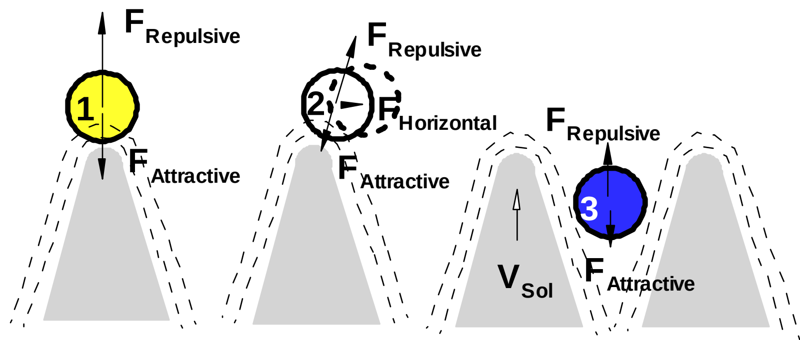


$F_{Horizontal}$: horizontal component of the total force.

**Figure 6.3. Illustration of particles in front of dendrites at the neutral stable, unstable and stable states.**

# CHAPTER 7. MODEL DESCRIPTION

The motion and capture of spherical particles in the continuous casters molds are investigated through computational modeling in this thesis. The three-dimensional time-dependent flow field obtained from LES is used for the Lagrangian particle transport simulations. Details on the computational model are described as follows.

## 7.1 Governing Equations for Lagrangian Particle Motion Simulations

Motions of spherical particles during continuous steel casting can be simulated by solving the Basset-Boussinesq-Oseen (BBO) equation: [111, 112]

$$\frac{d\mathbf{x}_p}{dt} = \mathbf{v}_p \tag{7.1}$$

$$m_p \frac{d\mathbf{v}_p}{dt} = \mathbf{F}_{\mathrm{D}} + \mathbf{F}_{\mathrm{L}} + \mathbf{F}_{\mathrm{Press}} + \mathbf{F}_{\mathrm{stress}} + \mathbf{F}_{\mathrm{A}} + \mathbf{F}_{\mathrm{H}} + \mathbf{F}_{\mathrm{G}} \tag{7.2}$$

where the terms on the right hand side (RHS) in Equation (7.2) are the steady-state drag force, the lift force, the pressure gradient force, the stress gradient force, the added mass force, the Basset history force and the gravitational force. Because the sizes of the particles interested in this work are small ($\leq$~$10^2$μm), extra terms arising from the non-uniformity of the flow can be neglected. The forces in Equation (7.2) are modeled in the way presented as follows.

### 7.1.1 Steady-State Drag Force

The drag force acting on a small sphere in a uniform flow can be expressed as: [112]

$$\mathbf{F}_{\mathrm{D}} = \frac{1}{8} p\, d_p^2 r_f C_D \left|\mathbf{v}_f - \mathbf{v}_p\right| \left(\mathbf{v}_f - \mathbf{v}_p\right) \tag{7.3}$$

where:

$$C_D = f_{\mathrm{Re_p}} \left( {}^{24}\!\big/_{\mathrm{Re}_p} \right) \tag{7.4}$$

$$\mathrm{Re_p} = {}^{\left|\mathbf{v}_f - \mathbf{v}_p\right| d_p}\!\big/_{n} \tag{7.5}$$

in which $C_D$ is known as the drag coefficient and $f_{\mathrm{Rep}}$ is the correction factor due to a finite particle Reynolds number, which can be found through Eq. (7.6) for $Re_p \leq 800$: [112]

$$f_{\mathrm{Re}_p} = \left(1 + 0.15\mathrm{Re}_p^{0.687}\right) \tag{7.6}$$

## 7.1.2 Shear Lift Force

Saffman [113, 114] derived the lift force on solid spheres in an unbounded linear shear flow with the following form:

$$F_{L,Saff} = 1.61 m d_p \left|\mathbf{v}_f - \mathbf{v}_p\right| \sqrt{\mathrm{Re}_G} \tag{7.7}$$

$$\mathrm{Re}_G = {}^{G d_p^2}\!\big/_{n} \tag{7.8}$$

where $G$ is the velocity gradient. It was assumed in Saffman's derivation that both the particle Reynolds number $\mathrm{Re}_p$ and the shear Reynolds number $\mathrm{Re}_G$ are much less than unity and $\mathrm{Re}_p \ll \sqrt{\mathrm{Re}_G}$. [113] Equation (7.7) can also be written as follows: [112]

$$\mathbf{F}_{L,Saff} = 1.61 d_p^2 \left(m r\right)^{1/2} \left|\nabla \times \mathbf{v}_f\right|^{-1/2} \left[\left(\mathbf{v}_f - \mathbf{v}_p\right) \times \left(\nabla \times \mathbf{v}_f\right)\right] \tag{7.9}$$

Corrections due to a finite Reynolds number and the near-wall effects were derived by McLaughlin: [115] [116]

$$F_L \big/ F_{L,Saff} = 0.443 J(e, l^*) \tag{7.10}$$

where: $$e = \sqrt{\mathrm{Re}_G} \,/\, \mathrm{Re}_p \tag{7.11}$$

$$l^* = l_w \left( G \big/ n \right)^{1/2} \tag{7.12}$$

Because of the complexity of the general expression for *J*, [115] Mei [117] reconstructed it for particles far from the wall [115] using curve fitting for 0.1≤ε≤20:

$$J(e) \approx 0.6765 \left\{1 + \tanh\left[2.5 \log_{10} e + 0.191\right]\right\} \left\{0.667 + \tanh\left[6\left(e - 0.32\right)\right]\right\} \tag{7.13}$$

If the particle is close to the wall ($l^* \le 0.1$), $J(e, l^*)$ can be computed by: [116]

$$J(e) = \frac{p^2}{16} \left( \frac{1}{e} + \frac{11}{6} l^* \right) \tag{7.14}$$

Derivations and discussions on the lift force corrections can be found in [116-118].

### 7.1.3 Pressure Gradient Force and Stress Gradient Force

The pressure gradient force, which contributes to the hydrostatic component of the buoyancy, can be important when the particle density is comparable or lighter than the fluid.  It can be calculated through the following equation: [112]

$$\mathbf{F}_{press} = -\frac{p\, d_p^3}{6} \nabla p \tag{7.15}$$

By applying the divergence theorem, a similar expression for the stress gradient force is reached: [112]

$$\mathbf{F}_{stress} = -\frac{p\, d_p^3}{6} \nabla t_{ij} \tag{7.16}$$

Adding the two forces yields a simple expression as follows:

$$\mathbf{F}_{press} + \mathbf{F}_{stress} = -\frac{p\, d_p^3}{6} \frac{D\mathbf{v}_f}{Dt} \tag{7.17}$$

## 7.1.4 Added Mass Force and Basset History Force

Both the added mass force and the Basset history force are unsteady forces due to the acceleration of the relative velocity between the particle and its surrounding fluid. Previous studies suggest that they might be important for neutral-buoyant particles. [119] These two forces have been neglected in previous studies of particle transport during continuous steel casting. To investigate their importance, they are included in one simulation of this thesis. The computed magnitudes are compared with the other forces in section 9.6.

The added mass force arises from the acceleration of the surrounding fluid by the particle. It can be expressed as follows: [112, 120]

$$\mathbf{F}_A = \frac{C_A\, r p\, d_p^3}{12} \left( \frac{D\mathbf{v}_f}{Dt} - \frac{d\mathbf{v}_p}{dt} \right) \tag{7.18}$$

$$C_A = 2.1 - \frac{0.132}{0.12 + \mathrm{Ac}^2} \tag{7.19}$$

$$\mathrm{Ac} = \frac{\left| \mathbf{v}_f - \mathbf{v}_p \right|^2}{d_p \dfrac{d\left| \mathbf{v}_f - \mathbf{v}_p \right|}{dt}} \tag{7.20}$$

where $C_A$ is the correction factor due to the acceleration effect and *Ac* is the acceleration parameter. [120] Notice that in Equation (7.18) *D/Dt* ($= \partial / \partial t + (\mathbf{v} \cdot \nabla)$) is the total derivative.

The Basset history force is due to the lag of the development of the particle wake. [112] It is formulated as follows: [112, 121]

$$\mathbf{F}_H = \frac{3}{2} C_H d_p^2 \sqrt{prm} \left[ \int_0^{t_p} \frac{1}{\sqrt{t_p - t'}} \left( \frac{D\mathbf{v}_f}{Dt'} - \frac{d\mathbf{v}_p}{dt'} \right) dt' + \frac{\left(\mathbf{v}_f - \mathbf{v}_p\right)_{t=0}}{\sqrt{t_p}} \right] \tag{7.21}$$

$$C_H = 0.48 + \frac{0.52}{\left(1 + \mathrm{Ac}\right)^2} \tag{7.22}$$

where $C_H$ is the correction factor due to the acceleration of the relative velocity. [121] Because all the particles in this thesis are introduced into the computational domain with the same velocity as the local fluid, the second term in Equation (7.21) always has a value of zero. The numerical evaluation of the Basset integral is given in the solution procedure section.

## 7.1.5 Gravitational Force

Particle buoyancy is incorporated via the upward hydrostatic component of the pressure gradient force and the downward gravity force:

$$\mathbf{F}_g = \frac{1}{6} p \, d_p^3 r_p \mathbf{g} \tag{7.23}$$

Substituting Equations (7.3), (7.7), (7.9), (7.10), (7.17), (7.18), (7.21) and (7.23) into Equation (7.2) yields the BBO equation for particles in a uniform velocity field shown as the follows:

$$\begin{aligned} \left(1 + \frac{C_A r}{2 r_p}\right) \frac{d\mathbf{v}_p}{dt} = {} & \frac{\left(1 + 0.15\mathrm{Re}_p^{0.687}\right)}{t_V} \left(\mathbf{v}_f - \mathbf{v}_p\right) + 0.07568 J \frac{d_p}{t_V} \left|n \nabla \times \mathbf{v}_f\right|^{-1/2} \left[\left(\mathbf{v}_f - \mathbf{v}_p\right) \times \left(\nabla \times \mathbf{v}_f\right)\right] \\ & + \left(1 + \frac{C_A}{2}\right) \frac{r}{r_p} \frac{D\mathrm{v}_f}{Dt} + C_H \sqrt{\frac{9}{2p} \frac{r}{r_p}} \frac{1}{\sqrt{t_V}} \left[ \int_0^{t_p} \frac{1}{\sqrt{t_p - t_p'}} \left( \frac{D\mathbf{v}_f}{Dt_p'} - \frac{d\mathbf{v}_p}{dt_p'} \right) dt_p' + \frac{\left(\mathbf{v}_f - \mathbf{v}_p\right)_{t=0}}{\sqrt{t_p}} \right] + \mathbf{g}\left(1 - \frac{r}{r_p}\right) \end{aligned} \tag{7.24}$$

where $\tau_V$ is the particle velocity response time defined as:

$$t_V = \frac{r_p d_p^2}{18m} \tag{7.25}$$

Equations (7.1) and (7.24) are integrated using a fourth-order Runge-Kutta method, as shown in more details in section 7.7.

## 7.2 Forces on a Particle Close to a Solidification Interface

Figure 7.1 illustrates a spherical particle in front of solidifying dendrites of steel. In addition to the six hydrodynamic forces just discussed (with the drag and buoyancy being the most significant ones), it experiences five additional forces including the lubrication force ($\mathbf{F}_{\mathrm{Lub}}$), the Van der Waals interfacial force ($\mathbf{F}_{\mathrm{I}}$), the surface energy gradient forces ($\mathbf{F}_{\mathrm{Grad}}$), the reaction force ($\boldsymbol{F}_{\mathrm{N}}$) and the friction force($\boldsymbol{F}_{\mathrm{f}}$). It should be noted that the reaction and the friction forces (denoted as dashed lines) may not exist and they are not important for particle capture, which will be further discussed in section 7.3. The first three forces are only significant when the particle is very close to the solid-liquid boundaries.

### 7.2.1 Lubrication Force: [93, 105]

The lubrication force arises from the flow in the gap between the particle and the dendrite tip induced by the particle motion, as discussed in section 6.2. To maintain a constant gap thickness, the particle is assumed to move at the same velocity as the dendrite (particle pushing). Under the condition that the thickness ($h_0$) of the gap is much smaller than both the particle and the dendrite tip radii and larger than the critical distance ( $h_0^{cr}$ ), the lubrication force acting on the particle along the particle radius towards the dendrite tip, which tends to aid particle capture, can be expressed as: [93, 95, 105]

$$F_{Lub,n} = 6pmV_{sol}\,\frac{R_p^2}{h_0}\left(\frac{r_d}{r_d + R_p}\right)^2 \qquad (7.26)$$

Detailed derivation of Equation (7.26) can be found in [93, 95, 105].

### 7.2.2 Van der Waals Interfacial Force: [93, 94]

Following the derivation of Potschke and Rogge, the Van der Waals interfacial force acting on a spherical particle in front of a solidifying interface with a convex curvature radius of $r_d$ can be expressed as: [94]

$$F_I \doteq 2p\Delta s_0 \frac{r_d R_p}{r_d + R_p}\frac{a_0^2}{h_0^2} \qquad (7.27)$$

$$\Delta s_0 = s_{sp} - s_{sl} - s_{pl} \qquad (7.28)$$

where $s$ is the surface energy, the subscripts $s$, $p$ and $l$ denotes solid, particle and liquid respectively and $a_0$ is the atomic diameter of the liquid ($h_0 \geq a_0$).

### 7.2.3 Surface Energy Gradient Force Induced by a Concentration Gradient of an Interfacial Active Solute: [100, 101, 108, 122]

The surface energy of liquid steel changes with temperature and composition. [123] It is shown in APPENDIX B that the surface energy change of Fe alloys due to a temperature gradient is much smaller than that induced by a concentration gradient of an interfacial active element such as sulfur (S) or oxygen (O). It is also shown in APPENDIX B that sulfur is the major solute contributing to a surface energy gradient in killed steel, where oxygen content is very low. The surface energy change due to other dissolved elements such as carbon can be neglected. Therefore, this thesis considers sulfur as the only interfacial active solute.

The surface energy gradient force acting on a particle is dependent on the interface morphology and the solute concentration distribution. Kaptay derived the equation for this force for a spherical particle in front of a planar interface with the following expression: [100]

$$F_{Grad} = -2p\, R_p d_c \frac{ds_{pl}}{dn} \qquad \text{for } d_c \leq 2R_p \tag{7.29}$$

$$F_{Grad} = -4p\, R_p^2 \frac{ds_{pl}}{dn} \qquad \text{for } d_c \geq 2R_p \tag{7.30}$$

where $d_c$ is the thickness of the concentration (and also the surface energy gradient) boundary layer and $\frac{ds_{pl}}{dn}$ is the surface energy gradient. The $d_c$ in front of a planar interface was recommended to be estimated by: [124]

$$d_c = \frac{2D_s}{\mathrm{v}_{sol}} \text{ [124]} \tag{7.31}$$

and the surface energy gradient for particles in a Fe-sulfur solution was proposed to be calculated by: [101]

$$\left(\frac{ds_{pl}}{dn}\right)_{\text{interface}} = \frac{m \cdot n \cdot k}{k + n \cdot C_0} \frac{\mathrm{v_{sol}}}{D_s} \frac{1-k}{k} C_0 \tag{7.32}$$

where $m$ and $n$ are semi empirical coefficients as shown in APPENDIX B, $k$ is the distribution coefficient of the solute. [101]

The surface energy gradient force acting on a spherical particle close to a hemispherical dendrite tip is derived in APPENDIX C, with the following form:

$$F_{Grad} = -\frac{mbpR_p}{x^2}\left\{\frac{\left(x^2 - R_p^2\right)}{b}\ln\left[\frac{\left(x+R_p\right)\left[a\left(x-R_p\right)+b\right]}{\left(x-R_p\right)\left[a\left(x+R_p\right)+b\right]}\right] + \frac{2R_p}{a} - \frac{b}{a^2}\ln\left[\frac{a\left(x+R_p\right)+b}{a\left(x-R_p\right)+b}\right]\right\} \tag{7.33}$$

$$a = 1 + nC_0 \tag{7.34}$$

$$b = nr_t\left(C^* - C_0\right) \tag{7.35}$$

$$x = R_p + r_t + h_0 \tag{7.36}$$

where $m$ and $n$ are empirical constants defined in Equation (B.2) with values of 0.17J/m$^2$ and 844(mass%)$^{-1}$ for Fe-S alloy and $L$ is the distance between the particle and dendrite tip centers. This force is in a direction along the particle radius towards the dendrite tip center.

## 7.3 Criterion for Particle Capture by a Dendritic Interface

Particle pushing and capture (including entrapment and engulfment) are important phenomena that impurity particles encounter in continuous steel caster molds. Particles that reach the mushy zone front may be trapped by the solidifying shell or repulsed back to the molten steel. The capture and pushing are associated with the solidifying dendrite morphology, the concentration boundary layer of the interfacial active solute (sulfur) and the velocity boundary layer. The flow velocities close to the dendritic interface can be estimated from the LES results. However, accurate resolution of the dendrite shape and the concentration boundary layer is computationally prohibitive [125] and beyond the scope of this study. Alternatively, they can be estimated based on data and semi-empirical equations reported in previous studies. A simple criterion for particle pushing and capture is developed in this thesis on the basis of a force balance analysis shown as follows.

### 7.3.1 Particles Smaller than the PDAS

It is intuitive that particles smaller than the primary dendrite arm spacing (PDAS) can easily get in between the dendrite arms without major disturbance on the primary dendrite arms while larger particles cannot. Recapitulate Figure 7.1, if the particle is smaller than the PDAS, it will be surrounded by the growing dendrites at a latter time, with the help of attractive surface energy gradient force (please also refer Figure 6.3). Previous experimental studies [92] in quiescent solidification systems also found many particles smaller than the PDAS being entrapped even when the dendrite growth speed was much lower than the critical value for the particle PET. Therefore, particles smaller than the PDAS is modeled as being captured by the shell once they touch the computational boundary representing the mushy zone front.

### 7.3.2 Particles Larger than the PDAS

Unlike the smaller particles, particles larger than the local PDAS cannot fit in-between the dendrite arms. As depicted in Figure 7.1, a spherical alumina particle contacts the solidifying dendrites through a thin film of liquid steel at the critical distance. To avoid being captured, the particle has to move in the solidification direction at a speed no slower than the dendrite growth speed. For this condition to exist, the forces acting on the particle while is touching the shell must be either in stable equilibrium or in the direction away from the dendrite tips. This requires consideration of all eleven forces which act on the particle in this region. The pressure gradient, stress gradient, Basset, and added mass forces are neglected here because they are found to be small (<15% of the buoyancy force) in the bulk region, and are expected to be smaller in the boundary layer. The condition of particle pushing or capture is determined through the following procedure:

Step 1: If the component of the total force ($F_{Tot}$) acting on the particle in the solidification direction (χ in Figure 7.1) is larger than zero, then the particle will be pushed away from the interface. This escape criterion is expressed as follows:

$$F_{Tot,c} = F_L - F_{D,c} - 2\left(F_{Lub} - F_{Grad} - F_I\right)\cos q > 0 \tag{7.37}$$

where:

$$q = acr\sin\left[0.5\mathrm{PDAS} \Big/ \left(R_p + r_d\right)\right] \tag{7.38}$$

Otherwise, check if the forces on the particle are large enough to avoid entrapment by pushing it along the interface.

Step 2: Under the condition that $F_{Tot}$,χ ≤ 0, if the force in η direction (across the solidification front) pushes the particle against a dendrite arm, it will cause a reaction force ($F_{N,1}$ or $F_{N,2}$) and a friction force ($F_{f,1}$ or $F_{f,2}$) at the contact point, as shown in Figure 7.1. Particle capture can then be determined by examining whether the particle can drift away due to rotation about the dendrite tip. Specifically, if either one of the following occurs, the particle will be captured:

(1) If the buoyancy ($F_B$) and the η component of the drag ($F_{D,h}$) are in the same direction and:

$$(F_{D,h} + F_{B,h})\cos q + \left(F_L - F_c\right)\sin q \le \left(F_{Lub} - F_{Grad} - F_I\right)\sin 2q \tag{7.39}$$

(2) If the buoyancy ($F_B$) and the η component of the drag ($F_{D,h}$) are in opposite directions, and either:

$$(F_{D,h} - F_B)\cos q + \left(F_L - F_c\right)\sin q \le \left(F_{Lub} - F_{Grad} - F_I\right)\sin 2q \text{ , if } F_{D,h} \ge F_B \tag{7.40}$$

or

$$(F_B - F_{D,h})\cos q + \left(F_L - F_c\right)\sin q \le \left(F_{Lub} - F_{Grad} - F_I\right)\sin 2q \text{ , if } F_B > F_{D,h} \quad (7.41)$$

then the particle will stay attached to the dendrites and is modeled as being captured. If neither condition is met, then the particle will rotate back into the flow and then be washed away with the liquid.

The above analysis procedure requires knowledge of the PDAS and the tip radius ($r_d$) of the primary dendrite arms. The estimation of these two parameters is presented in the next sub-section. It should be noted that results in APPENDIX D show that the Van der Waals interfacial force, the lubrication drag force and the surface energy gradient force are only important when the particle is very close to the solidification interface. Therefore, they can be neglected in the Lagrangian particle transport simulations. These three forces are only included for evaluating the capture criterion to predict the fate of a particle when it touches a computational boundary representing the mushy zone front.

The magnitudes of the forces acting on the particle shown in Figure 7.1 are evaluated in APPENDIX D. The results suggest that if dendrite tip radius is small (a few microns), the magnitudes of the Van der Waals interfacial force and the lubrication drag force are at least about several times smaller than the surface energy gradient force. Thus, the model predictions are not sensitive to the selection of the critical distance ( $h_0^{cr}$ ).

### 7.3.3 Estimation of PDAS, Dendrite Tip Radius and Concentration Boundary Layer Thickness

The PDAS and dendrite tip radius can be computed through expensive numerical computations of dendrite solidification. [125] However, this approach is computational prohibitive and beyond the scope of this thesis. The two parameters can also be estimated through analytical equations. Kurz and Fisher [126] derived a general framework to relate the dendrite tip radius, PDAS and interface under-cooling for binary alloy dendrite growth with the following expressions:

$$r_{tip} = 2p\left(\frac{D_0\, s_{sl}/S}{\mathrm{v}_{\mathrm{sol}} k \Delta T_0}\right)^{1/2} \tag{7.42}$$

$$\mathrm{PDAS} = \left(\frac{2.94 r_{tip} \Delta T_0}{dT/dn}\right)^{1/2} \tag{7.43}$$

$$\Delta T_0 = \left(T_L - T_S\right)_{C_0} \tag{7.44}$$

where $D_0$ is the diffusion coefficient of the solute, $s_{\mathrm{sl}}$ is the specific solid-liquid interface energy, $k$ is the distribution coefficient ($=C_s/C_L$), and S is the melting entropy. Further details on the evaluation of these equations are given in APPENDIX D. In addition, comparisons between the PDAS obtained from Equation (7.43) and measurements are shown to have reasonable agreement.

## 7.4 Particle Capture Criterion Validations with Experiments

The criterion for particle pushing and capture proposed in section 7.3 was built on the basis of a theory that is still in the development stage. In addition, the forces, especially the surface energy related forces, involved in the criterion should be validated by experiments involving liquid steel and cross-flow conditions. However, due to the difficulties involved for such measurements, especially for particles in metal melts, only limited experimental studies can be found in previous literature. Using the best available experimental data, the criterion is preliminarily examined using two systems of alumina particles in quiescent solidifying liquid steel [89] and zirconia particles in quiescent solidifying aluminum melt [97] by comparing the PET results with measurements. It is then employed to reproduce the results of the pushing of PMMA particles in solidifying water with tangential (cross) flow across the interfacial front. [99, 110]

### 7.4.1 Validation in Quiescent Metal Systems

Shibata et al. [89] measured the critical solidification speed for the PET of slag spheres (25%CaO-25%$SiO_2$-50%$Al_2O_3$) by a vertical solid-liquid interface in steel. The liquid steel in the experiment was stationary without significant cross-flow. The chemical composition of the steel is repeated in Table 7.1. [89] Parameters and material properties for the calculation of the forces are given in Table 7.2. Due to the debate on the selection of the critical distance, the current analysis tested four different critical distance proposed in previous literatures, with the value of 7 $a_0$ [98], 50 $a_0$ [107], $\left(\frac{\Delta \sigma_0 a_0^2}{3m R_p}\frac{\left(r_d+R_p\right)}{r_d}\right)^{1/2}$ [97] and $\left(4\frac{\Delta \sigma_0 R_p a_0^2}{\sigma_{sl}}\right)^{1/3}$ [102] respectively, as compared in Figure 7.2. The interface curvature radius was obtained from experimental observation [89] with a value of approximately four times the particle radius. The critical speed was obtained by equating the repulsive Van der Waals interface force and the sum of the lubrication drag and concentration gradient forces at the critical distance.

The calculated critical solidification speed is compared with the experimental data in Figure 7.3. It appeared that results from using the critical distance of $\left(4\frac{\Delta \sigma_0 R_p a_0^2}{\sigma_{sl}}\right)^{1/3}$ [102] have the best agreement with measurements. It is also seen that the force caused by the sulfur concentration gradient greatly reduces the solidification speed for PET. The magnitudes of the three forces are compared Figure 7.4 at the critical distance $\left(4\frac{\Delta\sigma_0 R_p a_0^2}{\sigma_{sl}}\right)^{1/3}$, showing the great importance of the surface energy gradient force.

Figure 7.5 compares the predicted critical solidification speed of PET for $SrO_2$ spheres in pure molten aluminum with measurements. [97] The critical distance $h_0^{cr}$ used for the prediction was calculated using $\left(4\frac{\Delta\sigma_0 R_p a_0^2}{\sigma_{sl}}\right)^{1/3}$, which generated the best match with experiments in the steel system. The critical speed for the PET is predicted to be approximately 0.7μm/s for the 500μm particle, which is consistent with the measured range between 0.5μm/s and 1.0 μm/s. [97]

The above comparisons prove that the pushing and engulfment of non-metallic particles in metal melts, especially the slag spheres in molten steel, can be predicted through a force balance analysis, and the forces calculated from Equations (7.26)-(7.33) reproduce the experimental results with reasonable accuracy. It also shows that the predicted results are highly dependent on the selected critical distance $h_0$, due to the significance of the Van der Waals and lubrication forces in the above configurations. However, as shown in APPENDIX D, because the small tip radius of dendrites in the continuous steel caster molds, these two forces become insignificant regardless of $h_0$. This makes the criterion unaffected by the controversial value $h_0^{cr}$.

### 7.4.2 Validation in an Ice-Water Solidification System

The particle pushing-capture criterion was then applied to the particle pushing experiment by Han and Hunt. [99] The experiment has been described in 6.2. Details on the experimental settings can be found elsewhere. [99, 110] The measured cell intervals (24.5μm and 18.5μm) under different solidification speed (4.2 μm/s and 68.8μm/s) were used for the prediction (analogue to the PDAS). Due to the lack of data, the cell tip radius was assumed to be 10 percent of the interval (24.5μm and 18.5μm) and the liquid was assumed to be pure water. The Van der Waals interfacial force on the particle in this system was found to be attractive. The critical distance $h_0$ was set to be $50\,a_0$. Material properties and parameters used for the force balance analysis are given in Table 7.3. The predicted results are compared with measurement in Figure 7.6. Both the experiment and the prediction suggest that the cross-flow speed needed to push the particle into motion increases with the particle size. However, the predicted speeds for particle pushing are slightly smaller than the measured values. In addition, the experimental study found that increasing the solidification speed increases the critical cross-flow speed, while the prediction shows an opposite trend. These discrepancies have several possible explanations. First, in the experiments, particles first settled on the interface while the solidification proceeded and consequently formed an increasingly larger dent to partially trap the particle. Flow speed was gradually increased after the solidification procedure started until the particle was pushed into motion. A faster solidification speed leads to a deeper dent for same time duration and consequently makes the particle more difficult to be drifted into motion. This time delay before starting fluid into motion was not modeled in the analysis, as the particles were computationally injected with the moving fluid. Another possible explanation is the pure water assumption in the analysis. The presence of an interfacial active solute increases the attractive force and consequently increases the critical cross-flow speed for particle pushing. Increasing the solidification speed causes a slightly thinner solute concentration boundary layer. However, it also increases the concentration gradient. The net effect could be a slight increase of the attractive surface energy gradient force and consequently a larger critical cross-flow speed for particle pushing. Due to the lack of information on the fluid composition for the experiment, no rigorous analysis could be given here.

In summary, the simple particle capture criterion has been used to predict experimental observations of particle pushing and capture in three different solidification systems. The predicted results have reasonable agreement with the measurements, suggesting the validity of this simple model.

## 7.5 Predicted Critical Cross-Flow Velocities in Continuous Steel Caster

Using the criterion developed in Section 7.3, the critical velocities of the flow relative to the downward moving shell for the capture of slag spheres were computed for typical conditions in a steel caster. The flow was assumed to be in the vertical direction. The results are shown in Figure 7.7 for the effect of PDAS and a complete range of particle sizes for two typical solidification conditions (500μm/s solidification speed and 2.1μm dendrite tip radius for Figure 7.7(a) and 200μm/s solidification speed and 3.4μm tip radius in Figure 7.7(b)) and the casting speed of 25.4mm/s. The results show that capture always occurs for particles smaller than the PDAS. Particles larger than the PDAS will be captured if the magnitude of the relative cross-flow velocity between the particle and the solidifying steel shell is smaller than a critical velocity. Velocities higher than the critical value prevent capture, transporting the particle away from the interface before it can get entrapped. This critical velocity of the fluid depends on the flow direction. Higher critical velocity magnitudes indicate easier capture. Particles are more easily entrapped in downward flow, resulting in higher critical velocity. This is because the upward buoyancy lowers the magnitude of the particle velocity (relative to that for upward flow conditions). A wedge-shaped region of the graph indicates a region where capture is possible. This region becomes narrower as particle size increases, owing to the increasing difficulty of the dendrites to prevent rotation of large particles. This region also becomes narrower with decreasing PDAS, again due to easier rotation of particles. The wedge tends towards the terminal velocity of the particle plus the casting speed. When the downward flow speed equals this sum, the particle will be stationary relative to the dendrites, so can always be captured (based on results for quiescent flow presented in Section 7.4.1). Comparisons of Figure 7.7(a) and (b) indicate that with increasing interface velocities, particle capture becomes easier so the magnitude of the critical cross-flow velocity increases. This effect is small compared with that of particle size.

## 7.6 Initial and Boundary Conditions

Having validated the capture criterion model, and incorporated it into the particle trajectory model, simulations of particle transport and capture are next performed for the continuous steel caster or its water model, using the fluid flow results computed by the LES model in Part I. In these simulations, particles were introduced into the computational domain from random positions at the domain inlet plane(s) with the local fluid velocities. The results from a separate simulation in the nozzle were used to determine the particle inlet positions for the mold simulation. Elastic re-bound was assumed when a particle hit the plastic wall of the water model or the outer surface of the nozzle in steel casters. Particles touching the top surface were assumed to be safely removed by the slag layer. Particle capture was judged based on performing the procedure shown in 7.3 for each occurrence of particle touching a boundary representing the solidifying shell. If particle pushing was determined, particles were artificially forwarded into the fluid for a distance of 5% particle radius.

## 7.7 Solution Procedure

Using the flow field obtained from LES as described in Part I, the particle transport equations (7.1) and (7.24) were integrated following the fourth order Runge-Kutta explicit procedure. [127] Specifically, for an ordinary differential equation (ODE) with the following form:

$$\frac{dx}{dt} = f\left(t,x\right) \tag{7.45}$$

The fourth-order Runge-Kutta method follows the procedure as the follows: [127]

$$k_1 = \Delta t \cdot f\left(t_n, x_n\right)$$

$$k_2 = \Delta t \cdot f\left(t_n + \frac{\Delta t}{2}, x_n + \frac{k_1}{2}\right)$$

$$k_3 = \Delta t \cdot f\left(t_n + \frac{\Delta t}{2}, x_n + \frac{k_2}{2}\right)$$

$$k_2 = \Delta t \cdot f\left(t_n + \Delta t, x_n + k_3\right)$$

$$x_{n+1} = x_n + \frac{k_1}{6} + \frac{k_2}{3} + \frac{k_3}{3} + \frac{k_4}{6} + O\left(\Delta t^5\right) \tag{7.46}$$

where the subscript $n$ represents the discrete time step and *Dt* is the integrating time interval for the particle simulation. The local fluid velocities, which are needed to compute the hydrodynamic forces acting on the particles, were evaluated from those at the nearest neighboring cells through a second-order interpolation. [127]

The Basset integral term was estimated numerically by following Reek and Mckee's suggestions: [128]

$$\int_0^{t_p} \frac{1}{\sqrt{t_p - t_p^{'}}}\left(\frac{D\mathbf{v}_f}{Dt_p^{'}} - \frac{d\mathbf{v}_p}{dt_p^{'}}\right)dt_p^{'} \doteq 2\sum_{n=0}^{N-1}\left[\sqrt{\Delta t}\,\frac{\left(\dot{\mathbf{v}}_f^n + \dot{\mathbf{v}}_f^{n+1}\right)}{2} - \frac{1}{\sqrt{\Delta t}}\left(\mathbf{v}_p^{n+1} - \mathbf{v}_p^n\right)\right]\left(\sqrt{N-n} - \sqrt{N-n-1}\right) \tag{7.47}$$

where: $$N\,\Delta t = t_p \tag{7.48}$$

The particle velocities and displacements were solved every time step after the fluid velocity field is solved. The integrating time steps for the particle simulations were chosen based on the particle response time in Equation (7.25):

$$\Delta t_p \le t_V \tag{7.49}$$

The particle integrating time-step $\Delta t_p$ determined by (7.49) is usually smaller than that for the flow simulation ($\Delta t$). When this occurs, several steps of integration for particle transport were performed between each two successive time steps of the flow simulation. Each particle was tracked in the simulation until it exited the computation domain from the outlet or was removed at the top surface or is captured in the shell.

It should be mentioned again that due to the low volume fraction of impurity particles for the continuous casting process (~0.01% for a typical steel with 30ppm oxygen), one-way coupling is employed in all the computations of this thesis.

**Table 7.1. Steel composition in the PET experiment by Shibata et al. [89]**

| Component | C | Si | Mn | P | S | Al |
|---|---|---|---|---|---|---|
| Content (wt pct) | 0.001 | 0.45 | 0.13 | 0.002 | 0.0028 | <0.001 |

**Table 7.2. Material properties of the PET prediction for slag particles in liquid steel.[89] [122]**

| Property/Parameter | Unit | Value |
|---|---|---|
| $s_{pv}$ | N/m | 0.750 |
| $s_{lv}$ | N/m | 1.635 |
| $s_{sp}$ | N/m | 2.330 |
| $s_{sl}$ | N/m | 0.20 |
| $s_{pl}$ | N/m | 1.167 |
| $Ds_0$ | N/m | 0.963 |
| $a_0$ | m | $2.5\times 10^{-10}$ |
| μ | N/m | $5.5 \times 10^{-3}$ |
| $C_0$ | mass% | 0.0028 |
| $k$ | N/m | 0.05 |
| $m$ | N/m | 0.171 |
| $n$ | $(\text{wt pct})^{-1}$ | 840 |

**Table 7.3. Material properties for the calculation of PMMA particle in solidifying water. [19][107] [129]**

| Property/Parameter | Unit | Value |
|---|---|---|
| $s_{pv}$ | N/m | 0.041 |
| $s_{lv}$ | N/m | 0.07 |
| $s_{sp}$ | N/m | 0.020 |
| $s_{sl}$ | N/m | $3.4\times10^{-4}$ |
| $s_{pl}$ | N/m | 0.021 |
| $Ds_0$ | N/m | -0.001 |
| $a_0$ | m | $2.82\times 10^{-10}$ |
| μ | N/m | $1.0 \times 10^{-3}$ |

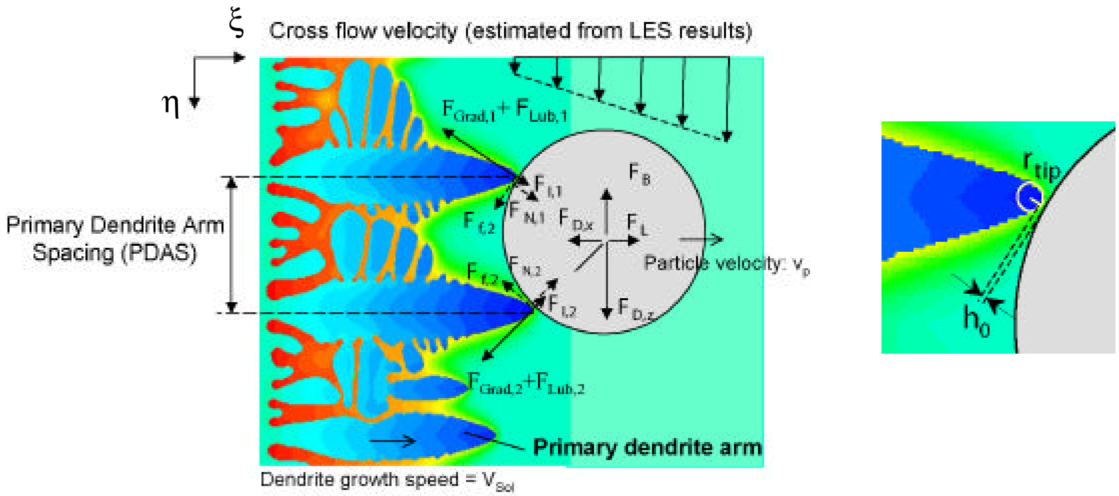


$F_D$: Drag force;
$F_{Grad}$: Surface energy gradient force;
$F_I$: Van der Waals interfacial force;
$F_{Lub}$: Lubrication drag force;
$F_L$: Lift force;
$F_B$: Buoyancy force;
$F_N$: Reaction force;
$F_f$: Friction force.

**Figure 7.1. Illustration of forces acting on a particle in front of solidifying dendrites.**

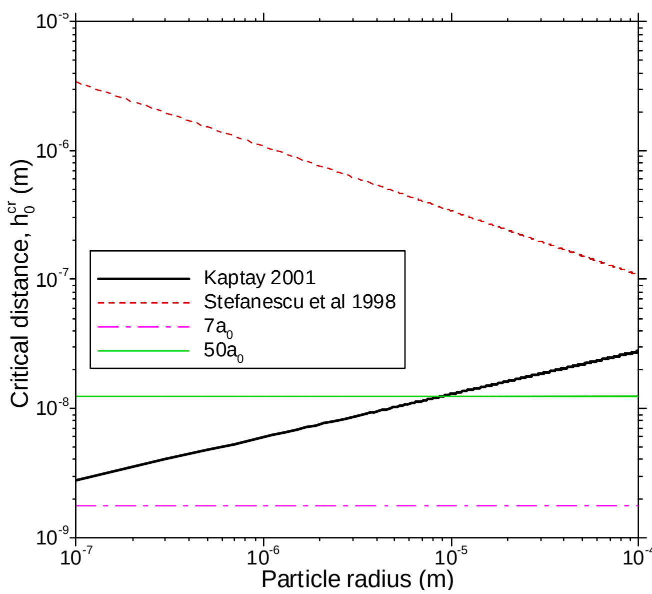


**Figure 7.2. Comparison of critical distances proposed by different researchers.**

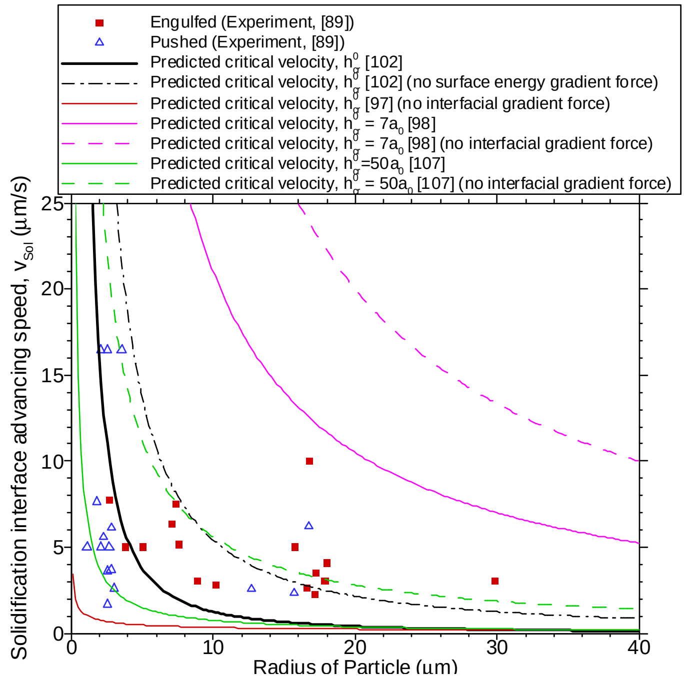


**Figure 7.3. Critical solidification speed for PET of slag spheres in front of a smooth solidifying interface of steel.**

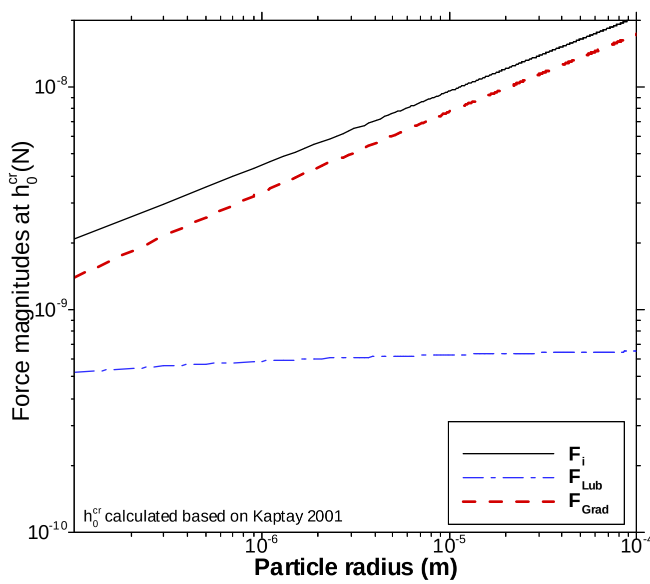


**Figure 7.4. Comparison of forces acting on slag spheres in liquid steel at the critical distance $h_0^{cr}$ .**

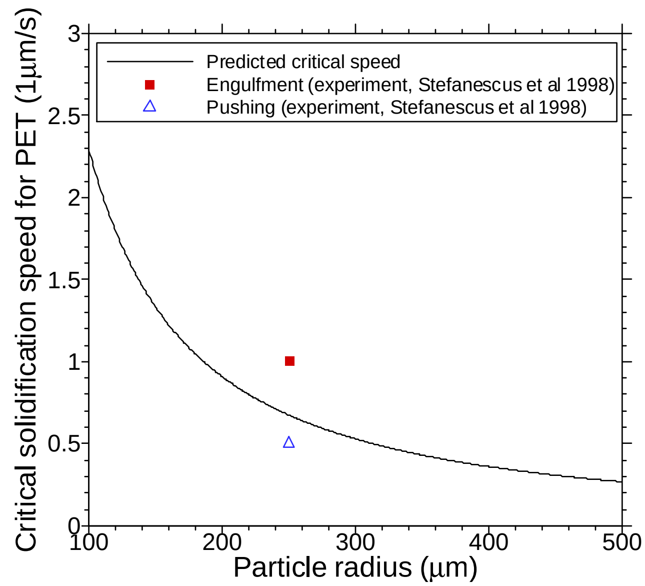


**Figure 7.5. Critical solidification speed of PET for $SrO_2$ in liquid aluminum.**

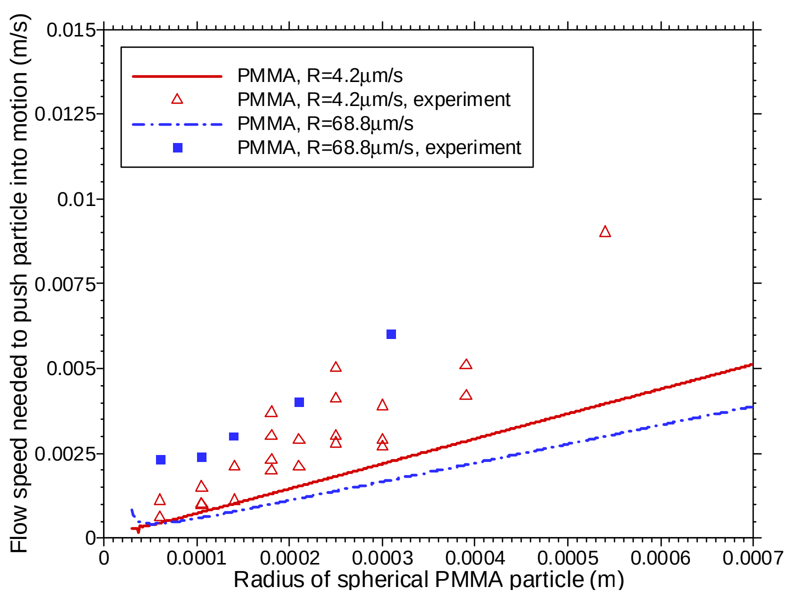


**Figure 7.6. Predicted critical cross-flow speed to push PMMA spheres into motion in front of a cellular solidifying interface of ice, compared to measurements.** [99]

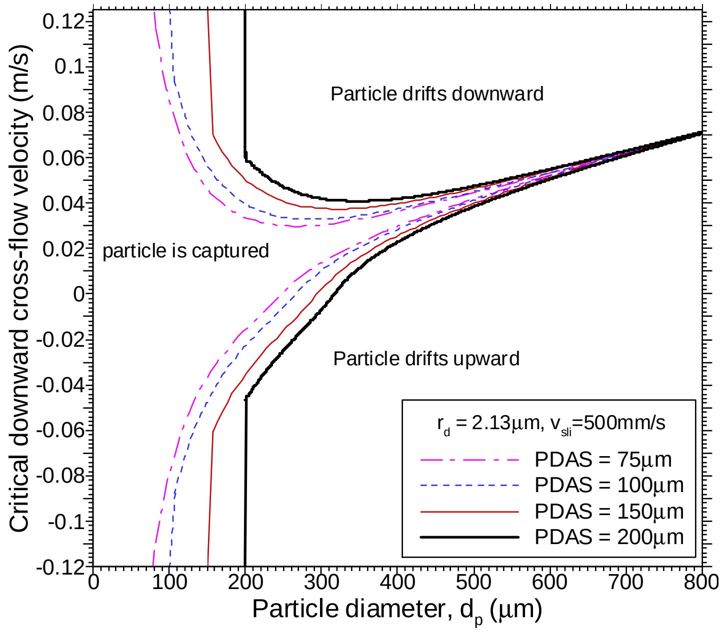


**(a)**

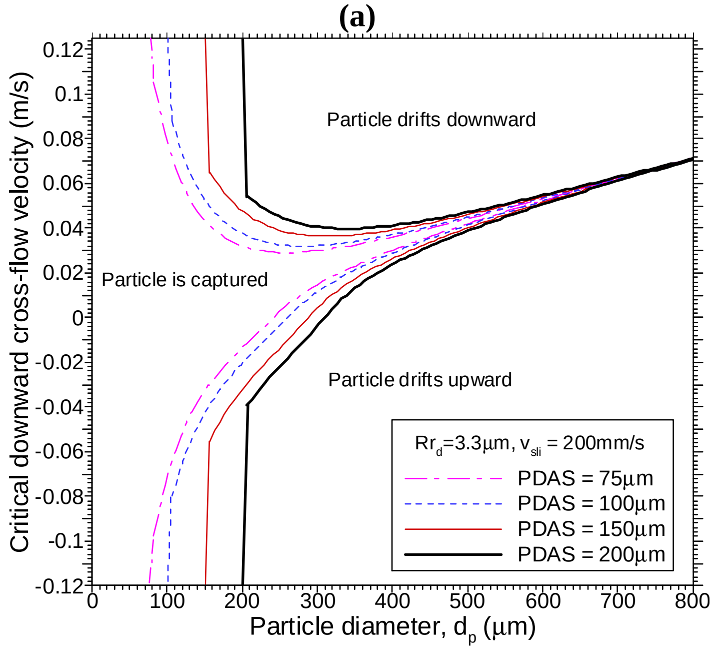


**(b)**

**Figure 7.7. Critical downward cross-flow velocities for slag droplets in molten steel.**

# CHAPTER 8. MODEL VALIDATION IN A FULL-SCALE WATER MODEL

The computational model presented in CHAPTER 7 was applied to simulate particle motions and removal fractions in the full-scale water model for the standard-thickness-slab caster (*Case 1*) [17, 69] presented in Part I. In this chapter, the computed fractions of particles removed by a screen close to the top surface are compared with experimental results in order to validate the model. [69] The LES predicted flow velocities presented in CHAPTER 4 were employed for the particle transport simulation.

## 8.1 Computational and Experimental Settings

In the experiments, [69] around 8,000-30,000 elliptical disk-shaped plastic beads were injected into the mold with water through the nozzle over a few seconds. The density and size of the beads were chosen to aid visualization while approximating the vertical terminal velocity expected for typical 300μm alumina inclusions in liquid steel. [69] To model the removal of particles by the top surface slag layer, a screen was positioned near the top surface and the SEN (see Figure 8.1) to trap plastic beads as they flowed across the top surface towards the SEN and headed downwards. The experiments were repeated at least five times and the average fraction of particles removed by the screen was reported. [69]

Only half of the mold region was modeled to reduce the computational cost. The trapping of particles by the screen was modeled by summing the particles that crossed the screen from the top. The screen influenced neither the fluid velocity field (CHAPTER 4) nor the particle transport. The simulation employed 17,500 spherical particles with diameters of 3.8mm and densities of 998Kg/$m^3$  They were divided into five groups of 500 particles and another six groups of 2,500 particles, in order to investigate statistical variations and the effect of the number of particles.  The particles were introduced into the domain through the nozzle port over the time periods given in Table 8.1.  Only the drag and the buoyancy forces were included in the simulation.  Computational results from CHAPTER 9 prove that they are the two most significant forces, and that other forces are about six times smaller for most of the times.

## 8.2 Particle Distributions

The motions of the six groups of 2,500 particles and five groups of 500 particles were simulated.  The four snapshots in Figure 8.1 reveal the distribution of all six groups of 2,500 particles (15,000 particles) together at four time instants.  A video of the transient particle motion is available elsewhere. [130]  The extended line inside the mold shows the position of the screen used to capture particles.  This figure shows that particles move within the jet after injection (Figure 8.1(a)) and split into two parts (Figure 8.1(b)), corresponding to the upper and the lower rolls, after they hit the narrow face.  By 100s (Figure 8.1(d)), the particles are well dispersed throughout the domain.  Some of the particles flow along the top surface and are removed.  Other particles flow out of the mold bottom with the outflow fluid and represent particles that would be trapped deeper in the steel caster, leading to defects in the solid steel strand.

## 8.3  Representative Particle Trajectories

Typical trajectories of four particles are shown in Figure 8.2 for 100s of computation or until they contact the top surface (first frame) or exit the domain (second frame). Particles in the last two frames are still moving. While moving with the flow, the particles gradually drift upward, with a typical particle Reynolds number of 10, which validates the assumption in Equation (7.6). These irregular trajectories illustrate the effect of turbulent fluid motion on particle transport.

## 8.4 Particle Removal

It is sometimes postulated that particles exiting the top portion of the nozzle should have a better chance to be transported to the top surface. This is examined in Figure 8.3. Figure 8.3(a) shows the initial positions of all six groups of 2,500 particles at the nozzle port exit plane. Figures 8.3(b) and (c) reveal the initial positions of particles which were removed to the top surface during 0s-10s and 10s-100s respectively. Time was counted starting from the instant when the first particle was introduced into the domain. All three distributions are observed to be uniformly random, indicating that chances for particles to be transported to the top surface are independent of their initial positions. This is likely because the turbulence dispersion of the jet and flow in the mold made the particle initial position irrelevant.

The simulated trajectories of the 17,250 particles were then processed to determine the fractions of particles removed to the top surface (lines) in Figure 8.4, which are compared with measured fractions removed by the screen (symbols) in the water model. After 10s, approximately 23% of the particles are removed, and by 100s about 55% have been removed. Considering the uncertainties in the experiments, and variability in the turbulent computations, the agreement between the computational and experimental results within 5% is encouraging. The results also show that the screen appears to simulate surface removal well at early times, but under-predicts it at later times (100s). The computation suggests that the total removal fraction is very large (nearly 80%) when the walls are unable to trap particles.

## 8.5 Number of Particles for Reliable Statistics

The particle fractions removed by the screen for the 2,500 and 500 particle groups are presented in Table 8.2, and are also compared with measurements. The average removal fractions for both groups agree with experiments within ±5%. However, the removal fraction varies greatly between groups, especially for the first 10s after the particle entered the mold. This is reflected by the standard deviation, ( $s_u = \sqrt{\sum_{i=1}^{N} \left(u_i - u_{mean}\right)^2 / N}$ ) which decreases from 5.5% (500 particle groups) and 4.8% (2,500 particle groups) for 0-10s to 2.9% and 1.4% for 10-100s. The standard deviation of the 2,500 particle groups is always lower than that of the 500 particle groups, as expected due to the improvement in statistical confidence with increasing population size. However, the improvement is small for 0-10s. This suggests that during early times, particle removal is more influenced by the turbulent inlet jet. To obtain a more reliable statistical estimate of the mean would require injecting particles during different time intervals. Increasing the number of particles improves the statistics at later times, (e.g. 10-100s) as indicated by the standard deviation which drops in half. This is because the particles become better dispersed in the liquid pool and random statistics become valid.

**Table 8.1. Details on particle injections for the simulation (*Case 1*).**

| Number of particles | Time of introduction |
|---|---|
| 15000 | 0s – 1.6s |
| 500 | 2s – 2.4s |
| 500 | 4s – 4.4s |
| 500 | 6s – 6.4s |
| 500 | 8s – 8.4s |
| 500 | 10s –10.4s |

**Table 8.2. Comparison of fractions of particles removed by the screen (*Case 1*).**

| Run # | 0-10 seconds | 10-100 seconds |
|---|---|---|
| **LES - 500 PARTICLE GROUPS** | | |
| 1 | 27.2 pct | 23.4 pct |
| 2 | 17.8 pct | 27.2 pct |
| 3 | 26.2 pct | 23.0 pct |
| 4 | 23.8 pct | 23.2 pct |
| 5 | 33.0 pct | 18.2 pct |
| **Average** | **25.6 pct** | **23.0 pct** |
| Standard deviation | 5.5 pct | 2.9 pct |
| **LES - 2500 PARTICLE GROUPS** | | |
| 1 | 27.2 pct | 25.9 pct |
| 2 | 26.8 pct | 27.1 pct |
| 3 | 20.0 pct | 26.5 pct |
| 4 | 23.3 pct | 27.8 pct |
| 5 | 31.8 pct | 24.1 pct |
| 6 | 32.6 pct | 24.9 pct |
| **Average** | **27.0 pct** | **26.1 pct** |
| Standard deviation | 4.8 pct | 1.4 pct |
| **Experiment - Average** | **22.3 pct** | **27.6 pct** |

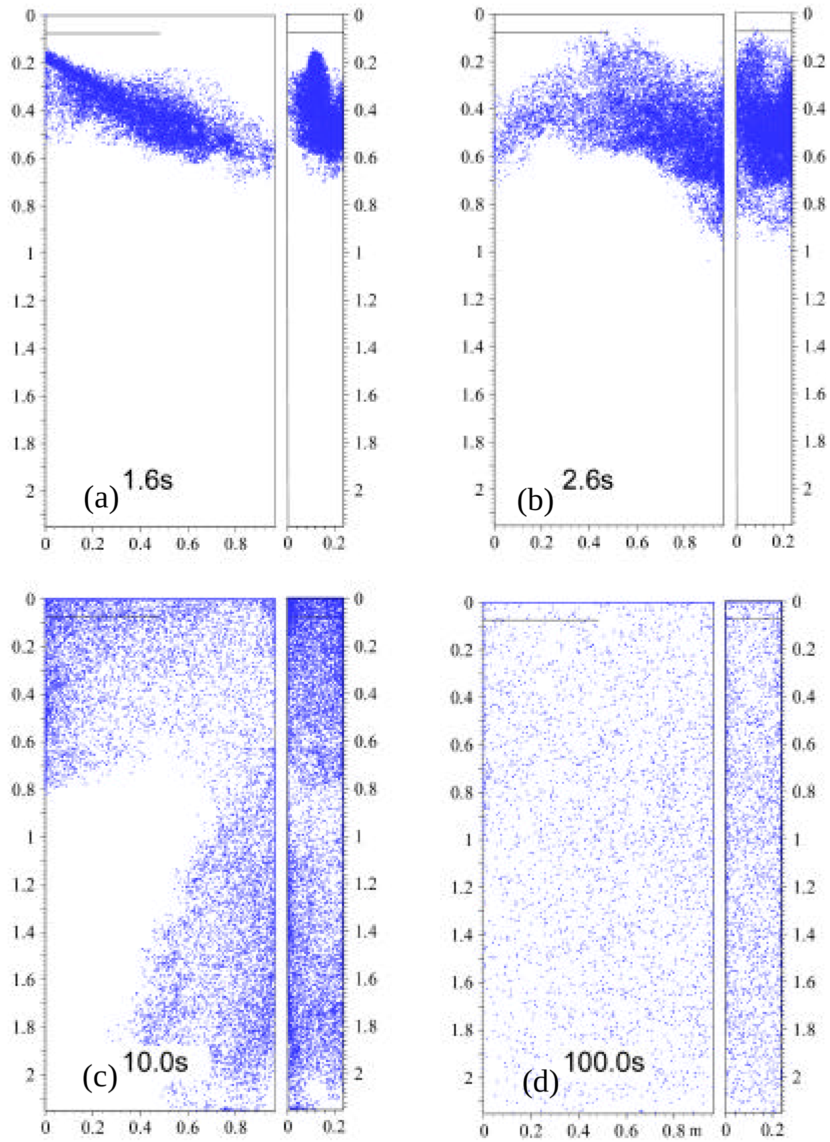


**Figure 8.1. Distribution of the 15,000 particles in *Case 1* at four time instants after their injection, view from wide face (left) and narrow face (right).**

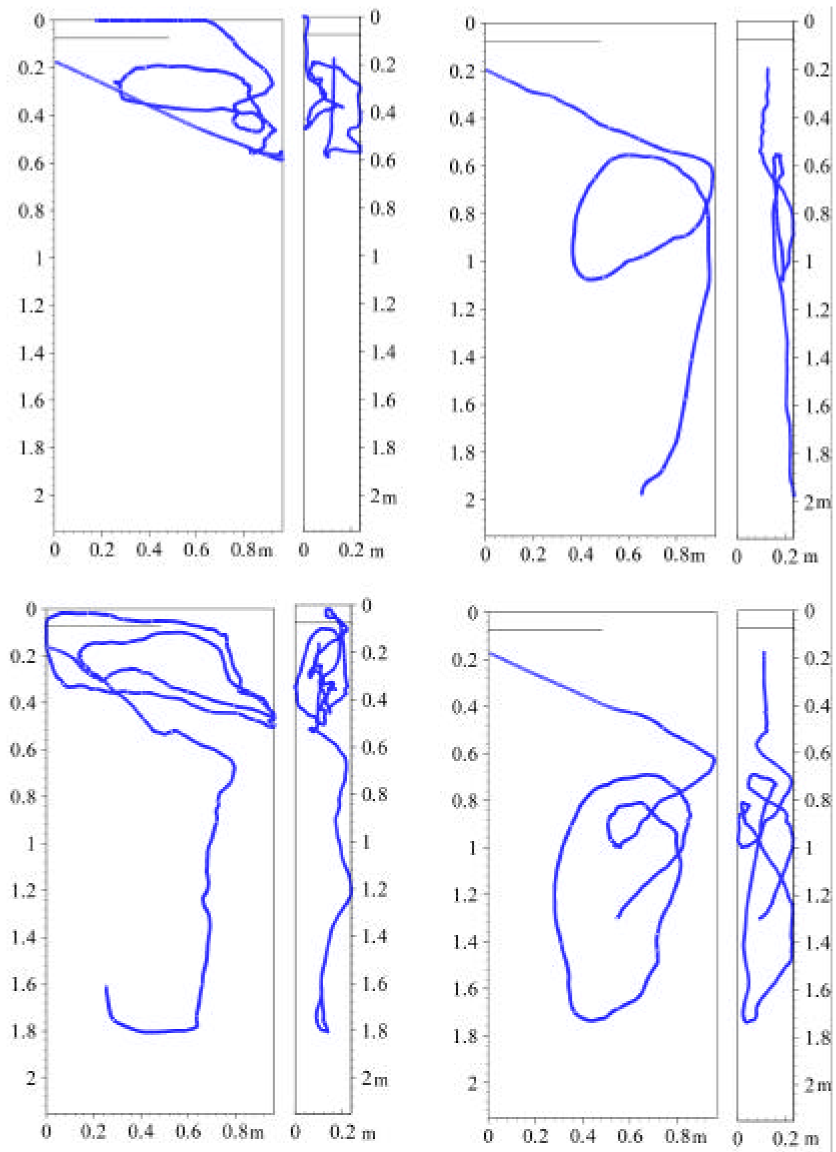


**Figure 8.2. Representative particle trajectories observed in the computation of *Case 1*.**

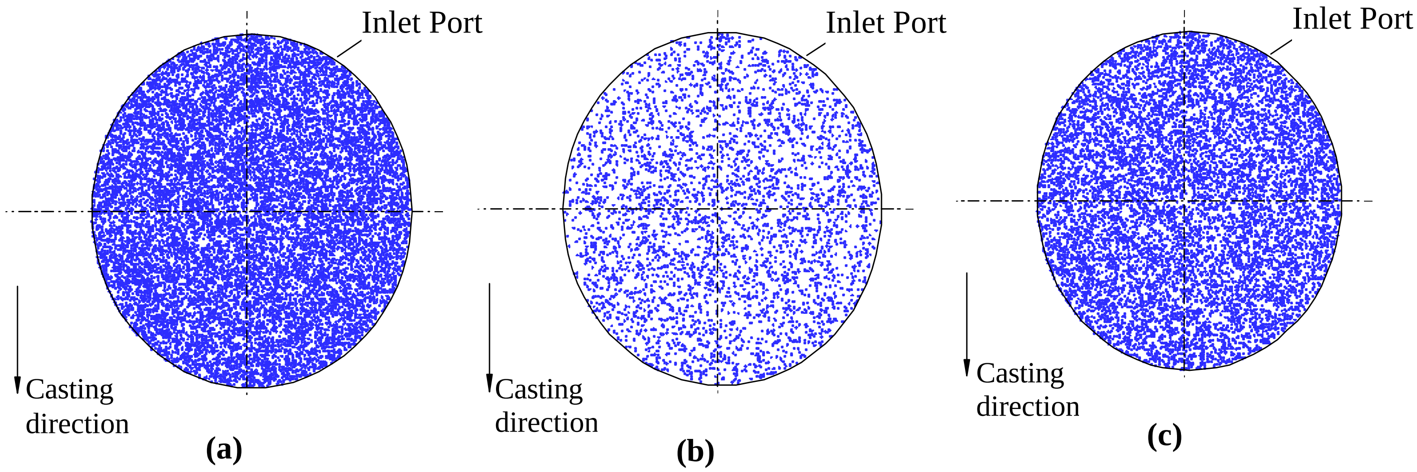


**Figure 8.3. Initial positions at the nozzle port of (a) all 15,000 particles and those removed to the top surface in (b) 0-10 s and (c) 0-100 s after entering the liquid-pool (*Case 1*).**

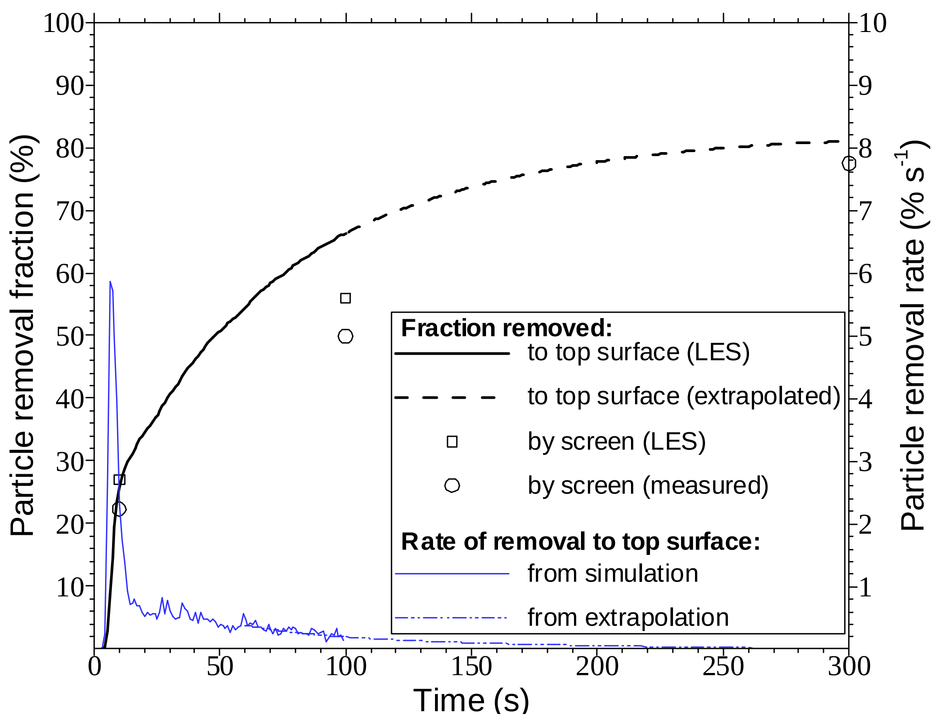


**Figure 8.4. Particle removal to the top surface in the full-scale water model (*Case1*).**

# CHAPTER 9. PARTICLE TRANSPORT IN A THIN-SLAB CASTER

The computational model for particle transport was validated by the experiment in the standard-thickness full-scale water model. It was then applied to investigate the transport and removal or capture of impurity particles in the thin-slab steel caster (*Case 2-S*) described in Part I. [71, 76, 131] The fluid velocities were obtained from an LES presented in CHAPTER 5. The caster operating conditions and material properties were given in Table 5.1.

## 9.1 Computational Details

Computations were conducted to investigate the transport and capture of slag droplets in the thin-slab steel caster depicted in Figure 5.1. The computation included seven groups of 10,000 particles and three groups of 4,000 particles. Among them five groups of 10,000 particles have a density of 2700 kg/m$^3$ and diameters of 10μm, 40μm, 100μm, 250μm and 400μm respectively. Two groups of 10,000 small particles (10μm and 40μm) with a density of 5000 kg/m$^3$ were also included to investigate the effect of particle density on particle transport. These particles could represent alumina clusters with varying amounts of entrained steel filling internal voids and thus raising its density. However, it should be realized that the hydrodynamic forces and capture mechanism for these complex-shape particles are more complicated. In this thesis, all the particles are assumed to be spheres. Each of the seven groups of 10,000 particles was introduced into the mold region from the nozzle ports in 9s. As listed in Table 9.1, the four groups of 10,000 small (10μm and 40μm) particles each were injected together at the nozzle ports at locations randomly chosen from the distribution calculated in a nozzle simulation. After they all left the domain, three groups of larger (100μm, 250μm and 400μm) particles, each consisting of 10,000 particles, were injected into the mold. During the actual continuous casting process, fingers of the liquid slag layer may be emulsified into the liquid steel from the top surface mold slag layer and broken into spheres by the flow. To model this, a computation was conducted where three groups of 4,000 particles with sizes of 100μm, 250μm and 400 μm entered the domain near the center of the top surface, where such emulsification most likely occur. They were injected computationally over 1.8s into two symmetrical 20mm×6mm×7mm(x×y×z) volumes located just below the top surface. The height of the two volumes was chosen based on the steel-slag interface profile presented in Figure 5.21.

Consistent with the flow simulations presented in CHAPTER 5, particle motion in the nozzle and in the mold was simulated separately. The nozzle domain includes a bottom part of the tundish and the entire 1.11m long trifurcated submerged entry nozzle. The mold domain includes the top 2.4m of the liquid pool enclosed by the shell. This 2.4m computational domain is part of the 3m straight section of the caster. The side boundaries of the domain were curved to account for the shell growth, and had mass flowing through them to represent solidification. The shell thickness increases from 0mm at the meniscus to 26mm (wide face) or 25mm (narrow face) at domain exit as shown in Figure 5.2. All of the forces shown in Equation (7.2) were included for the simulation of large particles ($d_p \geq 100\mu m$). Only the drag, buoyancy and lift forces were included for small particles, as the other forces are small. For the integration of particle trajectories, the fluid flow time step was divided into smaller time steps $\Delta t_p$, which were chosen based on the particle velocity response time defined in Equation (7.25).

## 9.2 Particles in the SEN

The simulation in the submerged entry nozzle revealed locations where particles touched an inner wall of the nozzle, shown in Figure 9.1. About 16% of the particles exiting the tundish touched an inner wall of the nozzle and another 10% touched the stopper rod. These inclusions might stick to cause nozzle clogging in a real caster, depending on the properties of the nozzle material and thermodynamic reactions at the interface. Note that most of the inclusions touched the bottom portion of the stopper rod or the nozzle walls just below the stopper rod. This coincides with the location of clogging sometimes observed in practice. [132] Some particles touched the bottom of the SEN near the outlet ports. The distributions of the particles in the jets that exit the nozzle ports are shown in Figure 9.2. This figure reveals that almost no particles exited from the top or bottom portions of the nozzle ports, which are regions of reverse flow entering the nozzle (see CHAPTER 5).

## 9.3 Small Particles in The Mold Region

### 9.3.1 Small Particle Distribution

The computed distributions of the 40,000 small particles (10μm and 40μm) in the mold region are shown as three snapshots in Figure 9.3. The locations where particles were trapped by the solidifying shell front are shown as red dots in the figure. An animation for the particle motion is available at http://ccc.me.uiuc.edu. The computed particle motion is similar to that in the standard-thickness slab water model (*Case 1*) presented in the last chapter. Particles move with the jet and reach the narrow face about 0.6 seconds (33.6s total flow simulation time) after first injection (33.0s). The 40,000 small particles split into two groups about 2 seconds after injection (33.0s) and enter the upper and lower rolls. After 15s, the particles in the upper rolls become well dispersed and the fastest have penetrated deep into the lower recirculation zone. Although the particles were symmetrically introduced from the nozzle port and had a relatively symmetrical distribution for approximately 10 seconds, a noticeable asymmetry is seen in the last frame. This is caused directly by the flow asymmetry observed and reported in Figure 5.22. Specifically, the fluid had a larger downward velocity near the right-hand narrow face from 36-40s, which the particles followed. It was also shown in Figure 5.22 that this transient asymmetry was not directly caused by the inflow asymmetries from nozzle, but originated from dynamic flow instabilities. Similar asymmetries have also been observed in water model experiments. [16, 22] The asymmetries were more severe when the bottom wall of the water model was deeper. [16] This suggests that intermittent inclusion asymmetries of the magnitude reported here may not be avoided by simply changing the nozzle design. Because the fluid velocities fluctuate greatly with time (Figure 5.22), particles injected at other times would show a different distribution. Knowledge of such behavior is important, as particles which are transported deeper are more likely to become permanently entrapped in the steel.

### 9.3.2 Small Particle Trajectories

Figure 9.4 shows five representative trajectories for the small particles which floated for 220 seconds in the strand or contacted a boundary. The first trajectory (labeled 1) shows a particle which exited the left nozzle port, recirculated around the upper roll and eventually touched the top surface and thereby were removed. The second trajectory shows a particle entering the mold from the center port, being drawn upward into the left side, recirculating and finally touching the top surface. Two trajectories (3 and 4) show particles flowing out from the domain bottom, after wandering between the upper and lower rolls or moving directly with the flow down the narrow faces into the lower region. These particles would most likely be entrapped in the final product. The last trajectory (5) shows a particle that became trapped at the wide face approximately 0.8m below the top surface. These irregular trajectories are similar to those observed in the water model (*Case 1*). They confirm the effect of turbulent flow structures on particle transport in actual steel casters.

### 9.3.3 Removal and Capture Fractions for Small Particles

The removal and capture history in the strand for the four groups of 10μm and 40μm particles are compared in Figure 9.5 and Table 9.2. Particles exiting the nozzle ports could touch the outer nozzle walls, reach the top surface of the liquid pool to be removed, become captured by the shell by touching the solidification front (sides) or exit the domain from the bottom. Particles floated deeper through the domain bottom were assumed to be trapped at a deeper position. All the small particles in Figure 9.5 have approximately the same capture and removal histories. Thus, the statistics in Table 9.2 are independent of particle size and density. This is expected because the small buoyancy force relative to drag for these small particles (≤40μm), as indicated in Equation (7.24) produces small terminal velocities (≤0.65mm/s) relative to the fluid.

Approximately 8% of the particles that exited the nozzle ports were removed by the top surface. A further 8% of the particles touched the outside of the nozzle wall while recirculating in the mold region and might be removed, depending on the inclusion composition and nozzle properties. Most (90%) of these particles reached the surface within ~50s (Figure 9.5). Most (90%) of the captured particles flowed for less than ~70s. The final statistics (Table 9.2) were compiled after all the particles exiting the nozzle ports were either removed or captured, which took approximately 220 seconds. Approximately 51% of the particles were captured by the shell in the upper 2.4m of the strand where the shell thickness was less than 25mm (narrow face) or 26mm (wide face). Around 32% of the particles exited the domain from the bottom and would be captured at a deeper (and more interior) position in the solid slab. These results suggest that most (84%) of the small inclusions which enter the mold become entrapped in the final product. Thus, nozzle design and mold operation should focus on controlling flow at the meniscus to avoid the entrainment of new inclusions rather than altering the flow pattern to encourage removal of inclusions entering the mold. This conclusion may differ for large inclusions or if gas bubbles were present.

### 9.3.4 Capture of Small Particles in Solid Steel Slabs after a Sudden Burst

A sudden "burst" of inclusions entering the liquid pool may occur in the continuous casting process caused by upstream events such as vortex entrainment of slag during a tundish level drop, release of a nozzle clog or other disturbance. [3, 133] Knowledge of the inclusion distribution in cast steel slabs caused by such a burst is important for the subsequent inspection and dispositioning of the product. The particle study in *Case 2-S* can be considered as a 9s burst of 40,000 small particles and 30,000 large particles entering the mold region. By relating the total time traveled by each particle with the casting speed and its capture position, the distance of each of the 51% of the captured particles down the final solidified slab was calculated. The final positions of these particles are shown in Figure 9.6, as transverse projections onto the wide and narrow faces. Zero on the vertical axis indicates the slice of the shell which was at the meniscus at the time when the first particle entered the strand (33.0s). All slices continuously moved downward with the whole shell at the casting speed during the process. The shadowed length in Figure 9.6 is the distance traveled by the strand during the 9s burst. Note that the left boundary of the wide face in this front view figure corresponds to the right boundary in Figure 9.3, and vice versa. The simulation shows that the 220 seconds needed for all 51% particles to be captured corresponds to a length of around 7m. Most (78.5%) of those particles were captured within 1m above and below the zero-slice. Only a slight asymmetry of the capture positions can be observed from both view angles. This indicates that the flow asymmetries discussed earlier are not significant relative to particle capture. The significant asymmetries in defects sometimes observed in practice [10] must have been caused by much larger flow asymmetries resulting from transient events such as a slide gate opening change, or asymmetrical release of a nozzle clog or gas accumulation. Such events were not considered in this study, but are investigated elsewhere. [39]

### 9.3.5 Total Oxygen Distribution in Thin Steel Slabs

Total oxygen is often measured to evaluate the content of oxidized inclusions such as alumina in steel slabs. [1] It can also be calculated based on the computed positions and times of capture of small particles, which comprise most of the inclusion mass. [1] The distribution of particles captured under a condition of continuous injection is found from the results in the previous section by assuming the 9s burst of particles to repeat every 9 seconds. The molten steel was assumed to exit the nozzle with a steady oxygen content of 10ppm (by mass), from pure alumina ($Al_2O_3$) inclusions. The oxygen distribution in a typical cross section through the solidified slab was obtained by first projecting the entire computational domain onto a transverse x-y section to define a 2-D grid of 3-D cells. The cell transverse dimensions, $\Delta x$ and $\Delta y$, vary from 0.5mm to 6mm according to distance beneath the strand surface. The cell vertical dimension, $\Delta z$, is the length cast, 228.6mm, during the 9s burst. The total oxygen concentration in each cell, $C_O$, was calculated by dividing the mass of oxygen in all particles entrapped in that cell by the cell mass (including both cast steel and particles):

$$C_o = \frac{(48/102)\ M_p}{r\left(\Delta x?\, y?\, z\right) + (1 - r\,/\,r_p)M_p} \tag{9.1}$$

where $M_p = \sum_{i=1}^{N_C} \frac{p\, d_p^3\, r_p}{6}$ and $N_c$ are the total mass and number of particles entrapped in the cell. The central region representing the area of the liquid pool at the domain exit was treated as a single large cell. This cell would contain all of the inclusions that exited the domain.

The number of particles entrapped in each cell, $N_C$, was obtained by summing the contributions from a series of 9s bursts. Each burst represents the contribution from a different time interval. The entrapment locations for each burst are obtained by translating the results in Figure 9.6 vertically by $\Delta z$*i. The burst number i is an integer with a minimum value from the z coordinate of the last particle captured (-5.2m from Fig. 13) divided by $\Delta z$. The maximum i value is the domain bottom coordinate (+1.9m) divided by $\Delta z$. The final particle distribution is obtained from the sum of the entrapment distributions from each value of i within this range.

The results are given in the cross section of the steel strand shown in Figure 9.7. The dashed line represents the boundaries of the central large cell and is the solidification front at the domain exit (2.4m below meniscus). The highest total oxygen content (about 170ppm) is predicted near the corners, closely followed by intermittent patches on the narrow faces. Intermittent patches with high oxygen concentrations (50-150ppm) are also found in the middle region of the strand (approximately 10-20mm beneath the slab surface). These results indicate that most of the captured particles (69%) are entrapped within the shell approximately 0.4-1.5m below meniscus (corresponding to a shell thickness of 10-20mm). The finding of increased inclusion capture across the slab width towards the narrow faces agrees with previous measurements [69] and calculations. [84] Other measurements find sliver defects concentrated at the surface more towards the wide face centerlines. This is only a slight trend here, owing to impingement from the bottom central port. More severe centerline concentrations would have been predicted if some of the inclusions hitting the top surface were able to continue moving with the flow towards the SEN before being captured in the steel shell at the meniscus. Alternatively, the larger particles which contribute the most to sliver defects have more complex capture criteria as discussed in CHAPTER 7 and simulated in section 9.4.

Figure 9.8 reveals the oxygen content along the two centerlines shown in Figure 9.7. Higher inclusion concentrations are found towards the surfaces. Similar variations in total oxygen distribution have been measured in other steel slabs, in which particles were found to concentrate most within 20mm of the slab surface. [134] Small regions with high oxygen content are also distributed sparsely towards the center of the wide faces. This is caused by groups of particles from the center nozzle port. Small patches with low total oxygen close to zero are randomly distributed in the cross section, indicating the effects of turbulent motion of the fluid. Asymmetries can be observed in this symmetrical domain, confirming the influence of fluid instabilities on particle transport and capture. No significant difference is observed between the inside and outside radius, which is consistent with the lack of buoyancy of the small particles considered in this work. In practice, large inclusions are generally of more relevance to quality problems, so future work will focus on developing a capture model for large particles.

## 9.4 Large Particles from Nozzle Ports

### 9.4.1 Large Particle Distribution

Three groups of 10,000 large particles with diameters of 100μm, 250μm and 400μm were introduced into the computational domain ~230s later than the smaller ones. Snapshots of the simulated particle distributions are shown in Figures 9.9 and 9.10. The first two snapshots in Figure 9.9 are seen to be similar to those for small particles presented in Figure 9.4. However, more significant asymmetrical distributions are seen in the next two snapshots corresponding 18s and 45s after the injection of the first particle. This asymmetry is expected due to a more unbalanced flow between the two halves in the lower region (Figure 5.23) at the corresponding times. It was seen that larger downward flow velocities persisted in the left half of Figure 5.23 ($x<0$, which corresponds to the right half in Figures 9.9 and 9.10) for more than 50s before the flow became balanced for some time then, a similar unbalanced flow pattern occurred again after another 70s. The strong asymmetrical flow deep in the lower recirculation region, which was also observed by Gupta and Lahari [16] in water model studies, was the cause for more particles being transported deeper through the domain exit, as shown in both Figures 9.9 and 9.10. A comparison of the last two snapshots in Figures 9.9 and 9.10 indicates that more large (400μm) particles were transported to the upper recirculation region and floated to the top surface than small ones (100μm). This is due to the larger terminal velocities for the larger particles: the terminal velocities for the 100μm, 250μm and 400μm slag spheres in liquid steel were found to be 3.9mm/s, 17.9mm/s and 33.5mm/s respectively, by equating the drag and buoyancy terms given in Equation (7.24). As the velocity profile for the flow in the deep region becomes nearly uniform with a value approximately equal to the casting speed, particles with terminal velocities less than the casting will most likely be captured in some interior location once they are transported deeper through the domain exit. Therefore, the 100μm and 250μm particles which exited the domain from the bottom exit should be eventually captured in slab interior. However, the 400μm particles still have a small chance to float back into the domain and eventually escape to the top surface. This was not modeled in the simulation and believed to be a minor effect.

### 9.4.2 Capture of Large Particles in Steel Slabs after a 9s of Sudden Burst

Following the same procedure as described in section 9.3.4, the final distribution of the large particles captured in the steel slab was obtained and is presented in Figures 9.11-9.13 for the 100μm, 250μm and 400μm particles respectively. Note that in these figures, the left narrow face boundary in the wide-face and top views correspond to the right boundary in Figures 9.9 and 9.10, and vice versa. Zero on the z axis again represents the meniscus location at the time when the first particle entered the mold. The shadowed length denotes the strand translating distance during the 9s of particle injection. The wide face, narrow face and top view plots reveal three projections of the distribution of the particles captured by the shell when it was in the 2.4m domain, which corresponds to a shell thickness of 25mm and 26mm at the domain exit for the narrow face and wide face respectively (Figure 5.2). The number of captured particles decreases as the particle size increases due to two main reasons. First, the terminal velocity increases with particle size, which encourages larger particles to float towards the top surface after entering the domain with the jet and thereafter increases the particle removal fraction. In addition, small particles (e.g. 50 μm) have more chances of being captured by the shell especially if they are smaller than the PDAS, which varies from 45μm to 250μm for this caster (Figure D.3). The last plot of Figures 9.11-9.13 reveal the locations where particles left from the domain outlet 2.4m below the top surface. The outlet is shown enclosed by the dashed lines representing the mushy zone front. The plots clearly reveal more particles left the domain from the left half, due to the asymmetrical flow. These particles will likely further cause asymmetrically-distributed inclusion-defects in the steel slabs. Such asymmetry in defects between left and right has been observed in commercial cast product. [68]

### 9.4.3 Removal and Capture Fractions for Large Particles

Figure 9.14 shows the removal and capture histories for the 100μm-400μm particles, which were computationally introduced into the mold domain from the nozzle ports in 9s. The first plot shows that most (~90%) of the removal occurred in the first

~50s after the first particle entered the domain. Most (90%) of the captured particles traveled with the flow for less than ~70s. The final particle removal and capture fractions are also given in Table 9.3, showing final removal fractions of 12.6%, 42.5% and 69.9% for the 100μm, 250μm and 400μm particles respectively. These results are consistent with plant observations that particles with sizes ranging from 50μm and 200μm were found the be the main cause for inclusion defects in steel slab. The results suggest that larger particles can be effectively removed from the mold region. Alternatively, the less-buoyant smaller particles always experience small removal fractions. They cause less quality problems owing to their smaller size. Intermediate-sized particles of 100μm and 250μm are large enough to cause severe quality problems and are predicted to have high capture rates. Thus, it is important that they are removed from the steel prior to entering the mold.

## 9.5 Large Particles Injected near The Top Surface

Three groups of 4,000 particles with diameters of 100μm, 250μm and 400μm were introduced into the mold region near the top surface. Figure 9.15 presents four snapshots of the distribution of the 00μm particles. Again, the blue dots denotes the moving particles and red represents the removed or captured ones. It is seen in plot (a) that immediately after the injection, some of the particles floated to the top surface and were consequently removed. The other particles followed the flow in the upper recirculation region (plot (b)), joined the oblique jet (plot (c)) and then behaved as if they were injected from the nozzle ports. Figure 9.16 gives the removal and capture histories for these “top surface particles”. It is seen that more than 95% of the 400μm particles were safely removed in the first 2s after being entrained into the flow from the top surface slag layer. Thus, for both the 250 μm and 400μm particles, the final removal fractions exceeded 92%. However, the removal fraction dropped to 44.6% for the 100μm less buoyant particles. After the particles joined the jet (~5s as shown in Figure 9.15(c)), the capture history for these top surface particles becomes similar to that for particles injected from the nozzle ports. The final removal and capture fractions are give in Table 9.4.

## 9.6 Hydrodynamic Forces Acting on Particles

The importance of the hydrodynamic forces acting on the particles are examined in Figure 9.17. The computed magnitudes of the instantaneous values of the drag, the buoyancy, the lift, the pressure gradient and stress gradient, the added mass and the Basset forces are compared. Three representative particles with diameters of 100μm, 250μm and 400μm are shown. The results reveal that the drag and the buoyancy forces are always the most significant forces. Note that these two forces, which act in opposite, usually almost balance. The pressure gradient and stress gradient force, the added mass force and the Basset history force have approximately the same magnitude. Usually, their magnitudes are less than 15 percent of that of the buoyancy force. This suggests that the three forces could be neglected for engineering calculations. The lift force is seen not to exceed 2-3 percent of the buoyancy so is the least important force.

## 9.7 Summary

(1) Complex particle trajectories are seen in both the water model (*Case 1*) and the thin-slab steel caster, showing the important influence of turbulence on particle transport.

(2) Significant asymmetric particle distributions are observed in the mold region, which are caused by transients of fluid turbulence, rather than imposed by the inlet condition at nozzle ports. This only leads to slight asymmetries in the particle distribution in a depth of about 25mm from the slab surface. However, more severe asymmetrical inclusion defects may be found in the interior region.

(3) The top surface is predicted to remove only 8% of small particles (10μm and 40μm) in the thin slab steel caster. An equal fraction touches the outside of the nozzle walls in the mold. These removal fractions are independent of both particle size and density, owing to the inability of the small, low-buoyancy particles simulated here to deviate significantly from the surrounding fluid flow.

(4) The removal fractions are predicted to be 12.6%, 42.4% and 69.8% for the large particles with diameters of 100μm, 250μm and 400μm respectively, which entered the mold from the nozzle ports. Most of the removal occurs in the first 50s after particles enter the mold region. The results suggest that the removal of large particles (e.g. 400μm) may be influenced by flow conditions in the mold.

(5) The computation shows that after a 9s sudden burst of particles with diameters from 10μm-400μm enters the steel caster, about 3-4 minutes are needed for all of them to be captured or removed for the casting conditions assumed here. The captured particles concentrate mainly within a 2-m long section of slab.

(6) With a steady oxygen content of 10ppm from inclusions in the molten steel supplied from the nozzle ports, intermittent patches of high oxygen content (50-150ppm) are found concentrated within 10-20mm beneath the slab surface, especially near the corner, and towards the narrow faces. The interior averages 6.1ppm.

(7) The removal of slag particles entrained from the top surface is found to be highly dependent on the particle size. Most (>92%) of the 250μm and 400μm droplets simply return to the slag layer. However, more than half of the 100μm particles are eventually captured, leading to sliver defects.

(8) The drag and buoyancy forces are found to be the most significant hydrodynamic forces acting on the slag spheres. The pressure gradient and stress gradient, added mass and Basset forces are found to be about the same magnitude and to be less than 15% of the buoyancy force for most of the time. The lift force is at most 2-3 percent of the buoyancy force.

**Table 9.1 Particle groups simulated.**

| Particle Diameter($\mu$m) | Particle Density (kg/$m^3$) | Starting Time for Injection (s) | Number of Particles |
|---|---|---|---|
| 10 | 2700 | 33.0 | 10,000 |
| 10 | 5000 | 33.0 | 10,000 |
| 40 | 2700 | 33.0 | 10,000 |
| 40 | 5000 | 33.0 | 10,000 |
| 100 | 2700 | 260 | 10,000 |
| 250 | 2700 | 260 | 10,000 |
| 400 | 2700 | 260 | 10,000 |
| 100 | 2700 | 269 | 4,000 |
| 250 | 2700 | 269 | 4,000 |
| 400 | 2700 | 269 | 4,000 |

**Table 9.2. Final capture and removal fractions for small particles.**

| Details of particles | Group 1 | Group 2 | Group 3 | Group 4 | Average |
|---|---|---|---|---|---|
| Diameter ($\mu$m) | 40 | 40 | 10 | 10 | - |
| Density (kg/$m^3$) | 5000 | 2700 | 5000 | 2700 | - |
| Fraction captured by shell | 51.58 pct | 51.51 pct | 50.79 pct | 51.00 pct | 51.22 pct |
| Fraction transported deeper | 32.22 pct | 32.07 pct | 32.77 pct | 32.54 pct | 32.40 pct |
| Fraction removed by top surface | 8.03 pct | 8.49 pct | 8.23 pct | 8.20 pct | 8.24 pct |
| Fraction removed by nozzle wall | 8.12 pct | 7.83 pct | 8.03 pct | 8.15 pct | 8.03 pct |

**Table 9.3. Final capture and removal fractions for large particles from nozzle ports.**

| Diameter ($\mu$m) | 100 | 250 | 400 |
|---|---|---|---|
| Fraction captured by shell | 39.01pct | 24.30 pct | 11.29pct |
| Fraction transported deeper | 43.90 pct | 26.90 pct | 16.24 pct |
| Fraction removed by top surface | 12.58 pct | 42.5 pct | 69.89 pct |
| Fraction of floating particles | 4.51 pct | 6.30 pct | 2.58 pct |

**Table 9.4. Final capture and removal fractions for large particles from top surface.**

| Diameter ($\mu$m) | 100 | 250 | 400 |
|---|---|---|---|
| Fraction captured by shell | 24.93 pct | 4.03 pct | 0.40 pct |
| Fraction transported deeper | 27.48 pct | 2.58 pct | 0.43 pct |
| Fraction removed by top surface | 44.60 pct | 92.58 pct | 99.05 pct |
| Fraction of floating particles | 2.99 pct | 0.81 pct | 0.12 pct |

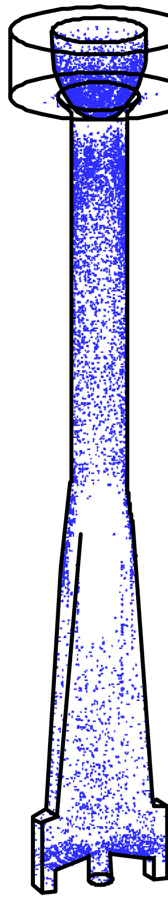

**Figure 9.1. Inclusion entrapment positions in nozzle inner wall.**

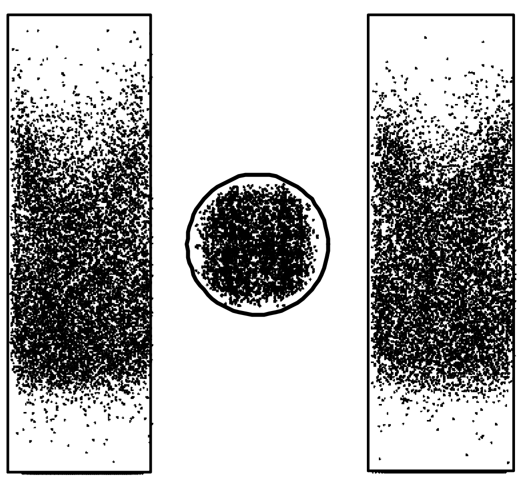

**Figure 9.2. Locations where inclusions exit nozzle ports.**

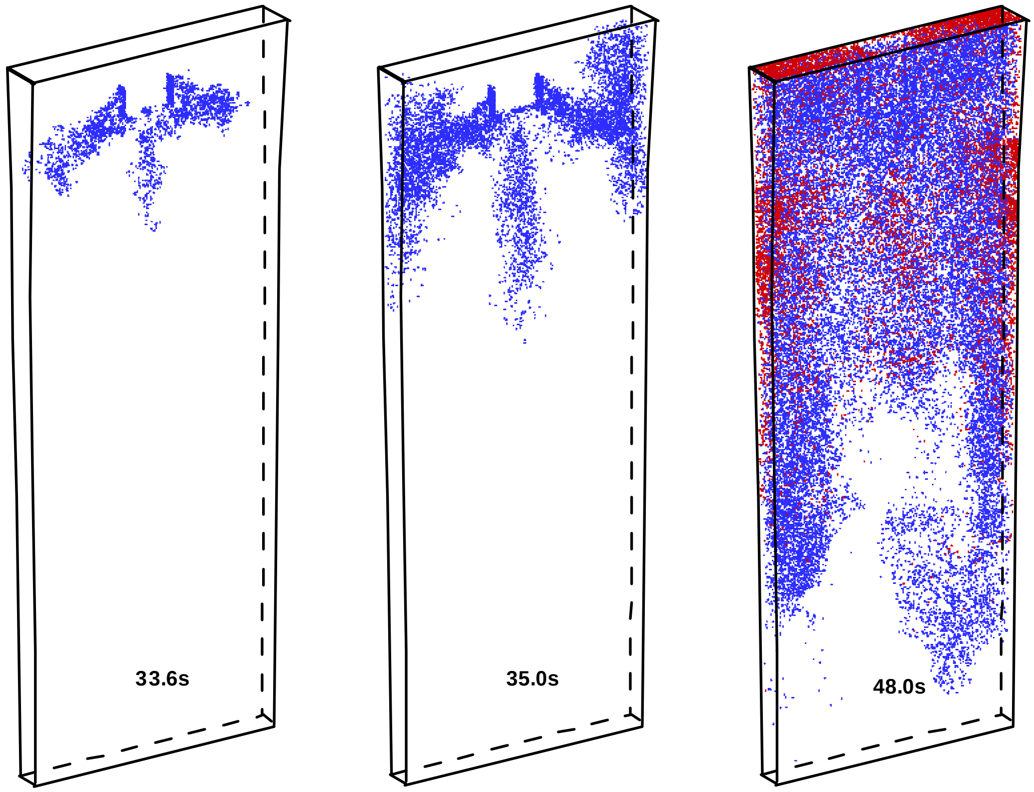


**Figure 9.3. Distribution of particles £40mm at three instants.**

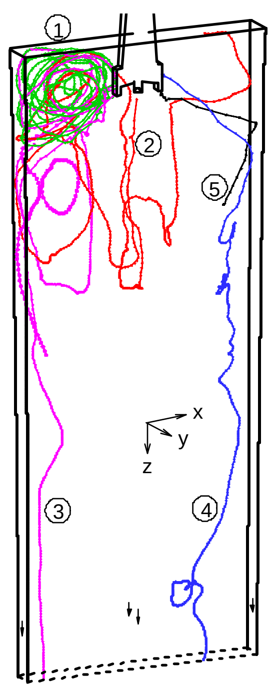


**Figure 9.4. Predicted representative particle trajectories.**

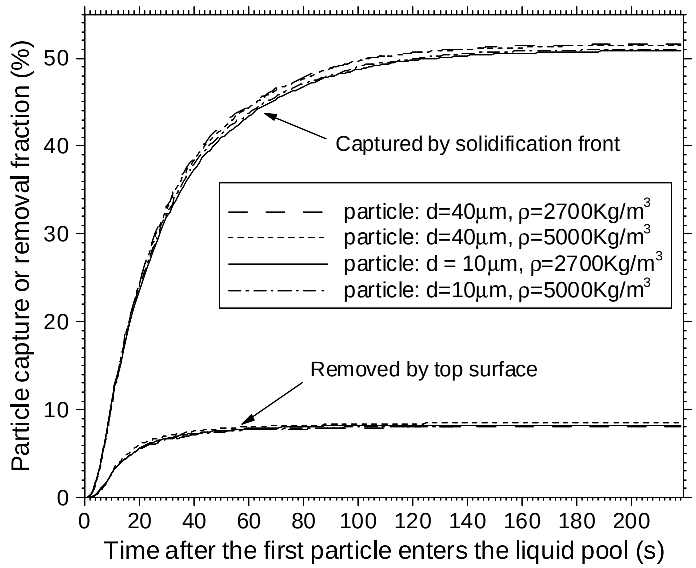


**Figure 9.5. Removal and entrapment histories of particles £40mm.**

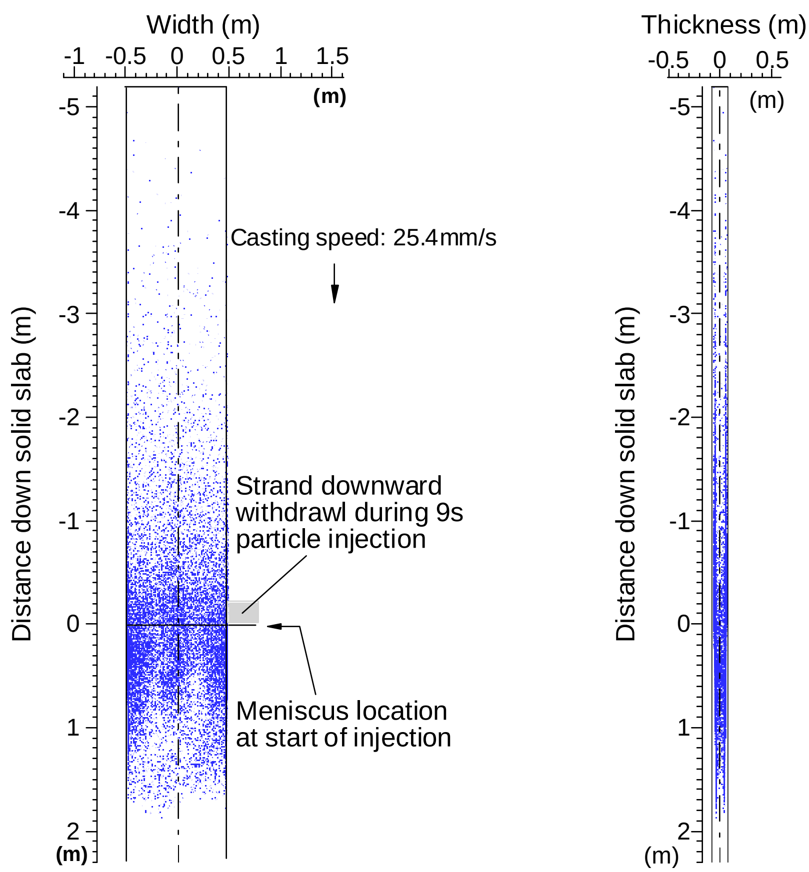


**Figure 9.6. Locations of captured particles for 9s injection of 40,000 particles (£40mm): view from wide face (left) and from narrow face (right).**

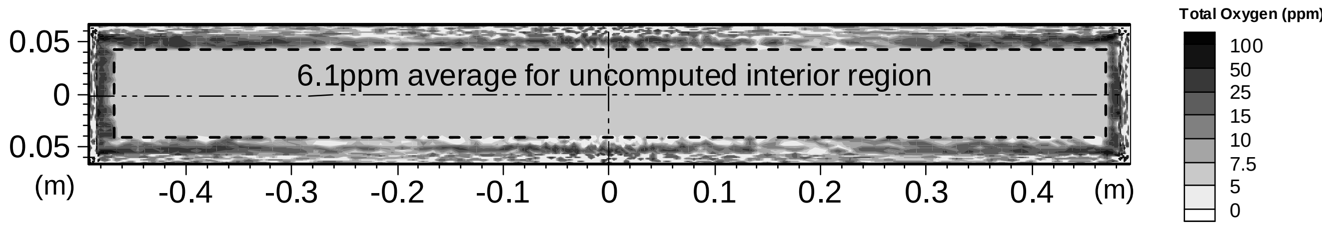


**Figure 9.7. Predicted oxygen concentration averaged in the length direction (10ppm oxygen at nozzle ports).**

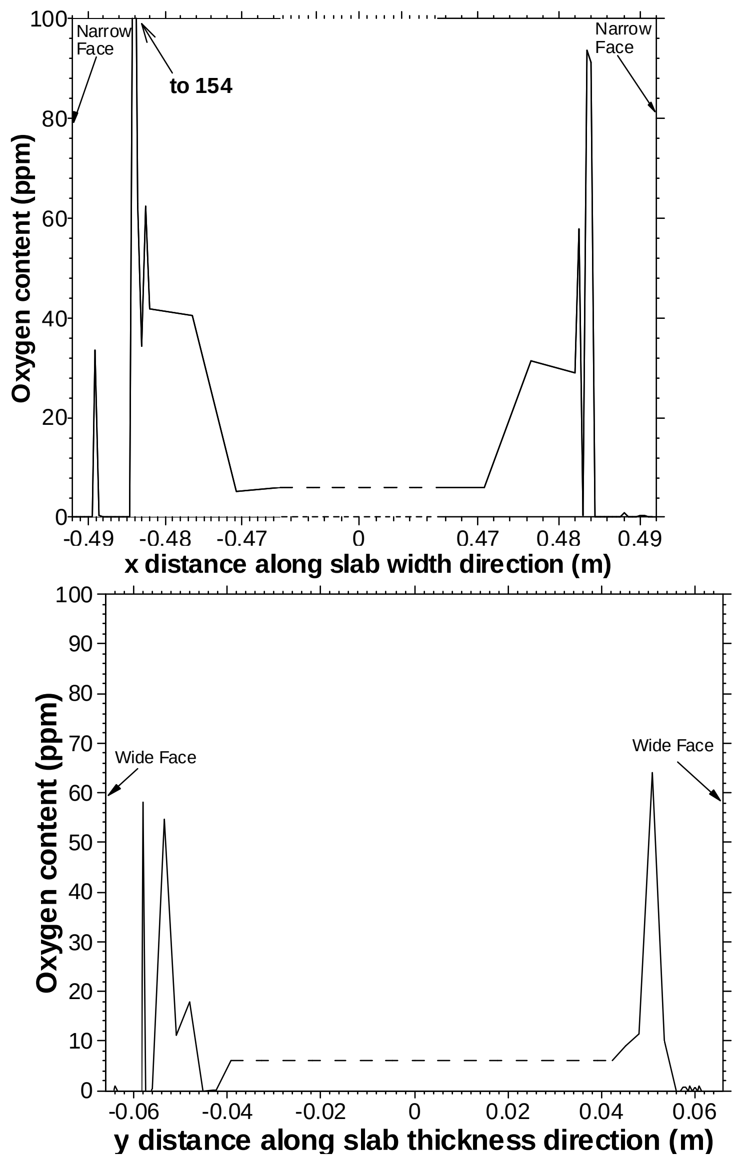


**Figure 9.8. Oxygen content along the centerlines in Figure 9.7.**

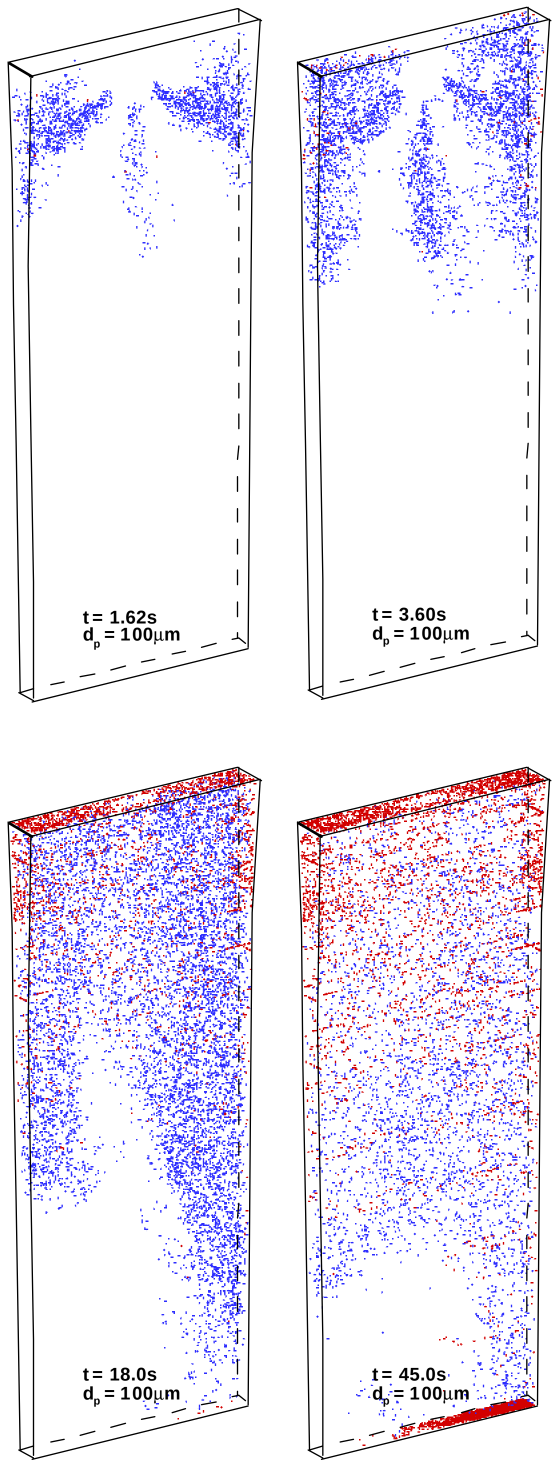


**Figure 9.9. Distributions of 100mm slag particles at four time instants.**

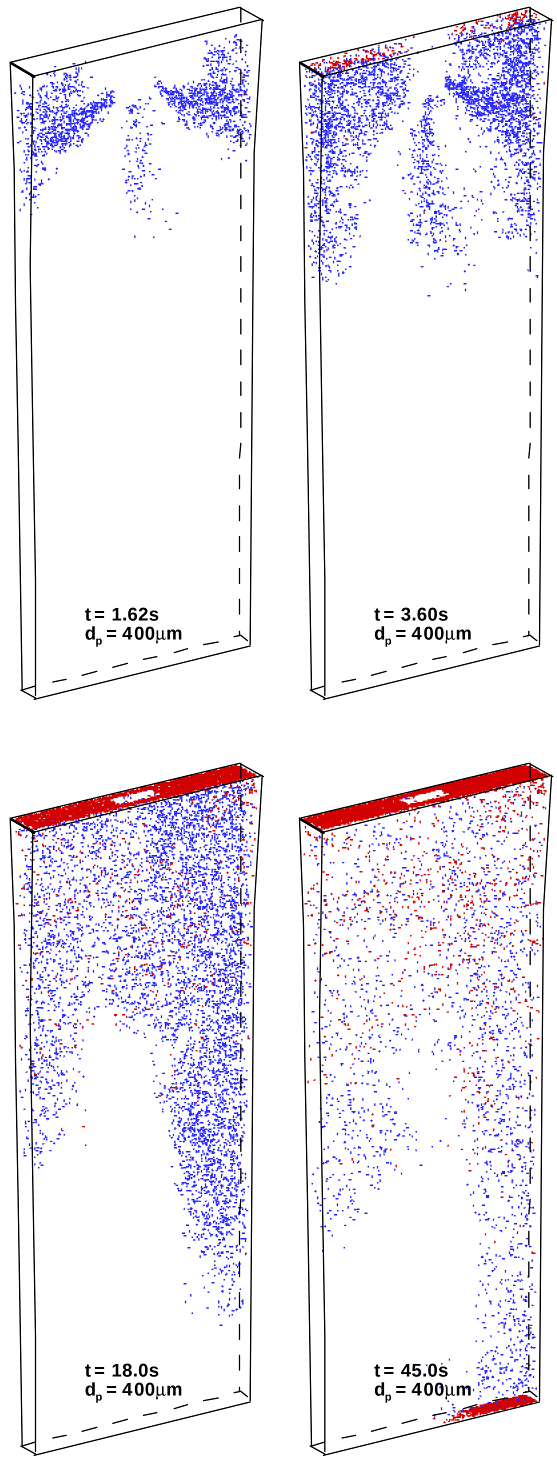


**Figure 9.10. Distributions of 400mm slag particles at four time instants.**

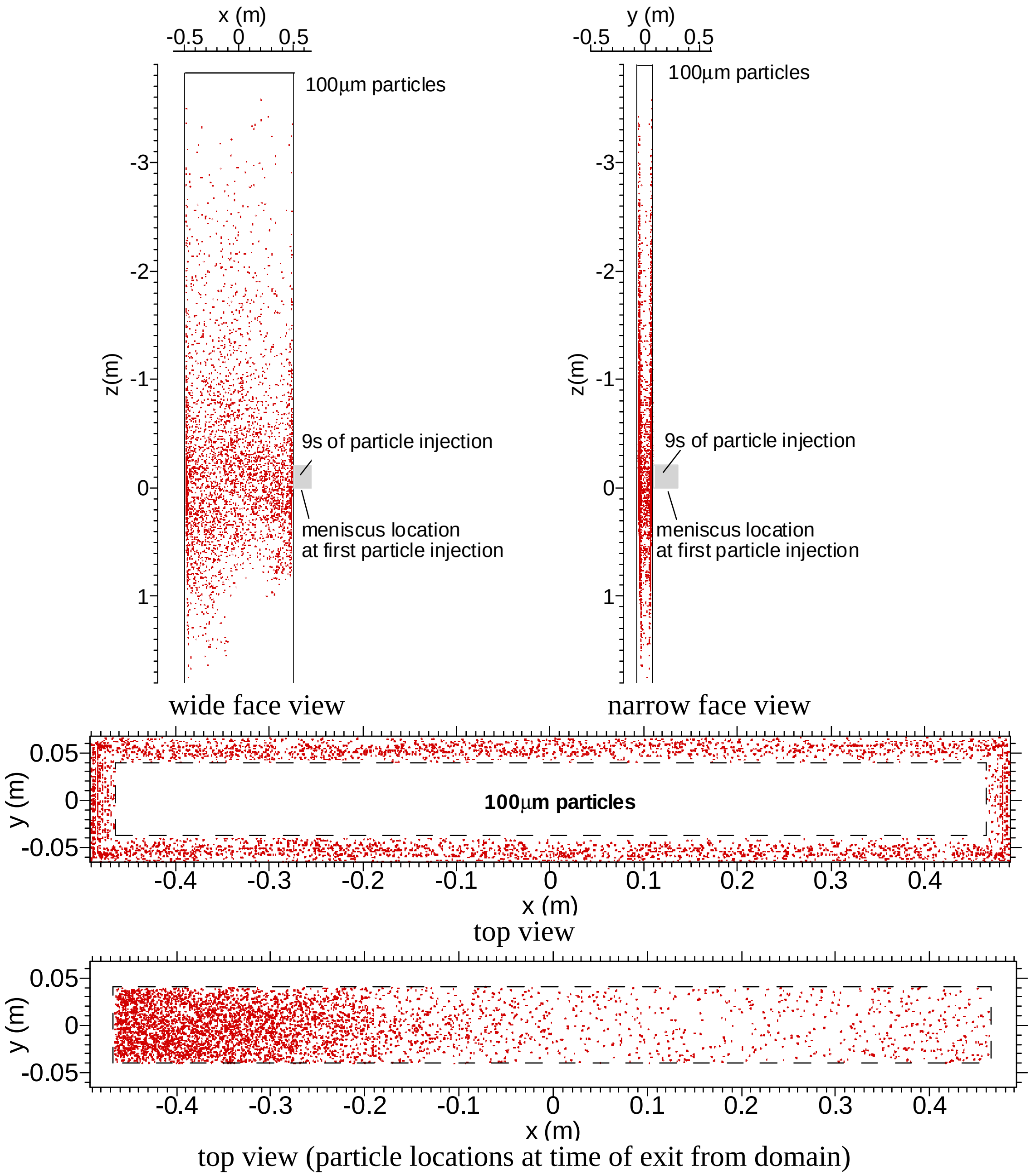


**Figure 9.11. Locations of captured particles after 9s injection of 10,000 particles with diameters of 100mm.**

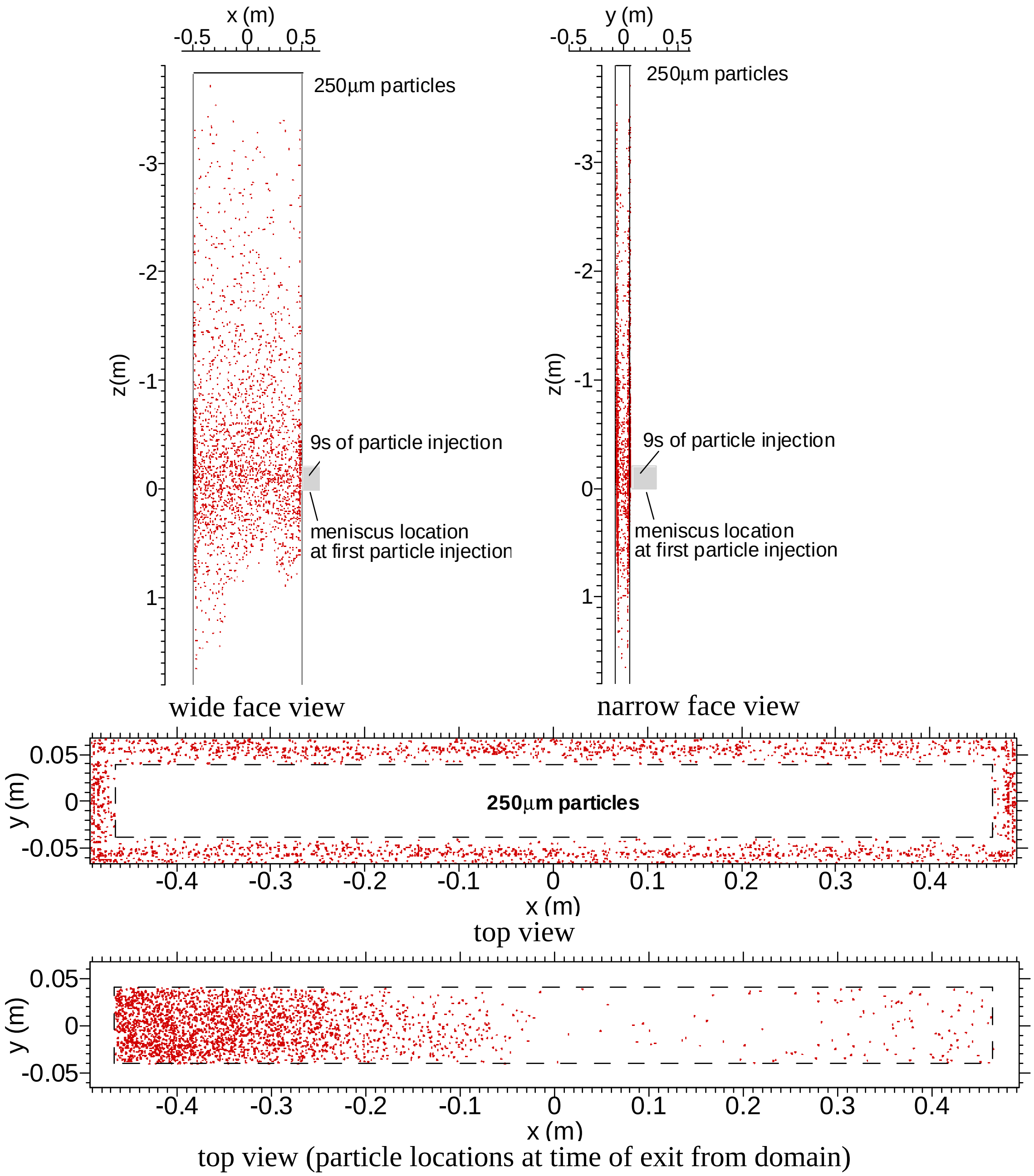


**Figure 9.12. Locations of captured particles after 9s injection of 10,000 particles with diameters of 250mm.**

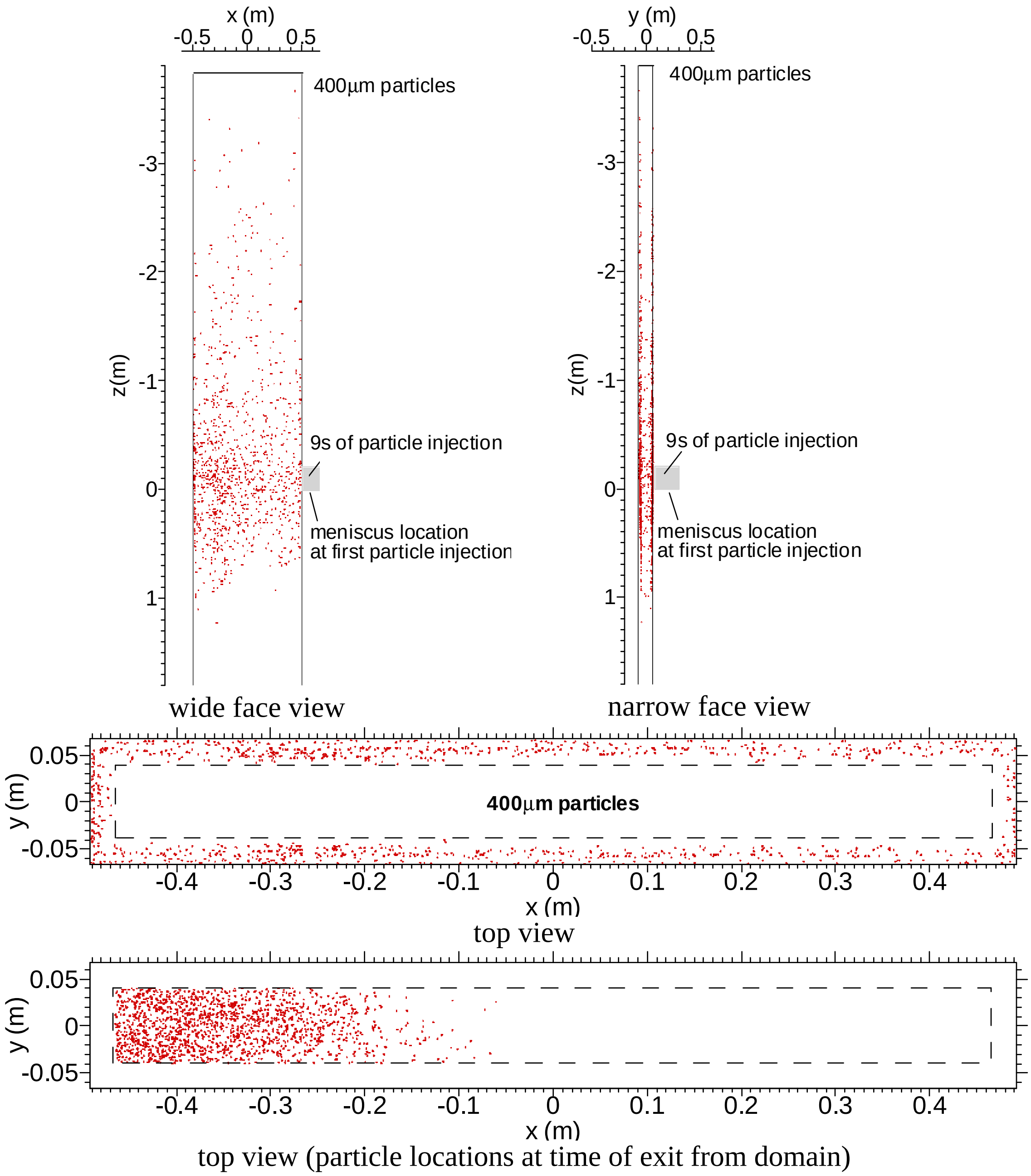


**Figure 9.13. Projections of 400μm particles captured between slab surface and 25mm below and a more interior region (enclosed by dashed lines).**

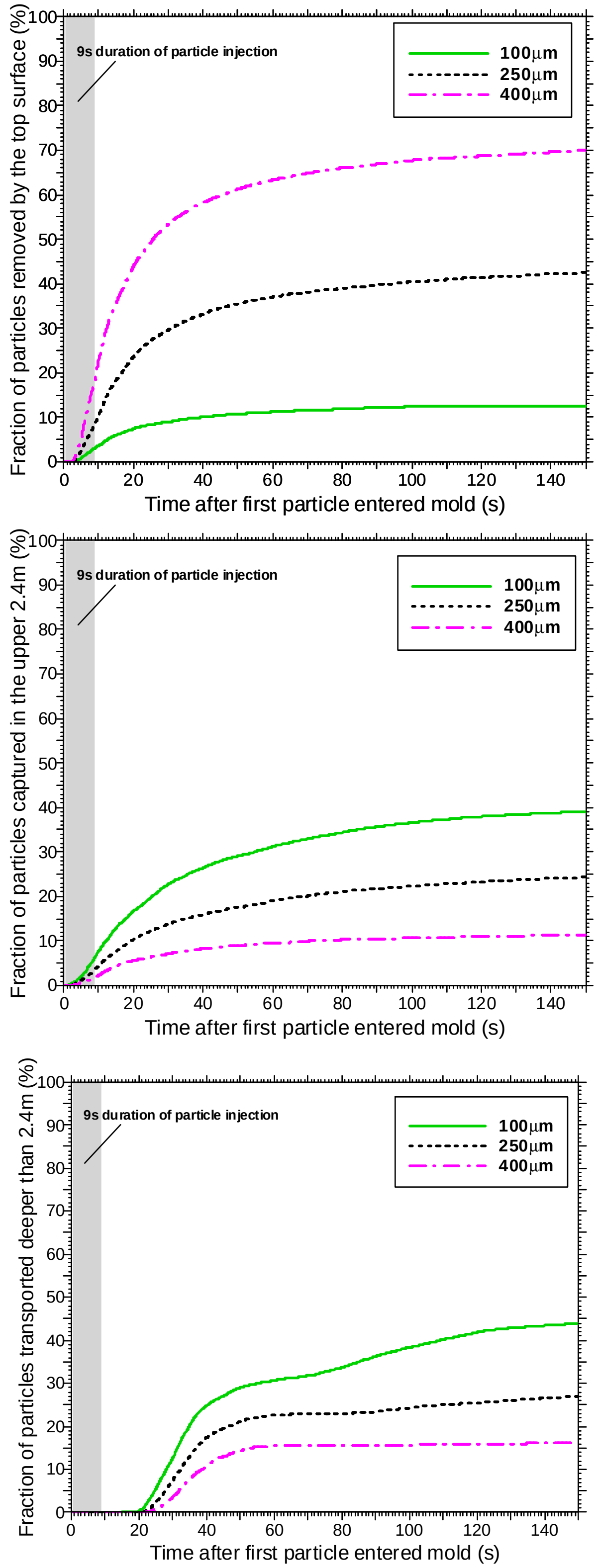


**Figure 9.14. Removal and entrapment histories of large particles (≥100μm) which entered the mold region from nozzle ports.**

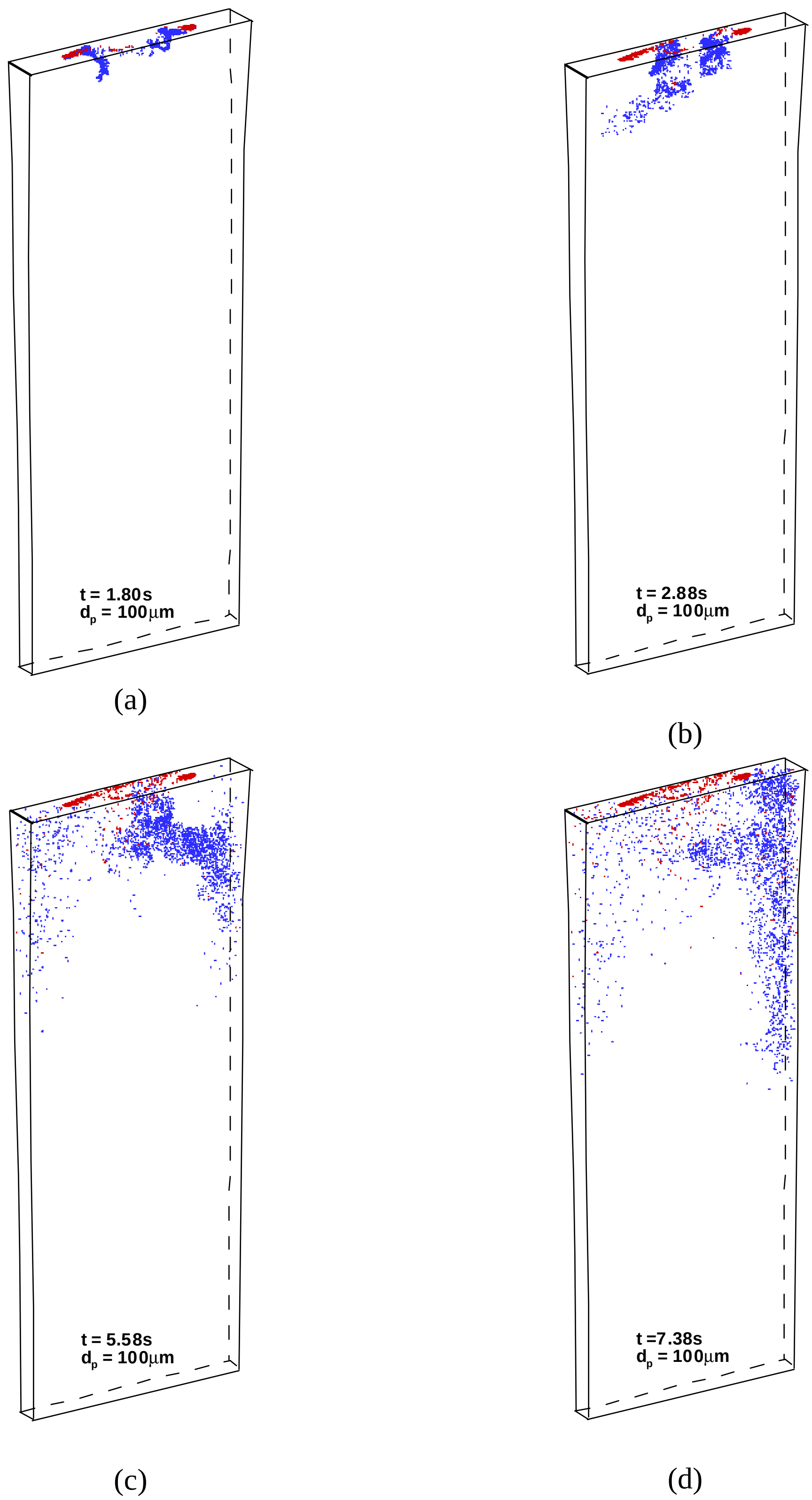


**Figure 9.15. Distributions of 4,000 slag particles with diameters of 100mm which entered mold from the top surface.**

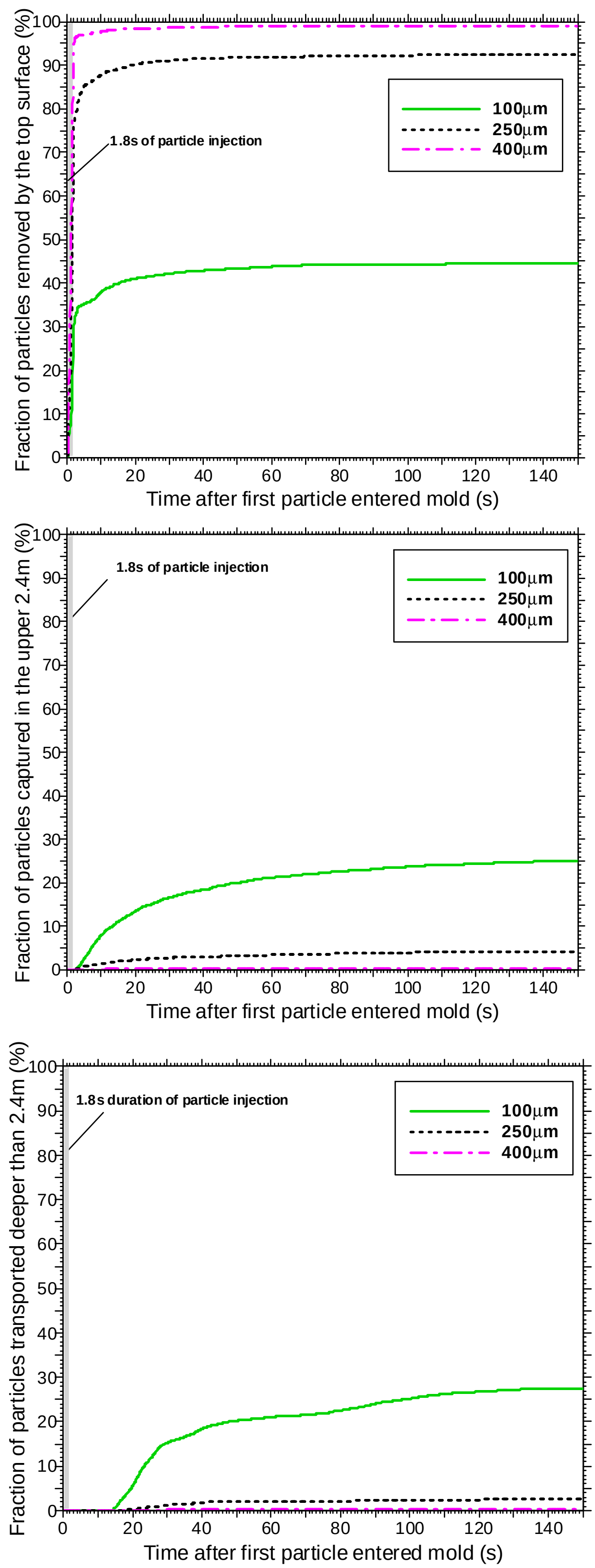


**Figure 9.16. Removal and entrapment histories of large particles (³ 100mm) entrained to the mold region from top surface center.**

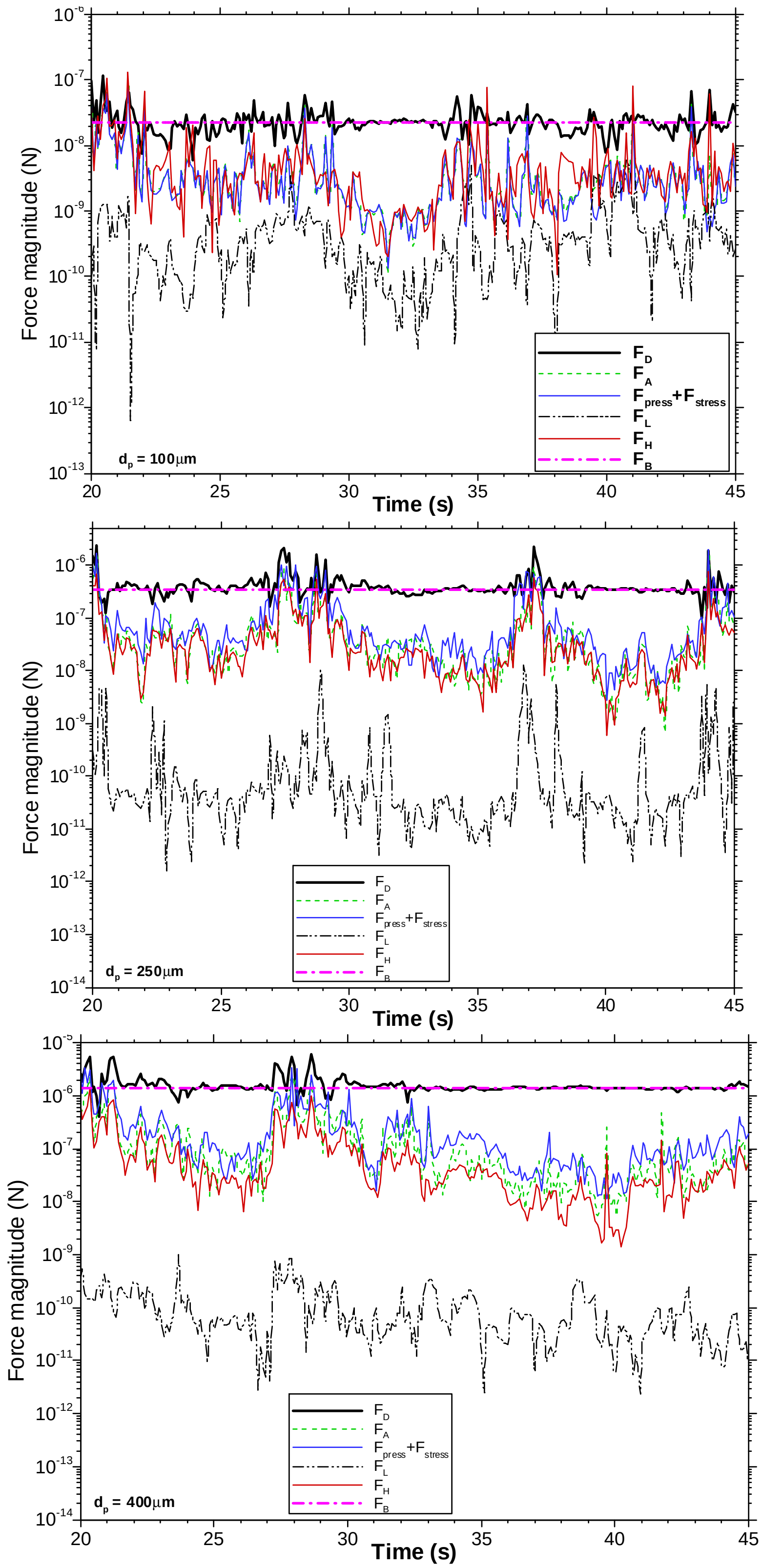


**Figure 9.17. Comparisons of the hydrodynamic forces acting on three particles with diameters of 100μm, 250μm and 400μm.**

# CHAPTER 10. CONCLUSIONS AND RECOMMENDATIONS

## 10.1 Conclusions

A Large Eddy Simulation (LES) and Lagrangian particle transport approach was applied in this thesis to investigate the turbulent flow and particle transport during continuous casting of steel slabs. The LES predicted flow fields were validated with prior experimental results such as PIV data, hotwire anemometry and dye-injection video images and in water models. The predicted time-averaged and *rms* velocities agree reasonably well with measurements across the top surface, along the jet and in the lower roll region. Spectral analyses suggest that the predicted velocity-fluctuations have similar frequency modes as in measurements. The predicted particle removal fractions from the Lagrangian approach were validated by matching prior measurements. A simple criterion for particle pushing and capture was developed. The criterion was preliminarily validated with three different sets of available experimental data and applied to continuous casting of steel. The interfacial energy force induced the sulfur gradient in front of the steel dendrites was found to be the most significant force to attract slag particles and consequently to encourage particle capture. Cross-flow has an important effect to prevent capture of large particles. The particle transport model incorporates six different hydrodynamic forces. The drag and buoyancy forces were found to be most significant. Three more forces that act near the solidification interface are included in the capture criterion. The results from the simulations in this thesis suggest the following insights into the flow and particle behavior during the process:

(1) In the slide-gate controlled caster, the partial opening of the slide-gate induces a long, complex recirculation zone in the SEN. It further causes strong swirling cross-stream velocities comparable to the stream-wise component in the jets exiting from the nozzle ports. The jet at the outlet plane of the nozzle port involves complex cross-flow structures consisting of single and multiple vortices evolving in time. In contract, the cross-stream velocities were found to be small in the stopper-rod controlled system.

(2) The instantaneous jets in the upper mold cavity alternate between two typical flow patterns in a 0.4-scale water model where the flow rate is controlled by a slide-gate: a stair-step shaped jet induced by the cross-stream swirl in the jet, and a jet that bends upward midway between the SEN and the narrow face. The stair-step flow pattern, which is missing in the stopper rod controlled systems, is likely due to the cross-stream swirl in the jet induced by the slide gate. The flow in the upper region oscillates between a large single vortex and multiple vortices of various smaller sizes. The jet usually wobbles with a period of 0.5-1.5s.

(3) Significant flow asymmetries were observed in both the water model and the steel caster. A ~50s average reduces the difference between flow in the two halves of the upper mold region. However, significant asymmetric flow structures persist for longer times in the lower mold region. For instance, PIV measurements reveal such asymmetry lasts longer than 200s in the lower region of the 0.4-scale water model. The 400s LES of flow in the thin-slab caster shows the velocity in one side is dominantly large, which sometime leads to a single roll pattern in the lower region,

for longer than 50s, and a similar pattern repeats another 70s later. The unbalanced flow between the two sides may cause significant asymmetrical inclusion defects.

(4) The instantaneous top surface velocity was found to fluctuate with sudden jumps (for instance, 0.01m/s to 0.24m/s occurring in a short time of ~0.7s in the 0.4-scale water model). These velocity jumps were observed in full-mold simulations of both the water model and the steel caster. They were also seen in PIV measurements. However, this feature was not reproduced if a symmetry condition is imposed at the mold center between narrow faces. This indicates that interactions between flow in the two halves encourage large velocity fluctuations across the top surface. Level fluctuations near the narrow face occur over a wide range of frequencies, with the strongest having periods of ~7 and 11-25s.

(5) The velocity fields obtained from half-mold simulations with approximate inlet velocities generally agree with the results of the full-mold simulations and PIV measurements. However, they do not capture the interaction between flows in the two halves, such as the instantaneous sudden jumps of top surface velocity.

(6) Water models are generally representative of steel casters, especially in the upper region far above the water model outlet. However, steel casters are likely to have somewhat more evenly distributed downward flow in the lower roll zone, where the influence of shell thickness becomes significant.

(7) The top surface level can be reasonably predicted from the top surface pressure distribution. The top surface level profile rises more near the narrow face in the steel caster than in the water model, which has no slag layer to displace.

(8) Significant anisotropy exists in the turbulent flow in the mold region. The most important flow structures have very long time scales. Spectral analysis confirms this as most of the energy is contained in the low frequency region (0-5Hz).

(9) Complex particle trajectories are seen in both the water model (*Case 1*) and the thin-slab steel caster (*Case2-S*), showing the important influence of turbulence on particle transport. Significant asymmetric particle distributions were observed in the mold region, which are caused by transients of fluid turbulence, rather than imposed by the inlet condition at nozzle ports. This only leads to slight asymmetries in the particle distribution in a depth of about 25mm from the slab surface. However, more severe asymmetrical inclusions defects may be found in the interior region.

(10) The top surface is predicted to remove only 8% of small particles (10μm and 40μm) in the thin slab steel caster. An equal fraction touches the outside of the nozzle walls in the mold. These removal fractions are independent of both particle size and density, owing to the inability of the small, low-buoyancy particles simulated here to deviate significantly from the surrounding fluid flow.

(11) The removal fractions are predicted to 12.6%, 42.4% and 69.8% for the large particles with diameters of 100μm, 250μm and 400μm respectively, which entered the mold from the nozzle ports. Most of the removal occurs in the first 50s after particles enter the mold region. The results indicate that large particle (e.g. 400μm) may be effectively removed from the mold region.

(12) The computation shows that after a 9s sudden burst of particles with diameters from 10μm-400μm enters the steel caster, about 3-4 minutes are needed for all of them to

be captured or removed for the casting conditions assumed here. The captured particles concentrate mainly within a 2-m long section of slab.

(13) With a steady oxygen content of 10ppm from inclusions in the molten steel supplied from the nozzle ports, intermittent patches of high oxygen content (50-150ppm) are found concentrated within 10-20mm beneath the slab surface, especially near the corner, and towards the narrow faces.

(14) The removal of slag particles entrained from the top surface is found to be highly dependent on the particle size. Most (>92%) of the 250μm and 400μm droplets simply return to the slag layer. However, more than half of the 100μm particles are eventually captured, leading to sliver defects.

## 10.2 Recommendations for Future Work

The criterion for particle pushing and capture developed in this work, which was preliminary validated, deserves further validation by fundamental experiments and simulations focusing on behavior involving a dendritic solidification front and cross-flow velocity. For better understandings of particle transport and improving steel cleanness, the following further studies are suggested:

(1) Quantify effects of different casting conditions on particle removal, such as effects of the casting speed and mold curvature;

(2) Investigate the particle transport and capture for different types of particles (e.g. argon bubbles) and steel with different sulfur content;

(3) Explore techniques to improve particle removal to the top surface slag layer by altering the double-roll flow pattern. These include new nozzle designs, electromagnetic stirring.

# APPENDIX A. DERIVATION OF THE VELOCITY BOUNDARY CONDITIONS AT THE SHELL FRONT

The effect of the moving solidifying shell on the internal flow in the liquid pool can be represented using a velocity boundary condition, which is illustrated as follows. A stationary control volume in the Euler frame, shown in Figure A.1, comprises a piece of solid shell. A normal velocity of the molten steel entering the control volume through the solidification front (sloped edge) can be obtained from mass conservation:

$$\frac{d\left(\rho_s \mathbf{V}\right)}{dt} = \rho_s A_1 V_{casting} + \rho_l A_3 \mathrm{v}_\mathrm{n} - \rho_s A_2 V_{casting} \tag{A.1}$$

By assuming that both the shell shape and the solid density stay constant in this Eulerian frame, the normal velocity can be expressed as:

$$\mathrm{v}_n = \frac{\rho_s\left(A_2 - A_1\right)}{\rho_l A_3} V_{casting} = \left(\frac{\rho_s}{\rho_l}\sin\theta\right) V_{casting} \tag{A.2}$$

This imposed normal velocity accounts for the mass flow caused by continuous solidification and shell withdrawal. The non-slip condition is assumed to hold tangential to the front:

$$\mathrm{v}_t = V_{casting}\cos\theta \tag{A.3}$$

Written in terms of the x, z velocity components:

$$\mathrm{v}_x = \mathrm{v}_n\cos\theta - \mathrm{v}_t\sin\theta = \left(\frac{\rho_s}{\rho_l} - 1\right)\sin\theta\cos\theta V_{casting} \tag{A.4}$$

$$\mathrm{v}_z = \mathrm{v}_n\sin\theta + \mathrm{v}_t\cos\theta = \left(\frac{\rho_s}{\rho_l}\sin^2\theta + \cos^2\theta\right) V_{casting} \tag{A.5}$$

Equations (A.4) and (A.5) gives the velocity boundary condition at the shell front position.

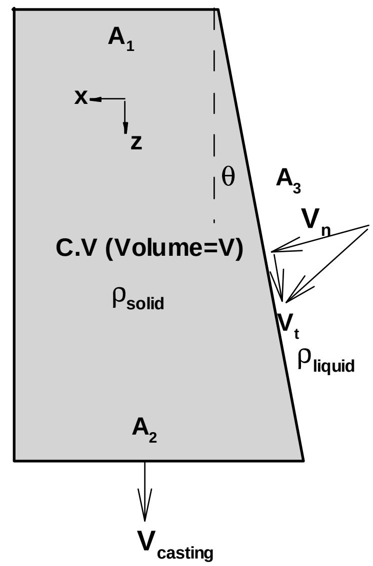


**Figure A.1. The control volume for calculating boundary velocities at the shell front.**

# APPENDIX B. SURFACE ENERGY VARIATIONS OF BINARY FE-ALLOYS DUE TO CONCENTRATION AND TEMPERATURE GRADIENTS

The surface energy between a slag sphere and the liquid steel can be calculated from the formula by Girifalco and Good: [135]

$$s_{pl} = s_{pv} + s_{lv} - 2\Phi\left(s_{pv} s_{lv}\right)^{1/2} \tag{B.1}$$

where the subscripts $p$, $l$, v represent the slag particle, liquid steel and vacuum respectively. Jimbo and Cramb [136] found a value of 0.55 for the liquid steel slag interface. Surface energy is measured in units of $J/m^2$ or N/m. A change of either temperature or the solute concentration in the liquid steel can cause variations of the surface energy of the liquid steel $s_{pv}$ and consequently change $s_{pl}$.

The dependency of the surface energy of liquid Fe-X alloys on the temperature and the content of the solute X were reviewed by Keene. [123] Plots from Keene's review [123] are selectively repeated here. Figure B-1 [123] presents the surface energy of the liquid steel $s_{lv}$ as a function of the content of carbon, chromium and sulfur, showing a much stronger dependency of $s_{lv}$ on sulfur than the other compositions. Mukai and Lin [122] wrote the steel surface energy as a function of the dissolved sulfur concentration by curve fitting the measured data with the following form:

$$s_{lv} = s_0 - m\ln\left(1 + nC_s\right) \quad \text{if } C_s \leq 0.5 \tag{B.2}$$

where $\sigma_0$, $m$ and $n$ are empirical constants with values of $1.970 J/m^2$, $0.17 J/m^2$ and 840(1/wt pct), and $C_S$ (wt pct) is the weight concentration of sulfur in the steel. Therefore, $\partial s_{lv} / \partial C_S$ can be written as:

$$\frac{\partial s_{lv}}{\partial C_s} = \frac{-mn}{1+nC_s} \tag{B.3}$$

Using the data at 1550°C in Figure B.1, and $\partial s_{lv} / \partial C_C$ has $\partial s_{lv} / \partial C_{Cr}$ have constant values shown in Table B-1. The range is due to different experimental data sets by different researchers. The surface energy gradient is then estimated at a planar solidification interface advancing at a speed of 200μm/s. Results in Table B-1 clearly reveal that sulfur is the most activate element to influence the surface energy field.

Figure B-2 further presents the surface energy of steel as a function of temperature. All the data suggest that the temperature has little influence on the steel surface energy. Therefore, this thesis only included the surface energy gradient that is caused by a gradient of the sulfur concentration.

Table B-1. Comparison of dependency of $s_{lv}$ on concentration of different solutes.

| x | Carbon | Chromium | Sulfur ($C_s$=0.001) |
|---|---|---|---|
| $\frac{\partial s_{lv}}{\partial C}$ (J/(m$^2$ wt pct)) | -0.007 to -.060 | -0.0055 to -0.012 | $-1.4\times10^5$ |
| $C_0$ (wt pct) | 0.047 | 16.71 | 0.001 |
| $k$ | 0.19 [72] | 0.95 [72] | 0.05 [72] |
| $D_X$ (m$^2$/s) | $5.5\times10^{-5}$ [72] | $5.5\times10^{-7}$ [72] | $3.4\times10^{-9}$ [101] |
| $\frac{\partial C}{\partial n}$ (wt pct/m) [101] | 0.33 | 2062 | 1622 |
| $\sigma_{lv}/\ n$ (J/m$^3$) | -0.0023 to 0.020 | -11 to 25 | $-2.3\times10^8$ |

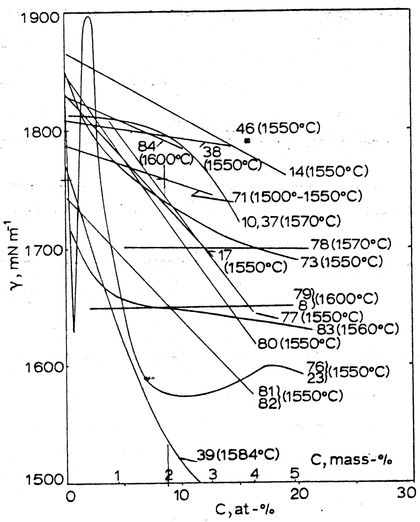


(a)

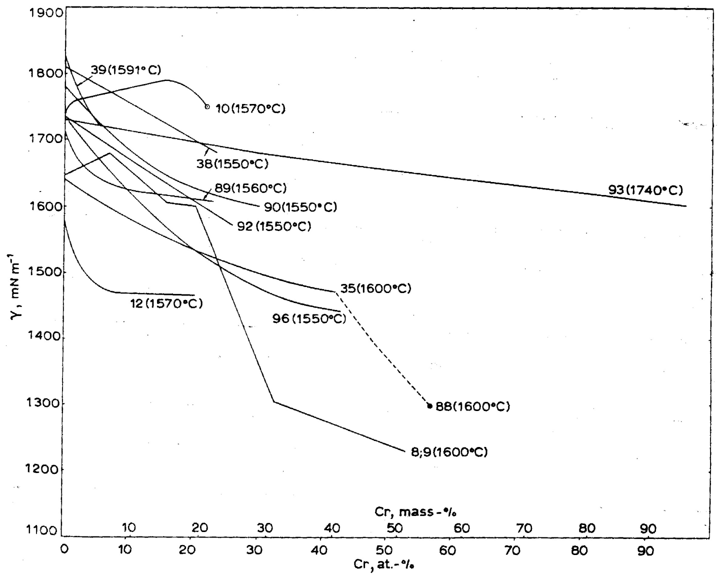


(b)

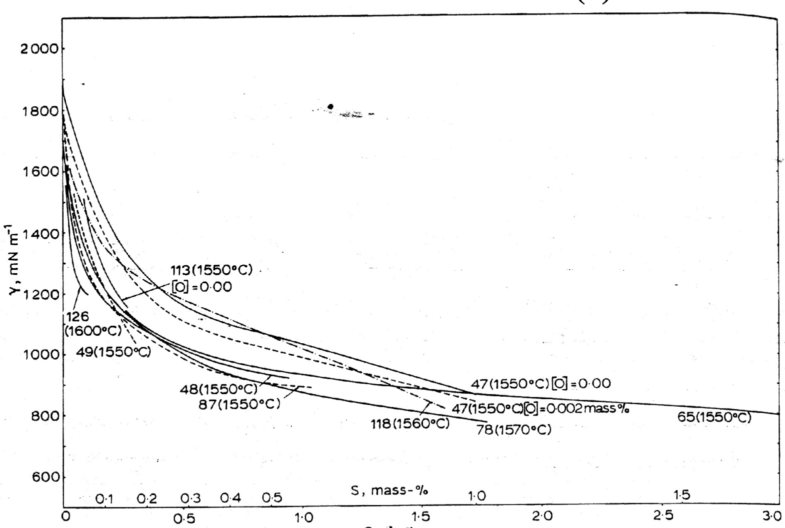


(c)

**Figure B.1. Dependency of the surface energy ($\gamma=\sigma_{lv}$) of the liquid steel on the dissolved: (a) carbon, (b) chromium and (c) sulfur. [123]**

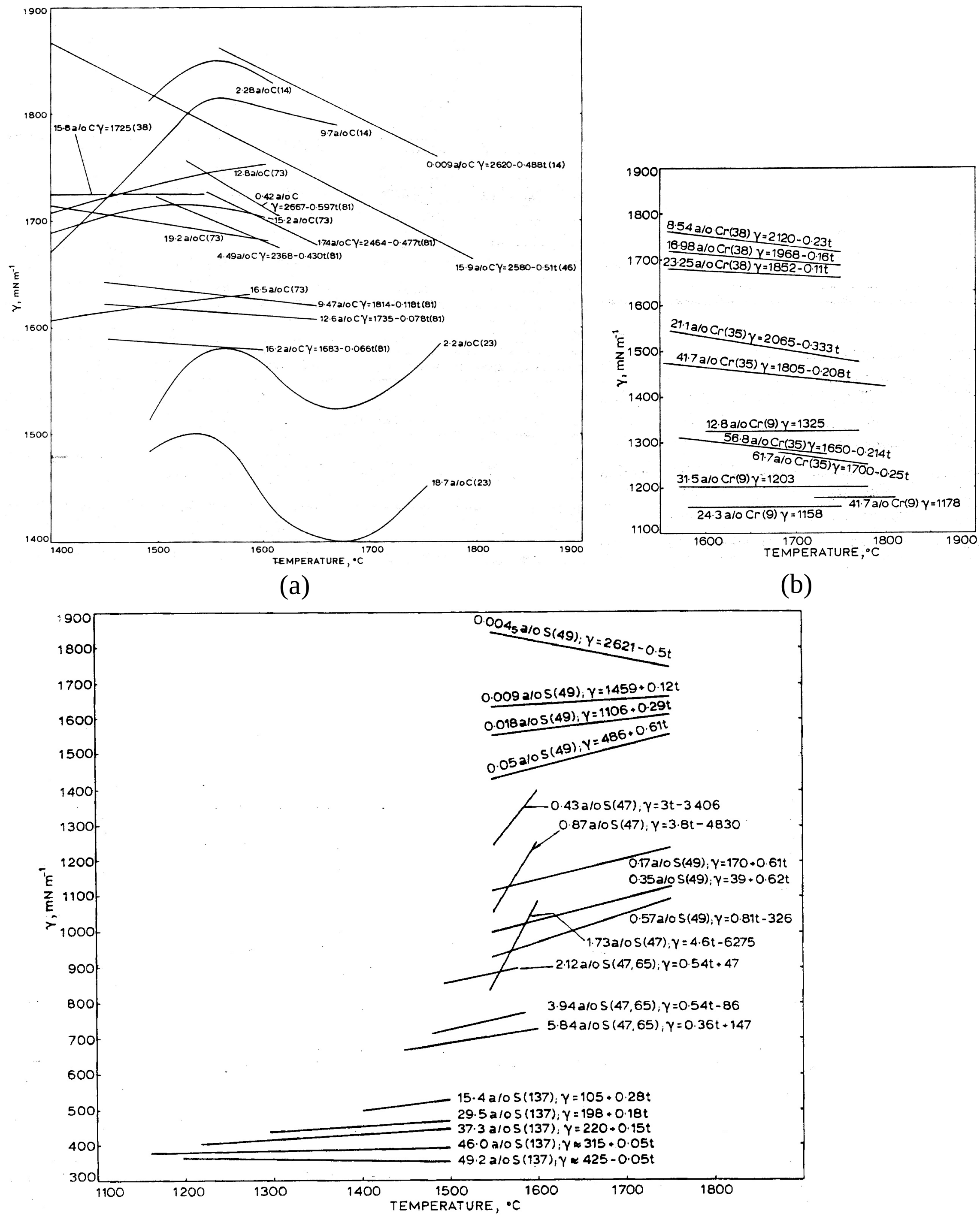


(c)

**Figure B.2. Surface energy dependency on the temperature in (a) Fe-C, (b) Fe-Cr and (c) Fe-S alloy solutions.**

# APPENDIX C. DERIVATION OF THE SURFACE ENERGY GRADIENT FORCE ACTING ON A SPHERE IN FRONT OF A DENDRITE

This section derives the surface energy gradient force acting on a particle close to a dendrite, which is induced by a concentration gradient of an interfacial active solute. Figure C.1 schematically illustrates a slag droplet close to a solidifying dendrite of Fe alloy separated by a thin-film of liquid steel. Based on the analysis in APPENDIX B, sulfur is the only solute considered to cause a significant surface energy gradient force. The complex shape of the dendrite tip is simplified as a smooth hemisphere. $O_d$ and $O_p$ are the centers of the dendrite tip and the particle respectively, and ? is the distance between the 2 points. The input parameters are: the particle radius ($R_p$), the dendrite tip radius ($r_t$) which can be estimated from Equation (7.42), the distribution coefficient ($k=C_s/C_l$), the diffusion coefficient of sulfur in steel ($D_s$), the sulfur content of the steel which is also the far field concentration ($C_0$), the solidification front speed ($v_{sol}$) and the empirical constants $m$ and $n$ defined in Equation (B.2) for calculating the surface energy between the slag droplet and the liquid steel with dissolved sulfur.

To avoid expensive numerical computations, the sulfur concentration field in the liquid steel is estimated using the analytical solution by Kurz and Fisher, [137] with the following additional assumptions: (1) the mass transport in the region enclosing the dendrite tip and the particle is dominated by diffusion; (2) the particle prevents localized liquid cross-flow and (3) the particle does not influence the concentration field. The concentration field is then expressed as follows:

$$C(r) = C_0 + \frac{r_d}{r}\left(C^* - C_0\right) \tag{C.1}$$

$$\frac{v_{sli} r_d}{2D_s} = \frac{C^* - C_0}{C^*\left(1-k\right)} \tag{C.2}$$

where $r$ is the radial distance from the dendrite tip center as shown in Figure C.1. The total surface energy $E_{sur}$ across the particle surface ($A_p$) can be written as:

$$E_{sur} = \int_{A_p} \sigma_{pl} dA \tag{C.3}$$

where $\sigma_{pl}$ is given in Equation (B.2). From Figure C.1, $dA$ can be expressed as:

$$dA = 2\pi R_p \sin\theta R_p d\theta \tag{C.4}$$

Substituting $dA$ into Equation (C.3) yields:

$$E_{sur} = \int_0^{\pi} \sigma_{pl} \left(2\pi R_p \sin\theta R_p\right) d\theta \tag{C.5}$$

The surface energy gradient force acting on the particle, $F_{grad}$, can be written as:

$$F_{Grad} = -\frac{\partial E_{sur}}{\partial x} \tag{C.6}$$

Substituting Equation (C.5) into (C.6) gives:

$$\begin{aligned} F_{Grad} &= -\int_0^{\pi} \frac{\partial \sigma_{pl}}{\partial x}\left(2\pi R_p \sin\theta R_p\right) d\theta \\ &= -2\pi R_p^2 \int_0^{\pi} \frac{d\sigma_{pl}}{dC(r)} \frac{dC(r)}{dr} \frac{\partial r(x,\theta)}{\partial x} \sin\theta d\theta \end{aligned} \tag{C.7}$$

where:

$$r = \left(x^2 + R_p^2 - 2xR_p \cos\theta\right)^{1/2} \tag{C.8}$$

From Equations (B.2), (C.1) and (C.8), the following three derivatives can be found:

$$\frac{\partial \sigma_{pl}}{\partial C} = \frac{-mn}{1+nC} \tag{C.9}$$

$$\frac{\partial C}{\partial r} = -\frac{r_d\left(C^* - C_0\right)}{r^2} \tag{C.10}$$

$$\frac{\partial r}{\partial x} = \frac{2x - 2R_p \cos q}{2\left(x^2 + R_p^2 - 2x R_p \cos q\right)^{1/2}} \tag{C.11}$$

By introducing a new variable $x = \left(x^2 + R_p^2 - 2x R_p \cos q\right)^{1/2}$ and substituting Equations (C.9)-(C.11) into (C.7) yields:

$$F_{Grad} = -\frac{mbp R_p}{x^2} \int_{x-R_p}^{x+R_p} \left[ \frac{x^2 - R_p^2}{(a x + b)x} + \frac{x}{a x + b} \right] dx \tag{C.12}$$

where:

$$a = 1 + nC_0 \tag{C.13}$$

$$b = nr_t\left(C^* - C_0\right) \tag{C.14}$$

Integrating Equation (C.12) yields the following equation:

$$F_{Grad} = -\frac{mbp R_p}{x^2}\left\{ \frac{\left(x^2 - R_p^2\right)}{b} \ln\left[ \frac{\left(x + R_p\right)\left[a\left(x - R_p\right) + b\right]}{\left(x - R_p\right)\left[a\left(x + R_p\right) + b\right]} \right] + \frac{2R_p}{a} - \frac{b}{a^2} \ln\left[ \frac{a\left(x + R_p\right) + b}{a\left(x - R_p\right) + b} \right] \right\} \tag{C.15}$$

The value of $F_{grad}$ is usually negative, which indicates an attractive force on the particle towards the interface, which encourages capture.

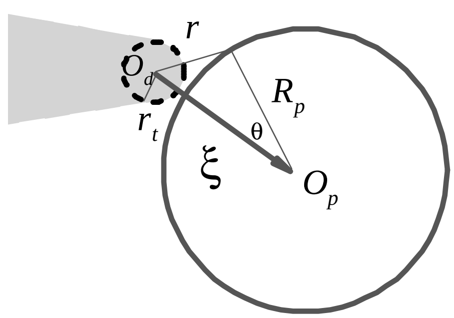


**Figure C.1. Schematics of a particle with radius $R_p$ close to a solidifying dendrite.**

# APPENDIX D. EVALUATION OF DENDRITE PDAS, TIP RADIUS AND FORCES ACTING ON A SLAG SPHERE CLOSE THE A PRIMARY DENDRITE ARM

Equations (7.42) and (7.43) give estimates of the dendrite tip radius and the PDAS respectively. [126] These two equations were derived for binary alloys. However, the steel investigated in *Case 2-S* of this thesis consists of multiple components as shown in Table 5.2. This leads to difficulty determining the diffusion coefficient $D_0$ and the distribution coefficient $k$. This problem is handled in the thesis as follows.

Substituting Equation (7.42) into (7.43) yields the following expression:

$$\mathrm{PDAS} = 4.30\left(\frac{D_0 \Delta T\, {}^{s_{sl}}\!/_{S}}{k}\right)^{1/4} \left(\mathrm{v}_{\mathrm{sol}}\right)^{-1/4} \left({}^{dT}\!/_{dn}\right)^{-1/2}$$

where the term $\left(\frac{D_0 \Delta T\, {}^{s_{sl}}\!/_{S}}{k}\right)^{1/4}$ is a constant for a specific alloy, $\mathrm{v}_{\mathrm{sol}}$ is the shell growth speed, which can be obtained from measurements or COND1D predictions as shown in Figure D.1 for *Case 2-S*, and *dT/dn* is the normal temperature gradient at the shell front, which can be obtained from simulations. [138] Figure D.2 shows the contour of an LES predicted *dT/dn* at the wide face and narrow face for *Case 2-S*. [138] Therefore, the constant $\left(\frac{D_0 \Delta T\, {}^{s_{sl}}\!/_{S}}{k}\right)^{1/4}$ can be estimated if measure PDAS data are available at some positions. Figure D.3 shows a few measured PDAS data on the narrow face and the wide face in *Case 2-S*. The constant $\left(\frac{D_0 \Delta T\, {}^{s_{sl}}\!/_{S}}{k}\right)^{1/4}$ was calculated using the measured wide face PDAS at the top surface. The PDAS and the dendrite tip radius across the wide face and narrow face walls were then determined from Equations (7.42) and (7.43). The computed PDAS along two dashed lines shown in Figure D.2 is seen to agree well the measurement (Figure D.3).

The surface energy gradient, lubrication and interfacial forces acting on a slag droplet close to a solidifying dendrite can then be computed from Equations (7-26), (7-27) and (7-33) using the estimated dendrite tip radii. Figure D.4 compares the magnitudes of the three forces for a 100μm slag sphere in front of a 2.1μm dendrite tip, which grows at a speed of 500 μm/s. The smallest $h_0$ equals to seven times the liquid atomic diameter ($7a_0$). It is seen that the surface energy gradient force is at least five times larger than the Van der Waals force and the lubrication force.

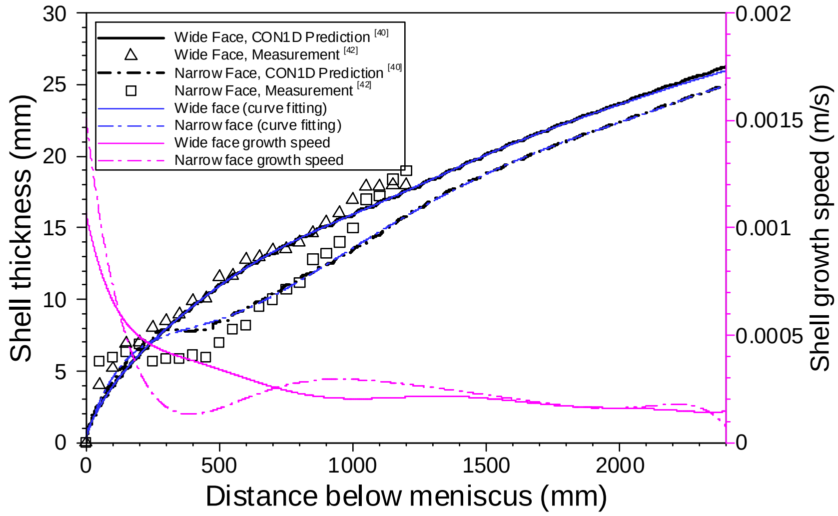


**Figure D.1. Shell thickness of the thin-slab caster (*Case 2-S*) and the shell growth speed.**

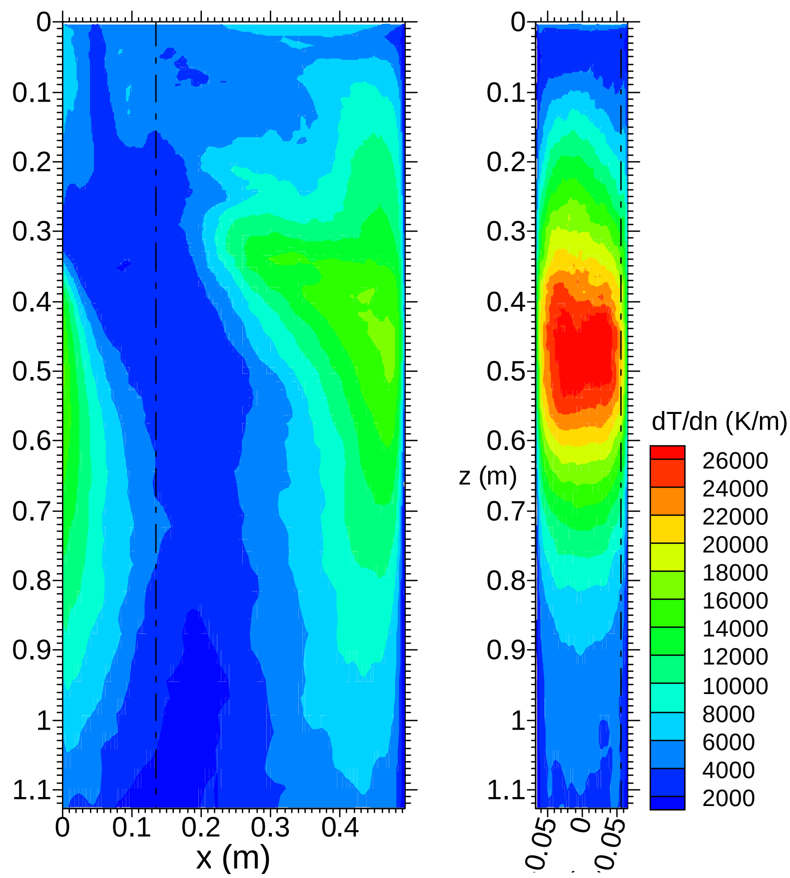


**Figure D.2. LES predicted temperature gradient at the wide face and narrow face walls.** [138]

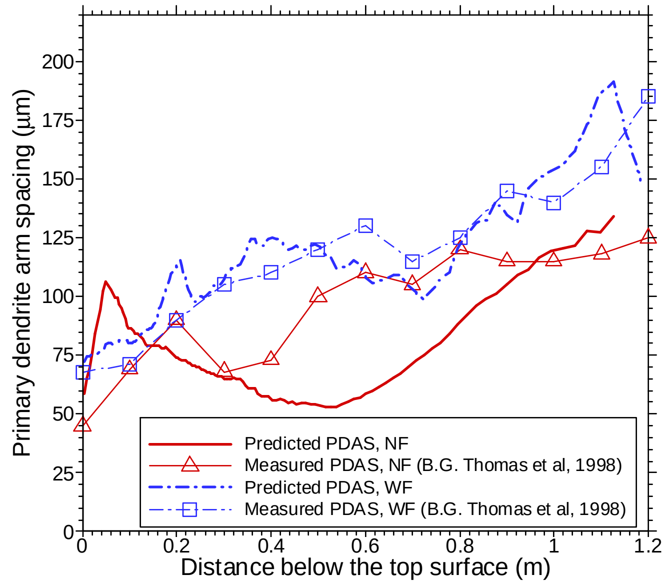


**Figure D.3. Comparisons of the predicted and measured PDAS.**

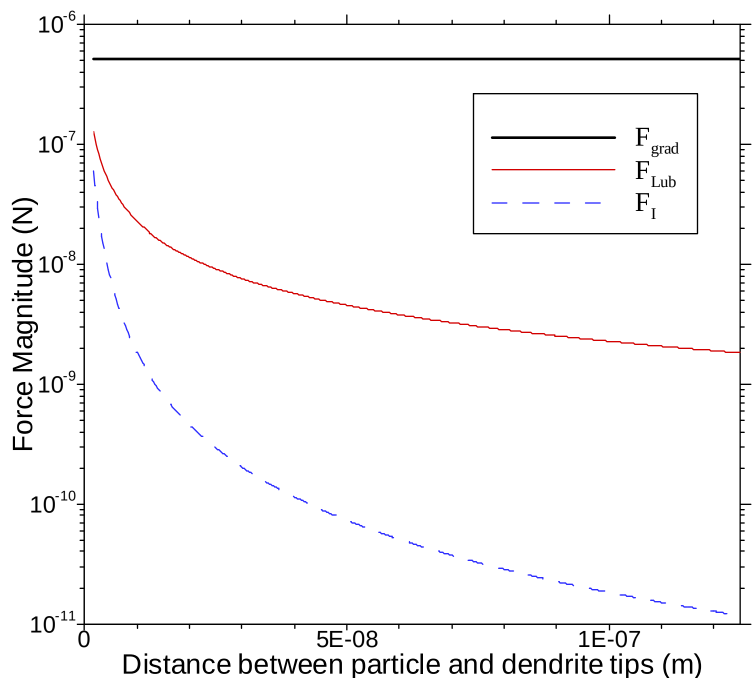


**Figure D.4. Comparison on the magnitudes of the surface energy gradient, lubrication and interfacial forces.**

# REFERENCES


1. Zhang, L. and Thomas, B.G.: "State of the Art in Evaluation and Control of Steel Cleanliness", ISIJ International, 2003, vol. 43 (3), pp. 271-291.
2. Emling, W.H., Waugaman, T.A., Feldbauer, S.L. and Cramb, A.W.: "Subsurface Mold Slag Entrainment in Ultra-Low Carbon Steels", Steelmaking Conference Proceedings, vol. 77, ISS, Warrendale, PA, pp. 371-379, 1994
3. Thomas, B.G.: "Chapter 14: Fluid Flow in the Mold", The Making, Shaping and Treating of Steel, 11th Edition, Casting Volume, The AISE Steel Foundation, p. 24, 2003
4. Herbertson, J., He, Q.L., Flint, P.J. and Mahapatra, R.B.: "Modeling of Metal Delivery to Continuous Casting Moulds", Steelmaking Conf. Proceedings, vol. 74, ISS, Warrendale, PA, pp. 171-185, 1991
5. Lawson, G.D., Sander, S.C., Emling, W.H., Moitra, A. and Thomas, B.G.: "Prevention of Shell Thinning Breakouts Associated with Widening Width Changes", Steelmaking Conference Proceedings, vol. 77, Iron and Steel Society, pp. 329-336, 1994
6. Bommaraju, R., Glennon, R. and Frazee, M.: "Analysis of the Cause and Prevention of Longitudinal Midface Cracks and Depressions on Continuously Cast Free-Machining Steel Blooms", Continuous Casting Vol. 9, ISS, Warrendale, PA, pp. 307-318, 1997
7. Thomas, B.G., Lui, D. and Ho, B.: "Effect of Transverse and Oscillation Marks on Heat Transfer in the Continuous Casting Mold", Applications of Sensors in Materials Processing, TMS, Warrendale, PA, pp. 117-142, 1997
8. Billany, T.J.H., Normanton, A.S., Mills, K.C. and Grieveson, P.: "Surface Cracking in Continuously Cast Products", Ironing and Steelmaking, 1991, pp. 403-410.
9. Yuan, Q., Zhao, B., Vanka, S.P. and Thomas, B.G.: "Investigation of Numerical Issues in Large Eddy Simulation of Turbulent Flow During Continuous Casting", in preparation: to be submitted to Applied Mathematical Modeling, 2003.
10. Knoepke, J., Hubbard, M., Kelly, J., Kittridge, R. and Lucas, J.: "Pencil Blister Reduction at Inland Steel Company", Steelmaking Conference Proceedings, vol. 77, ISS, Warrendale, PA, pp. 381-388, 1994
11. Thomas, B.G., Yuan, Q., Sivaramakrishnan, S., Shi, T., Vanka, S.P. and Assar, M.B.: "Comparison of Four Methods to Evaluate Fluid Velocities in a Continuous Casting Mold", ISIJ International, 2001, vol. 41 (10), pp. 1262-1271.
12. Assar, M.B., Dauby, P.H. and Lawson, G.D.: "Opening the Black Box: Piv and Mfc Measurements in a Continuous Caster Mold", Steelmaking Conference Proceedings, vol. 83, ISS, Warrendale, PA, pp. 397-411, 2000
13. O'Malley, R.J.: private communication, 2003.

14. Sobolewski, R. and Hurtuk, D.J.: "Water Modeling of Slab Caster Flow Conditions", 2nd Process Technology Conf. Proc., Iron and Steel Society, Warrendale, PA, 1982, pp. 160-165.

15. Gupta, D. and Lahiri, A.K.: "Water Modeling Study of the Jet Characteristics in a Continuous Casting Mold", Steel Research, 1992, vol. 63 (5), p. 201~204.

16. Gupta, D. and Lahiri, A.K.: "A Water Model Study of the Flow Asymmetry inside a Continuous Slab Casting Mold", Metallurgical and Materials Transactions B, 1996, vol. 27B (5), pp. 757-764.

17. Thomas, B.G., Huang, X. and Sussman, R.C.: "Simulation of Argon Gas Flow Effects in a Continuous Slab Caster", Metallurgical and Materials Transactions B, 1994, vol. 25B (4), pp. 527-547.

18. Thomas, B.G. and Zhang, L.: "Mathematical Modeling of Fluid Flow in Continuous Casting", ISIJ International, 2001, vol. 41 (10), pp. 1181-1193.

19. White, F.M.: Viscous Fluid Flow, Second ed., Mcgraw-Hill Series in Mechanical Engineering, McGraw-Hill, Boston, 1991, p. 614.

20. Thomas, B.G. and Huang, X.: "Effect of Argon Gas on Fluid Flow in a Continuous Slab Casting Mold", 76th Steelmaking Conference Proceedings, (Dallas, TX, March 28-31), Iron and Steel Society, Warrendale, PA, 1993, pp. 273-289.

21. Honeyands, T. and Herbertson, J.: "Oscillations in Thin Slab Caster Mold Flows", 127th ISIJ Meeting, ISIJ, Tokyo, Japan, 1994, pp.

22. Gupta, D., Chakraborty, S. and Lahiri, A.K.: "Asymmetry and Oscillation of the Fluid Flow Pattern in a Continuous Casting Mould: A Water Model Study", ISIJ International, 1997, vol. 37 (7), pp. 654-658.

23. Eckert, E.R.G.: "Chapter 2. Physical Laws of Fluid Mechanics and Their Applications to Measurement Techniques", Fluid Mechanics Measurements, Taylor&Francis, pp. 65-114, 1996

24. Yuan, Q., Thomas, B.G. and Vanka, S.P.: "Study of Transient Flow and Particle Transport in Continuous Steel Casting Molds: Part I. Fluid Flow", Metallurgical and Materials Transactions B, 2003, (in press).

25. Adrian, R.J.: "Chapter 4. Laser Velocimetry", Fluid Mechanics Measurements, Taylor&Francis, pp. 175-299, 1996

26. Lawson, N.J. and Davidson, M.R.: "Oscillatory Flow in a Physical Model of a Thin Slab Casting Mould with a Bifurcated Submerged Entry Nozzle", Journal of Fluids Engineering, 2002, vol. 124 (6), pp. 535-543.

27. Adrian, R.J.: "Particle-Imaging Techniques for Experimental Fluid Mechanics", Annu. Rev. Fluid Mech., 1991, vol. 23, pp. 261-304.

28. Lawson, N.J. and Davidson, M.R.: "Oscillatory Flow in a Physical Model of a Thin Slab Casting Mould with a Bifurcated Submerged Entry Nozzle", Journal of Fluids Engineering, 2002, vol. 124, pp. 535-543.

29. Xu, D., Jones, W.K. and Evans, J.W.: "Piv Physical Modeling of Fluid Flow in the Mold of Continuous Casting of Steel", Processing of Metals and Advanced Materials: Modeling, Deisgn and Properties, TMS, Warrendale, PA, pp. 3-14, 1998

30. Sivaramakrishnan, S.: Transient Fluid Flow in the Mold and Heat Transfer through the Molten Slag Layer in Continuous Casting of Steel, M.S. Thesis, University of Illinois at Urbana-Champaign, Urbana, 2000.

31. Pope, S.B.: Turbulent Flows, Cambridge University Press, Cambridge, UK, 2000, p. 771.

32. Hershey, D.E., Thomas, B.G. and Najjar, F.M.: "Turbulent Flow through Bifurcated Nozzles", Int. J. Num. Meth. in Fluids, 1993, vol. 17, pp. 23-47.

33. Najjar, F.M., Hershey, D.E. and Thomas, B.G.: "Turbulent Flow of Steel through Submerged Bifurcated Nozzles into Continuous Casting Molds", Fourth FIDAP Users Conference, (Evanston, IL, Fluid Dynamics International, Inc., 500 Davis Ave., Suite 400, Evanston, IL, 1991, pp. 1-55.

34. Bai, H. and Thomas, B.G.: "Turbulent Flow of Liquid Steel and Argon Bubbles in Slide-Gate Tundish Nozzles, Part I, Model Development and Validation", Metallurgical and Materials Transactions B, 2001, vol. 32B (2), pp. 253-267.

35. Bai, H. and Thomas, B.G.: "Turbulent Flow of Liquid Steel and Argon Bubbles in Slide-Gate Tundish Nozzles, Part Ii, Effect of Operation Conditions and Nozzle Design", Metallurgical and Materials Transactions B, 2001, vol. 32B (2), pp. 269-284.

36. Thomas, B.G., Mika, L.M. and Najjar, F.M.: "Simulation of Fluid Flow inside a Continuous Slab Casting Machine", Metall. Trans. B, 1990, vol. 21B, pp. 387-400.

37. Aboutalebi, M.R., Hasan, M. and Guthrie, R.I.L.: "Coupled Turbulent Flow, Heat, and Solute Transport in Continuous Casting Processes", Metallurgical and Materials Transactions B, 1995, vol. 26B (4), pp. 731-744.

38. Lan, X.K., Khodadadi, J.M. and Shen, F.: "Evaluation of Six K-E Turbulence Model Predictions of Flow in a Continuous Casting Billet-Mold Water Model Using Laser Doppler Velocimetry Measurements", Metallurgical and Materials Transactions B, 1997, vol. 28B (2), pp. 321-332.

39. Huang, X. and Thomas, B.G.: "Modeling of Transient Flow Phenomena in Continuous Casting of Steel", Canadian Metall. Quart., 1998, vol. 37 (304), pp. 197-212.

40. Thomas, B.G.: Mathematical Models of Continuous Casting of Steel Slabs, Continuous Casting Consortium, University of Illinois at Urbana-Champaign, 2000.

41. Smagorinsky, J.: "General Circulation Experiments with the Primitive Equations, I. The Basic Experiment", Monthly Weather Review, 1963, vol. 91, pp. 99-164.

42. Schumann, U.: "Subgrid Scale Model for Finite Difference Simulations of Turbulent Flows in Plane Channels and Annulii", J. Comput. Phys., 1975, vol. 8, pp. 376-404.

43. Schumann, U.: "Subgrid Length-Scales for Large Eddy Simulations of Stratified Turbulence", Theoretical and Computational Fluid Dynamics, 1991, vol. 2 (279-290).

44. Horiuti, K.: "Large Eddy Simulation of Turbulent Channel Flow by One-Equation Modeling", Journal of the Physical Society of Japan, 1985, vol. 54 (8), pp. 2855-2865.

45. Jahnke, S., Kornev, N., Leder, A. and Hassel, E.: "Les Simulation of Jet Mixing Processes with Heat Transfer in Turbulent Pipe Flow", Chemical Engineering Technology, 2004, vol. 27 (3), pp. 243-248.

46. Jones, W.P.: "Large Eddy Simulation of Turbulent Combustion Processes", Computer Physics Communications, 2002, vol. 147, pp. 533-537.

47. Rodi, W., Ferziger, J.H., Breuer, M. and Pourquie, M.: "Status of Large Eddy Simulation: Results of a Workshop", Trans. ASME, 1997, vol. 119, pp. 248-262.

48. Rodi, W.: "Large-Eddy Simulations of the Flow Past Bluff Bodies - State of the Art", JSME International Journal Series B-Fluids & Thermal Engineering, 1998, vol. 41 (2), pp. 361-374.

49. Rodi, W.: "Comparison of Les and Rans Calculations of the Flow around Bluff Bodies", Journal of Wind Engineering & Industrial Aerodynamics, 1998, vol. 71, pp. 55-75.

50. Michelassi, V., Wissink, J.G., Frohlich, J. and Rodi, W.: "Large-Eddy Simulation of Flow around Low-Pressure Turbine Blade with Incoming Wakes", AIAA Journal, 2003, vol. 41 (11), pp. 2143-2156.

51. Takatani, K., Tanizawa, Y., Mizukami, H. and Nishimura, K.: "Mathematical Model for Transient Fluid Flow in a Continuous Casting Mold", ISIJ International, 2001, vol. 41 (10), pp. 1252-1261.

52. Schmidt, H. and Schumann, U.: "Coherent Structure of the Convective Boundary Layer Derived from Large-Eddy Simulation", Journal of Fluid Mechanics, 1989, vol. 200, pp. 511-562.

53. Kim, W.W. and Menon, S.: "Application of the Localized Dynamic Subgrid-Scale Model to Turbulent Wall-Bounded Flows", AIAA 97-0210, 1997.

54. Thomas, B.G. and Najjar, F.M.: "Finite-Element Modeling of Turbulent Fluid Flow and Heat Transfer in Continuous Casting", Applied Mathematical Modeling, 1991, vol. 15, pp. 226-243.

55. Harlow, F.H. and Welch, J.E.: "Numerical Calculation of Time Dependent Viscous Incompressible Flow of Fluid with Free Surface", Physics of Fluids, 1965, vol. 8 (112), pp. 2182-2189.

56. Crank, J. and Nicolson, P.: "A Practical Method for Numerical Evaluation of Solutions of Partial Differential Equations of the Heat-Conduction Type", Proc. Cambridge Philos. Soc., 1947, vol. 43, pp. 50-67.

57. Sampine, L.F. and Gordon, M.K.: Computer Solution of Ordinary Differential Equations: The Initial Value Problem, W.H. Freeman, ed. San Francisco, 1975.

58. User's Manual: Hypre - High Performance Preconditioners, Center for Applied Scientific Computing, Lawrence Livermore National Laboratory, 2001.

59. Madabushi, R. and Vanka, S.P.: "Large Eddy Simulation of Turbulence-Driven Secondary Flow in a Square Duct", Physics of Fluids, 1991, vol. 3 (11), pp. 2734-2745.

60. Tennekes, H. and Lumley, J.L.: "Chapter 6:The Statistical Description of Turbulence", A First Course in Turbulence, The MIT Press, pp. 197-222, 1992

61. Bai, H. and Thomas, B.G.: "Effects of Clogging, Argon Injection and Continuous Casting Conditions on Flow and Air Aspiration in Submerged Entry Nozzles", Metallurgical and Materials Transactions B, 2001, vol. 32B (4), pp. 707-722.

62. Najjar, F.M., Thomas, B.G. and Hershey, D.E.: "Turbulent Flow Simulations in Bifurcated Nozzles: Effects of Design and Casting Operation", Metall. Trans. B, 1995, vol. 26B (4), pp. 749-765.

63. Bai, H.: Argon Bubble Behavior in Slide-Gate Tundish Nozzles During Continuous Casting of Steel Slabs, PhD Thesis, University of Illinois at Urbana-Champaign, Urbana, 2000.

64. Cramb, A., Chung, Y., Harman, J., Sharan, A. and Jimbo, I.: "The Slag/Metal Interface and Associated Phenomena. A History of Pneumatic Steelmaking", Iron and Steelmaker, 1997, vol. 24 (3), pp. 77-83.

65. Yuan, Q., Thomas, B.G. and Vanka, S.P.: "Study of Transient Flow and Particle Transport in Continuous Steel Casting Molds: Part Ii. Particle Transport", Metallurgical and Materials Trans. B, 2003, (in press).

66. Sivaramakrishnan, S., Bai, H., Thomas, B.G., Vanka, P., Dauby, P. and Assar, M.: "Transient Flow Structures in Continuous Cast Steel", Ironmaking Conference Proceedings, vol. 59, ISS, Warrendale, PA, pp. 541-557, 2000

67. Gupta, D. and Lahiri, A.K.: "Water-Modeling Study of the Surface Disturbances in Continuous Slab Caster", Metallurgical and Materials Transactions B, 1994, vol. 25B (2), pp. 227-233.

68. Gass, R.: Inland Steel, Inc., private communication, 1992.

69. Sussman, R.C., Burns, M., Huang, X. and Thomas, B.G.: "Inclusion Particle Behavior in a Continuous Slab Casting Mold", 10th Process Technology Conference Proc., vol. 10, Iron and Steel Society, Warrendale, PA, pp. 291-304, 1992

70. Assar, M.B.: LTV Steel, private communication, 2000.

71. Thomas, B.G., O'Malley, R.J. and Stone, D.T.: "Measurement of Temperature, Solidification, and Microstructure in a Continuous Cast Thin Slab", Modeling of Casting, Welding, and Advanced Solidification Processes, (San Diego, CA, TMS, Warrendale, PA, 1998, pp. 1185-1199.

72. Meng, Y. and Thomas, B.G.: "Heat Transfer and Solidification Model of Continuous Slab Casting: Con1d", Metallurgical and Materials Transactions B, 2003, vol. 34B (5), pp. 685-705.

73. Wygnanski, I. and Fiedler, H.: "Some Measurements in the Self-Preserving Jet", J. of Fluid Mech., 1969, vol. 38 (577-612).

74. Anagnostopoulos, J. and Bergeles, G.: "Three-Dimensional Modeling of the Flow and the Interface Surface in a Continuous Casting Mold Model", Metallurgical and Materials Transactions B, 1999, vol. 30B (6), pp. 1095-1105.

75. Press, W.H., Teukolsky, S.A., Vetterling, W.T. and Flannery, B.P.: Numerical Recipes: The Art of Scientific Computing, Cambridge University Press, 1992, pp. 490-600.

76. Thomas, B.G., O'Malley, R., Shi, T., Meng, Y., Creech, D. and Stone, D.: "Validation of Fluid Flow and Solidification Simulation of a Continuous Thin Slab Caster", Modeling of Casting, Welding, and Advanced Solidification Processes, vol. IX, Shaker Verlag GmbH, Aachen, Germany, pp. 769-776, 2000

77. Loth, E.: "Numerical Approaches for Motion of Dispersed Particles, Droplets and Bubbles", Progress in Energy and Combustion Science, 2000, vol. 26, pp. 161-223.

78. Squire, K.D. and Eaton, J.K.: "Particle Response and Turbulence Modification in Isotropic Turbulence", Physics of Fluids, 1990, vol. 2 (7), pp. 1191-1203.

79. Elghobashi, S. and Truesdell, G.C.: "Direct Numerical Simulation of Particle Dispersion in a Decaying Isotropic Turbulence", Journal of Fluid Mechanics, 1992, vol. 242, pp. 655-700.

80. Wang, Q. and Squire, K.D.: "Large Eddy Simulation of Particle Deposition in a Vertical Turbulent Channel Flow", Int. J. Multiphase Flow, 1996, vol. 22 (4), pp. 667-683.

81. Wang, Q. and Squire, K.D.: "Large Eddy Simulation of Particle-Laden Channel Flow", Physics of Fluids, 1996, vol. 8 (5), pp. 1207-1223.

82. Boivin, M.S. and Squire, K.D.: "On the Prediction of Gas-Solid Flows with Two-Way Coupling Using Large-Eddy Simulation", Physics of Fluids, 2000, vol. 12 (8), pp. 2080-2090.

83. Zhang, H. and Ahmadi, G.: "Aerosol Particle Transport and Deposition in Vertical and Horizontal Turbulent Duct Flow", Journal of Fluid Mechanics, 2000, vol. 406 (55-80).

84. Grimm, B., Andrzejewski, P., Muller, K. and Tacke, K.-H.: "Inclusions in Continuously Cast Steel Slabs-Numerical Model and Validation", Steel Res., 1999, vol. 70 (10).

85. Asai, S. and Szekely, J.: "Turbulent Flow and Its Effects in Continuous Casting", Ironmaking Steelmaking, 1975, vol. 3, p. 205.

86. Thomas, B.G., Dennisov, A. and Bai, H.: "Behavior of Argon Bubbles During Continuous Casting of Steel", Steelmaking Conference Proceedings, vol. 80, ISS, Warrendale, PA., pp. 375-384, 1997

87. Ho, Y., Chen, C. and Hwang, W.: "Analysis of Molten Steel Flow in Slab Continuous Caster Mold", ISIJ International, 1994, vol. 34 (3), pp. 255-264.

88. Ho, Y. and Hwang, W.: "The Analysis of Molten Steel Flow in Billet Continuous Casting", ISIJ International, 1996, vol. 36 (8), pp. 1030-1035.

89. Shibata, H., Yin, H., Yoshinaga, S., EMI, T. and Suzuki, M.: "In-Situ Observation of Engulfment and Pushing of Nonmetallic Inclusions in Steel Melt by Advancing Melt/Solid Interface", ISIJ International, 1998, vol. 38 (2), pp. 149-156.

90. Winkler, C.M.: Large Eddy Simulations of Particle Dispersion and Deposition in a Turbulent Square Duct Flow, Ph.D. Thesis, University of Illinois at Urbana-Champaign, Urbana-Champaign, 2002.

91. Rani, S.L.: Direct Numerical Simulations of Two-Way Coupling Effects in a Particle-Laden Turbulent Pipe Flow & Evaluation of the Equilibrium Eulerian Approach for the Evolution of Particle Concentration in Isotropic Turbulence, Ph.D. Thesis, University of Illinois at Urbana-Champaign, Urbana, 2002.

92. Wilde, G. and Perepezko, J.H.: "Experimental Study of Particle Incorporation During Dendritic Solidification", Materials Science & Engineering A, 2000, vol. 283, pp. 25-37.

93. Uhlmann, D.R. and Chalmers, B.: "Interaction between Particles and a Solid-Liquid Interface", Journal of Applied Physics, 1964, vol. 35 (10), pp. 2986-2993.

94. Potschke, J. and Rogge, V.: "On the Behavior of Foreign Particle at an Advancing Solid-Liquid Interface", J. Crystal Growth, 1989, vol. 94, pp. 726-738.

95. Shangguan, D., Ahuja, S. and Stefanescu, D.M.: "An Analytical Model for the Interaction between an Insoluble Particle and an Advancing Solid/Liquid Interface", Met. Trans. A, 1992, vol. 23A (2), pp. 669-680.

96. Stefanescu, D.M. and Catalina, A.V.: "Note: Calculation of the Critical Velocity for the Pushing/Engulfment Transition of Nonmetallic Inclusions in Steel", ISIJ Int., 1998, vol. 38 (5), pp. 503-505.

97. Stefanescu, D.M., Juretzko, F.R., Dhindaw, B.K., Catalina, A. and Sen, S.: "Particle Engulfment and Pushing by Solidifying Interfaces: Part Ii. Microgravity Experiments and Theoretical Analysis", Metallurgical and Materials Transactions A, 1998, vol. 29A, pp. 1697-1706.

98. Catalina, A.V., Mukherjee, S. and Stefanescu, D.M.: "A Dynamic Model for the Interaction between a Solid Particle and an Advancing Solid/Liquid Interface", Metallurgical and Materials Transactions A, 2000, vol. 31A (10), pp. 2559-2568.

99. Han, Q. and Hunt, J.D.: "Particle Pushing: Critical Flow Rate Required to Put Particles into Motion", J. Crystal Growth, 1995, vol. 152, pp. 221-227.

100. KAPTAY, G. and KELEMEN, K.K.: "The Forces Acting on a Sphere Moving Towards a Solidification Front Due to an Interfacial Energy Gradient at the Sphere/Liquid Interface", ISIJ International, 2001, vol. 41 (3), pp. 305-307.

101. Kaptay, G.: "Reduced Critical Solidification Front Velocity of Particles Engulfment Due to an Interfacial Active Solute in the Liquid Metal", Metallurgical and Materials Transactions A, 2002, vol. 33A (6), pp. 1869-1873.

102. Kaptay, G.: "Interfacial Criterion of Spontaneous and Forced Engulfment of Reinforcing Particles by an Advancing Solid/Liquid Interface", Metallurgical and Materials Transactions A, 2001, vol. 32A (4), pp. 993-1005.

103. Kaptay, G.: "Discussion of "Particle Engulfment and Pushing by Solidifying Interfaces: Part Ii. Microgravity Experiments and Theoretical Analysis"", Metallurgical and Materials Transactions A, 1999, vol. 30A (7), pp. 1887-1890.

104. Stefanescu, D.M., Juretzko, F.R., Catalina, A., Dhindaw, B.K., Sen, S. and Curreri, P.A.: "Author's Reply", Metallurgical and Materials Transactions A, 1999, vol. 30A (7), pp. 1890-1894.

105. Bolling, G.F. and Cisse, J.A.: "A Theory for the Interaction of Particles with a Solidification Front", J. Crystal Growth, 1971, vol. 10, pp. 55-66.

106. Batchelor, G.K.: An Introduction to Fluid Dynamics, Cambridge University Press, Cambridge, UK, 1967, pp. 219-224.

107. Sen, S., Dhindaw, B.K., Stefanescu, D.M., Catalina, A. and Curreri, P.A.: "Melt Convection Effects on the Critical Velocity of Particle Engulfment", J. Crystal Growth, 1997, vol. 173, pp. 574-584.

108. Wang, Z., Mukai, K. and Lee, J.: "Behavior of Fine Bubble in Front of the Solidifying Interface", ISIJ International, 1999, vol. 39 (6), pp. 553-562.

109. Stefanescu, D.M., Juretzko, F.R., Dhindaw, B.K., Catalina, A. and Sen, S.: "Particle Engulfment and Pushing by Solidifying Interfaces: Part I. Ground Experiments", Metallurgical and Materials Transactions A, 1998, vol. 29A (6), pp. 1691-1696.

110. Han, Q.: The Mechanisms for Particle Pushing, Ph.D. thesis Thesis, University of Oxford, Oxford, UK, 1994.

111. Maxey, M.R. and Riley, J.J.: "Equation of Motion for a Small Rigid Sphere in a Nonuniform Flow", Physics of Fluids, 1983, vol. 26 (4), pp. 883-889.

112. Crowe, C., Sommerfild, M. and Tsinji, Y.: Multiphase Flows with Droplets and Particles, CRC Press, 1998, pp. 23-95.

113. Saffman, P.G.: "The Lift on a Small Sphere in a Slow Flow", Journal of Fluid Mechanics, 1965, vol. 22, p. 385.

114. Saffman, P.G.: "Corrigendum to "the Lift on a Small Sphere in a Slow Shear Flow"", Journal of Fluid Mechanics, 1968, vol. 31, p. 624.

115. McLaughlin, J.B.: "Inertial Migration of a Small Sphere in Linear Shear Flow", Journal of Fluid Mechanics, 1991, vol. 224 (262-274).

116. McLaughlin, J.B.: "The Lift Force on a Small Sphere in Wall-Bounded Linear Shear Flows", Journal of Fluid Mechanics, 1993, vol. 246, pp. 249-265.

117. Mei, R.: "Brief Communication: An Approximate Expression for the Shear Lift Force on a Spherical Particle at Finite Reynolds Number", Int. J. Multiphase Flow, 1992, vol. 18 (1), pp. 145-147.

118. Wang, Q., Squires, K.D., Chen, M. and McLaughlin, J.B.: "On the Role of the Lift Force in Turbulence Simulations of Particle Deposition", Int. J. Multiphase Flow, 1997, vol. 23 (4), pp. 749-763.

119. Barton, I.E.: "Computation of Particle Tracks over a Backward-Facing Step", Journal of Aerosol Science, 1995, vol. 26 (6), pp. 887-901.

120. Odar, F. and Hamilton, W.S.: "Forces on a Sphere Accelerating in a Viscous Fluid", Journal of Fluid Mechanics, 1964, vol. 18, pp. 302-314.

121. Odar, F.: "Verification of the Proposed Equation for Calculation of the Forces on a Sphere Accelerating in a Viscous Flow", Journal of Fluid Mechanics, 1966, vol. 25 (591-592).

122. Mukai, K. and Lin, W.: "Behavior of Non-Metallic Inclusions and Bubbles in Front of Solidifying Interface of Liquid Iron", Tetsu-to-Hagane, 1994, vol. 80 (7), pp. 533-538.

123. Keene, B.J.: "Review of Data for the Surface Tension of Iron and Its Binary Alloys", International Materials Reviews, 1988, vol. 33 (1), pp. 1-37.

124. Kurtz, W. and Fisher, D.J.: Fundamentals of Solidification, Trans Tech Publications LTD, Aedermannsdorf, Switzerland, 1986, pp. 47-96.

125. J-H.Jeong, Goldenfeld, N. and Dantzig, J.A.: "Phase Field Model for Three-Dimensional Dendritic Growth with Fluid Flow", Physical Review E, 2001, vol. 64, pp. 1-14.

126. Kurz, W. and Fisher, D.J.: "Dendrite Growth at the Limit of Stability: Tip Radius and Spacing", Acta Metall., 1981, vol. 29, pp. 11-20.

127. Press, W.H., Flannery, B.P., Teukolsky, S.A. and Vetterling, W.T.: Numerical Recipes, Cambridge University Press, New York, NY, 1988, p. 963.

128. Reeks, M.W. and Mckee, S.: "The Dispersive Effect of Basset History Forces on Particle Motion in a Turbulent Flow", Physics of Fluids, 1984, vol. 27, pp. 1573-1582.

129. Lim, H., Cho, Y., Cho, J. and Kim, K.-J.: "Surface Treatment and Characterization of Pmma, Phema and Phpma", Journal of Vacuum Science and Technology,A, 2001, vol. 19 (7), p. 14901496.

130. Thomas, B.G., Yuan, Q., Sivaramakrishnan, S. and Vanka, S.P.: Transient Fluid Flow in the Continuous Steel-Slab Casting Mold, JOM-e (Journal of Metals

Electronic Edition), 2002, http://www.tms.org/pubs/journals/JOM/0201/Thomas/Thomas-0201.html.

131. O'Malley, R.J.: "Observations of Various Steady State and Dynamic Thermal Behaviors in a Continuous Casting Mold", 82nd Steelmaking Conference, (Chicago, IL, March 21-24), TMS, 1999, pp. 21.

132. O'Malley, R.: AK Steel, private communication, 2003.

133. Schade, J.H., O'Malley, R.J., Kemeny, F.L., Sahai, Y. and Zacharias, D.J.: "Chapter 13: Tundish Operations", The Making, Shaping and Treating of Steel, 11th Edition, Casting Volume, The AISE Steel Foundation, 2003

134. Zhang, L. and Thomas, B.G.: "Inclusion Investigation During Clean Steel Production at Baosteel", ISSTech 2003, (Indianapolis, IN, 2003, pp. 577-592.

135. Girifalco, L.A. and Good, R.J.: "A Theory for the Estimation of Surface and Interfacial Energies. I. Derivation and Application to Interfacial Tension", Journal of Physical Chemistry, 1957, vol. 61 (7), pp. 904-909.

136. Jimbo, I. and Cramb, A.W.: "Interfacial Tension and Contact Angle Variations", The 6th International Iron and Steel Congress., (Nagoya, Japan, Oct. 26), ISS, 1990, pp. 499-504.

137. Kurz, W. and Fisher, D.J.: "Appendix 2: Solute and Heat Transfer Calculations Related to Microstructure Formation", Fundamentals of Solidification, vol. 153-173, Trans Tech Publications, 1986

138. Zhao, B.: Master Thesis Thesis, University of Illinois at Urbana-Champaign, Urbana, 2004.